Free-space transmission with passive two-dimensional beam steering for indoor optical wireless networks

Free-Space Transmission with Passive Two-Dimensional Beam Steering for Indoor Optical Wireless Networks

PROEFSCHRIFT

ter verkrijging van de graad van doctor aan de
Technische Universiteit Eindhoven, op gezag van de
rector magnificus prof.dr.ir. F.P.T. Baaijens, voor een
commissie aangewezen door het College voor Promoties,
in het openbaar te verdedigen op
donderdag 9 maart 2017 om 16.00 uur

door

Chin Wan Oh

geboren te Petaling Jaya, Maleisië

Dit proefschrift is goedgekeurd door de promotoren en de samenstelling van de promotiecommissie is als volgt:

voorzitter:	prof.dr.ir. A.B. Smolders
1^e promotor:	prof.ir. A.M.J. Koonen
copromotor(en):	dr.ir. E. Tangdiongga
leden:	prof.dr. D. O'Brien (University of Oxford)
	prof.dr. C. Lim (University of Melbourne)
	Priv.-Doz.Dr.rer.nat. V. Jungnickel
	(Fraunhofer Heinrich Hertz Institute)
	prof.dr. K.A. Williams
	prof.dr.ir. P.G.M. Baltus

Het onderzoek of ontwerp dat in dit proefschrift wordt beschreven is uitgevoerd in overeenstemming met de TU/e Gedragscode Wetenschapsbeoefening.

A catalogue record is available from the Eindhoven University of Technology Library.
ISBN: 978-90-386-4228-4
NUR 959
Title: Free-Space Transmission with Passive Two-Dimensional Beam Steering for Indoor Optical Wireless Networks
Author: Chin Wan Oh
Eindhoven University of Technology, 2017.

Keywords: Optical wireless communication / Beam steering / Infrared / Laser / Indoor

Typeset using LaTeX, printed in The Netherlands.

Acknowledgments

I would like to take this opportunity to thank everyone who has made this PhD possible.

Firstly, I would like to thank my supervisors, especially to Prof. Koonen, for the opportunity to do a PhD in the BROWSE project, which is part of the Advanced Investigator Grant project of Prof. Koonen, funded by the European Research Council within the FP7 program. His knowledge and enthusiasm continuously motivated me in my work. I would also like to thank the thesis committee, including reserved member Dr. Erwin Bente, not only for their insightful comments and encouragement, but also the constructive feedbacks which have definitely lead to a better thesis.

My sincere gratitude goes to colleagues of the ECO group especially to my camaraderie collaborators, my dear officemates and also to my lunch buddies not only for the fun discussions but also for their being there which made every lunch seemed more tasty.

My deepest appreciation also goes to collaborators from Keysight Technologies Netherlands, Rob Streeder and Gustaaf Sutorius, for their voluntary support, without which some experiments would not have been possible. Special thanks to Dr. Sylwester Latkowski from PHI group, and also to Prof. Johan Bauwelinck and Prof. Xin Yin from Ghent University for their constructive discussions and support. I am also grateful to my master students, Adrián Pérez Oliveros and Martijn Bech, whom have contributed to the work of this thesis.

My heartfelt gratitude goes to my ex-colleagues from Siemens Malaysia, Siemens-CLab Paderborn, Osram Opto Semiconductors Malaysia and Avago Technologies Malaysia, whom I was working closely with, whom I learned a lot from and whom have guided me during my early career years. I am grateful for the valuable trainings, advice and knowledge which have definitely contributed to my worthy experiences, skills and intellect.

Finally, I am eternally indebted to my family for the love and support all throughout my life. Also, I am very thankful for the lovely and supportive Bosman family. A big thanks also to my dearest and life-long friends for their continuous support. Last but not least, a hearty thanks to Hedde, whose love, support, patience and humor have rescued me from peril more times than I can remember.

Summary

Free-Space Transmission with Passive Two-Dimensional Beam Steering for Indoor Optical Wireless Networks

This work is part of the Beam-steered Reconfigurable Optical-Wireless System for Energy-efficient communication (BROWSE) project, funded by the European Research Council within the Seventh Framework Program. The main focus of the BROWSE project is to implement an indoor communication network employing short range Optical Wireless Communication (OWC) using pencil beams.

Recently, OWC has become increasingly important due to the shortage of available radio spectrum. Presently, new wireless services must share the same spectrum with existing services, thus, overcrowding the radio spectrum. This leads to interference among wireless devices, poor wireless link performances and unnecessary high wireless power consumption. In order to counter this problem, BROWSE is taking a radical new approach by performing wireless communication using optical rather than radio techniques by deploying optical pencil beam technologies to provide wireless users with access to an indoor optical fiber infrastructure. An architecture based on free-space optics has been adopted. The narrow infrared beam is seen as a high-potential solution because of its ability to optimally carry all the information which the optical fiber can transport, in an energy-efficient way.

The key to practical implementation of such high bandwidth optical beam links is in the technique to be used to direct these high capacity links in providing wireless channels to many users individually, simultaneously and dynamically. Beam-steering modules, termed as Pencil Radiating Antenna (PRA), are required to direct the beams to multiple users for the "last meters", bridging the gap between end-users and the fiber infrastructure. In this thesis, PRAs which are constructed using passive diffractive optics in conjunction with remotely controlled wavelength tuning at the central communication controller for beam steering are proposed. This results in solutions that not only fit the requirements mentioned but also enable easy plug-and-play without the need for local powering, thus, reducing installation complexities and promoting a remote software-controlled dynamic backbone network. The systems proposed are also easily scalable; additional beams can be created by just adding wave-

lengths, and thus, more users can be accommodated independently without affecting the channel capacity of other users.

In this thesis, early analysis has indicated the suitability of employing echelle gratings for beam steering purposes. Following this, a basic 1D-steered free-space transmission system is designed. The characteristics of the diffracted beams and the limits are theoretically analyzed. Then, the characteristics and the channel performances of the steered beams of different wavelengths are thoroughly evaluated on a bandwidth-limited testbed system deploying telecom transceivers with 10 Gigahertz (GHz) bandwidth. The results show a good correlation between theory and practice, achieving an angular coverage of 17.16° with a tuning range between 1500 nm and 1630 nm. The channel performances demonstrate a record high aggregate data rate of 36.7 Gigabit per second (Gbps) per channel, at the Forward Error Correction (FEC)-limit (BER $\leq 2 \times 10^{-3}$), over 2.5 m free-space distance using Discrete Multitone (DMT) modulation.

Following these positive results, a 2D PRA is designed and constructed. In order to have 2D area coverage with scanning functionality, two gratings are orthogonally cascaded to each other. The idea is that the first grating has multiple times smaller Free Spectral Range (FSR) than the second grating. An initial two-line scan is implemented using two reflective echelle gratings. A record high data rate is achieved with DMT signaling, with an aggregate data rate of 42.8 Gbps per channel at the FEC-limit, over 2 m reach. An angular coverage of $5.61° \times 12.66°$ is achieved with a wavelength tuning range between 1529 nm and 1611 nm. From the characterization study, two major drawbacks are identified. Firstly, there is considerable power loss, measured to be between -13.5 dB and -16 dB, for wavelengths between 1530 nm and 1600 nm. Secondly, the steering is only limited to a two-line scan.

With further analysis on the steering limits achievable, the 2D PRA design is further improved by using a reflective echelle grating cross-mounted with a transmission grating. Distinct improvements are obtained by having a loss of only between -4.79 dB and -6.15 dB for wavelengths between 1518 nm and 1600 nm. Also, an improvement from a two-line to seven-line scan is achieved, within an angular coverage of $5.62° \times 12.15°$ with wavelength tuning between 1511 nm and 1627 nm. At a free-space transmission distance of 2 m, the system demonstrates aggregate data rates of up to 41.4 Gbps per channel at the FEC-limit with DMT signaling and up to 15 Gbps at error-free (BER $\leq 2 \times 10^{-9}$) with On-Off-Keying (OOK)-Non-Return-to-Zero (NRZ) signaling. With 4-PAM signaling, up to 32 Gbps at FEC-limit is achieved at a distance of 3 m. The concept of the passive steering systems, the static and dynamic characterization, and the transmission performances will be detailed in the dissertation.

In consideration for practical implementation, several other related techniques are proposed and demonstrated. Firstly, a wide angle lens is employed to enlarge the Field of View (FoV) of the receiver. Then, beam expansion

and angular magnification techniques are explored to manipulate the pencil beams for wider angular coverage and variable size beams. Further, in a more advanced outlook, an all-optical full-duplex communication system has been demonstrated using the carrier recovery technique. A novel full-duplex all-optical wireless system supporting symmetric 10 Gbps channels over a free-space distance of 3 m with OOK-NRZ signaling is demonstrated. In a measure to fully utilize the laser source and lower the system cost, a time-slotted laser sharing system is demonstrated.

In conclusion, this thesis aims to provide high performance and large bandwidth wireless connectivity to indoor users by creating a synergy in technology between wired (optical fiber) and wireless (free space) communication. This dissertation reports the promising potential of the proposed 2D-steered pencil-beam infrared optical wireless solution for the realization of future ultra-high capacity energy-efficient wireless indoor networks.

Contents

List of Figures

List of Tables

Acronyms

1D	one-dimensional
2D	two-dimensional
3D	three-dimensional
4G	Fourth Generation
5G	Fifth Generation
ANSI	American National Standards Institute
AP	Access Point
AWG	Arbitrary Waveform Generator
AWGr	Arrayed Waveguide Grating
APD	Avalanche Photodetector
AEL	Accessible Emission Limit
ASE	Amplified Spontaneous Emission
BER	Bit Error Rate
BiCMOS	Bipolar Complementary Metal-Oxide-Semiconductor
BtB	Back-to-Back
BROWSE	Beam-steered Reconfigurable Optical-Wireless System for Energy-efficient communication
BERT	Bit Error Rate Tester
BFL	Back Focal Length
CAP	Carrier-less Amplitude and Phase
CCC	Central Communication Controller

CMOS Complementary Metal-Oxide-Semiconductor

CPC Compound Parabolic Concentrator

DBIR Directed-beam Infrared

DBR Distributed Bragg Reflector

DFE Decision Feedback Equalizer

DFB Distributed Feedback Laser

DFIR Diffused Infrared

DMT Discrete Multitone

DPO Digital Phosphor Oscilloscope

DSL Digital Subscriber Line

DSSS Direct sequence spread spectrum

ECL External Cavity Laser

EDFA Erbium-Doped Fiber Amplifier

EFL Effective Focal Length

EMI Electromagnetic Interference

EMP Electrowetting Microprism

ER Extinction Ratio

FCC Federal Communications Commission

FEC Forward Error Correction

FFoV Full-Field of View

FFT Fast Fourier Transform

FITH Fiber-In-The-Home

FoV Field of View

FPR Free Propagation Region

FS Free Space

FSO Free-Space Optics

FSR Free Spectral Range

FHSS Frequency Hopping Spread Spectrum

FTTB Fiber-To-The-Building

FTTH Fiber-To-The-Home

FWHM Full Width Half Maximum

Gbps Gigabit per second

GBaud Gigabaud

GHz Gigahertz

GRIN Graded Index

GS/s Gigasymbol per second

HDTV High-Definition Television

HetNet Heterogeneous Network

IEC International Electrotechnical Commission

IEEE Institute of Electrical and Electronics Engineers

IFFT Inverse Fast Fourier Transform

IL Insertion Loss

IM-DD Intensity Modulation - Direct Detection

IoT Internet of Things

IR Infrared

IrDA Infrared Data Association

ISI Inter-Symbol Interference

ISM Industrial Scientific and Medical

kbps kilobit per second

LAN Local Area Network

LC Liquid Crystal

LCoS Liquid Crystal on Silicon

LD Laser Diode

LED Light Emitting Diode

LiFi Light Fidelity

LIDAR Light Detection and Ranging

LoS Line-of-Sight

MAC Medium Access Control

Mbps Megabit per second

MEMS Micro-Electro-Mechanical System

MHz Megahertz

MIMO Multiple-Input-Multiple-Output

MMF Multimode Fiber

MOEMS Micro-Opto-Electromechanical System

MPE Maximum Permissible Exposure

MZI Mach-Zehnder Interferometer

MZM Mach-Zehnder Modulator

NLoS Non-Line-Of-Sight

NRZ Non-Return-to-Zero

NA Numerical Aperture

OWC Optical Wireless Communication

OOK On-Off-Keying

OFDM Optical Frequency Division Multiplexing

OPA Optical Phased Array

OXC Optical Cross-Connect

OEIC Optoelectronic Integrated Circuit

OFDM Orthogonal Frequency Division Multiplexing

OSA Optical Spectrum Analyzer

OA Optical Amplifier

PAM Pulse Amplitude Modulation

PD Photodetector

PDL Polarization Dependent Loss

PIC Photonic Integrated Circuit

PIN P-doped Intrinsic N-doped

PLC Power Line Carrier

PoE Power over Ethernet

PON Passive Optical Network

PRA Pencil Radiating Antenna

PRBS Pseudo Random Binary Sequence

PtP Point-to-Point

PTR Photo-Thermo-Refractive

QAM Quadrature Amplitude Modulation

QDIR Quasi-Diffuse Infrared

QoE Quality of Experience

QoS Quality of Service

QPSK Quadrature Phase-Shift Keying

RAP Radio Access Point

RoF Radio-over-Fiber

RC Resonant-Cavity

RF Radio Frequency

RGB Red+Blue+Green

REAM Reflective Electro-absorption Modulator

RSOA Reflective Semiconductor Optical Amplifier

RTO Real-Time Oscilloscope

RZ Return-to-Zero

SOA Semiconductor Optical Amplifier

SOI Silicon-On-Insulator

SLM Spatial Light Modulator

SMF Single Mode Fiber

SNR Signal-to-Noise Ratio

TE Transverse-Electric

THz Terahertz

TIA Transimpedance Amplifier

TLS Tunable Laser Source

TM Transverse-Magnetic

TRx Transceiver

UV Ultraviolet

US United States

USB Universal Serial Bus

VBG Variable Blaze Grating

VCSEL Vertical Cavity Surface Emitting Laser

VIPA Virtually Imaged Phased Array

VLC Visible Light Communication

VLCC Visible Light Communication Consortium

WDM Wavelength Division Multiplexing

WiFi Wireless Fidelity

WiGig Wireless Gigabit

WGR Waveguide Grating Router

Chapter 1

Introduction

Contents

The arrival of a wide variety of connected devices in relation to the Internet of Things (IoT) phenomena has been received with enthusiasm as technology evolves into more sophisticated forms and functions. With the advancement in technology towards enabling smart devices, smart buildings and smart cities, people, devices and information are becoming more interconnected than ever. In order to keep up with the demands for ubiquitous on-demand connection anytime and anywhere, the proliferation of mobile yet connected devices and high bandwidth demand applications is starting to revolutionize wireless communication, from simple gadgets such as a connected watch, alarm clock or coffee maker to complex devices and environments. As can be seen in Figure 1.1, in the year 2008, there were already more devices connecting to the internet than there are people on earth [1]. However, according to Cisco®, the IoT phenomena will be driving an exponential increase in the number of connected devices, up to a figure of 50 billion, by the year 2020. The impact of such

a huge scale of increase in connected devices is not subtle. Huge transfers of information are happening at a tremendous capacity every day.

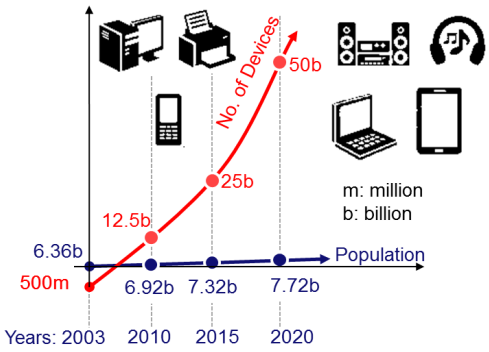

Figure 1.1: Exponentially increasing number of connected devices, compared to population increase between year 2003 and 2020 [1].

In 2004, Phil Edholm, who was then Nortel's chief technology officer and vice president of network architecture, noted that we may someday see the end of wireline for the last few meters connection to the users (people/machine) [2]. According to Edholm's law, cellular and Wireless Fidelity (WiFi) data rates would converge around year 2030. In addition, with the increasing amount of consumer products, about 80 % of mobile data is generated indoors [3]. High-speed and on-the-spot communication has been a persistent demand since the data over wireless technology was introduced. As a consequence, this has resulted in today's heavy congestion of the Industrial Scientific and Medical (ISM) bands, as shown in Figure 1.2, which are allocated for unlicensed operation.

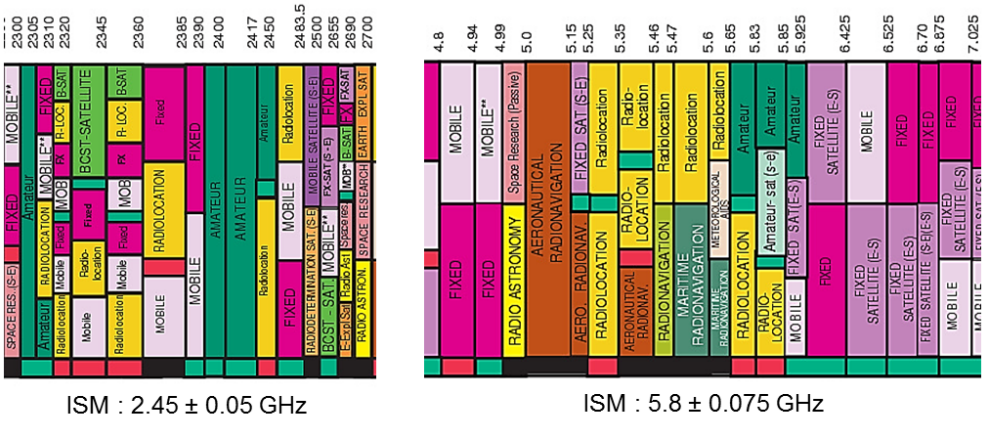

Figure 1.2: Spectrum allocation within the FCC unregulated ISM bands centered at 2.45 GHz and 5.8 GHz. Cropped from [4].

Since 2009, data over wireless has been supported by WiFi, which offers a maximum bitrate of up to 600 Megabit per second (Mbps) with the Institute of Electrical and Electronics Engineers (IEEE) 802.11n standard which uses the 2.4 Gigahertz (GHz) and the 5 GHz band. At the end of 2013, IEEE 802.11ac has been released at the 5 GHz band (which has less congestion) which supports a bitrate of up to 6.93 Gigabit per second (Gbps). However, these speeds are hardly seen in practice as these speeds are offered on a medium shared by multiple users. The Medium Access Control (MAC) protocols partition the speed among multiple users and this requires some overhead to do that properly. Additionally, the IEEE 802.11ad protocol was released in 2012 based on the 60 GHz band and supports a bitrate of up to 7 Gbps (57 to 64 GHz) for ultra-high-speed operation within a room. The unregulated 60 GHz ISM band provided by the Federal Communications Commission (FCC) is limited to only 7 GHz of the spectrum [5, 6]. Continuous growth of traffic led by the increase in high bandwidth applications such as High-Definition Television (HDTV), high quality video conferencing, 3D videos, online video gaming, peer-to-peer networking, etc. will demand ever more bandwidth. According to Cisco, mobile data traffic will increase to a whopping ten-fold between 2014 and 2019 [7]. It is becoming clear that the available radio spectrum is getting exhausted due to bandwidth limitations [8]. Consequently, interference among devices decreases channel throughput, degrades the Quality of Service (QoS), increases wireless power consumption and inevitably results in costly services due to the inability of wireless service providers to provide more capacity.

Counter measures such as the acquisition of underused licensed sub-bands are very costly [9]. Efforts are seen in advocating small cells architectures such as femtocells and picocells in order to support the increase in network capacity for indoor networks [10, 11]. Cellular network operators implement data-offloading from cellular traffic to fixed wireless Local Area Network (LAN) or femtocell networks [12, 13, 14] wherever possible. In 2015, mobile offload exceeded cellular traffic for the first time with 51% of total being mobile data traffic offloaded. This is a cost-effective way for mobile operators while at the same time, mobile users also enjoy the higher speed in LAN networks. At the moment, there are still many efforts in trying to squeeze more and more data into the available radio bandwidths at the ISM bands centered at 2.4 GHz, 5 GHz and 60 GHz, to improve spectral efficiency in order to support larger capacity. Inevitably, complex digital signal processing and advanced modulation formats are needed, which will take a toll on the energy consumption of radio communication and result in higher operating cost. However, the inherent spectrum limit prevents radio wireless bandwidth from approaching the capacity achievable in the optical spectrum.

In an unlicensed approach, Optical Wireless Communication (OWC) is an area which offers a promising technology in combating the radio spectrum crisis. The optical spectrum offers bandwidths orders of magnitude higher than that available in the Radio Frequency (RF) spectrum. OWC solutions

are usually proposed in the visible and Infrared (IR) spectrum. The radio spectrum ranges between 3 kHz and 300 GHz while the visible and infrared optical region covers the spectrum from the 200 Terahertz (THz) up to 750 THz. This very high frequency optical spectrum region literally brings with it a huge amount of bandwidth. In other words, the optical spectrum can easily support high bandwidth channels that can carry ultra-high data rates.

Corresponding to the hundreds of Terahertz frequency band, the wavelengths of the optical spectrum is in the micrometer range. This very short wavelengths result in a distinct wave behavior. Optical waves do not penetrate walls, and therefore, have high physical security and their spectrum is unregulated. However, the inability to propagate through opaque surfaces could be a disadvantage due to possible blockage of communication links leading to the risk of a connection drop, which on the other hand, can also be perceived as more secure or sensitive to eavesdropping. Optical waves are also insensitive to Electromagnetic Interference (EMI) thereby making it ideal for electromagnetic sensitive places such as hospitals and air planes. In addition, it can offer spatial diversity that prevents multipath fading due to short carrier wavelength and large-area square-law detector [15]. In a direct-detection receiver, the square law nature doubles the effective path loss (in dB) when compared to a linear detector [16]. Additionally, a diverging optical wave will be affected by the inverse square loss law, whereby power loss is proportional to distance-squared. Also, background noise due to lamps and sunlight contributes additional noise. In diffuse systems, multipath distortion causes Inter-Symbol Interference (ISI). Another limitation is imposed by regulations that for all intents and purposes, the transmitted power of the optical beams has to be compliant to skin- and eye-safety regulations enforced by the American National Standards Institute (ANSI) Z136 [17] and International Electrotechnical Commission (IEC) 60825 [18] standards for indoor use.

1.1 Optical wireless communication for indoors

OWC is a form of optical communication in which Ultraviolet (UV), visible and IR light can be used to carry a communication signal [19]. It is the earliest form of communication. In ancient times, the need for communication has been fulfilled by beacon fires and smoke to signal messages from one location to another. Sunlight has been used to signal messages by reflecting the sun using reflective objects. Centuries later, in 1888, Alexander Graham Bell and his assistant, Charles Sumner Tainter, came up with an ingenious invention which is known as the “photophone”. It is an apparatus for the production and reproduction of sound by means of light [20, 21]. With the advantage of its inability to be intercepted by war enemies, the application of the photophone was limited to military and space communication.

The idea of optical wireless communication became interesting again with

the invention of the laser [22], IR Light Emitting Diode (LED) [23, 24], and fiber optics in 1960's. In the 90's, the idea of using ground-to-satellite and satellite-to-ground communication using red and green laser became popular [25]. After year 2000, Free-Space Optics (FSO) technologies gained interests in civil and military applications ranging from standard telecommunication [26, 27] to undersea [28] and inter-satellite or space [29] communication employing wavelengths from 1 up to 10 μm [25, 30]. Besides communication, FSO technologies are also popular in optical metrology for "no-contact" measurement systems [31]. More recently, due to its prominent bandwidth advantage, OWC is seen as an access technology, complementary to radio for high-speed short-range communication links in the Fourth Generation (4G) and Fifth Generation (5G) networks [3, 32, 33].

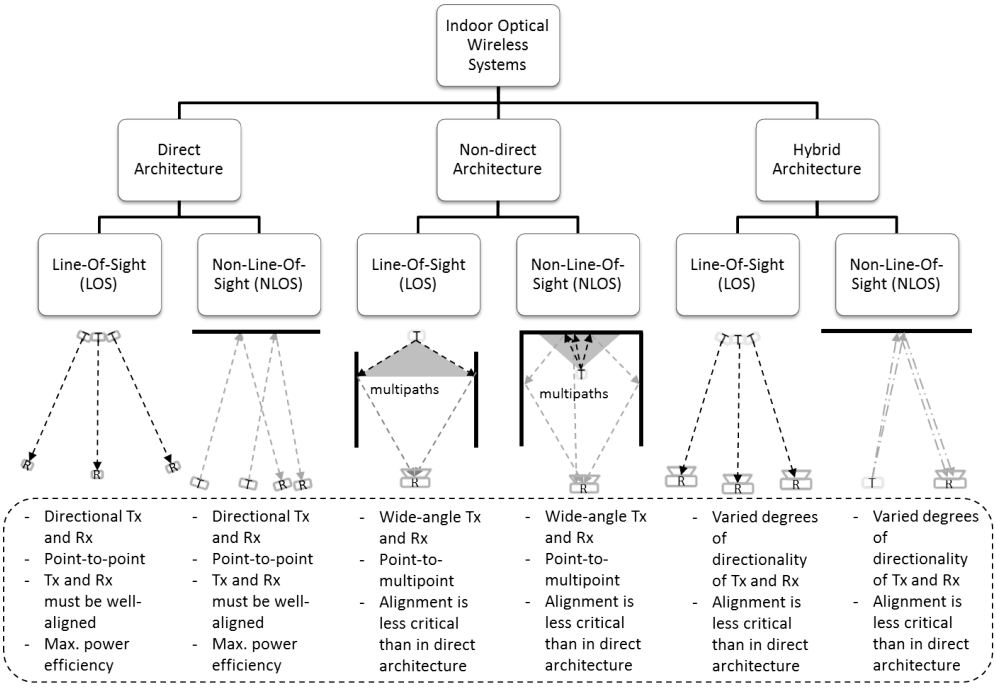

Figure 1.3: Types of indoor optical wireless architecture [15, 34].

Figure 1.3 shows an overview of the basic types of architectures for indoor optical wireless systems [15, 34]. Each type of architecture, i.e. the direct, the non-direct and the hybrid types, can be implemented using Line-of-Sight (LoS) or Non-Line-Of-Sight (NLoS) methods. In general, the direct architecture provides a point-to-point configuration and requires good alignment while the non-direct architecture enables point-to-multipoint configuration and a less critical alignment is needed. In fact, the direct architecture is able to provide a higher link power budget in a particular direction, which could mean

that mobility could be limited unless a dense tabulation of location points is carefully designed. Besides this, localization and continuous tracking functionalities could help to maintain connections in order to provide mobility to users [35, 36, 37, 38]. On the other hand, LoS links are susceptible to severe shadowing or blockage. In hybrid systems, a combination of transmitters and receivers of varying degrees of directionality can be employed.

In 1979, F.R. Gfeller and U. Bapst proposed in-house infrared communication via a diffuse beam operating at 950 nm and achieved 1 Mbps [39]. The concept was further explored for in-building [40] applications, for e.g., in-office systems [41, 42, 43], local wireless networks [44], and short-range intercom systems [45]. Several early works in the late 80's and early 90's have achieved data rates in the order of Mbps [46]. In 1994, 1 Gbps was successfully demonstrated in the lab by BT Labs using a wide angle LoS cellular scheme [36, 47]. The cellular architecture was to combine the mobility advantage in diffuse beam with the low power and high speed LoS architecture. These pioneering works largely employed infrared lasers as the source of transmission [15, 34, 46, 48]. Besides the higher bandwidth of a laser diode, it has the advantage of large market applications. For example, the compact disc players contributed to the availability of infrared laser diodes in the 800 nm - 950 nm wavelengths, which are both robust and inexpensive [44]. The Infrared Data Association (IrDA) standard was formed in 1993, thereafter the standard was widely adopted for short range communication. In 2010, the European Community project OMEGA demonstrated a bi-directional OWC one-dimensional (1D) system operated at 1.25 Gbps at (Bit Error Rate (BER) $\leq 1 \times 10^{-9}$) Non-Return-to-Zero (NRZ) On-Off-Keying (OOK) format [49]. The access point terminal had three transmitter sections forming a Field of View (FoV) of $25^\circ \times 8^\circ$ over 3 m. Angular diversity receivers of similar FoV were used.

Unlike infrared free-space communication, the Visible Light Communication (VLC) technology combines both communication and illumination by piggy-backing communication on the existing lighting infrastructure which is based on LED. VLC was driven by the progress of white LED for solid state lighting [50, 51]. An early experiment was reported in 1999 by G. Pang et al. in which they have modulated visible LEDs for audio broadcast from an LED traffic signal head constructed using 441 high brightness LEDs [52]. Also, Y. Tanaka and T. Komine proposed VLC using white LED in 2001 and 2004, respectively [53, 54].

A data rate of 3.22 Gbps over more than 25 cm distance in a VLC system was demonstrated by F.-M. Wu et al. in 2013 [55]. The technique of Wavelength Division Multiplexing (WDM) using Red+Blue+Green (RGB) LEDs and transmission using Carrier-less Amplitude and Phase (CAP) signaling were employed. In 2014, a 3 Gbps Orthogonal Frequency Division Multiplexing (OFDM) VLC transmission at Forward Error Correction (FEC) limit [56] was reported by D. Tsonev et al [57]. This was achieved using a Gallium Nitride μLED of at least a -3 dB modulation bandwidth of 60 Megahertz (MHz),

with a transmission distance set to 5 cm, limited by the optical power of the μLED. In 2015, G. Cossu et al. demonstrated a duplex system with data rates of up to 5.6 Gbps for downlink and 1.5 Gbps uplink at 1.5 m. They used a WDM of 4 wavelengths and employed the Discrete Multitone (DMT) modulation format [58]. Recently, in 2016, by using a combination of red Resonant-Cavity (RC)-LED, blue μLED and green μLED, H. Chun et al. [59] achieved an aggregate data rate of 11.2 Gbps with an average BER of 3.3×10^{-3} at 984 lux over 1.5 m reach. The -3 dB bandwidth for each LED is approximately 100 MHz. Also in 2016, a record transmission data rate of 5 Gbps with OFDM modulation format and by employing a single μLED has been reported by R.X.G. Ferreira [60]. The μLED and photodetector were kept at approximately 75 cm apart.

Further developments on FSO communication systems, which are based on narrow-beam OWC systems with beam steering requirements, will be elaborated in Chapter 2 (Related work).

1.2 Visible light communication versus infrared optical wireless communication

1.2.1 Visible light communication

OWC in the visible light spectrum spans over a range between 400 nm (750 THz) and 700 nm (430 THz). It is also known as VLC. Typically LEDs are used as the transmission source. Laser diodes can also be used but they are normally deployed with a diffuser for eye-safety reasons. White LEDs are now a popular source of lighting as an alternative to tungsten and fluorescent lamps due to their long lifetime and low power consumption. LEDs nowadays have competitive efficacy (lumen/Watt), cost (lumen/dollar) and lifetime. Thus, LED lighting platforms are considered interesting for communication purposes [61, 62, 63].

White LEDs are commonly constructed using two combinations. The first is a combination of a blue LED with phosphor and the other is a combination of red, blue and green LEDs. The blue LED chip typically has a -3 dB frequency response of approximately 15-20 MHz while its performance can be limited by the phosphor layer which has a -3 dB bandwidth of approximately 2 MHz. The tricolor RGB white LED has a frequency response of approximately 10-20 MHz for each LED chip. The limited bandwidth is due to the carrier recombination lifetime in the semiconductor material of the LED. These LEDs can only support communication with speeds of Mbps. However, the current μLED and RC-LED, have a bandwidth of approximately 100 MHz.

In terms of backbone network infrastructure, LED lighting can be integrated with the Universal Serial Bus (USB), Power over Ethernet (PoE) or Power Line Carrier (PLC) technologies depending on the distances needed.

They can provide power and data on the same medium and transport them to the lamps. In 2015, Y. Wang et al. have proposed a Single Mode Fiber (SMF) based network architecture for VLC using OFDM modulation format with a total bi-directional throughput of 8 Gbps at a BER of $< 3.8 \times 10^{-3}$, over 65 cm free space propagation distance [64].

Recently, the term Light Fidelity (LiFi) is introduced to describe a complete VLC networking system [65, 66]. Early VLC standardization in the IEEE 802.15.7, which focused on point-to-point communication and dimming support, is being revised to include LiFi, which supports bi-directional multiuser communication and user mobility [67, 68].

1.2.2 Infrared optical wireless communication

OWC operating in the infrared spectrum commonly centered at 850 nm (353 THz), 1310 nm (229 THz) and 1550 nm (193 THz), in a Point-to-Point (PtP) configuration, is widely known as IR FSO communication. As typically IR lasers are employed, the source has a narrow beam compared to an LED. Correspondingly, a very high bandwidth transmission can be achieved which in most cases, the bandwidth of the system is only limited by practical implementation constraints such as eye-safety compliant power, transceiver bandwidth, filter and photoreceiver bandwidths, and switching and modulation speeds.

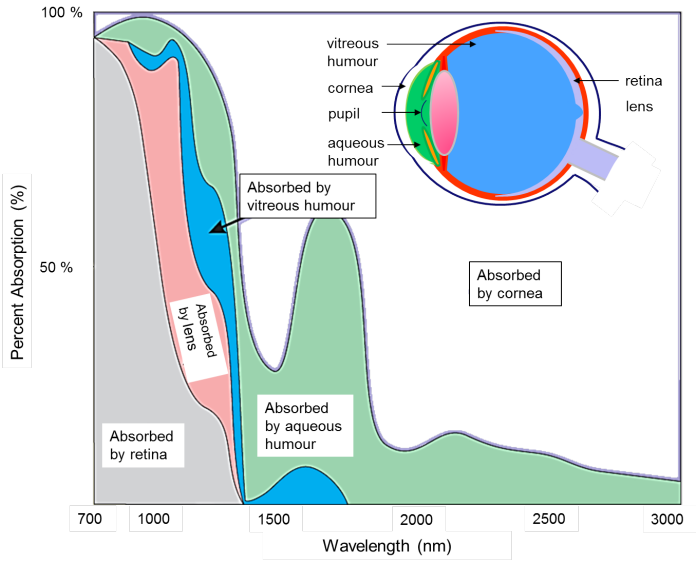

Figure 1.4: Absorption of infrared radiation by various ocular structures as a function of wavelength [69]. An eye model is provided at the top right as a reference to the corresponding absorption layers of the eye.

Since IR radiation is non-visible, it is subjected to eye-safety regulations by the IEC 60825 [18] and ANSI Z136 [17]. In fact, the eye-safety limits are

related to the absorption of light at different wavelengths in the eye (see Figure 1.4). The cornea and the lens absorb a small but significant amount of near-IR wavelengths of 780 nm to 1400 nm [69]. A small amount is absorbed by the aqueous and vitreous humours, while the remaining goes to the retina. Wavelengths > 1400 nm are largely absorbed in the cornea, followed by the aqueous and a small amount in the vitreous humours, thus, preventing its reach to the retina. As a result, the threshold damage is higher in the IR regime for $\lambda > 1400$ nm compared to visible light regime. This leads to a more relaxed constraint on the permissible transmission power and beam width from the visible to IR wavelengths > 1400 nm [44, 48, 70, 71]. Please refer to Section 4.5 for eye-safety calculations.

In practical system implementation, IR systems operating in the O-to-L bands (1260 nm to 1625 nm) could benefit from the existing telecom facilities [72]. The low-loss optical fiber technology in the telecoms bands, as shown in Figure 1.5, facilitates an infrastructure that carries a huge bandwidth covering not only over intercontinental distances but also within our homes. This is exemplified in the quickly expanding Fiber-To-The-Home (FTTH) and Fiber-To-The-Building (FTTB) network with Europe reaching more than 35.9 million subscribers in 2015 while the total FTTH subscribers in the United States (US) has surpassed 100 million in 2014 [73, 74]. In fact, this huge bandwidth can be harvested also for wireless short reach by tapping off the light signal propagating in the fiber, and redirecting it to free space for communication. The system implementation can be potentially low-cost by reusing fiber communication devices which are available commercially. Also, it can benefit from the possibility of direct-feeding of high-speed signal from the access networks. Besides, the backbone indoor network can be implement by an optical fiber (e.g. SMF, Multimode Fiber (MMF)) distribution network for high-speed information transfer.

1.2.3 Ambient light effect on visible light communication and infrared free-space optical communication

VLC and IR FSO systems are prone to ambient lighting which contributes shot noise in the photoreceivers. The effects are more severe in a VLC system since it shares the same spectrum as lighting sources such as LED, sunlight, fluorescent lamps and to some extent, the incandescent lamp [44]. An incandescent lamp, which has a high spectral content in the IR spectrum does more harm to the IR system but incandescent lamps are now being gradually replaced by fluorescent and LED lamps.

1.3 The proposed system in the BROWSE project

The work reported in this dissertation is part of the Beam-steered Reconfigurable Optical-Wireless System for Energy-efficient communication (BROWSE)

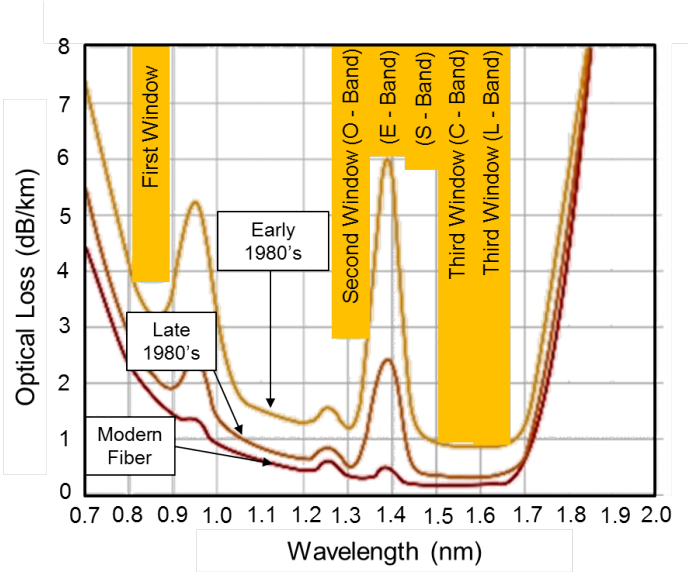

Figure 1.5: Fiber attenuation versus wavelength and the transmission windows with different telecom bands indicated. Modified from [72].

Advanced Grant project, funded by the European Research Council within the Seventh Framework Program (FP7). Motivated by the shortage of available radio spectrum, the BROWSE project's mission is to take a radical approach by performing wireless communication using the optical rather than the radio spectrum. There are two main objectives in the BROWSE project. The first objective is to deploy the mature technologies of optical communication in the wireless communication arena, in order to make a significant improvement in available wireless capacity. The second objective is to disclose and allocate this giant wireless capacity in a well-structured, energy-efficient and dynamic (on-demand) way to the users, while this capacity has to be dynamically tailored to their service requirements and varying locations.

The main challenge of the project is in combining novel free-space optical communication techniques with techniques for intelligent autonomic signal routing through an optical fiber indoor backbone network and for advanced radio communication, in a powerful blend which can realize a giant step forward in wireless communications. In facing this challenge, the BROWSE project proposes to deploy narrowly confined optical pencil beams aided by fast beam steering for ultra-high capacity interference-free communication, intelligent signal routing through an optical fiber backbone network, advanced radio techniques for accurate device localization, and an autonomic network management and control system for the tracking of users, for overall routing of services and for service delivery tailoring. The BROWSE project has been divided into five subprojects:

1. **Free-space optical communication with optically controlled beam steering.**
   This subproject concerns the implementation of passive 2D beam-steered optical pencil beams for downstream communication. The system should be scalable to large amounts of beams per room, each providing an ultra-high data capacity, and should use steering techniques which enable user-tracking by means of remote control from the central unit which houses the network management intelligence.

2. **Format-transparent dynamical optical signal routing in fiber backbone network.**
   This subproject concerns the implementation of a dynamic routing indoor fiber backbone network using radio over fiber techniques which supports optical downstream and 60 GHz radio upstream communication.

3. **Advanced radio communication techniques including device location discovery and tracking.**
   This subproject manages the radio antennas based on phased array techniques and investigates device localization techniques. Location information from the upstream radio link could be obtained from the multiple antenna elements located at the respective multiple Access Points (APs).

4. **Autonomic network management and control.**
   This subprojects concerns the implementation of network intelligence by implementing suitable protocols, routing logics and autonomous resource management to localize and track users, to control signal routing to different rooms and steering coordination inside a room.

5. **System integration, performance analysis and validation.**
   The objective of this subproject is to integrate, evaluate and validate the complete system which consists of the subsystems from the four subprojects mentioned above.

The five subprojects are founded as five different work packages. Correspondingly, this dissertation addresses the first subproject, which is to realize a free-space optical communication system with optically controlled beam steering. The main objective of this dissertation is to analyze and to implement narrowly-confined optical pencil beams using wavelength-controlled beam steering to provide orders of magnitude higher data capacity per user at ultra-high optical carrier frequencies.

The proposed architecture of the in-building hybrid optical-radio wireless-equipped home with optical beams is shown in Figure 1.6. The model can be divided into three major sections, being the Central Communication Controller (CCC), the wireless communication medium and the receiving end. The fiber backbone network routes data signals in a point-to-point manner from the CCC

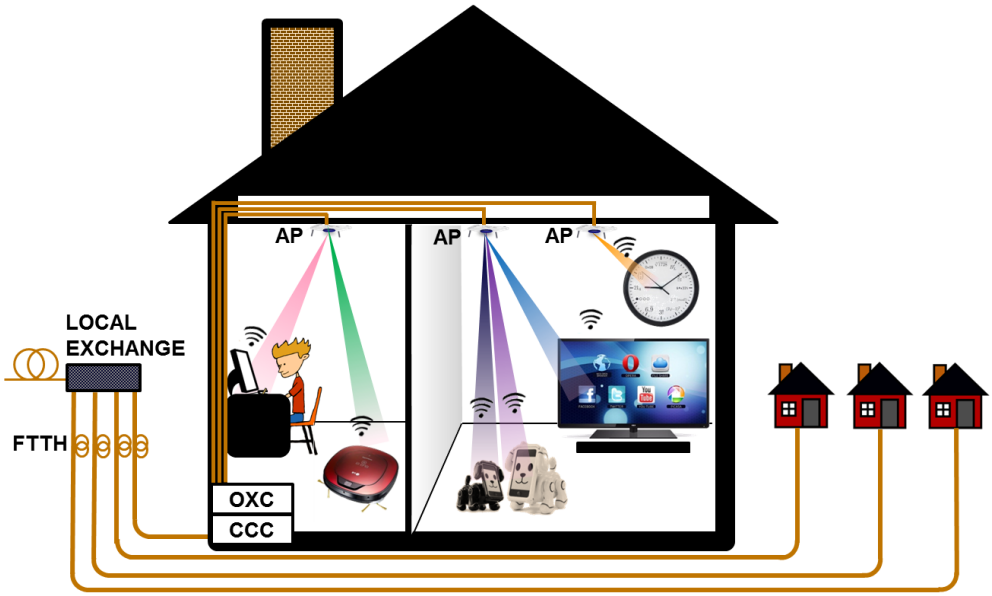

Figure 1.6: Architecture of BROWSE project's hybrid optical-radio wireless smart building. AP: Access Point, OXC: Optical Cross-Connect, CCC: Central Communication Controller.

to each AP. Multiple APs, with each containing a 2D optical beam-steering device, can be employed to increase the coverage area, to act as a backup link in the case where the beam from a certain direction is blocked, and to aid in user localization and tracking.

1.3.1 Central communication controller

At the transmitter side, the CCC manages the interfacing between the indoor and outdoor networks. The indoor network is totally independent of the access network. In the case in Figure 1.6, data signals from the access network are transported to the smart home using the FTTH technology while the in-building network uses Fiber-In-The-Home (FITH) technologies. Network interfacing protocols, routing logics and autonomous resource management are installed at the CCC. Data signals are routed by the Optical Cross-Connect (OXC) to the corresponding APs through the optical fiber distribution network. SMF or MMF fibers, which typically have a huge bandwidth, can transport a large amount of data to the APs. These fibers can be, for e.g., embedded within the walls of the building.

The fundamental intention of the system is to provide a single beam to each individual device. In order to provide multiple beams simultaneously, multiple tunable lasers will be required in the CCC. This can be realized by putting multiple tunable laser devices in parallel and combine their outputs onto the

fiber feeding the AP, or by an on-chip integrated array of tunable lasers. In such scenarios, several wavelengths can be provided simultaneously depending on the number of devices in the room [75]. On-chip widely tunable sample-grating distributed Bragg reflector laser and Distributed Feedback Laser (DFB) diode array have been reported in [76] and [77], respectively, with each enabling 30 nm tuning range. The selection of the source to be installed will depend on the timely progress and costs of these sources. Alternatively, to reduce the number of lasers needed and to benefit from the fast laser tuning times available, one may opt for a time-slotted system in which each user is served by a specific wavelength during a specific time slot and where the tunable laser changes its wavelength in the guard time between these time slots. This will obviously reduce the capacity attainable per device, but also reduce the CCC's costs.

1.3.2 Wireless communication medium

In the wireless communication medium, we use free-space LoS pencil beam techniques for the downlink, and 60 GHz radio and Radio-over-Fiber (RoF) technique for the uplink. In each individual room one or more APs, each equipped with a beam-steering module termed as Pencil Radiating Antenna (PRA) and a Radio Access Point (RAP), shall be implemented depending on the size of the coverage area. As we are working with LoS optical pencil beams, beam steering is necessary in order to direct the LoS beams from the AP toward multiple users. Practical considerations for selecting a steering method include the ease of installation, enabling plug-and-play, without any local processing and without local powering. In order to maintain data integrity and speedy service provision for a group of users simultaneously, with as low as possible transmission power, the beam-steering module has to be optimized for low-loss in the wavelength range of operation, has to be accurate, has to be reliable, has to support scalability, has to require little or no maintenance, has to have high response speed and a good coverage area, and its beam steering should be easily controllable from a remote location (i.e. the CCC). Taking into account these key requirements, we propose the use of passive diffraction gratings for beam steering in cooperation with remote wavelength-tuned source in the CCC. The passive nature of the beam-steering module renders it independent from moving parts or electronically-controlled elements, which may be prone to failure.

Regarding eye-safety, the Maximum Permissible Exposure (MPE) is expressed in W/m^2 and is typically defined for full human pupil opening of 0.39 cm^2 [78]. Infrared light with a wavelength longer than about 1400 nm is absorbed by the transparent parts of the eye before it reaches the retina, which means the MPE is higher than for visible light [78]. This is a major reason BROWSE opted for 1.5 μm wavelength region.

Since typically the upstream speed is lower than the downstream speed (asymmetric network), a radio technique for upstream can suffice. Preliminary

work in the 60 GHz domain which reported a reconfigurable indoor network using a photonic integrated chip was recently reported in [79]. Bi-directional transmission rates of > 35 Gbps have been achieved using DMT signaling. The 60 GHz signals are carried via an RoF technique back to the CCC. This configuration can be implemented with a Reflective Semiconductor Optical Amplifier (RSOA) or a Reflective Electro-absorption Modulator (REAM)-Semiconductor Optical Amplifier (SOA) to modulate the upstream data.

In support for mobility, it is important that users are quickly localized and also tracked in order to minimize connection latency or failure. For this purpose, radio and optical localization techniques can be employed to locate and track the positions of the mobile devices. Radio techniques can be used to implement coarse localization. In [80], Winkler et al. have presented the capability of achieving accuracies of up to 50 cm using 60 GHz for localization. To complement the radio localization, fine-tuning shall be implemented optically by means of wavelength tuning and beam-manipulation. In 2011, G. Cossu et al. introduced a visible light localization technique with receiver tracking. The transmission distance was 90 cm and the angular resolution achieved was $< 1^\circ$ [81]. In [82], Wang et al. have demonstrated an average accuracy within 2.41 cm using background light power estimation in a 2 m transmission. In [83], Gomez et al. have demonstrated localization and tracking with an accuracy of 0.05° (pointing accuracy of 2.5 mm at 3 m distance) using a Complementary Metal-Oxide-Semiconductor (CMOS) camera at the base station observing LED IR tags at the nomadic user terminal.

1.3.3 Receiving end

At the receiver side, the mobile device is equipped with a simple optical receiver and a radio transmitter in order to receive the downlink optical signal and to transmit a radio signal for the uplink. For fallback scenarios, the system can be backed up at the WiFi bands for bi-directional communication in case the optical link fails due to shadowing loss of the LoS condition or due to system error.

Finally, to benefit from the already existing facilities used in the core, metro and access networks, the system is proposed to operate in the 1500 to 1600 nm telecom band. The advantages from the above wired-wireless indoor model are expected to emerge from its huge unlicensed bandwidth, high power efficiency and effective highly confined data beams, support of mobility, scalability in terms of data rate as well as its capability to accommodate the increasing number of devices, provisioning of secure channels, high privacy levels, mass availability of telecom band devices for ensuring cost effectiveness, ease of installation or integration, and higher link power budget compared to VLC systems. In the case of LoS blocking, with the use of multiple APs, another AP can establish an LoS path. Key performance indices of the hybrid wireless system include reliability, throughput, ubiquity, scalability, interoperability with

prior technologies, integrability with other systems, cost, easy plug-and play, quality-of-service, quality-of-experience and finally, adherence to regulations and standards.

1.4 Organization and contributions of dissertation

This thesis investigates and demonstrates the feasibility of narrowly confined optical pencil beams and beam-steering techniques in order to provide ultra-high speed FSO communication for indoors together with passive 2D beam-steering techniques. The main aim of this dissertation is to analyze and to implement narrowly-confined optical pencil beams using wavelength controlled beam steering by a passive diffractive module, in order to provide orders of magnitude higher data capacity per user at ultra-high optical carrier frequencies.

In general, a main challenge in the implementation of such a system is in the design and construction of the beam-steering module. This thesis addresses this by demonstrating that diffractive optics are a viable choice to construct a passive 2D beam-steering module, and by means of characterization and transmission performance evaluations, showing the excellent performance thereof. Moreover, this thesis addresses limitations on the receiver side. These include the receiver collimation, the bandwidth of photoreceivers, and the adherence to eye- and skin-safety regulations. It is shown that even within such limits, ultra-high speed communication can be achieved over adequate indoor distances.

The main contributions of this thesis are categorized in the coming chapters and sections, according to the challenges each contribution addresses, as follows:

Chapter 2 presents an overview of related work regarding optical beam deflection. Further discussions are provided for active and passive beam-steering elements. The state-of-the-art of optical wireless beam steering in optical wireless communication systems, demonstrated in recent publications, are introduced.

Chapter 3 discusses the proposed beam-steering techniques in BROWSE. The theory and derivations required in designing the passive beam-steering modules using diffraction gratings are presented.

Chapter 4 introduces and discusses several design aspects of the systems implemented in the experimental demonstrations of this thesis. This chapter also serves as a transition for readers from the theoretical work into practical system-level experiments. The main components are first mentioned, followed by several technical details on the optics used. The design aspects that will be mentioned include the beam diameter, eye-safety, theoretical formulas for the arrangement of cascaded gratings, angular magnification, lateral beam expansion, beam-steering control and localization.

Chapter 5 starts with proof-of-principle evaluation of a 1D beam-steering

system which employs a reflective echelle grating with 79 grooves/mm blazed at 75°. Initial characterization, such as the tabulation of diffracted spots at different orders and different wavelengths, will be presented. In the first 1D steering system demonstration, this thesis proposes the use of the single grating for a multi-beam system due to the availability of several diffraction orders. The second experiment uses a tunable laser to demonstrate 1D steering using wavelength tuning. Promising results are obtained for the deployment of gratings as the beam-steering element for an indoor optical wireless system.

Chapter 6 presents the experimental demonstration of two-dimensional (2D) beam-steering based on two steering module designs. The first is an initial 2D steering setup based on the use of orthogonally cascaded reflection gratings. This first module provides a 2-line scan within an angular coverage of $12.66° \times 5.61°$ with wavelength tuning between 1529 nm and 1611 nm. The second is an improved pair of cascaded gratings, by employing two orthogonally cascaded reflection and transmission gratings. The new module provides a 7-line scan in an angular coverage of $12.15° \times 5.62°$ between wavelengths of 1511 nm and 1627 nm. This chapter will present a detailed characterization and the transmission performances, and their corresponding trade offs.

Chapter 7 presents a novel full-duplex all-optical wireless system supporting symmetric 10 Gbps channels over a free-space distance of 3 m with OOK-NRZ signaling by employing a carrier recovery method.

Chapter 8 will demonstrate strategies to improve on the passive 2D-steered system. This chapter will discuss wide angle lens receiver and angular magnification to increase the receiving angle and the angular coverage of the steering module. Then, the chapter will present the demonstration of a time-slotted transmission concept, which is considered feasible since most services require less bandwidth than can be delivered. In addition, this method also promotes the use of resource sharing. Depending on the number of lasers used, three different supported modes of operation, i.e. unicasting, multicasting and broadcasting, can be implemented.

Chapter 9 presents an alternative method for 2D beam steering, i.e. by using a 2D array of fibers connected to a high port count arrayed waveguide grating, to construct a passive 2D steering module.

Finally, **Chapter 10** summarizes the findings of this thesis and a section that discusses the possible areas for improvements, which could be further pursued in future work on narrow beam optical wireless communication.

1.5 List of publications

The work of this thesis has led to the following publications:

[1] **C. W. Oh**, E. Tangdiongga, and A. M. J. Koonen, "Simultaneous 1.5 Gbps multilink indoor optical wireless system using diffractive optics," in *Proceedings of the 18th Annual Symposium of the IEEE Photonics Benelux Chapter, 25-26 November*, Eindhoven, The Netherlands, 2013, pp. 121–124.

[2] A. M. J. Koonen, **C. W. Oh**, and E. Tangdiongga, "Reconfigurable free-space optical indoor network using multiple pencil beam steering," in *Proceedings of the 19th Optoelectronics and Communications Conference (OECC) and the 39th Australian Conference on Optical Fibre Technology (ACOFT),6-10 July*, Melbourne, Australia, 2014, pp. 204–206.

[3] **C. W. Oh**, E. Tangdiongga, and A. M. J. Koonen, "Steerable pencil beams for multi-Gbps indoor optical wireless communication," *Optics Letters*, vol. 39, no. 18, pp. 5427–5430, 2014.

[4] **C. W. Oh**, F. M. Huijskens, Z. Cao, E. Tangdiongga, and A. M. J. Koonen, "Toward multi-Gbps indoor optical wireless multicasting system employing passive diffractive optics," *Optics Letters*, vol. 39, no. 9, pp. 2622–2625, 2014.

[5] Z. Cao, F. Li, Y. Liu, J. Yu, Q. Wang, **C. W. Oh**, Y. Jiao, N. C. Tran, H. P. A. van den Boom, E. Tangdiongga *et al.*, "61.3-Gbps hybrid fiber-wireless in-home network enabled by optical heterodyne and polarization multiplexing," *Journal of Lightwave Technology*, vol. 32, no. 19, pp. 3227–3233, 2014.

[6] Z. Cao, F. Li, A. C. F. Reniers, **C. W. Oh**, H. P. A. van den Boom, E. Tangdiongga, and A. M. J. Koonen, "Spatial filtering in a broadband in-home OFDM radio-over-fiber network," *IEEE Photonics Technology Letters*, vol. 26, no. 6, pp. 575–578, 2014.

[7] **C. W. Oh**, E. Tangdiongga, and A. M. J. Koonen, "Indoor optical wireless communication system using beam-steering by cascaded diffractive optical elements," in *Proceedings of the 19th Annual Symposium of the IEEE Photonics Benelux Chapter, 3-4 November*, Enschede, The Netherlands, 2014, pp. 27–30.

[8] **C. W. Oh**, F. M. Huijskens, S. Zou, H. Chen, E. Tangdiongga, and A. M. J. Koonen, "36.7 Gbps spectrum-efficient indoor optical wireless system with beam-steering," in *European Conference on Optical Communication (ECOC), 21-25 September*, Cannes, France, 2014, paper We.3.6.5.

[9] **C. W. J. Oh**, E. Tangdiongga, and A. Koonen, "42.8 Gbit/s indoor optical wireless communication with 2-dimensional optical beam-steering," in *Optical Fiber Communication Conference (OFC),22-26 March*, Los Angeles, California, USA, 2015, paper M2F.3.

[10] **C. W. Oh**, E. Tangdiongga, and A. M. J. Koonen, "Time-sharing resources for low cost and high performance indoor optical wireless networks," in *European Conference on Optical Communication (ECOC),27 September - 1 October*, Valencia, Spain, 2015, paper P.7.4.

[11] T. Koonen, **J. Oh**, K. Mekonnen, and E. Tangdiongga, "Ultra-high capacity indoor optical wireless communication using steered pencil beams," in *International Topical Meeting on Microwave Photonics (MWP), 26-29 October*, Paphos, Cyprus, 2015, pp. 1–4.

[12] **C. W. Oh**, M. Bech, K. Mekonnen, E. Tangdiongga, and A. M. J. Koonen, "Capacity optimization with discrete multitone modulation for indoor optical wireless communication system," in *Proceedings of the 20th Annual Symposium of the IEEE Photonics Benelux Chapter, 26-27 November*, Brussels, Belgium, 2015, pp. 233–236.

[13] Z. Cao, Q. Ma, A. B. Smolders, Y. Jiao, M. J. Wale, **C. W. Oh**, H. Wu, and A. M. J. Koonen, "Advanced integration techniques on broadband millimeter-wave beam steering for 5g wireless networks and beyond," *Journal of Quantum Electronics*, vol. 52, no. 1, pp. 1–20, 2016.

[14] Z. Cao, Y. Jiao, L. Shen, F. Yan, A. Khalid, T. LI, X. Zhao, N. Tessema, **J. Oh**, and T. Koonen, "Optical wireless data transfer enabled by a cascaded acceptance optical receiver fabricated in an InP membrane platform," in *Optical Fiber Communication Conference (OFC), 20-22 March*, Anaheim, California, USA, 2016, paper M2B.3.

[15] **C. W. J. Oh**, Z. Cao, E. Tangdiongga, and T. Koonen, "10 Gbps all-optical full-duplex indoor optical wireless communication with wavelength reuse," in *Optical Fiber Communication Conference (OFC), 20-22 March*, Anaheim, California, USA, 2016, paper Th4A.6.

[16] K. A. Mekonnen, **C. W. Oh**, A. M. Khalid, N. Calabretta, E. Tangdiongga, and A. M. J. Koonen, "PIC-assisted high-capacity dynamic indoor network utilizing optical wireless and 60-GHz radio-over-fiber techniques," in *IEEE Photonics Society Summer Topical Meeting Series (SUM), 11-13 July*, Newport Beach, California, USA, 2016, paper TuC4.3.

[17] A. M. Khalid, A. M. J. Koonen, **C. W. Oh**, Z. Cao, K. A. Mekonnen, and E. Tangdiongga, "10 Gbps indoor optical wireless communication employing 2D passive beam steering based on arrayed waveguide gratings,"

in *IEEE Photonics Society Summer Topical Meeting Series (SUM), 11-13 July*, Newport Beach, California, USA, 2016, paper TuC2.2.

[18] **C. W. Oh**, E. Tangdiongga, and A. M. J. Koonen, "All-optical indoor wireless communication system," in *IEEE Photonics Society Summer Topical Meeting Series (SUM), 11-13 July*, NewPort Beach, California, USA, 2016, paper MC4.4.

[19] T. Koonen, **J. Oh**, A. Khalid, K. Mekonnen, M. T. Vega, Z. Cao, and E. Tangdiongga, "2D beam-steered high-capacity optical wireless communication," in *IEEE Photonics Society Summer Topical Meeting Series (SUM),26-30 September*, NewPort Beach, California, USA, 2016, paper TuC2.2.

[20] **C. W. Oh**, Z. Cao, E. Tangdiongga, and T. Koonen, "Free-space transmission with passive 2D beam steering for multi-gigabit-per-second per-beam indoor optical wireless networks," *Optics Express*, vol. 24, no. 17, pp. 19 211–19 227, 2016.

[21] A. M. J. Koonen, **J. Oh**, K. A. Mekonnen, Z. Cao, and E. Tangdiongga, "Ultra-high capacity indoor optical wireless communication using 2D-steered pencil beams," *Journal of Lightwave Technology*, vol. 34, no. 20, pp. 4802–4809, Oct 2016.

[22] K. A. Mekonnen, **C. W. Oh**, Z. Cao, A. M. Khalid, N. Calabretta, E. Tangdiongga, and A. M. J. Koonen, "PIC-enabled dynamic bidirectional indoor network employing optical wireless and millimeter-wave radio techniques," in *European Conference on Optical Communication (ECOC), 18-22 September*, Düsseldorf, Germany, 2016, paper W.1.E.3.

[23] **C. W. Oh**, R. van der Linden, G. Sutorius, E. Tangdiongga, and A. M. J. Koonen, "2D passive optical beam-steering module with 7 scan lines within $12.2° \times 5.6°$ for free-space indoor communication," in *European Conference on Optical Communication (ECOC), 18-22 September*, Düsseldorf, Germany, 2016, paper Tu2.C.

[24] **C. W. Oh** and A. M. J. Koonen, "Free-space communication with diffractive optics for indoors," in *European Optical Society bi-Annual Meeting, 26-30 September*, Berlin, Germany, 2016, paper TOM4S05.

[25] **C. W. Oh**, R. van der Linden, G. Sutorius, H. H. W. J. Bosman, K. A. Mekonnen, and A. M. J. Koonen, "2D beam-steered indoor optical wireless network with 4- and 8-PAM modulation," in *Proceedings of the 21st Annual Symposium of the IEEE Photonics Society Benelux Chapter, 17-18 November*, Ghent, Belgium, 2016, pp. 119–122.

[26] K. A. Mekonnen, **C. W. Oh**, Z. Cao, N. M. Tessema, E. Tangdiongga, and A. M. J. Koonen, "Reconfigurable optical backbone network for ultra-high capacity indoor wireless communication," in *International Topical Meeting on Microwave Photonics (MWP), 2-6 October*, Hawaii, USA, 2016, paper TuM1.3.

[27] A. M. Khalid, P. Baltus, A. R. Dommele, M. K. A., Z. Cao, **C. W. Oh**, M. Matters, and T. Koonen, "35-Gbit/s 2D beam steered optical wireless downlink and 5-Gbit/s localized 60-GHz communication uplink for hybrid bi-directional indoor wireless systems," in *Optical Fiber Communication Conference (OFC), 19-23 March*, Los Angeles, California, USA, 2017, (paper Th1E.6, accepted).

[28] K. A. Mekonnen, **C. W. Oh**, J. H. C. van Zantvoort, N. Calabretta, E. Tangdiongga, and A. M. J. Koonen, "Over 40 Gb/s dynamic bidirectional all-optical indoor wireless communication using photonic integrated circuits," in *Optical Fiber Communication Conference (OFC), 19-23 March*, Los Angeles, California, USA, 2017, (paper Tu2F.1, accepted).

[29] **C. W. Oh**, Z. Cao, K. A. Mekonnen, E. Tangdiongga, and A. M. J. Koonen, "Low-crosstalk full-duplex all-optical indoor wireless transmission with carrier recovery," *IEEE Photonics Technology Letters*, 2017, (accepted).

[30] **C. W. Oh** et al., "2D optical beam-steering employing cascaded reflection and transmission gratings for optical wireless communication," 2017, (internal review).

Chapter 2

Related work and state-of-the-art

Contents

Before presenting the core work of this thesis, an overview of related work in optical beam deflection or steering techniques is discussed in this chapter. The first part of this chapter gives a brief introduction to these techniques, their principle of operation, and the related work from former and recent years, which employed such techniques. In the second part of this chapter, the state-of-the-art free-space communication systems for indoors which employ optical beam steering techniques are detailed. As we will show, there are various types

of optical beam steering methods each with its specific benefits and drawbacks in terms of power consumption, mechanical motion, steering angle, speed of response, fabrication complexities, maintenance and control requirements, etc.

Refractive and diffractive optical elements and optical phased arrays are popular techniques to implement devices of which the fundamental functionality is to direct or sense optical beams to/from a particular target(s) or position(s). As such, it is not uncommon that many areas of work share the same techniques for different applications. These techniques can be used for sensing, scanning, pointing, tracking, switching and steering. They are used in various applications such as bar code scanning, Light Detection and Ranging (LIDAR), spectroscopy, projectors, 3D imaging, and confocal microscopy.

In general, steering elements can be divided into two large categories, i.e. active and passive elements.

2.1 Active beam steering techniques

Active beam steering modules require electrical powering to provide the energy to create heat, electro-magnetic fields or mechanical movements to enable a change of state, as required by the particular steering element, in order to be able to direct beams accordingly. Here, we explore discrete element techniques and optical phased array techniques for optical beam steering. Optical Phased Arrays (OPAs) enable optical beam steering without moving parts and are capable of creating phase profiles which steer, focus, fan out or correct phase aberrations on a beam [84]. OPAs are commonly used in laser communication applications ranging from data modulators, optical switches, add-drop multiplexers, optical cross-connects [85], to scanning [86] and steering. They are also used in applications such as gas sensing, imaging and LIDAR. On the other hand, passive techniques without mechanical movements are sought after due to their ability for higher response speed, stability, accuracy, efficiency and reliability, and lack of maintenance and local powering requirements.

2.1.1 Steering mirror

An effective and simple choice of steering is by simply reflecting a beam using a moving reflective surface, e.g. a mirror, in combination with rotation platforms. The movements of these mounts can be controlled using motors and galvanometers [87] or actuators, such as piezo actuators or voice coils. Scanning mirrors are commonly used for laser scanning. Light weight and fast tuning mechanical mirror-based gimbals are commonly used in space-based (satellite communication) applications for scanning and tracking [88]. Although mechanical beam-steering could achieve a wide angle steering, it requires mechanical moving parts which are prone to mechanical wear, vibrations, and thermal expansion. Therefore, it does not support random pointing, but only continuously addressable scanning due to the change in the movement of the mirror

until it achieves the desired position. Also, due to inertia, they are limited in steering speed [89]. Devices which support random pointing could save latency time needed for the mechanical tuning of the mirror.

2.1.2 Micro-electro-mechanical system optical phased arrays

One variant of OPA implementation is by using Micro-Electro-Mechanical System (MEMS) mirrors. Such mirrors are small and they are lightweight, and therefore, are more power-efficient and have faster response time (up to kHz range) compared to a single macroscopic mirror. However, as an example, the well-known microscopic gimbaled mirrors, which are mounted by only at a few micro meters off a substrate, are inhibited from pivoting at large angles [90]. Also, as the size of the mirrors is typically in the 100's of micrometers to millimeters range, the aperture sizes are limited to a few millimeters [91]. In terms of speed, in comparison to electromagnetic and electro thermal actuation, electrostatic actuation has negligible power consumption and could operate at a higher speeds of up to $\sim$ 10 kHz [92]. Gimbal-less wavelength selective switches with less than 2 ms at scan angles $\pm 4.4^\circ$ at 90 V and $\pm 3.4^\circ$ at 91.5 V are reported by J. Tsai et. and M. C. Wu in [93].

MEMS phased arrays can also be achieved using Variable Blaze Gratings (VBGs) [94]. VBG enables an adjustable blaze angle to direct the reflected light into a selectable diffraction order. VBGs have high fill factors and can handle large apertures ($>$ 3 mm). The slat's tilt angle is the VBG blaze angle. A voltage between the slats and substrate is used to control the tilt with electrostatic force. The device has a low power consumption as electrostatic actuation requires almost no current. The actuated VBG supports up to 5 steered beam positions. At 0° direction with 0 V applied, the diffraction efficiency was 48.9%, and at 1.81° direction with 29.4 V, a diffraction efficiency of 53.1% was reported. As the direction of each diffraction order depends on the wavelength of the incident light, VBGs are used to steer only monochromatic (or nearly monochromatic) light. The direction of the mth diffraction order as a function of incident wavelength, λ, and grating period, d, for a normally incident light:

$$\theta_m = \arcsin(\frac{m\lambda}{d}) \tag{2.1}$$

In 2013, a MEMS OPA, with an 8×8 array of high-index-contrast subwavelength grating (HCG) mirrors (designed to have 99.9% reflectivity at $\lambda = 1550$ nm) that are electrostatically actuated, was reported [95]. The device was reported to have a steering range of $\pm 1.26^\circ \times 1.26^\circ$ with a time response in the order of microseconds. The beam-steering angle for a normally incident beam is expected to be:

$$\sin\theta = \pm\frac{\lambda}{2\Lambda} \tag{2.2}$$

where λ is the design wavelength for the phased array, 1550 nm, and Λ is the mirror pitch, 35 μm.

Another variant of MEMS OPA is the microlens phased array. In 2001, A. Tuantranont et al. [96] reported a two-dimensional (2D) MEMS-controllable microlens array integrated with a Vertical Cavity Surface Emitting Laser (VCSEL) array, fabricated on a MEMS X-Y translation plate, as shown in Figure 2.1. The target application was board-to-board or chip-to-chip optical interconnects. By employing electro-thermal actuators, a beam-steering of 70 mrad (4°) was achieved. The VCSEL beam is steered by laterally translating individually controllable microlenses which directs the beams to a hologram array.

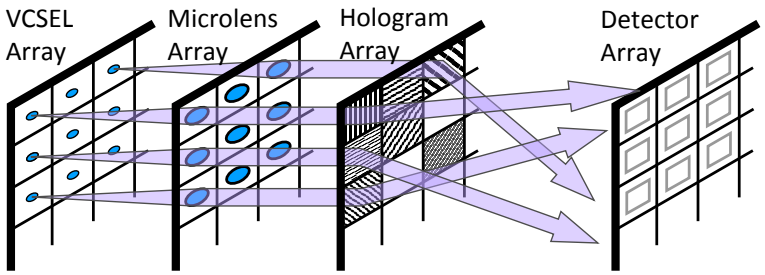

Figure 2.1: MEMS-controllable microlens array in operation with a VCSEL array, hologram array and detector array [96].

The steering angle can be calculated using:

$$\theta = \arctan\left(\frac{\Delta d}{f}\right) \tag{2.3}$$

where θ is the steering angle, Δd is the lateral displacement of the lens from the optical axis and f is the back focal length.

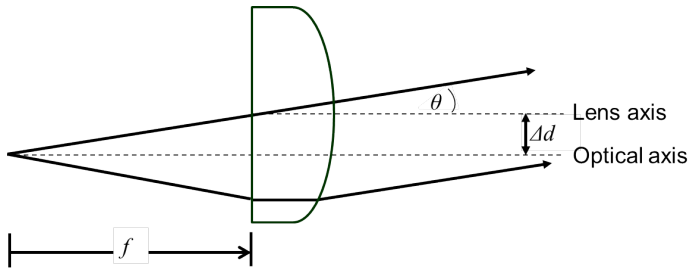

Figure 2.2: Steering angle due to decentered microlens [96].

Recently, J. Morrison et al. has reported an electrothermally actuated tip-tilt-piston micromirror with varifocal capability which demonstrated deflection angles of ± 40° along two axis [97]. The device supports beam steering along two axes, piston mode deflections and dynamic focusing, which sums up to four

separately controllable degrees of freedom in a single device. The focal length was reported to be able to dynamically change from -0.48 mm to +20.5 mm with 27 mW of power. A mechanical response time of approximately 5 ms can be achieved. For further detail, see Reference [97].

2.1.3 Liquid crystal optical phased arrays

Liquid Crystal (LC) based phased arrays require very low power consumption (low electrical drive voltages) and can support large apertures (10 - 50 cm) [84, 98, 99]. For example, a 10 cm device has a typical dissipation of approximately 1 W [98]. LC devices can achieve up to 20° deflection with a large number of precisely controlled beams ($10^4 - 10^5$). Pointing accuracy is improved by non-mechanical motion and could achieve greater than 1/4 beamwidth [98]. LC devices are generally known to be insensitive to accelerations. For example, an array of optical phase shifters can be realized through lithographic patterning of an electrical addressing network on the superstrate of an LC waveplate [84]. With only < 10 V applied on the electrodes, sufficient refractive index change can be achieved to enable full-wave differential phase shifts. LC techniques, however, are limited in speeds to < 10 kHz [100].

Deflection through LC can be achieved using voltage-controlled phase modulation for both reflective [98] and transmissive [101] operations. When a voltage is applied, the LC molecules rotate. Consequently, an incident beam will see a refractive index change due to the birefringent behavior of the LC molecules (see Figure 2.3). This effectively causes a changed optical path length or phase shift. By applying appropriate voltages to the electrodes, the beam can be steered to a particular direction in one-dimensional (1D). In order to construct a blazed phase profile, the voltages at each electrode are chosen such that the phase gradient matches the linear phase gradient. The thickness, t, of the LC layer required for a 2π phase shift at a design wavelength, λ is given by [84]:

$$t \geq \frac{\lambda}{\Delta n} \tag{2.4}$$

where $\Delta n = n_e - n_o$ is the birefringence of the material.

The blazed grating has a modulo-2π sawtooth phase profile, as shown in Figure 2.4. When phase shift of 2π is introduced in a wavelength, the periodic subtraction from the phase front does not affect the far field pattern. By using stair-step approximation of the blazed profile, a theoretical beam steering efficiency, η, can be calculated using [84]:

$$\eta = \left(\frac{\sin(\pi/N_{step})}{\pi/N_{step}}\right)^2 \tag{2.5}$$

where N_{step} is the number of steps in the blaze profile.

For structures without the use of 'resets', defined as in Figure 2.4, only a small angle or small aperture size can be achieved [84]. Larger steering angles

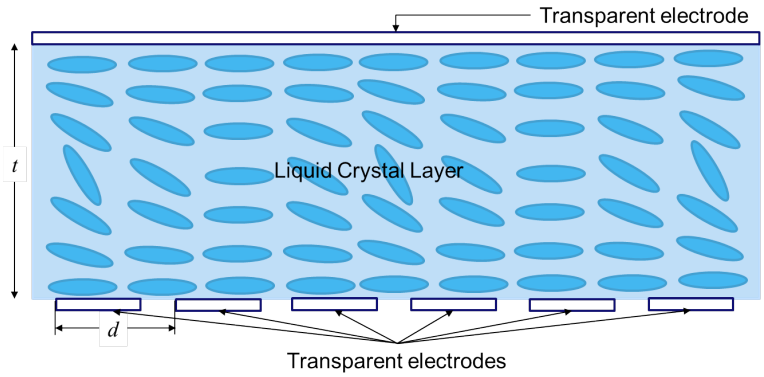

Figure 2.3: LC phase shifters. As voltage is applied to the electrodes, the LC layer will experience a refractive index change. Periodic electrodes are used for inducing a periodic behavior such as a blazed grating. d: period of the grating, t: thickness of the LC layer.

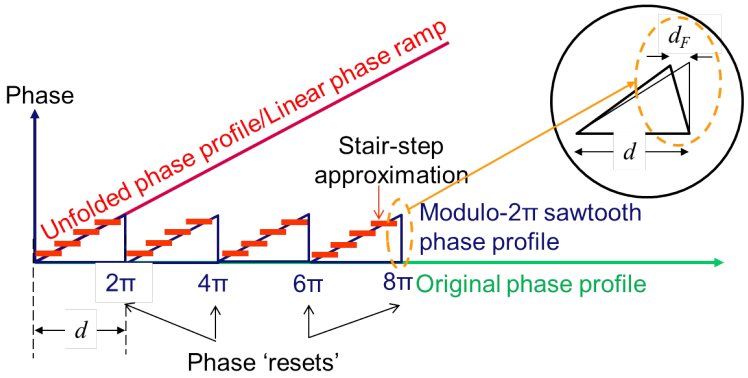

Figure 2.4: Unfolded phase profile with linear phase ramp and modulo-2π sawtooth profile. Stair-step approximation method is overlaid on the sawtooth profile. It shows the corresponding phase shifter at each electrode segment. The sawtooth profile 'resets' after a 2π phase shift. Subset: "Flyback" due to the minimum finite spatial extent needed for LC molecular orientation. d: Period of the sawtooth profile, d_F is the "Flyback" spatial extent.

are supported by structures with 2π 'resets'. However, the 'resets' are only for the design-wavelength and the linear phase ramp deviates when another wavelength is used. This results in a variation of the phase 'resets' which causes dispersion due to an incorrect phase shift [84]. Wavelengths other than the design wavelength is steered to a different angle.

The efficiency of LC steering device can be affected by the spatial "Flyback" (see Figure 2.4). Wavelengths falling on the "Flyback" region will be deviated from the intended steering angle. The resulting diffraction efficiency, η, in the desired order can be approximated using [84]:

$$\eta = (1 - \frac{d_F}{d})^2 \tag{2.6}$$

where d_F is the "Flyback" spatial extent and d is the period of the grating.

The steering angle for a normally incident beam is given by [84]:

$$\theta = \sin^{-1}(\frac{\lambda_o}{d}) \tag{2.7}$$

where λ_o is the design wavelength and d is the period of the staircase ramp. d can be obtained by multiplying the period of the staircase ramp and the center-to-center spacing between phase shifters or the width of the phase shifter.

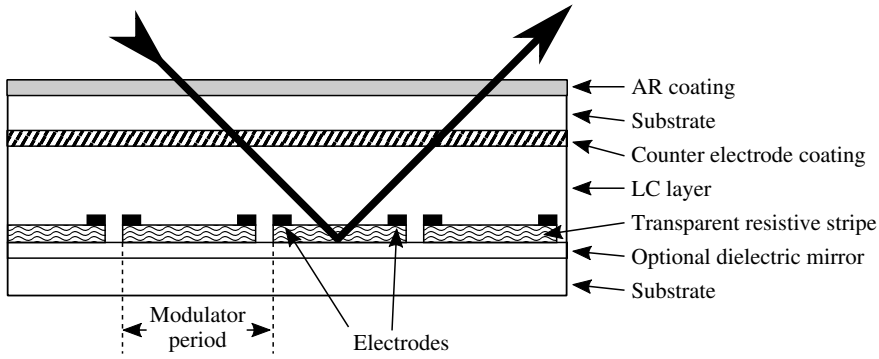

Figure 2.5: Blazed phase liquid crystal beam steering device by R.M. Matic et al. [98].

In 1994, R.M. Matic et al. proposed a novel LC device for steering laser beams [98]. The device was constructed using an array of optical phase modulators which contain a thin and active LC layer sandwiched between two substrates, as shown in Figure 2.5. Each of the phase modulators can produce a linear (blazed) phase gradient profile unlike the constant phase profile which is typical in other liquid crystal devices. The benefits of the device include high diffraction efficiency with large diffraction angles, supports operations between long Infrared (IR) to Ultraviolet (UV), simpler fabrication and simpler

electronic control as the size of the phase modulator is independent of and can be larger than the operating wavelength. A challenge in this approach is the requirement to operate the LC in the linear region. Power limitations arise from nonlinearities which are caused by heat due to absorption or changes in the orientation of the LC. The LC device was demonstrated for a blazed deflection at 1.064 μm laser beam and achieved over $\pm 5^\circ$ angles although at a low diffraction efficiency of 9% and at a response time of 61 millisecond. In 2004, using LC OPA, S.A. Khan and N.A. Riza have demonstrated a continuous scan for one, two and three dimensions with a continuous scan, all at $\lambda = 1550$ nm, up to a maximum of 40.92° with a scanner aperture of 1 cm.

2.1.4 Photonic integrated circuits optical phased arrays

OPAs based on waveguide phased array allow independent control in the array of uncoupled channel waveguides to achieve the wanted steering characteristics. The working principle of such an OPA is based on the interference of individual radiating optical waves with their neighboring waves forming the desired wavefront in a particular direction.

In 1993, F. Vasey et al. [102] presented a 1D steering by using electro-optic tuning for waveguide phased array. Electron-beam lithography-patterned diffraction gratings were used to couple beams to and from free space. A 43-element rib waveguide array for discrete beam steering was demonstrated at 850 nm for ~ 2 mm beam diameter. This was followed by a continuous deflection over $\pm$ 7.2 mrad ($\sim 0.41^\circ$) at 900 nm. The beam has a width of 1.5 mrad (0.086°) and the maximum modulation voltage is -8.5 V. The extension to the second dimension (in the longitudinal direction) is possible by either varying the refractive index at the grating output coupler or by tuning the wavelength of operation.

With reference to Figure 2.6, the in-coupled beam from section (1), into each waveguide mode from g_1 to g_N is phase-shifted according to the electrode length and thereby, the electro-optically induced refractive index change in section (3). Each mode, g_j, remains uncoupled to the neighboring channels (g_{j-1}, g_{j+1}) and preserves its phase shift properties until being out-coupled. The independent modes diverge at out-coupling perpendicularly to the waveguide propagating direction, p. The beam radiation subsequently interferes with neighboring elements and forms a beam, d, and the beam is steered in s-direction, which is perpendicular to the channel waveguides.

The angular separation of the diffraction orders can be calculated using the grating equation:

$$\theta_{os} = \arcsin[m(\frac{\lambda}{\Lambda_s}) + \sin(\theta_{is})] \tag{2.8}$$

where m is the order of diffraction, λ is the wavelength of the beam, Λ_s is the array periodicity, θ_{is} is the incidence angle in the s-direction and θ_{os} is the diffracted angle in the s-direction.

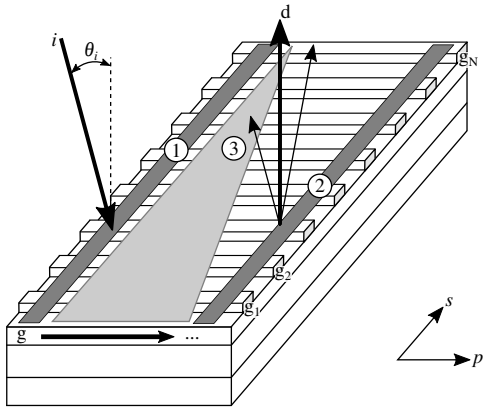

Figure 2.6: Optical phased-array implementation by F. Vasey et al. [102]. (1) In-coupling of a coherent beam into waveguide structure using a diffraction grating input coupler, g. (2) Out-coupling to free space using a grating output coupler (3) Phasing section with different electrode lengths. The lateral, s, and longitudinal, p, dimensions are not at the same scale.

In a 2D diffraction at the output coupler of periodicity Λ_p in the longitudinal direction, p, and the rib wavequide array of periodicity Λ_s in lateral direction, s, the positions can be estimated using [102]:

$$\theta_{os} = \arcsin[m_s(\frac{\lambda}{\Lambda_s})], m_s = 0, \pm1, \pm2, ... \tag{2.9}$$

$$\theta_{op} = \arcsin[n_{eff} - m_p(\frac{\lambda}{\Lambda_p})], m_p = 1, 2, ... \tag{2.10}$$

where n_{eff} is the rib waveguide effective index.

Although the electro-optic steering is inherently fast (in nanoseconds), challenges are foreseen in achieving larger steering angles, higher efficiencies, larger apertures and in the extension to two-dimension [84].

Work in recent years has shown tremendous progress in Photonic Integrated Circuit (PIC) OPAs. In 2011, J.K. Doylend et al. demonstrated a 16-channel, independently tuned waveguide surface grating OPA in silicon-on-insulator for 2D beam-steering, which has a total Field of View (FoV) of $20° \times 14°$, beam width of $0.6° \times 1.6°$ and a resolution of $< 1°$ [103].

J.C. Hulme et al. has further developed an integrated 2D beam scanner chip using the hybrid silicon platform [104]. The PIC consists of 164 components and is shown in Figure 2.7. A steering over $23° \times 3.6°$ with beam widths of $1° \times 0.6°$ was demonstrated.

Although the common approaches need active steering of all elements of which the phase can be controlled, Karel van Acoleyen et al. [105] demonstrated a compact yet simple design which is Complementary Metal-Oxide-Semiconductor (CMOS)-compatible and passive, relying on wavelength tuning

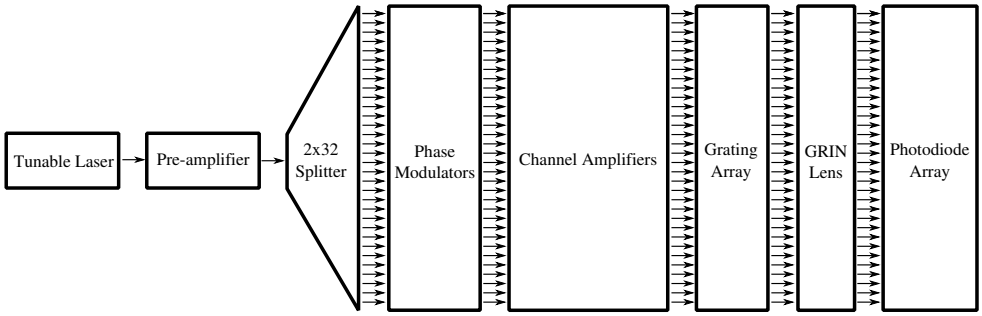

Figure 2.7: 32-channel fully-integrated PIC beam scanner [104].

for steering. As the technique is based on a fully passive PIC device, this work will be described in detail in Subsection 2.2.4.

2.1.5 Electro-optic deflectors

In electro-optic deflectors, the refraction index of a material is induced by an applied electric field, which subsequently results in a change in the direction of propagation. Electro-optic materials, such as Lithium Niobate, exhibit a refractive index change when an external electric field is applied. Such a beam deflector was reported in [106]. A deflection angle of 14.3° was observed by applying ±250 V with approximately 5 μA current to the Potassium Tantalate Niobate crystal. The voltages needed to induce phase changes are normally high at a few hundred of Volts.

An early work on using the electro-optical properties of crystals for OPAs was pursued by R.A. Meyer [107] in which he employed bulk Lithium Tantalate to achieve phase modulation in 1D. The phase modulator can be considered as an OPA antenna. In the antenna, 46 phase shifters were used and the results from the work correspond appropriately to a microwave phased array. Measurements on the masked modulator indicated approximately 32 V for 2π phase modulation with a linear voltage law.

In 1973, Ninomiya [108] realized an electro-optic phased array light deflector in 1D using electro-optic Lithium Niobate prisms. By applying equal voltages on the prisms, discontinuous deflected angles were obtained while continuous deflection can be obtained by varying the voltages applied on each crystal. It was experimentally shown that 50 resolved spots were achieved at ±600 V. The electro-optic prism array is shown in Figure 2.9 together with the optical setup. The electrodes are placed on both surfaces of a z-plate of the Lithium Niobate prism.

In a refractive steering approach, with the combination of an electro-optic beam-steerer utilizing liquid crystal clad optical waveguides together with a polarization grating coarse steerer, a continuous steering of 50° × 15° at a speed of 60 kHz was achieved [109]. The device had a large aperture of 1.2 cm, in a

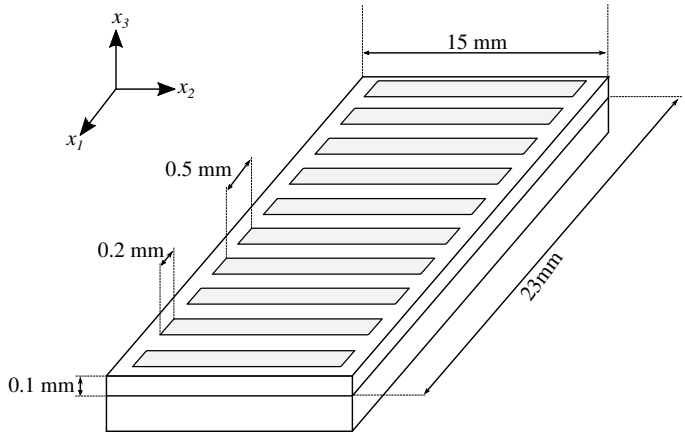

Figure 2.8: Multichannel Lithium Tantalate crystal for optical beam steering [107].

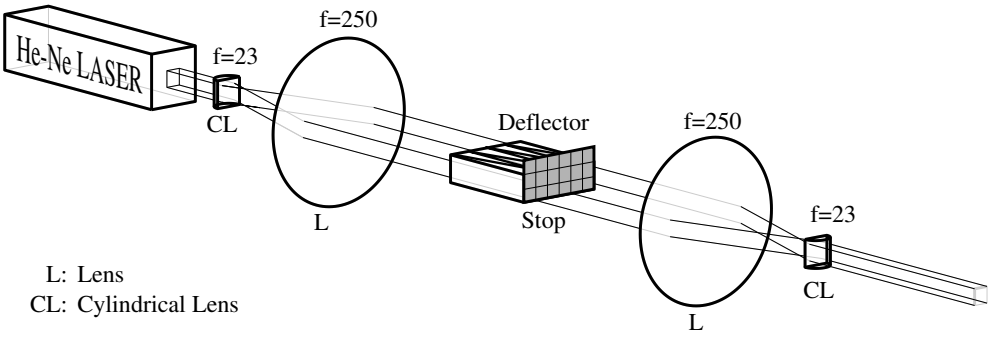

Figure 2.9: Optical setup with electro-optic prism array [108].

compact ~ 6 cm^3 size, with three electrodes of only a few mW power and operates at 1550 nm. As this method is not diffractive, the efficiency is independent of the angular steer range. Also, unlike diffractive OPAs which have 2π resets limiting their pointing precision, this approach provides a continuous angular coverage with high pointing accuracy with $>$ 10 Gigahertz (GHz) bandwidths.

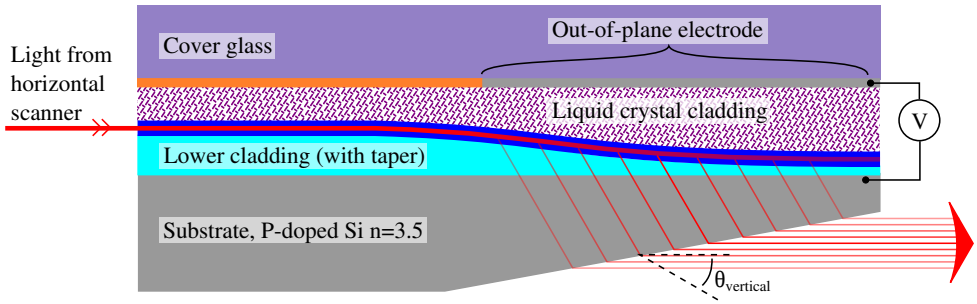

Figure 2.10: Voltage tunable refractive prisms for continuous $50° \times 15°$ 2D beam steering [109]. The light is steered via a voltage tunable Snell's law refraction, with prism electrodes for horizontal direction or an out-coupling prism for the vertical direction.

2.1.6 Acousto optic deflectors

Acousto-optics is based on the interaction between sound and light which was predicted by Brillouin in 1922. Acousto-optic devices have been made possible from the discovery of materials having excellent acoustical and optical properties with large photoelastic constants. Materials having a large refractive index give an added advantage [110, 111, 112].

The principle of acousto-optic deflector is to deflect a beam to different angular positions by an accompanying acoustic wave, by varying the acoustic frequency. By applying an Radio Frequency (RF) signal on an acoustic transducer to generate an acoustic wave through a crystal, a periodic modulation on the refractive index is induced via the elasto-optical effect [113], thus, the device behaves like a grating. Subsequently, an incident coherent optical beam will be diffracted. This is also known as the acousto-optic diffraction. There are two regimes of diffraction. The interaction regime is determined by the quality factor, Q [114].

$$Q = \frac{2\pi\lambda L}{n\Lambda^2} \tag{2.11}$$

where λ is the wavelength of the coherent beam, L is the transducer size or width of the acoustic wave, n is the refractive index of the crystal and Λ is the acoustic wavelength.

When $Q >> 1$, the interaction is in the Bragg regime, as shown in Figure 2.11(a). At the particular Bragg incident angle, only one diffraction order is

possible due to constructive interference. The Bragg angle is given by [114]:

$$\sin\theta_B = \frac{\lambda}{2\Lambda} \tag{2.12}$$

where λ is the wavelength of the coherent beam in the acoustic medium and Λ is the acoustic wavelength.

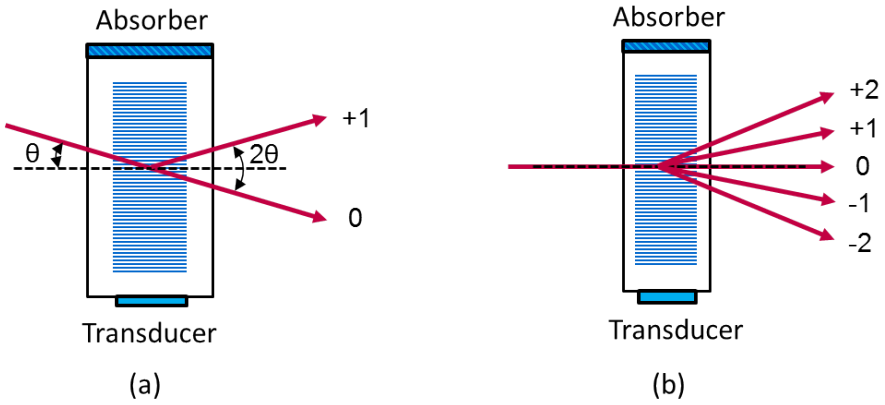

Figure 2.11: Acousto optic diffraction: (a) Diffraction in the Bragg regime. Upshifted Bragg diffraction due to positive Doppler shift [114]. (b) Diffraction in the Raman-Nath regime.

When $Q << 1$, the interaction is in the Debye-Sears, Lucas-Biquard or Raman-Nath regime, as shown in Figure 2.11(b). When the transducer size, L, is shortened, the sound waves will become less like a plane wave but with a broadened radiation pattern. The shorter L is, the more orders of diffraction will be observed. The n^{th} order is shifted in frequency by $n\omega$, which is the sound frequency.

Naturally, an application of Bragg diffraction is beam deflection. The deflection angle has a linear relationship with the frequency sweep [114]. The change in deflection angle, $\Delta\theta_d$, as a function of change in frequency, Δf, is given as:

$$\Delta\theta_d = (\frac{\lambda}{\upsilon})\Delta f \tag{2.13}$$

where $\Delta\theta_d$ is the change in angle, λ is the optical wavelength in vacuum, υ is the velocity of the acoustic wave in the acoustic device medium, and Δf is the change in frequency.

The speed of these devices can be in a few microseconds range [87]. However, acousto-optic deflectors are limited in their total angular range and may suffer from shift in optical frequency as sound waves spread as they propagate.

2.1.7 Electrowetting

Electrowetting Microprisms (EMPs) use the electrowetting modulation of liquid contact angle to realize the refraction characteristics of prisms [115]. Contact angle of several tens of degrees are achievable while switching speeds are limited to several milliseconds due to hydrodynamic response of the droplet. In 2006, N.R. Smith et al. demonstrated continuous beam steering of 14° with a liquid index of 1.359. Switching speeds of milliseconds and a high efficiency that is independent of deflection angle is possible [116]. Figure 2.12 illustrates the EMP device.

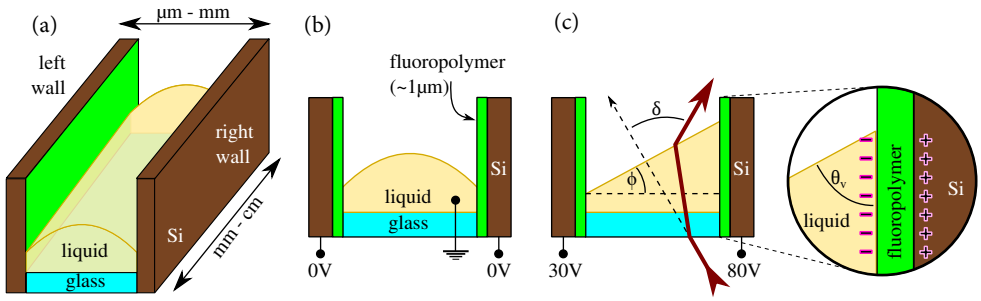

Figure 2.12: EMP structure [116]: (a) Angle view of the channel geometry, (b) and (c) EMP materials, voltage connections, prism apex angle (ϕ), deflection angle (δ), and liquid-fluoropolymer contact (θ_v).

2.2 Passive beam steering techniques

This section gives an overview of the available passive beam-steering techniques which do not require any powering or movement. These passive devices are usually wavelength or frequency dependent and are coupled with tunable sources such as electro-optic tuning of broadband laser [117], Wavelength Division Multiplexing (WDM) source [118], and frequency combs [119, 120]. These methods are widely used in spectrometry and interferometry. A pioneering work was carried out by I. Filinski and T. Skettrup in 1982. They proposed one-dimensional light scanning by employing passive dispersive optical components such as prisms, gratings, etc., while tuning the output wavelength of a broadband laser [117].

2.2.1 Holographic deflectors

Holography is also known as wavefront reconstruction photography [121] and was first demonstrated by Dennis Gabor [122]. It is a technique that enables the reproduction of three-dimensional (3D) images by using coherent radiation of a monochromatic beam or laser which has both temporal and spatial coherence.

Holographic diffractive optical elements refer to diffractive medias, such as gratings, which are made by holographic recording. Photopolymer films have been used for hologram recording since the late 1960's [123]. Photosensitive films or emulsions are used in recording volume phase or absorption holograms, and transmission or reflection holograms. Volume holograms are also known as thick holograms or Bragg holograms due to the thickness of the recording material which is larger than the wavelength used for recording.

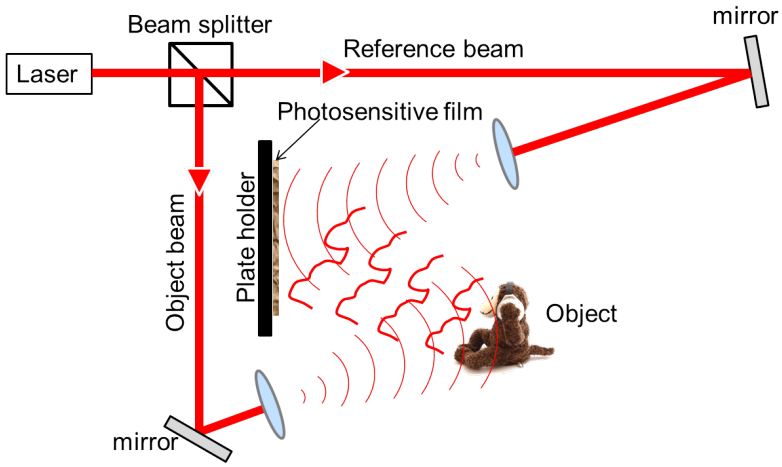

Figure 2.13: A holographic recording setup. Object image is captured by the interference of the reference beam and the object beam. The 3D image is recorded on a photosensitive film placed on the plate holder.

Holograms can be constructed, as shown in Figure 2.13, by illuminating part of a coherent monochromatic wave, known as the reference beam, on a photosensitive material or photographic plate. The other part of the beam, known as the object beam, is then illuminated on the object to be recorded. The beam that reflects from the object has amplitude and phase variations

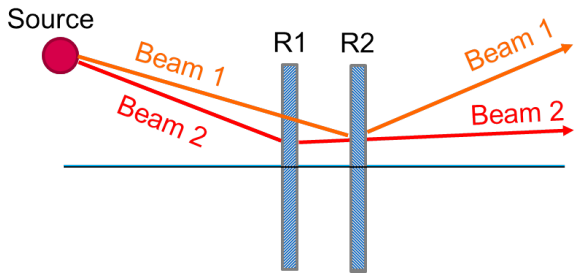

Figure 2.14: The use of holographic gratings, each for the deflection of one wavelength, in the invention of electro-optical deflection apparatus by J.P. Huignard et al. [124].

which represent the surface of the object. This reflected beam then interferes with the reference beam forming a complex interference pattern with magnitude and phase information at the photographic plate. The interference pattern is recorded on a fine grain holographic or photographic film. The developed piece of film is known as a hologram.

In 1976, J.P. Huignard et al. patented an electro-optical deflection apparatus invention using holographic gratings together with a primary beam deflector capable of deviating the incident beams into a multiple directions at the source [124], see Figure 2.14. The invention provides a deflection system which was attained by providing N holographic diffraction gratings, in which each of the gratings diffracts into only one of the N-directions. The gratings are positioned consecutively next to each other in an arrangement which can be made parallel or with a finite angle with each grating diffracting at least one incident beam. Each of the incident beams arrive at a slightly different incident angle. The output beams are then diffracted at an angle substantially larger than the incident angle. Factors which constitute a holographic grating are the refractive index, thickness and grating period.

In 1971, R. L. Forward patented his invention on using an adjustable frequency beam generator to generate a collimated monochromatic beam which was used together with a Bragg scanning volume to deflect the beam into the desired frequency-dependent direction [125]. By employing this technique, in 2003, Z. Yaqoob et al. demonstrated a 2D laser scanner which is constructed using multiple Photo-Thermo-Refractive (PTR) glass volumes (N), with each having multiple tilted Bragg-grating structures (M) with optimal diffraction efficiency, were stacked together to achieve $M \times N$ equivalent number of output beams for 2D scanning [126], as the wavelength of the laser source is tuned over the available tunable bandwidth. By using four PTR glass (one grating per PTR glass), with Bragg gratings of 816 lines/mm , a total scan of 5° with 4 points, were measured at wavelengths of 1520 nm, 1545 nm, 1570 nm and 1600 nm.

In year 2004, Z. Yaqoob and N. A. Riza demonstrated 1D scanners using a 940 lines/mm volume Bragg gratings stored in dichromated gelatin coupled with wavelength selection [127]. The scanner was operated at a center wavelength of 1560 nm. By continuous tuning over 80 nm (1520 nm to 1600 nm), an angular scan of 6.25° was achieved in 1D. By using an in-line scanner (see Figure 2.15) design constructed using two similar volume Bragg gratings, up to 13.42° was achieved with continuous tuning of wavelengths between 1520 nm and 1600 nm. A single grating has < 0.15 dB polarization dependent loss and an average scanner loss of only 0.4 dB over 70 nm around 1550 nm.

2.2.2 Arrayed Waveguide Grating

An Arrayed Waveguide Grating (AWGr) consists of an input waveguide, a free propagation zone where the beam diverges, a zone with many waveguides hav-

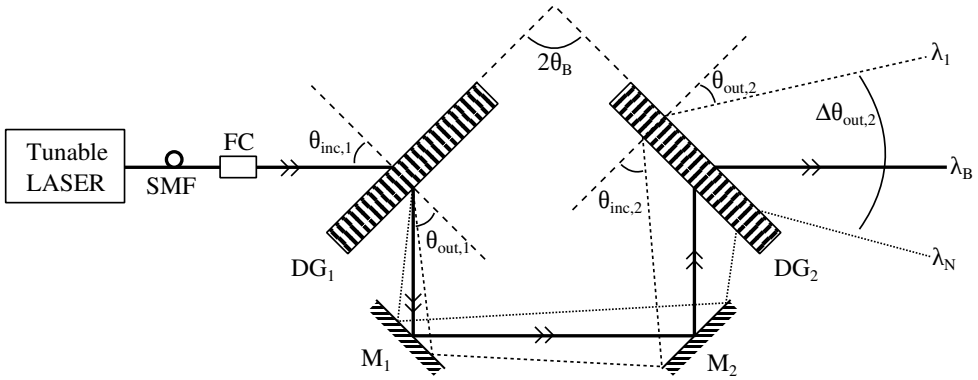

Figure 2.15: In-line wide angle free-space scanner known as W-MOS using two volume Bragg gratings [127].

ing slight length difference, a second free propagation region where the beam converges with equal amplitude and phase distribution [128], and an array of output waveguides. It is designed such that the field of an incoming beam is split into an array of output beams such that the different wavelengths which enter the input waveguide are directed to different output waveguides [129]. Physically, the linearly increasing length of the array waveguides which will cause the phase change, due to a change in the wavelength, to vary linearly along the output aperture [128]. AWGrs are also known as phased arrays (PHASARs) or Waveguide Grating Router (WGR). AWGr was first reported by M.K. Smit in 1988 [129, 130] and later by Takahashi in 1990 [131] and Dragone in 1991 [132]. The acronym AWG was introduced by Takahashi [131] and is commonly used nowadays. In this thesis, the acronym AWGr is used instead of AWG in order to avoid confusion with the acronym AWG to abbreviate arbitrary waveform generator, which will be used in subsequent chapters on experimental evaluations.

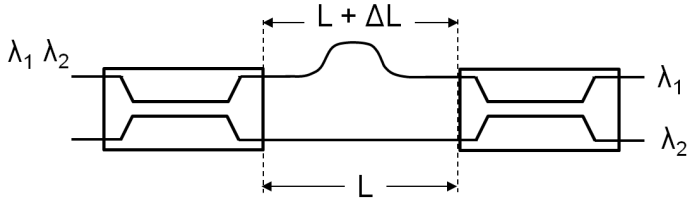

Figure 2.16: MZI structure illustrating the path length change to induce a phase change in one path.

The principle of operation can be explained by a simple Mach-Zehnder Interferometer (MZI) with unequal path lengths, as shown in Figure 2.16. An MZI is a device which splits a beam into two paths by which one path introduces a relative phase shift which can be varied by changing the length of one path

or by introducing a change of refractive index in one path. Passive couplers, which are made by changing the length of one arm, are commonly used in fiber optic communication. With a change of path length difference, ΔL, in one path, the phase difference, $\Delta\phi$, is given by:

$$\Delta\phi = kn_{eff}\Delta L \tag{2.14}$$

where k is the wave vector $2\pi/\lambda$ and n_{eff} is the effective refractive index of the waveguide.

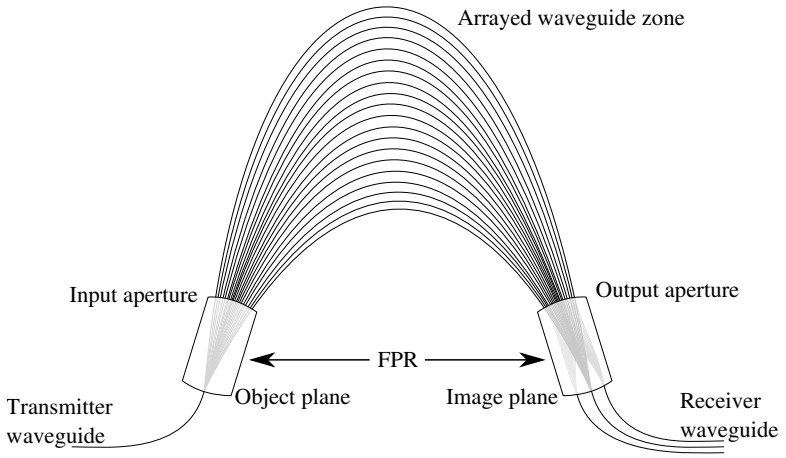

Figure 2.17: AWGr layout with linearly increasing length in the arrayed waveguides. FPR: Free Propagation Region [129].

AWGr can be seen as an extension to the MZI principle, in which it consists of multiple waveguides of linearly increasing constant path lengths thereby creating a linear phase shift in each waveguide, see Figure 2.17. The length difference can be calculated using [129]:

$$\Delta L = m\frac{\lambda_c}{n_{eff}} \tag{2.15}$$

where m is the order of the array, λ_c is the central wavelength and n_{eff} is the effective refractive index of the guided mode.

An interleaved multiplexer can be constructed using a higher order AWGr at the first stage, where each output waveguide directs an output with a specific Free Spectral Range (FSR). By cascading a second stage AWGr, the output corresponding to one diffraction order is further separated into individual channels. In 2002, Takada et al. presented a two-stage cascade of AWGrs, where the first-stage consisted of a single AWGr to create 25 channels spaced by 1 Terahertz (THz) (8 nm) [119, 134]. At the second-stage, each channel was further divided into 168 channels spaced at 5 GHz, with a total of 26 AWGrs. The fabricated AWGr had a loss of 3 dB in the 1.46 to 1.62 μm range.

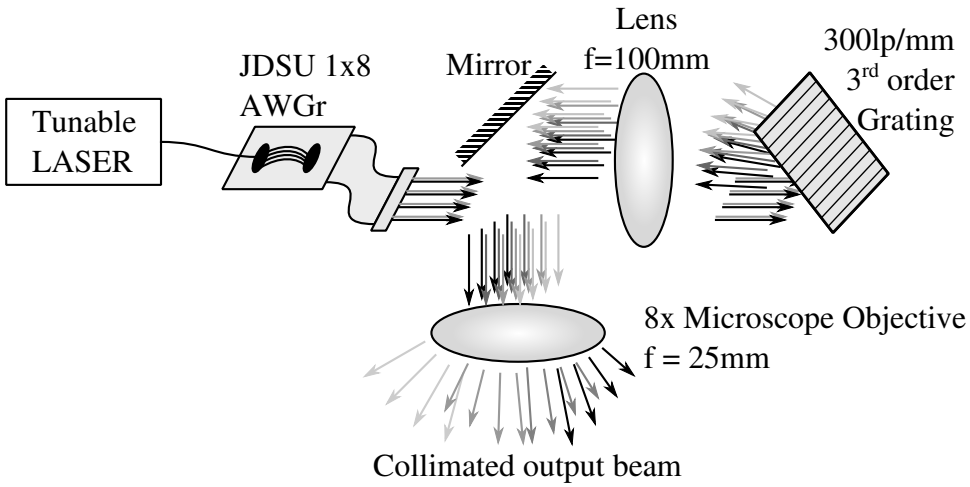

Figure 2.18: Beam scanning system using demultiplexed channels from AWGr, transmitted to free space using a V-groove array. The free space grating demultiplexer separated the multiple orders from the AWGr [133].

By adopting this concept, in 2007, a 2D demultiplexer was constructed using an AWGr and a free-space grating, and 1092 channels over 600 nm spectral band were demonstrated to support 10 Gbps error-free channels [119]. The AWGr was reported to have insertion losses of 4 dB at $\lambda = 1533.75$ nm, 5 dB near $\lambda = 1730$ nm and 7 dB at $\lambda = 1135$ nm. Further in 2008, T. Chan et al. used a highly dispersive (high diffraction order) AWGr in combination with a reflection grating to demonstrate a 2D beam steering. The setup employed a cyclic AWGr, where the number of scan lines is equal to the number of usable cycles. By tuning the wavelengths between 1545 nm and 1588.3 nm, an angular coverage of $10.3° \times 11°$ was achieved [133], see Figure 2.18. The paper suggested an insertion loss of approximately 8 dB within the scanning range.

2.2.3 Prisms

Dispersive optical prisms usually have a triangular geometry. Triangular prisms are used to disperse light by changing the angle of refraction which is dependent on the prism's refractive index, the geometry (the apex angle), the outer refractive index, and the optical incidence angle at the interface. The refractive index which an optical ray wavelength sees, is also dependent on its wavelength or frequency. Therefore, each different wavelength is refracted to a different angle, as can be calculated using Snell's Law. Consequently, light is dispersed into its spectral components. This is known as angular dispersion. The effective refractive index increases as wavelength decreases. However, the angular dispersion of a prism is typically smaller than diffraction gratings.

The light path deviation, δ (see Figure 2.20), from its original path, can be

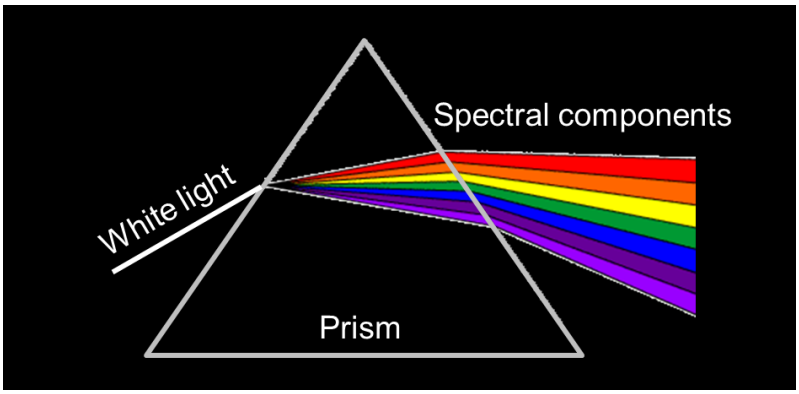

Figure 2.19: Prism and the spectral components of white light.

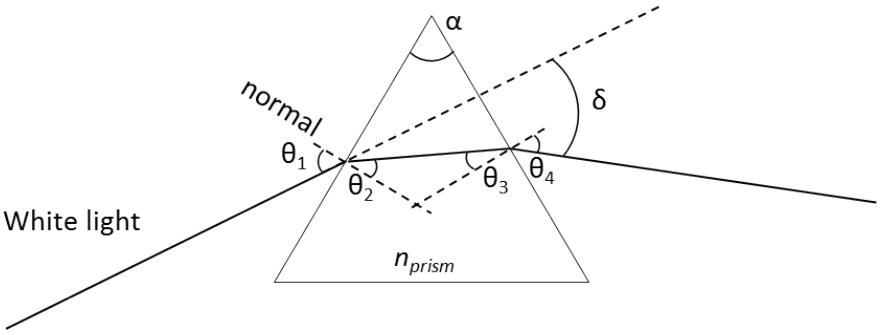

Figure 2.20: Refraction through a prism.

derived using the Snell's law of diffraction and trigonometry, with the following basic equations:

$$n(\lambda)_{ambience}.sin(\theta_1) = n(\lambda)_{prism}.sin(\theta_2) \tag{2.16}$$

$$n(\lambda)_{prism}.sin(\theta_3) = n(\lambda)_{ambience}.sin(\theta_4) \tag{2.17}$$

$$\theta_2 + \theta_3 = \alpha \tag{2.18}$$

where θ_1 is the incidence angle on the first surface, θ_2 is the refracted angle of the first surface, θ_3 is the incidence angle on the second surface, θ_4 is the refracted angle at the second surface, $n(\lambda)_{ambience}$ is the refractive index outside the prism, $n(\lambda)_{prism}$ is the wavelength-dependent refractive index of the prism, and α is the apex angle of the prism.

Finally, the wavelength-dependent deviation angle, $\delta(\lambda)$, is derived to be the following:

$$\delta(\lambda) = \theta_1 - \theta_2 + \theta_4 - \theta_3 \tag{2.19}$$

$$\delta(\lambda) = \theta_1 - \alpha + \arcsin\{n(\lambda)_{prism}.sin[\alpha - \arcsin(\frac{\sin\theta_1}{n(\lambda)_{prism}})]\} \tag{2.20}$$

where the third term in Equation 2.20 represents the wavelength-dependent deviation angle. The change in the refractive index with wavelength is known as dispersion and it varies according to material.

2.2.4 Diffraction gratings

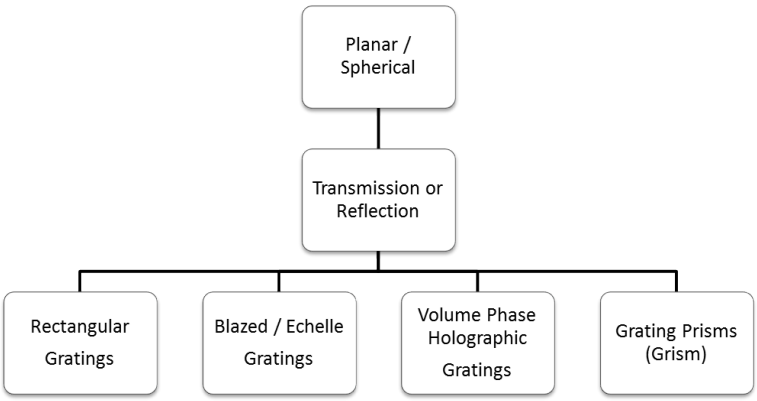

Figure 2.21: Overview of types of gratings.

Beam steering employing diffractive optics is studied in detail as this is the core technique of this dissertation. Diffraction gratings, like prisms, are one of the earliest forms of passive dispersive media used for beam steering. Figure 2.21 shows the different types of gratings. The first grating was invented in

1785 to observe light spectra. Gratings are wavelength-dependent and operates by diffracting light beams.

The principle of diffraction stems from the ability of waves to bend, leading to a divergent profile as it propagates away from its source. At the same time, waves coincide constructively and destructively with neighboring waves to give rise to interference. This phenomenon can be seen in the propagation of light through a single slit, thus, forming an array of bright and dark intensity patterns on the resulting screen. These bright patterns are the spots where diffracted light beams are constructively interfering.

Physically speaking, according to the Huygens-Fresnel's principle, any unobstructed point of a wavefront, at a given instant of time, serves as a source of spherical secondary waves (wavelets), with the same frequency as that of the primary wave. The amplitude of the optical field at any point beyond the new source plane is the superposition of all these wavelets. This leads to the forming of a new wavefront which envelopes the wavefronts of the secondary waves [135].

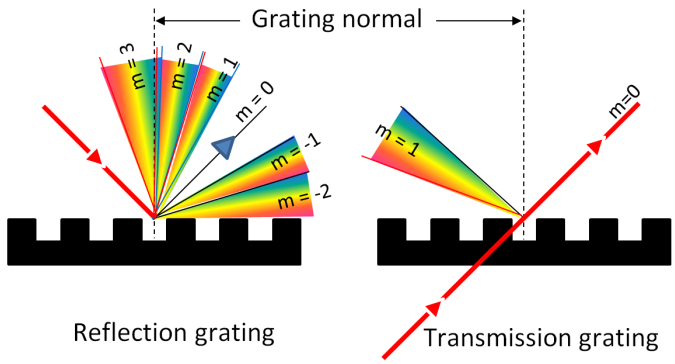

Figure 2.22: Diffraction spectra at different orders for transmission and reflection gratings.

The corresponding positions of the bright spots can be calculated using the famous grating equation for both transmission and reflection gratings, as shown in Figure 2.22:

$$m\lambda = d(n_1 \sin\theta_i \pm n_2 \sin\theta_m) \tag{2.21}$$

where m is the diffraction order, λ is the wavelength of interest, d is the period of the grating or distance between two neighboring grooves, θ_i is the incidence angle measured from the grating normal, θ_m is the diffraction angle measured from the grating normal, and n_1 and n_2 are the refractive index of the medium of incident beam and diffracted beam, respectively. The $\pm$ operation is dependent on the angle with reference to the optical axis.

The zero-th order mode always exists giving rise to a non diffracted transmission or specular reflection beam. The zeroth order mode occurs when

$\theta_i = \theta_m$, where most of the optical power is confined in. In order to optimize for maximum optical power in a desired diffraction order or angle, a blazed grating is used. Blazed gratings are designed for maximum efficiency at an order other than the zero-th order, with minimized residual power in all other orders. Blazed gratings which have a large blaze angle are known as echelle gratings. Notice from the grating equation also that only spectral orders where $|m\lambda/d| < 2$ can exist.

The angular dispersion can be derived from the derivative (where θ_i is kept constant):

$$\frac{d\theta}{d\lambda} = \frac{m}{d\cos\theta_m} \tag{2.22}$$

By substituting m/d from 2.21 into Equation 2.22, we obtain the general dispersion equation:

$$\frac{d\theta}{d\lambda} = \frac{\sin\theta_i + \sin\theta_m}{\lambda\cos\theta_m} \tag{2.23}$$

In a retroreflective or Littrow configuration, the incidence angle, θ_i, is equal to the diffracted angle, θ_m, reducing the grating equation 2.21 to:

$$m\lambda = 2d\sin\theta_m \tag{2.24}$$

and the angular dispersion in Littrow configuration can be further reduced to:

$$\frac{d\theta}{d\lambda} = \frac{2\tan\theta_m}{\lambda} \tag{2.25}$$

which is only valid when the angle of incidence is fixed [136]. In addition, when the angle of incidence is changing (for e.g. for the consecutive grating placed after the first), by differentiating the grating equation 2.21, we have [136]:

$$md\lambda = d(\cos\theta_i d\theta_i + \cos\theta_m d\theta_m) \tag{2.26}$$

Since in Littrow configuration, $\theta_i = \theta_m$ and $d\theta_i = d\theta_m$:

$$\frac{d\theta_m}{d\lambda} = \frac{m}{2d\cos\theta_m} \tag{2.27}$$

Interestingly, by substituting m/d from Equation 2.25, we see that the angular dispersion is only half that of the angle obtained using fixed angle of incidence [136]:

$$\frac{d\theta_m}{d\lambda} = \frac{\tan\theta_m}{\lambda} \tag{2.28}$$

As shown in Figure 2.23, the wavelengths are repeated in different orders. Also, at order $m > 1$, several ranges of wavelengths from different orders exists.

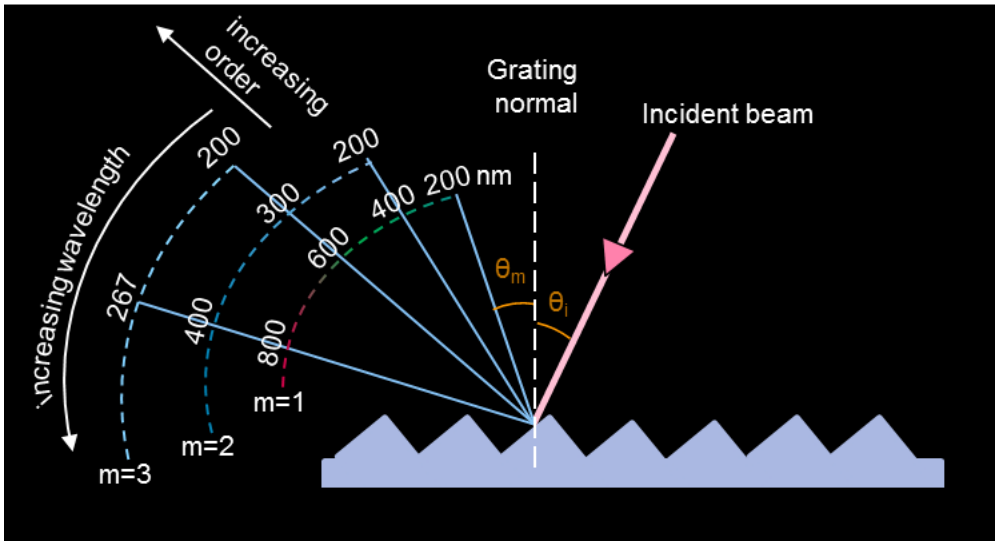

Figure 2.23: A comprehensive description of the basic diffraction orders with the overlapping spectra, which is valid for both transmission and reflection gratings operation. The basics of this illustration can be found in [137, 138].

This leads to overlapping wavelengths when they are diffracted into the same direction. When $\lambda/d << 1$, a large number of diffraction orders exists. High order gratings have a design wavelength which is much longer as can be seen in the following relation:
From Equation 2.25,

$$\begin{aligned} m\lambda &= 2d\sin\theta_m \\ \frac{m}{2}(2\lambda) &= 2d\sin\theta_m \\ &\vdots \\ \frac{m}{n}(n\lambda) &= 2d\sin\theta_m \end{aligned} \tag{2.29}$$

where n is an integer and n $\neq 0$.

The resolution of gratings is taken from the minimum wavelength difference which the grating is able to resolve between two wavelengths. Generally, the higher the number of grooves, so the smaller d, the higher the resolution will be.

Another important parameter, especially in bandwidth sensitive applications, is the spectral bandpass of a grating [140] in an optical system. The spectral bandwidth consists of the range of wavelengths that successfully falls onto the detector area or exit slit. For example, in dispersive spectrometer configurations as shown in Figure 2.24, the spectral bandpass is used to describe which portion of the spectrum can actually be isolated by the spectrometer.

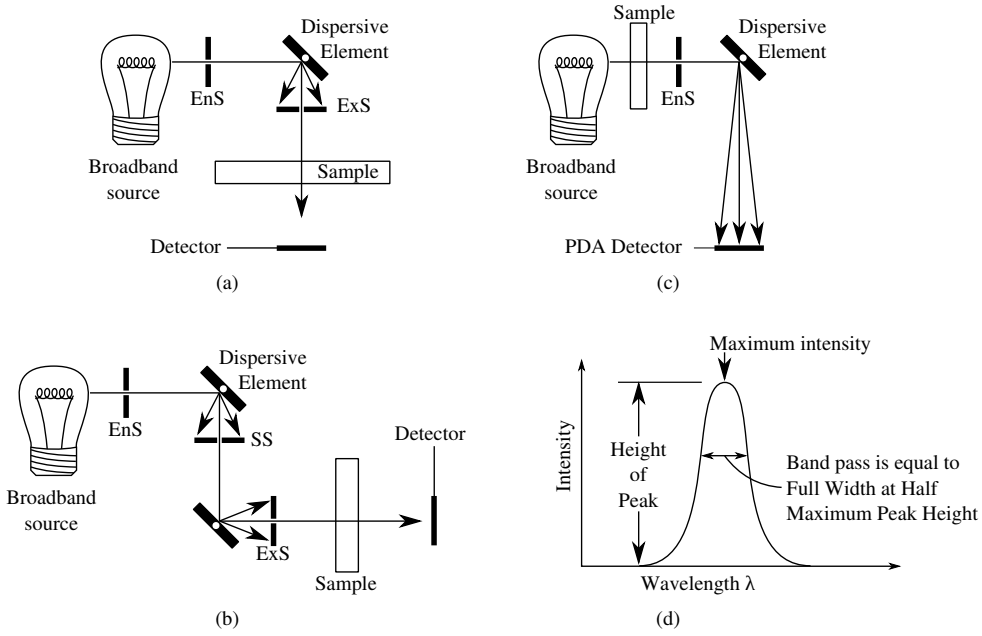

Figure 2.24: Dispersive optical configuration for spectrometers [139]: (a) Single monochromator system with EnS and ExS as the entrance slit and exit slit, respectively. (b) Double monochromator system with EnS, SS, and ExS as entrance slit, second slit and exit slit, respectively. (c) Diode array spectrophotometer with EnS as the entrance slit. (d) Spectral bandpass.

The spectrometer bandpass is dependent on the dispersion of the grating, the entrance and exit slit width. In a conventional spectrometer, the spectrum assumes a Gaussian-like curve as shown in Figure 2.24(d). The bandpass is determined at the Full Width Half Maximum (FWHM) of the normalized power or intensity curve. The spectral bandpass, B, is a product of the effective opening aperture of width, w and the reciprocal linear dispersion, P [138]:

$$B \approx wP \tag{2.30}$$

where P is simply the reciprocal linear dispersion of the effective distance, r, and the dispersion, $\frac{d\theta_m}{d\lambda}$:

$$P = \frac{1}{r\frac{d\theta_m}{d\lambda}} = \frac{d\cos\theta_m}{mr} = \frac{1}{Gmr\sec\theta_m} \tag{2.31}$$

Diffraction gratings may be replicated onto the surface of prisms to form grating prisms, called "Carpenter prism" or "grisms". A reflection grating replicated onto a prism allows light to diffract inside the prism to increase the dispersion.

In 2011, using a sophisticated approach, Karel van Acoleyen et al. [105] presented a 2D beam-steerer fabricated using silicon-on-insulator technology which has a steering range of $15° \times 50°$ over 100 nm wavelength shift with a beam width of $4°$ (or 50 resolvable spots in 2D space) in θ and ϕ-direction. In ϕ-direction the maximum dispersion was $10.7°$/nm with a minimum of $1.85°$/nm resulting in a maximum wavelength resolution of 2 nm due to the beam width limitations. For improvement, more grating couplers or waveguides can be added. However, in longer delay lines, phase errors due to sidewall roughness will broaden the beam. The beam-width in θ-direction depends on the strength of the gratings. By etching less than 70 nm, a weaker grating with a longer out-coupling length would narrow the beam.

2.2.5 Virtually imaged phased array

A Virtually Imaged Phased Array (VIPA) has a simple structure, has low cost, has low polarization dependence, and is a wavelength-dependent device capable of providing large angular dispersion [141]. The structure of a VIPA, as shown in Figure 2.25, is made of a thin plate of glass with a high-reflection film coating on one side and a 100% reflection film on the other side. There is an antireflection-coated window for the input beam.

In the first pass, for e.g., 5% of the input light passes through and diverges after the beam waist. 95% of the light is reflected. This 95% of light hits the second surface but at a point which is displaced by an amount, d, from the first point. Another 5% of the 95% beam passes through. In consecutive reflections, there will be many beams each separated by a distance of d. A virtual image of

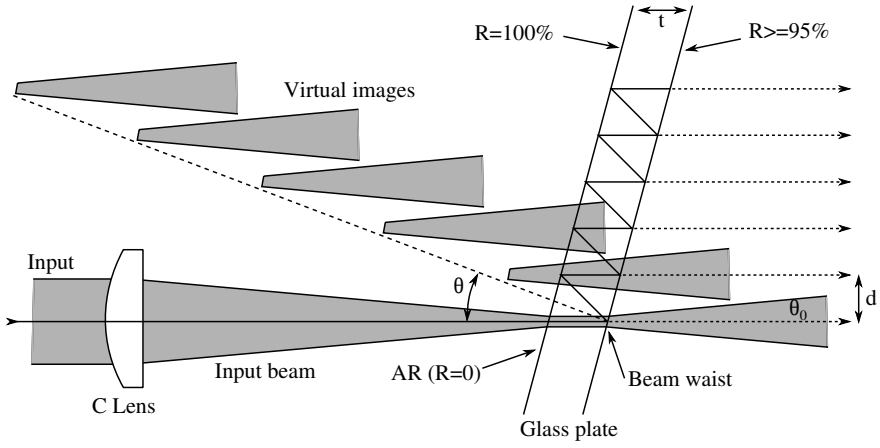

Figure 2.25: VIPA structure with a glass plate of approximately 100 μm thick [141]. t: Thickness of the plate, R: Reflectivity, C: Cylindrical, d: spacing of light paths, θ: incident angle in side the glass plate.

the beam waist is formed with constant spacing of $2t$ along the normal of the input side of the plate. Similar to a grating, the output light waves interfere and form a beam which propagates in a direction similar to the Bragg angle of diffraction. On the contrary, as the reflectivity has no phase difference nor angle difference, the beam profiles in all light paths are the same. When the field magnitude in a beam is constant at the output peak direction, the far field of the output beam is Lorentzian.

The spacing between the light paths can de determined using:

$$d = 2t \sin\theta \tag{2.32}$$

The difference in path lengths, P_L, between adjacent beams:

$$P_L = 2t \cos\theta \tag{2.33}$$

The angular dispersion can then be determined approximately using $n \cot\theta$ factor. The corresponding factor for a diffraction grating is $2 \tan\theta_m$ [142].
The VIPA equation is given in [143] as:

$$m\lambda = 2n_v t \cos(\theta - \theta_o) \tag{2.34}$$

where θ_o is the output angle and n_v is the refractive index of the plate material. The angular tuning range, $\Delta\theta_o$, when tuning over one FSR from λ to $\lambda + \Delta\lambda_{FSR}$ is [143]:

$$\Delta\theta_o = \theta_{o,2} - \theta_{o,1} = \arccos(\frac{\lambda}{2n_v t} m) - \arccos(\frac{\lambda}{2n_v t} \frac{m^2}{m-1}) \tag{2.35}$$

Koonen et al. also showed that the maximum $\Delta\theta_o$ is achieved when $m^2\lambda = 2n_v t(m-1)$, i.e. when, $\theta_{o,2} = \theta$, and is $\Delta\theta_{max} = \arccos(1 - 1/m)$.

2.2.6 Photonic crystals

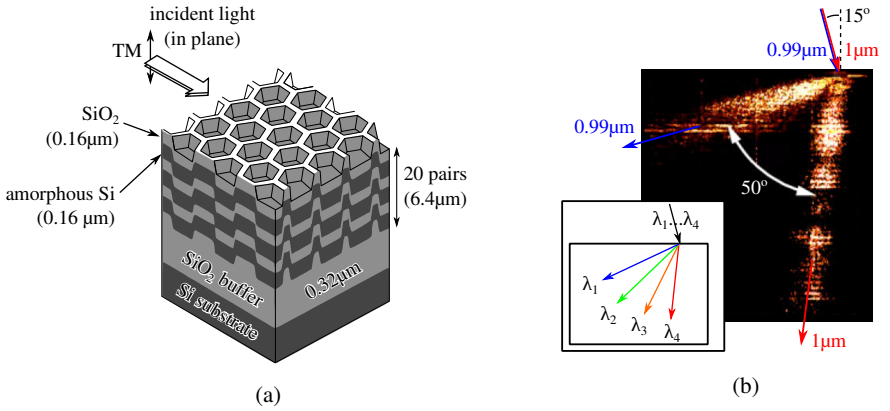

Figure 2.26: Photonic crystal [144]: (a) Schematic structure of the photonic crystal, which is a self-formed on a patterned Si substrate, having a graphite-like structure. (b) A photographed image of two light paths with an angular separation of 50° for incident wavelengths of 0.99 μm and 1 μm.

Photonic crystal operated with 1D wavelength-dependent angular beam-steering was presented by H. Kosaka et al. [144]. The high angular dispersion originates from the anisotropic dispersion in a photonic crystal. An angular separation of up to 50° was achieved at a wavelength of around 1 μm with only a deviation of 0.01 μm, as shown in Figure 2.26. The incoming beams are Transverse-Magnetic (TM) polarized laser beams incident at an angle of 15° from the normal.

2.3 State-of-the-art beam-steering for indoor free-space optical communication

In this section, the beam-steered optical wireless systems proposed in the recent past will be presented.

In year 2010, Ke Wang et al. from the University of Melbourne proposed a new hybrid optical-radio wireless system incorporating a high bandwidth Line-of-Sight (LoS) Free-Space Optics (FSO) system and radio frequency localization [145] as shown in Figure 2.27. This first demonstration in an indoor environment showed a feasibility of the system in achieving 2.5 Gigabit per second (Gbps) at error free, i.e. Bit Error Rate (BER) $< 1 \times 10^{-9}$, over 1 m distance with a Compound Parabolic Concentrator (CPC) receiver FoV of 45°. The system employed mirror-steering and demonstrated at the wavelength of 1550 nm with On-Off-Keying (OOK) modulation format.

In 2011, Ke Wang et. al further demonstrated a WDM-based system with 4×12.5 Gbps system using mirror steering [146]. The system was demon-

strated with OOK modulation format at wavelengths 1550.12 nm, 1550.92 nm, 1551.72 nm and 1552.52 nm. In 2012, the system was improved to support full-duplex communication over 2.56 m and a beam footprint of 88 cm [147]. Bitrates of up to 10 Gbps downlink at 7 mW transmission ($\lambda = 1550.12$ nm) and 500 Mbps uplink ($\lambda = 1551.72$ nm) at 5 mW transmission were achieved with OOK modulation format. In 2015, Ke Wang et al. have demonstrated a system with a transmission of 16-CAP (Carrierless-Amplitude-Phase) modulated signal achieving up to 10 Gbps downlink ($\lambda = 1550.92$ nm) at BER $< 1 \times 10^{-9}$ and 2 Gbps uplink ($\lambda = 850$ nm) at BER $< 1 \times 10^{-3}$ [82].

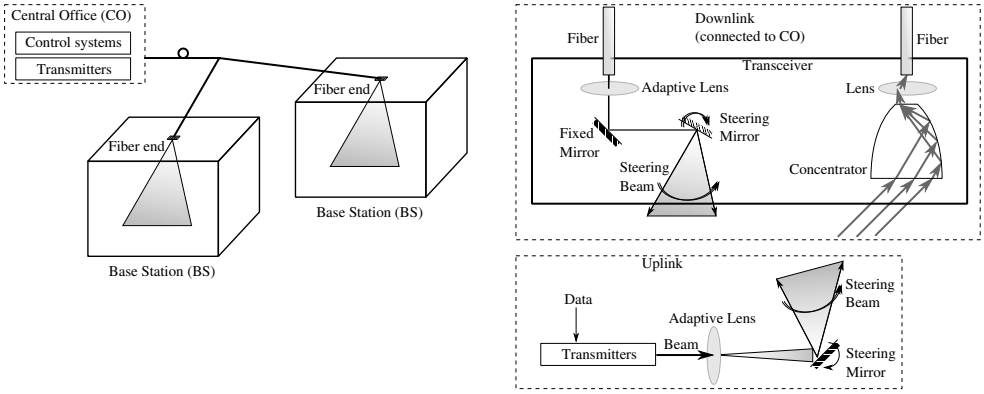

Figure 2.27: System configuration proposed by Ke Wang et al. [145]. Top subset: LoS optical wireless transmission with steering mirror and transceiver. Bottom subset: A similar structure is seen on the device side.

In 2013, Paul Brandl et al. proposed MEMS-based beam steering together with adaptive focus in order to be able to steer and to control the divergence of the beam [148]. The operational wavelengths are detectable using silicon Optoelectronic Integrated Circuit (OEIC). By using a directly-modulated VCSEL laser and a receiver chip in Bipolar Complementary Metal-Oxide-Semiconductor (BiCMOS) technology, they demonstrated an error-free 3 Gbps wireless transmission over 7 m with Pseudo Random Binary Sequence (PRBS) $2^{31} - 1$. As shown in Figure 2.28, the transmitter consist of a VCSEL and they had cleverly mounted a pickup from a commercial optical disc drive in the optical axis of the VCSEL beam. The steering is implemented using a gimbal-less two-axis scanning MEMS mirror which has a steering angle of $\pm 6°$. They also developed a novel receiver which has a low capacitance and is insensitive to common-mode noise.

As with the system of Ke Wang et al., Paul Brandl et al. employed mechanical mirror steering in which each channel will require an individual mirror. As the steering system is dependent on mechanical moving parts, the steering-system does not support random pointing, but only continuous scanning in which the positions depend on the movement of the mirror until it achieves the final position. Additionally, the steering speed is limited to the kHz range

by inertia. A further improvement can be made by using MEMS OPA to diffract beams of different wavelengths simultaneously to different directions, thus, improving latency time by avoiding mechanical motion for re-positioning.

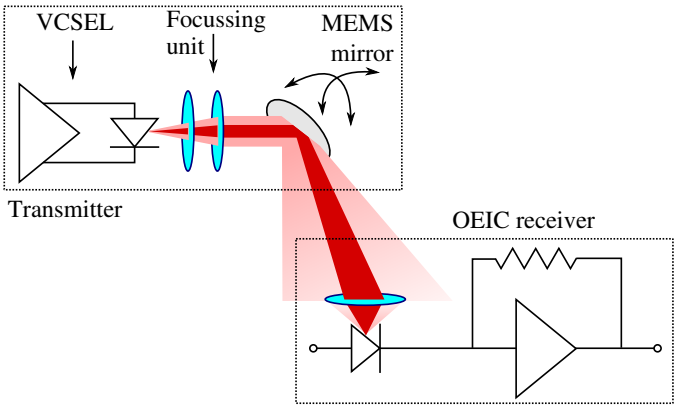

Figure 2.28: System configuration proposed by Paul Brandl et al. [148]. The transmitter consists of a 680 nm VCSEL and the adaptive beam is received by an OEIC receiver.

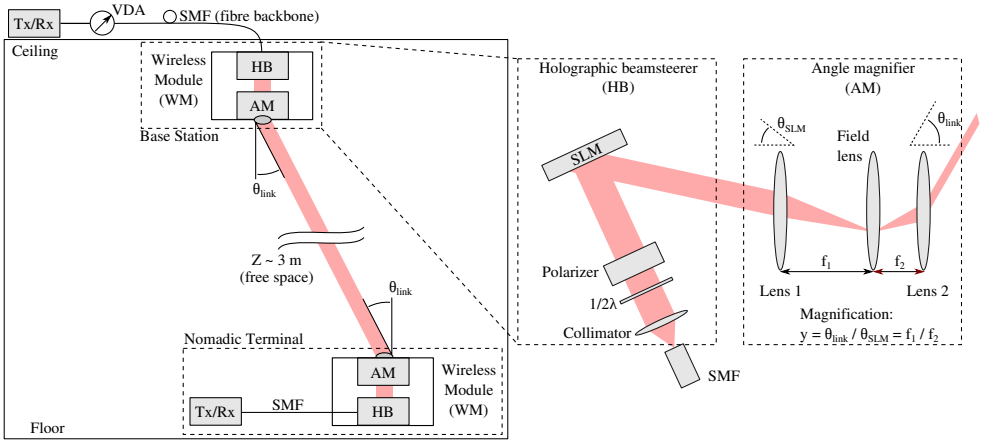

Figure 2.29: System configuration proposed by Ariel Gomez et al. [149]. A holographic beam-steering module is used together with an angle magnification module at the wireless module (WM) to increase the steering angles. The same configuration is seen on the user/nomadic terminal.

Ariel Gomez et al. have recently, in 2015, proposed a 2D bi-directional beam-steered system using Spatial Light Modulators (SLMs) and by using wavelength division multiplexing (WDM) of seven wavelengths from a seven channel Nyquist WDM transceiver together with coherent detection [149]. The output beam to free space has a maximum power of 10 dBm. The SLM (op-

timized for 1550 nm) used has a steering angle of $\sim 3°$ and used together with an angle magnifier to achieve $\pm 30°$. Software control is used to adapt the blaze profile of the SLM. Unlike the systems already mentioned, digital coherent WDM transmission instead of Intensity Modulation - Direct Detection (IM-DD) was used. Each channel was measured to be 37.38 Gbps. With Full-Field of Views (FFoVs) of 60° and 36°, up to 112 Gbps and 224 Gbps, respectively, were achieved. The large angle coverage with high bitrates are commendable. The transmission distance was ∼3 m. The system configuration is shown in Figure 2.29. In 2016, Ariel Gomez et al. further equipped the system with an integrated localization and tracking system which has an accuracy of up to 2.5 mm at 3 m using a CMOS camera at the base station observing Light Emitting Diode (LED) IR tags at the nomadic terminal [83]. Although this system is fascinating, it also has some drawbacks. As the SLM beam-steering module is based on active tuning, local powering will be required at each access point. In addition, software control is needed to adapt the blaze profile of the SLM. Regarding scalability, an SLM-based steering module needs a specific carefully controlled setting per beam, necessitating accurate local control per beam generated from the remote central site, and handling multiple beams would imply a complex segmented SLM or multiple SLMs with associated comprehensive remote control issues.

The pioneers, who proposed light scanning by employing passive dispersive optical components such as prisms, gratings, etc., while tuning the output wavelength of a broadband laser, were I. Filinski and T. Skettrup. The idea was published in 1982 [117]. However, they did not further implement the steering for communication purposes. In a not so recent work but related to the Beam-steered Reconfigurable Optical-Wireless System for Energy-efficient communication (BROWSE)'s steering technique, hereby we note the work of Nabeel Riza (1999) in which, he proposed the use of inertia-less optical scanners as agile free space light routing method within a multi-user free-space optical wireless network to realize all-optical advanced wireless networking [150]. A system demonstration of 2D and 3D scanner using a 1-to-4 demultiplexer incorporation with Graded Index (GRIN) lens for the third dimension and a mechanically tuned laser with 170 ms/nm was configured as shown in Figure 2.30 [151]. However, no data transmission was demonstrated.

In 2004, Kefei Liang et al. proposed a novel scheme which employed wavelength space division multiplexing in an LoS approach [152]. In their approach, a dispersive grating was proposed for 1D passive beam steering. Light is steered depending on the wavelength that illuminates the dispersive element. In the demonstration, a first order plane diffraction grating with a period of 1.1 μm was used to provide a 1D beam steering. It was successfully shown that a dispersive angle of $\sim 10°$ over a range of 30 nm C-band (1530 nm - 1560 nm) was obtained. A transmission of 1 Gbps using OOK signaling over 4.5 m with a receiver FoV of 12° was achieved. The system configuration is shown in Figure 2.31. Further simulation showed that by using two concave singlet lenses, up

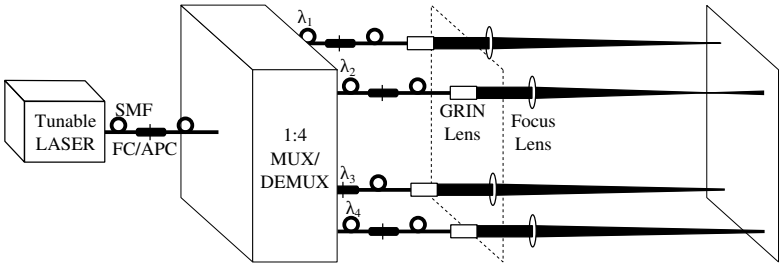

Figure 2.30: Experimental setup to demonstrated a 2D and 3D λ-scanner [151].

to 90° receiving angle is possible [152]. In an approach to achieve 2D steering, a secondary optical system with an array of fixed mirrors was proposed. This work has shown promising results in using diffractive optics for beam steering.

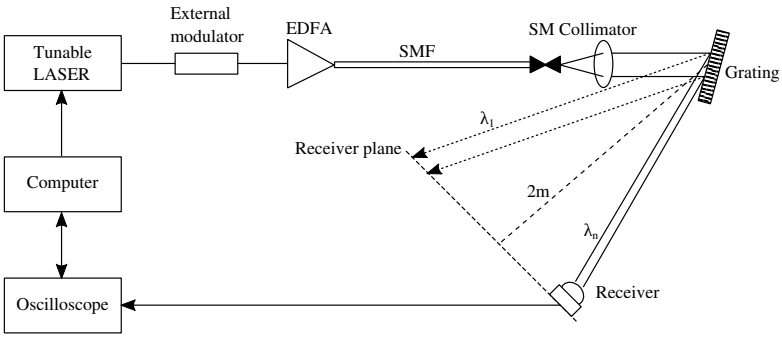

Figure 2.31: Experimental setup of a 1D downlink system demonstration with 2 m transmission between the grating and receiver [152].

The work of Kefei Liang was further developed into a 2D steering system. The steering module was constructed using a reflective diffraction grating and an array of 16 mirrors, together with a WDM source. An operational demonstration of 1 Gbps data transmission at a distance of 1.5 m was successfully demonstrated and reported in H. Shi et al in 2005 [153].

In 2013, similar to Kefei Liang et al.'s work, we reported in C.W. Oh et al. [154], a similar 1D steering system based on diffraction grating used together with a tunable laser source, a blazed grating with a period of 12.66 μm and a blaze angle of 75°. The data rate measured up to 10 Gbps using OOK-Non-Return-to-Zero (NRZ) format over a distance of 2.5 m. A steering angle of 17.16° was achieved over a wavelength range of 130 nm.

This thesis will elaborate my research work on narrow beam Optical Wireless Communication (OWC) with passive beam steering since 2013. Further, in developing a 2D beam-steered system, a steering module designed using 2D cascaded gratings is proposed. By using Discrete Multitone (DMT) modula-

tion format, up to 42.8 Gbps per-channel at Forward Error Correction (FEC)-limit (BER $\leq 2 \times 10^{-3}$) is achieved over 2.5 m distance. A steering angle of $5.61° \times 12.66°$ with a 2-line scan between 1529 nm and 1611 nm was achieved. With an improved cascaded gratings steering module, 7-line scan over 1511 nm and 1627 nm in an angular scan of $5.62° \times 12.15°$ with an improvement of at least 10.5 dB in power budget was achieved recently and reported in [155]. Using DMT modulation format, up to 41.4 Gbps per-channel is achieved at FEC-limit (BER $\leq 2 \times 10^{-3}$) over 2 m distance. In an effort to evolve indoor OWC to all-optical bi-directional approach, an all-optical 2D-steered system using optical carrier recovery technique has achieved 10 Gbps in both directions. Other progressive research activities will be further described in Chapter 8 and Chapter 9.

2.4 Chapter conclusion

The first section of this chapter has described many scanning techniques for active and passive beam-steering in order to give a general overview of the vast variety of techniques for steering, especially in terms of steering capabilities and complexities. Active steering techniques featured devices which require mechanical control or power for activating tuning mechanisms such as electro-optic heaters and micro-mechanical actuators. These methods also typically provide steering response in the order of milliseconds. In contrary, the passive steering mechanisms do not require any mechanical movement or power, but are wavelength-dependent in diffractive and refractive propagation. By using electro-optically tuned sources or with current-tunable lasers, a steering response of up to nanoseconds can be achieved.

In the second section of this chapter, the recent approaches in tackling optical wireless communication in an indoor environment were provided. Brief mentions were given on the capability of the systems and the beneficial features of each system in terms of simplicity, large FoV, adaptive beam control and transmission speed, as well as the corresponding drawbacks of the systems. In summary, the drawbacks of the given works include mechanical beam steering where its speed is limited due to inertia, single channel steering which means more elements such as mirrors or SLM segments are needed to steer more channels, and the need for local powering to activate control functions at the beam-steerer module.

The approach by Kefei Liang et al. is very interesting for the work in this thesis as it proposed a passive, non-mechanical steering based on diffractive optics, which is akin to the objective of this work. In Chapter 5, the evaluation of a passive 1D steering system using diffractive optics will be elaborated.

Chapter 3

Beam steering techniques in BROWSE

Contents

In a narrow beam Line-of-Sight (LoS) architecture, one of the biggest challenges in the free-space transmission is in directing these high capacity links to serve multiple users for the "last meters", bridging the gap between end-users and the fiber infrastructure. A multi-beam steering method is necessary in order to route the beams to different receiving devices simultaneously. The main considerations of a beam-steering method must take into account the steering efficiency and preservation of data integrity, which is of utmost importance in a communication system. The ideal beam-steering module is considered to be passive with no mechanical motions and low or no local powering needed, has high power efficiency, provides a large steering angle, supports bi-directionality, supports simultaneous steering of multiple beams, has short response time, is reliable, easy to configure, simple to manufacture and low-cost. User terminals with limited or full mobility naturally require real-time alignment, tracking and fast beam steering with large angular tuning range.

In Beam-steered Reconfigurable Optical-Wireless System for Energy-efficient communication (BROWSE), the main functionality of the beam-steerer is to flexibly direct the confined beams towards wireless devices using a combination of fully-passive optical elements at the remote access points and spectral tuning elements at the central controller. With reference to Figure 1.6 in Subsection 1.3, the beam-steerer is contained in a structure known as Pencil Radiating Antenna (PRA), which is to be positioned at the Access Point (AP). We shall

introduce the beam steering concept in Section 3.1 which was proposed by Ton Koonen in [156, 157].

My contribution on this work starts in Section 3.2 where I started by analyzing the grating equation (see also Subsection 2.2.4 for related grating equations) which is used to determine the parameters needed for constructing the steering module. Having chosen the suitable gratings, I continued by designing free-space transmission systems based on 2D beam steering. These proof-of-principle systems were then evaluated thoroughly with static and dynamic characterization, as will be reported in the next chapters.

3.1 Pencil radiating antenna beam steering concept

The PRA construction which was proposed is shown in Figure 3.1 [156, 157, 158, 159, 160]. It is constructed using two gratings to provide two-dimensional (2D) angular beam steering depending on the wavelength of the beam arriving at the PRA via the installed fiber. The beam out of the feeder fiber is collimated into a narrow beam. The first grating steers the beam in ϕ direction and the second grating steers it in ψ direction. The first grating has a small Free Spectral Range (FSR). The wavelengths are scanned a multiple times over ϕ direction in the range of the FSR. The second grating has a large FSR and the beam will be scanned across the orthogonal ψ direction. In this way, the (ϕ ,ψ) plane can be covered by spots of different wavelengths.

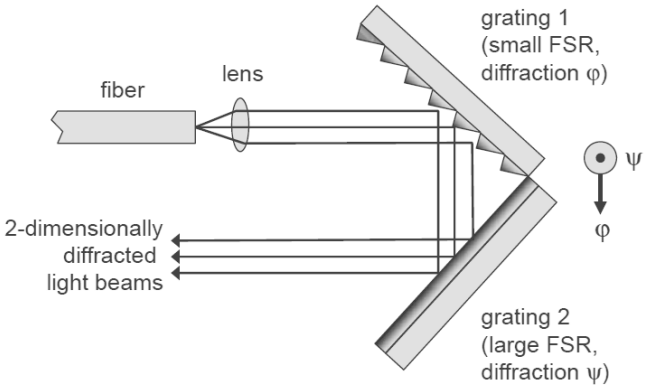

Figure 3.1: Crossed gratings for 2D beam steering by Ton Koonen et al. [143, 156].

In order to increase the dispersive power of the first grating, an integrated waveguide grating structure as shown in Figure 3.2 was proposed. The idea is to introduce a constant waveguide path difference, ΔL so that the FSR can be made small with the benefit of a higher angular dispersion. Neighboring waveguides have an optical path length difference ΔL_x, and are spaced at the

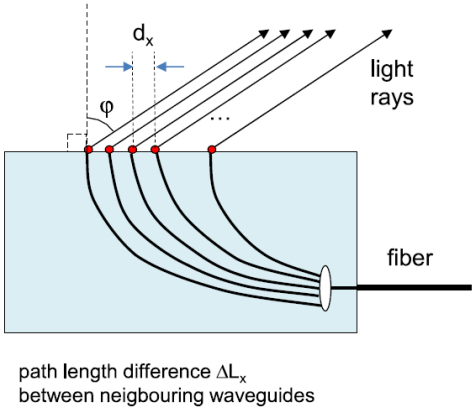

Figure 3.2: Integrated waveguide grating structure with small FSR [143].

end facet by d_x [143]. Multi-beam interference maxima occur in direction φ for $d_x \sin\varphi + \Delta L_x = m\lambda$. The FSR is then given as [143]:

$$\Delta\lambda_{FSR} = \frac{\lambda}{m-1} = \frac{\lambda^2}{\Delta L_x + d_x \sin\varphi - \lambda} \tag{3.1}$$

With a large internal optical path length difference, ΔL_x, a small FSR and a high order m can be achieved. The angular tuning range $\Delta\phi$ which is achieved when tuning over one FSR from λ to $\lambda + \Delta\lambda_{FSR}$ is [143]:

$$\Delta\varphi = \varphi_2 - \varphi_1 = \arcsin(\frac{1}{d_x}(m\lambda\frac{m}{m-1} - \Delta L_x)) - \arcsin(\frac{1}{d_x}(m\lambda - \Delta L_x)) \tag{3.2}$$

As $\Delta\varphi$ is largest when $\varphi_2 = \pi/2$, the maximum angular tuning range, $\Delta\varphi_{max}$, can be obtained using [143]:

$$\cos\Delta\varphi_{max} = 1 - (\frac{1}{m})(1 + \frac{\Delta L_x}{d_x}) \tag{3.3}$$

An alternative solution in obtaining small FSR and a high order, m, is by employing the Virtually Imaged Phased Array (VIPA) [143], which was introduced in 2.2.5.

3.2 Pencil radiating antenna beam steering design

The PRA, which functions as an area scanner, needs to be able to scan an area by scanning with beams of different wavelengths line-by-line. The range of the total angular scan and the density of scan lines are important parameters.

In order to realize the scanning using cascaded blazed diffraction gratings, a basic requirement is that the first grating have a small FSR whereby a range of wavelengths of different orders are overlapped in a 1D angular direction. A

second grating, placed orthogonally to the first grating will further diffract the wavelengths in an orthogonal direction to the first, hence, creating a 2D raster scan. In order to avoid overlapping beams, the large FSR of the second grating should accommodate at least the full range of wavelengths accommodated by the first grating. The range of spectrum in which it does not overlap the same spectrum in another order, m, is known as the FSR.

Let us consider a spectrum between λ_L and λ_U. We denote the lower wavelength as λ_L and the upper wavelength as λ_U. We can derive the appropriate FSR by using the lower or the higher wavelength as below:

$$\begin{aligned} m(\lambda_L + \mathrm{FSR}) &= (m+1)\lambda_L \\ FSR &= \frac{\lambda_L}{m} \end{aligned} \tag{3.4}$$

or as below:

$$\begin{aligned} m\lambda_U &= (m+1)(\lambda_U - FSR) \\ FSR &= \frac{\lambda_U}{m+1} \end{aligned} \tag{3.5}$$

The FSR equation can also be derived by considering that λ_1 of order m and λ_2 of order $m+1$ are diffracted to the same angle, θ_m. Therefore, the FSR can also be derived as:

$$\begin{aligned} m\lambda_1 &= d(\sin\theta_i + \sin\theta_m) \\ (m+1)\lambda_2 = \lambda_1 - \lambda_2 &= d(\sin\theta_i + \sin\theta_m)(\frac{1}{m(m+1)}) \end{aligned} \tag{3.6}$$

where θ_i is the incidence angle and θ_m is the diffraction angle.

By using equation 3.5, assuming a wavelength range between 1500 nm to 1600 nm, for the first, small FSR grating, an FSR of 10 nm will give an order of $m = (1600/10) - 1 = 159$. For the second grating, an FSR with a minimum of 100 nm, will give the order, $m \leq (1600/100) - 1 = 15$. Note that for grating 1, many orders m are passed when tuning from λ_L to λ_U (1500 nm to 1600 nm), and that the FSRs of these orders will be slightly different [143].

After determining the order of operation, in order to have a large angular dispersion, the blaze angle of the grating should be as high as possible or the period should be as small as possible as can be deduced from the dispersion equation shown in Equation 2.22. The required groove spacing and blaze angle can be determined using the Littrow configuration equation, i.e. Equation 2.24 ($m\lambda = 2d\sin\theta_m$). Note that Equation 2.24 only hold for a λ where $theta_i = theta_m$, so, in Littrow mount where $\lambda = \lambda_{Littrow} = \frac{2d}{m}\sin\theta_m$.

Correspondingly, the diffraction angle can be derived from the grating equation in Equation 2.21 for a constant incidence angle as:

$$\theta_m = \arcsin(\sin\theta_i - \frac{m\lambda}{d}) \tag{3.7}$$

By using Equation 3.2 and Equation 3.7 we can determine the largest scan range in a particular order. Figure 3.3 illustrates this relation in which the scanning range (delta diffraction angle between the largest and smallest wavelengths) increases as the blaze angle increases and groove spacing decreases. As the blaze angle increases, the scanning angle range also increases. The figure is computed for an FSR of 10 nm with $\lambda = 1600$ nm, therefore, $m = 159$ with steered wavelengths between 1590 nm and 1599 nm. The computed maximum angle that can be achieved at a blaze angle of 89° (7.86 grooves/mm) with wavelength tuning between 1590 nm and 1599 nm is approximately $\theta_{m\_max} = 6°$.

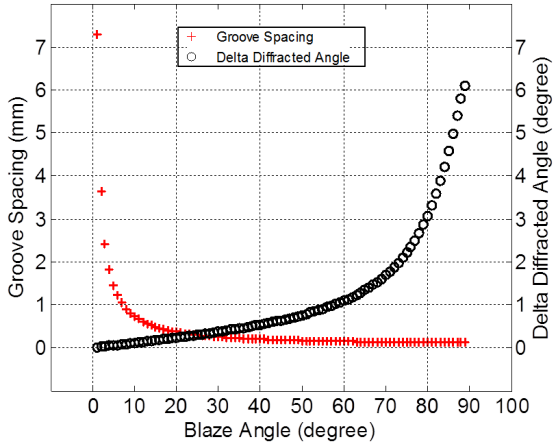

Figure 3.3: Dependency of scanning angle on groove spacing and blaze angle in a theoretical design using $\lambda_U = 1600$ nm.

Using the same method to determine the limit of steering on the low dispersive grating, using an FSR = 100 nm, with $\lambda = 1600$ nm, therefore, m = 15 with steered wavelengths between 1500 nm and 1599 nm. The computed maximum angle that can be achieved at a blaze angle of 89° (83.33 grooves/mm) with wavelength tuning between 1500 nm and 1599 nm is approximately $\theta_{m\_max} = 26°$.

If we do a sweep across the gratings using a wavelength range between 1499 nm to 1631 nm, we see that for the highly dispersive grating, the wavelengths will sweep across orders 155 to 169, and for the low dispersive grating from orders 14 to 16. The corresponding tabulation of diffracted spots is shown in Figure 3.4 and Figure 3.5, respectively. Do note that as the wavelengths are swept across different orders, the angular tuning range differs slightly.

Blazed gratings which have a large blaze angle are known as echelle gratings. In practice, echelle gratings provide more than one diffraction order for each wavelength. For beam steering purpose, in order to avoid interference from the next diffraction order of the same wavelength, only one diffraction order of the second grating is used.

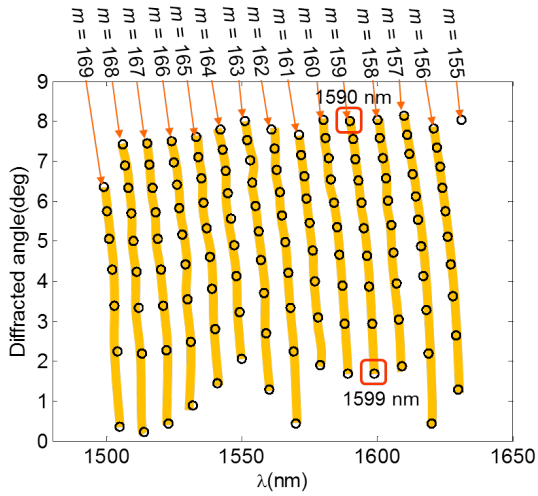

Figure 3.4: Diffraction angle versus wavelength tabulation for high dispersive grating.

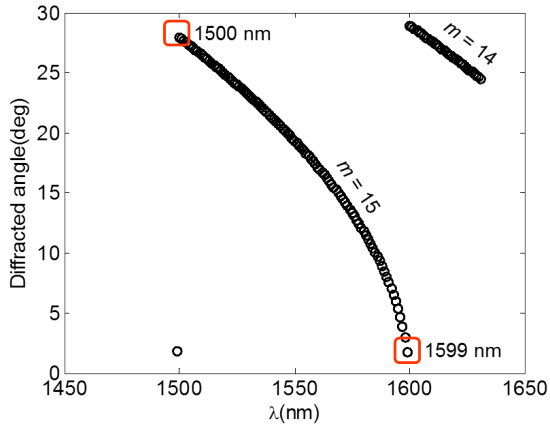

Figure 3.5: Diffraction angle versus wavelength tabulation for low dispersive grating.

3.3 Grating selection

In early 1D proof-of-principle experiments, a blaze grating from Thorlabs is selected due to the low cost. The parameters of the grating as specified by Thorlabs are:

Product number: GE2550-0875
Size: 25.0 mm × 50.0 mm × 9.5 mm
Number of grooves: 79
Grating period: 12.658 μm
Blaze angle: 75°
Blaze wavelength: 25 μm
Dispersion: 3.28 nm/mrad

In 2D beam-steering module which will be presented in Chapter 6, two diffraction gratings from Thorlabs were selected for the first 2D steering proof-of-principle experiments. The specification of the first grating (high dispersion) is as follows:

Product number: GE2550-0363
Size: 25.0 mm × 50.0 mm × 9.5 mm
Number of grooves per mm: 31.6
Grating period: 31.65 μm
Blaze angle: 63°
Blaze wavelength: 57 μm
Dispersion: 14.37 nm/mrad

The same grating as mentioned above (Thorlabs GE2550-0875) is employed as the second grating (low dispersion). The reason the gratings are used in this order is because the second grating has twice the FSR of the first grating. Unfortunately, efficiency curves are not specified for gratings from Thorlabs.

Due to the high loss and limited scanning lines of the first steering module, which was constructed using two reflection gratings, a new combination of gratings were sought after and carefully selected to construct an improved steering module which has a low loss, more scanning lines and a large angular dispersion. Thorough evaluation and comparison between the modules are elaborated in Chapter 6. From the calculation in Section 3.2, we would need a grating of order $m = 159$ and a grating of order $m \leq 15$. Finally, a commercially available high dispersion grating with a spectral order $m = 100$ at center wavelength 1480 nm is selected from a list of gratings provided by Newport [161]. It is not the ideal grating (according to the calculation) but it provides the closest available orders that are needed.

Information of this grating is as follows, and the efficiency curve is given in

Figure 3.6:
Product number: 53004BK06-182E [162]
Size: 30.0 mm × 30.0 mm × 10 mm
Number of grooves per mm: 13.33
Grating period: 75.02 μm
Blaze angle: 80.7°
Blaze wavelength: 148 μm
Coating: Aluminium

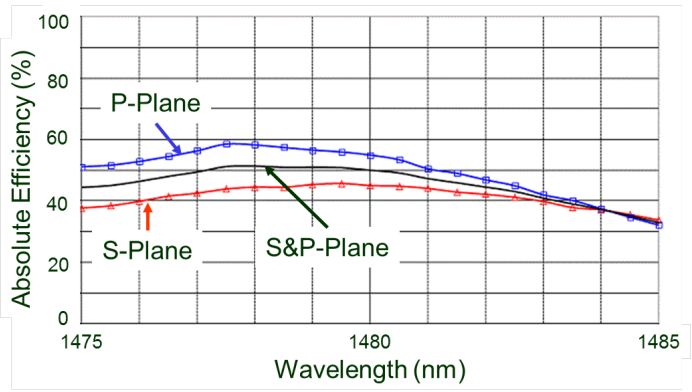

Figure 3.6: Efficiency curve for Newport's echelle grating blazed at 80.7°, with 13.33 grooves/mm at order $m = 100$ [163].

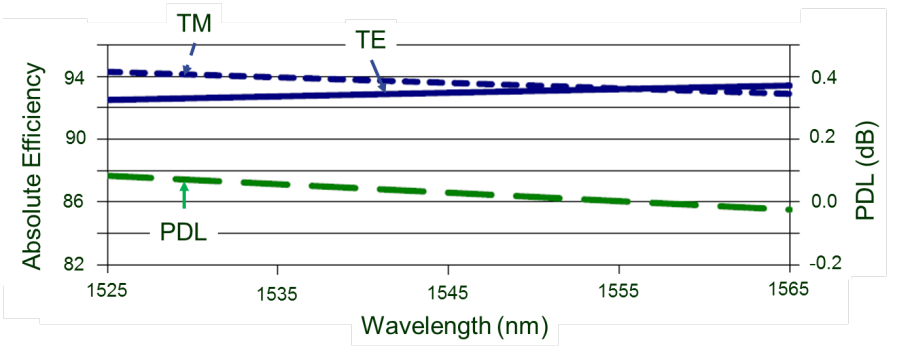

Figure 3.7: Efficiency curve for Ibsen Photonic's transmission grating of 1000 grooves/mm at order $m = 1$ [164].

As for the second grating (low dispersion), a transmission grating is selected from Ibsen Photonics [164]. Information of this grating is as follows, and the efficiency curve is given in Figure 3.7:

Product number: PING-sample-083 [164]
Size: 19.0 mm × 13.5 mm

Number of grooves per mm: 1000
Grating period: 1 μm
Angle of incidence: 49.9°
Materials: 100% dielectric
Grating technology: Surface relief, etched transmission grating

3.4 Verification of grating diffraction

In understanding the function of the grating from the equation to practical realization we shall first use the appropriate equations and present an actual verification setup implemented on a free-space testbed. The 79 grooves/mm, 75° blazed, echelle grating (Product number GE2550-0875) from Thorlabs, which is designed for use in high orders, was employed.

A testbed measurement was carried out to verify the diffraction spots and their locations as shown in the photo in Figure 3.8 and the schematic in Figure 3.9. The measurement was carried out using a red laser of wavelength, $\lambda = 657$ nm, at a free-space distance of 64 cm.

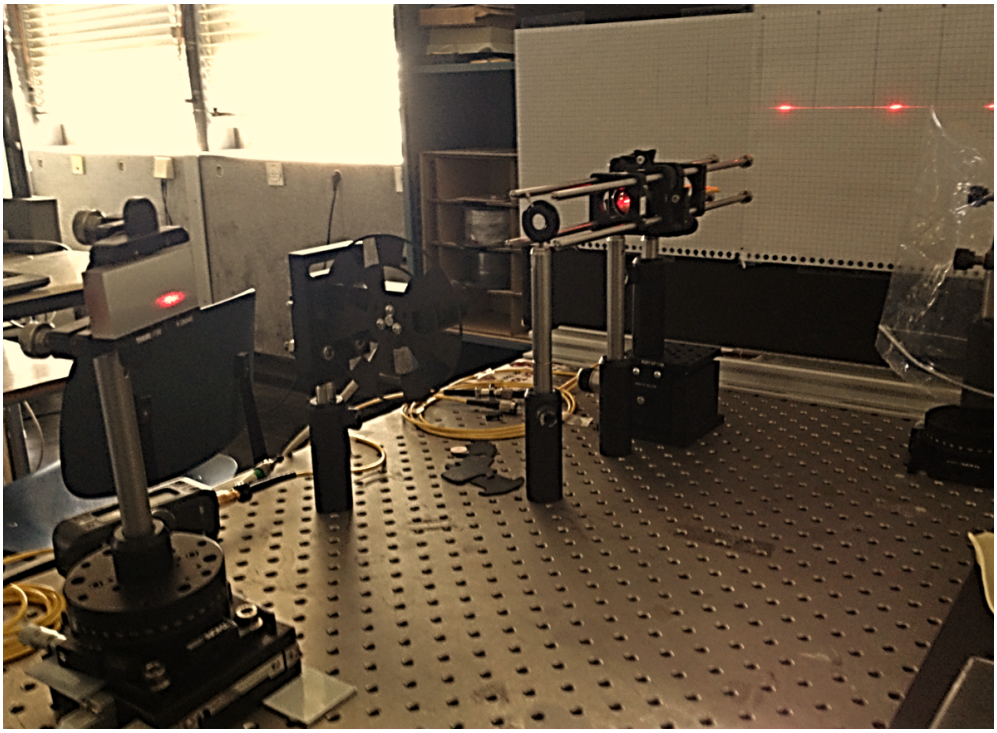

Figure 3.8: Testbed for 1D diffracted spots verification.

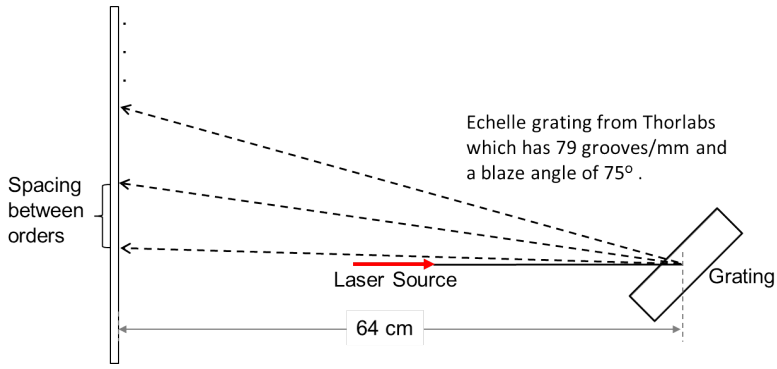

Figure 3.9: Experimental setup schematic for the verification of diffracted spots' positions. The grating is an echelle grating (Product number GE2550-0875) from Thorlabs, which has 79 grooves/mm and a blaze angle of 75°.

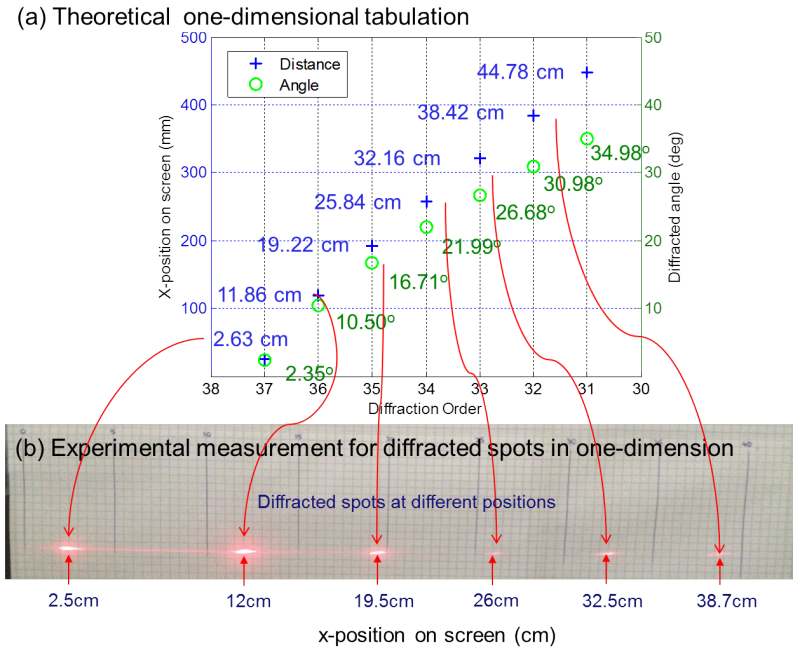

Figure 3.10: Measured grating spots in accordance with theoretically calculated positions.

Figure 3.10 shows the corresponding theoretically calculated spots using the equations given and experimentally verified spots. We see that the measured spots correspond well to the theoretical positions.

3.5 Chapter conclusion

The chapter gave an introduction on the beam-steering techniques proposed in BROWSE such as various types of gratings in realizing passive beam steering. The corresponding important equations, which are sufficient for the design of the cascaded grating approach, were presented. We further implemented a setup for the verification of the theoretical calculation of the positions on the diffracted spots, which is based on the formulas given. A brief theoretical calculation will also be given in each experimental demonstration in the following chapters.

Chapter 4

System design aspects

Contents

In this chapter, we shall first discuss the various design aspects of the free-space optical transmission system. In general, the construction of a free-space optical system is similar to the construction of an optical fiber communication system, except that the medium of transmission is in free space.

Figure 4.1(a) shows a basic optical fiber communication system and Figure 4.1(b) shows the basic optical free-space communication system. The main difference between the two is the medium of transmission, i.e. a fiber channel or a free-space channel. Therefore, in essence, a system that can be implemented in fiber channels can in principle be implemented in free space with the help of optical components. The fiber channel is affected by attenuation loss and dispersion effects in the fiber. On the other hand, indoor free-space channels also have losses but dispersion is negligible. The active components that make up the transmitter and receiver are essentially the same. The main components that are employed in the experimental testbed for this dissertation

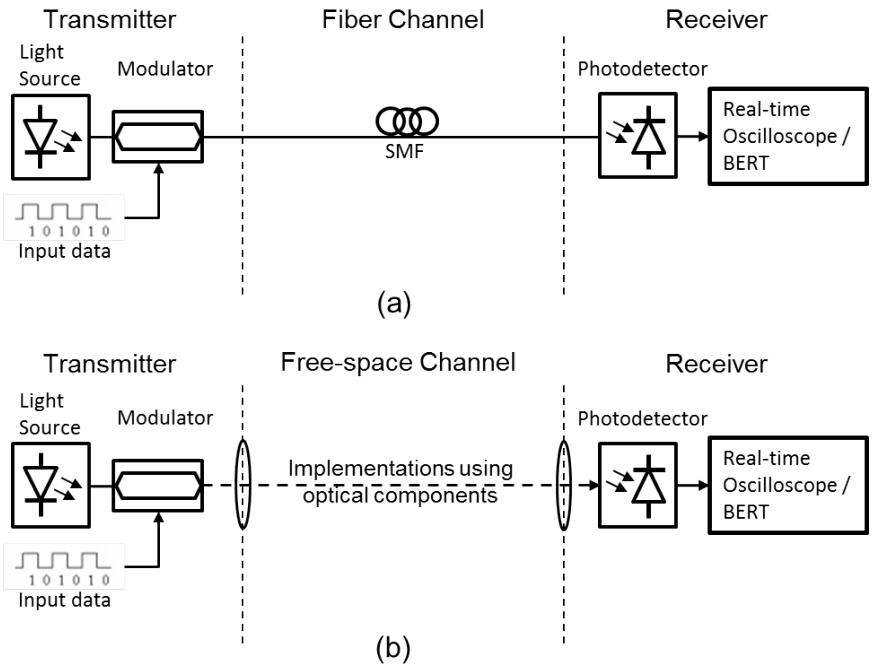

Figure 4.1: Optical fiber communication system versus free-space communication system.

include light sources, modulators, electrical and optical amplifiers and photodetectors. Data generation and data processing are carried out by instruments such as Arbitrary Waveform Generator (AWG), Pseudo Random Binary Sequence (PRBS) generator, Digital Phosphor Oscilloscope (DPO) and Bit Error Rate Tester (BERT).

4.1 Essential components for free-space transmission testbed

The components which are employed in the work of this dissertation are as follows:

Collimators
In this dissertation, a pigtailed triplet collimator lens from Thorlabs of type TC18FC-1550 with design wavelength at 1550 nm, is used. The collimator (of high beam quality ($M^2 \approx 1$) [165]) has a wavelength-adjusted focal length of 18.36 mm at wavelength of 1550 nm. The waist diameter (see Section 4.4) at 12.91 mm in front of the collimator housing, where the focal plane is at, is 3.33 mm. The diameter of the opening aperture of the lens is 10 mm. The spread of the beam can be analyzed using the Gaussian beam by taking the beam waist

where the focal plane is. For example, the diameter of the beams at 2 m, 2.5 m and 3 m are 3.53 mm, 3.64 mm and 3.78 mm, respectively. This type of collimator was chosen as it has a narrow beam with small divergence, as can be seen in Figure 4.2.

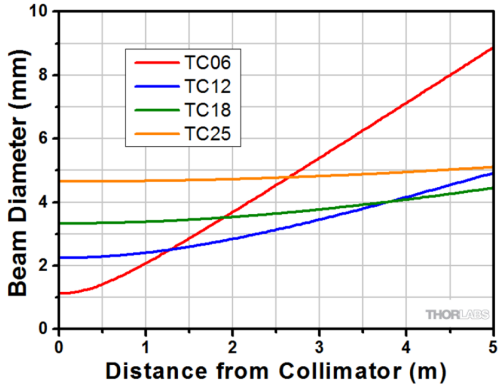

Figure 4.2: Beam diameter due to the divergence of Gaussian beam at distances up to 5 m, at alignment wavelength of 1550 nm. The types of collimators presented by Thorlabs in this figure are TC06, TC12, TC18 and TC25 [163]. The corresponding full-angle divergences based on the SMF-28e+ fiber are 0.101°, 0.047°, 0.034° and 0.024°, respectively.

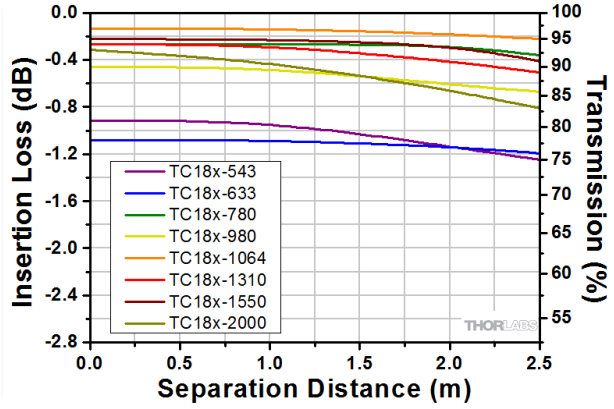

Figure 4.3: Thorlabs specified coupling loss and transmission efficiency for Thorlabs' triplet collimators. TC 18x-1550 represents both the 'Physical Contact FC/PC' and 'Angled Physical Contact (FC/APC)' connectorized type of collimators.

The collimator is also equipped with an anti-reflection coating which range between wavelengths of 1050 nm and 1648 nm. These anti-reflection coatings provide less than 1% maximum reflectance over the specified range. The operating wavelength range is specified to be between 1465 nm - 1648 nm, where

the coupling efficiency is decreased by approximately 1 dB due to focal shift which was measured by Thorlabs using two collimators at a separation distance of 200 mm.

Figure 4.3 shows the specification of the coupling loss of different triplet collimators designed at various wavelengths and their corresponding transmission efficiencies. For the collimators used in this thesis, i.e. TC18FC-1550, we refer to the curve for TC 18x-1550. 'x' represents the 'Physical Contact FC/PC' and 'Angled Physical Contact (FC/APC)' connectorized collimators. We observe that the insertion loss measured by the pair of triplet collimators is up to approximately 0.41 dB at a distance of 2.5 m. Correspondingly, it has a transmission efficiency of 91% [163].

Light sources

In this thesis, two types of lasers are used in the experimental setups. The first is a 10 Gigahertz (GHz) 1550 nm Distributed Feedback Laser (DFB) laser from Gooch & Housego model AA0701 which has a built in isolator, thermoelectric-cooler and thermistor. A DFB laser uses periodic Distributed Bragg Reflector (DBR) structures to form mirrors of the optical cavity. Temperature change induces changes in the refractive index of the material composition of the Bragg reflectors and inner cavity, and can result in wavelength change of a few nanometers. Therefore, in the earlier experiments, wavelength change has been induced using temperature control of the DFB laser. The second laser is a compact tunable laser source model 81960A from Keysight Technologies. It is an external cavity laser which has a wavelength tuning range from 1505 nm to 1630 nm and a capability to tune up to 200 nm/s.

Mach-Zehnder Modulators

Besides using direct modulation on the Gooch & Housego DFB laser, 10 Gbps amplitude modulators are employed for external data modulation. These modulators are from SDL Integrated Optics Limited (Product name: 10 Gb/s Amplitude Modulator. Model number: 10AP MOD9140).

Electrical and Optical Amplifiers

Electrical amplifiers which are used are from SHF Radio Frequency (RF) broadband amplifier 100APP (30 kHz to 12 GHz bandwidth) or 100BP (40 kHz to 25 GHz bandwidth) for a gain of 19 dB and 17 dB, respectively. As for optical amplifiers, there are two types, the first is an Erbium-Doped Fiber Amplifier (EDFA) and the other is a Semiconductor Optical Amplifier (SOA).

Photodetectors

A 2.5 GHz with unknown brand is used. Another is a 10 GHz Discovery Semiconductor PIN photodetector were employed (Part number DSC-R402AC-39-FC/UPC-K-2). PIN photodetectors are popular for indoor applications, in which economy is priority, due to the lower cost. There is also the option to

use the high performance Avalanche Photodetectors (APDs) which can have 10 dB advantage for an APD with a multiplication factor of 10 [166], however, at a higher cost in terms of price and high operating voltage.

Gratings
Please see Section 3.3 for information.

4.2 Modulation formats

In this section, we discuss briefly about the modulation formats employed in this dissertation. We shall first discuss the On-Off-Keying (OOK)-Non-Return-to-Zero (NRZ) modulation format, which is a binary non-return-to-zero modulation. NRZ differs from Return-to-Zero (RZ) which transitions to the '0' level for each bit by which it provides self-clocking but at the expense of double the bandwidth. An on-off signal or unipolar signal in optical transmission is known as on-off-keying. We see that there are two levels, that is the 'on' (when there is light) and the 'off' (when there is no light) levels.

When we transmit more than 1 bit/symbol, say 'n' bits, using amplitude modulation, we shall have 2^n-level modulation. N-PAM modulation is a multi-level signal, for e.g., a 4-level Pulse Amplitude Modulation (PAM) would mean a transmission of 2 bits/symbol. In fact, OOK is a 2-PAM system. OOK and PAM systems do not carry phase information, only amplitude information.

Another coding method is the Quadrature Amplitude Modulation (QAM) modulation format which has two dimensional modulation. The optical carriers of the same frequency have a phase difference of 90° with each other (see Figure 4.4).

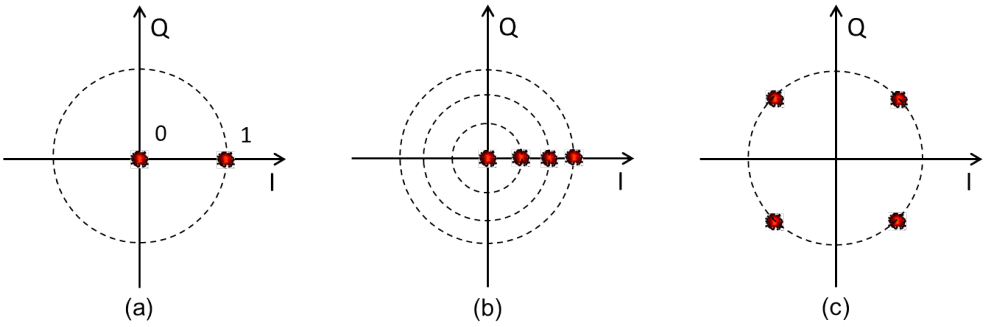

Figure 4.4: Example of constellation diagrams with I (in-phase or real) axis and Q (quadrature or imaginary) axis for (a) OOK, (b) 4-PAM and (c) 4-QAM.

The next modulation format is the Discrete Multitone (DMT) modulation, which is a variant of the Orthogonal Frequency Division Multiplexing (OFDM) technique and is widely used, for e.g., in copper-based Digital Subscriber

Line (DSL) user access networks for high speed transmission. DMT is a baseband multicarrier and multiplexing modulation technique that by its so-called bit-loading function can allocate the number of bits per subcarrier while adapting to the Signal-to-Noise Ratio (SNR) in order to optimize channel capacity in a transmission link. A rate-adaptive bit-loading algorithm is utilized to maximize the data rate over the available system bandwidth while staying below the threshold of Forward Error Correction (FEC) at a Bit Error Rate (BER) $\leq 2 \times 10^{-3}$. The operation of DMT transmit (modulation) and receive (demodulation) blocks in the digital domain is shown in Figure 4.5. From the transmitting end, a stream of serial input data is subdivided into parallel streams and modulated with QAM mapping. The complex signal is then multiplied with its conjugate satisfying the Hermitian symmetry for real-valued Inverse Fast Fourier Transform (IFFT) output. IFFT is performed to place the complex values and their conjugates on different sub-carrier frequencies. The signal is then converted from parallel streams to a single serial high-speed stream for transmission. At the receiving end, Fast Fourier Transform (FFT) is performed to demodulate the signal and the BER is calculated. For a more extensive treatment on DMT modulation techniques, please refer to [167, 168].

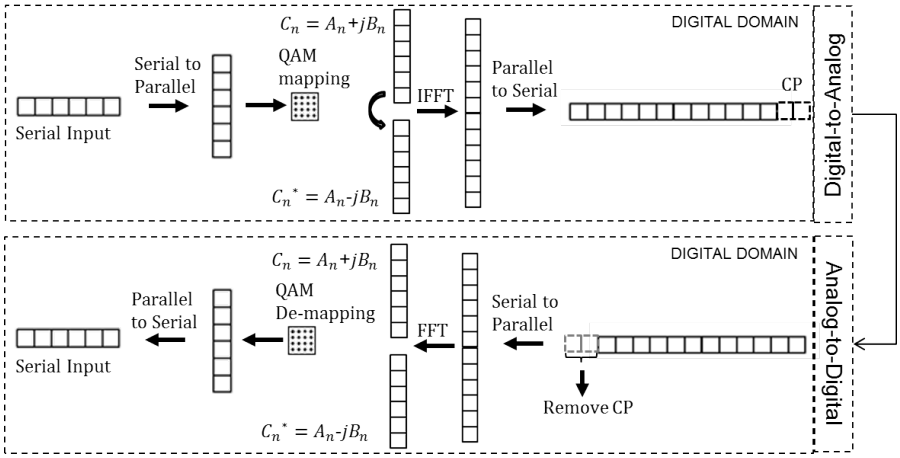

Figure 4.5: Discrete multitone modulation (DMT) operation blocks for transmitting and receiving DMT signals. Quadrature Amplitude Modulation (QAM), Cyclic Prefix (CP) [167].

4.3 Collimator full-field of view

The collimators employed in this dissertation have a Full-Field of View (FFoV), which is related to the full-angle divergence, θ_{div}. The theoretical maximum

specified is 0.034° at $1/e^2$, which can be calculated using:

$$FFoV = \theta_{div} = \frac{MFD}{f} \times \frac{180}{\pi} \tag{4.1}$$

where MFD is the mode field diameter of SMF-28e+ which is 10.4 ± 0.5 μm at 1550 nm [169].

4.4 Beam diameter

Since laser sources are used in this thesis we shall analyze the free-space beam using the well known Gaussian beam equations with the important parameters as shown in Figure 4.6. Laser beams are similar to plane waves but their intensity distributions are concentrated near the axis of propagation with a slightly curved phase fronts [170]. A field component, u, of the coherent light satisfies the wave equation:

$$\Delta^2 u + k^2 u = 0 \tag{4.2}$$

where $k = 2\pi/\lambda$ is the propagation constant in the medium, and

$$u = \Psi(x, y, z) \exp(-jkz) \tag{4.3}$$

where Ψ is a slowly varying complex function which represents characteristics such as non-uniform intensity distribution, expansion of the beam width with propagation distance, curvature of the phase front, etc.

The fundamental Gaussian beam is given by H. Kogelnik and T. Li as [170]:

$$u(r, z) = \frac{w_o}{w} \exp(-j(kz - \Phi) - r^2(\frac{1}{w^2} + \frac{jk}{2R})) \tag{4.4}$$

where $\Phi = \arctan(\lambda z/\pi w_o^2)$ and is known as the Guoy phase shift (See [170, 171] for the full derivation). The expression describes the behavior of the laser beam amplitude as a function of transversal coordinate, r, and axial coordinate, z.

A commonly accepted definition is that the Gaussian beam waist is the smallest radius of the beam and is denoted as, w_o, (see Figure 4.6) where the beam intensity or power has fallen to $1/e^2$ of the peak. Sometimes the position at half peak is used and this is known as the Full Width Half Maximum (FWHM) width. It is impossible to have a perfectly collimated beam due to diffraction of light waves.

The beam radius at z-position is given by:

$$w(z) = w_o \sqrt{1 + (\frac{z}{Z_R})^2} \tag{4.5}$$

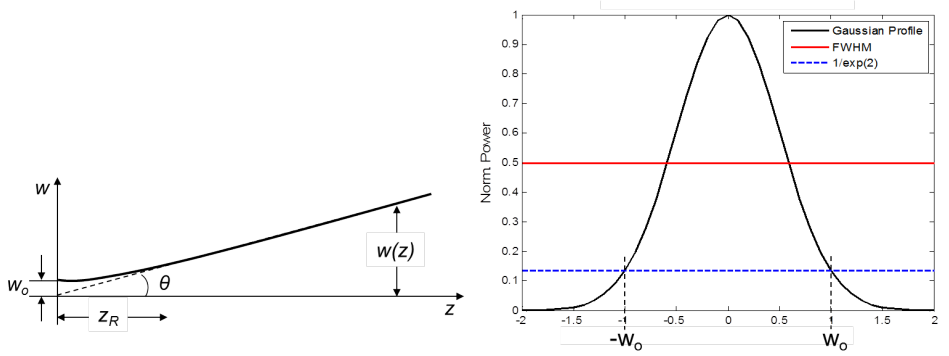

Figure 4.6: Profile of Gaussian beam which can be described using the parameters explained in the text. (a) Longitudinal and (b) Transversal power profile of the Gaussian beam amplitude, with a solid line indicating the full width at half maximum position and a dashed line indicating the $1/e^2$ position.

The radius of curvature at z-position is given by:

$$R(z) = z(1 + (\frac{Z_R}{z})^2) \tag{4.6}$$

where Z_R, which is known as the Rayleigh range, is where the beam waist has increased by a factor of $\sqrt{2}$.

The Rayleigh range can be calculated using:

$$Z_R = \frac{\pi w_o^2}{\lambda} \tag{4.7}$$

At far field ($z >> Z_R$), the half-divergence angle, can be calculated using:

$$\theta = \sqrt{\frac{2\lambda}{\pi b}} = \frac{\lambda}{\pi Z_o} \tag{4.8}$$

where $b = 2Z_R$ which is the depth of focus.

4.5 Eye-safety

As the optical channels will be propagating in free space, it is a must that skin- and eye-safety limits are taken into account. However, since the optical power limit for eye-safety is lower (more stringent) than the limit for skin-safety, the maximum permissible exposure (MPE) required for eye-safety is used in this dissertation. The Accessible Emission Limit (AEL) can be calculated as follows:

$$AEL = MPE \times \pi r^2 \tag{4.9}$$

where Maximum Permissible Exposure (MPE) [18] is the reference limit where a person can be exposed to without risk of injury, πr^2 is the beam area in which the beam radius, r, is commonly calculated at 63% or 87% power level, i.e. at $1/e$ or $1/e^2$, respectively [172]. Figure 4.7 shows the different MPE values for different wavelength for several exposure duration. Much higher MPE value is given for wavelengths above 1400 nm. This means a more relaxed optical power constraint is attainable for infrared beams of wavelengths above 1400 nm compared to shorter wavelengths in visible light communication (see Subsection 1.2.2).

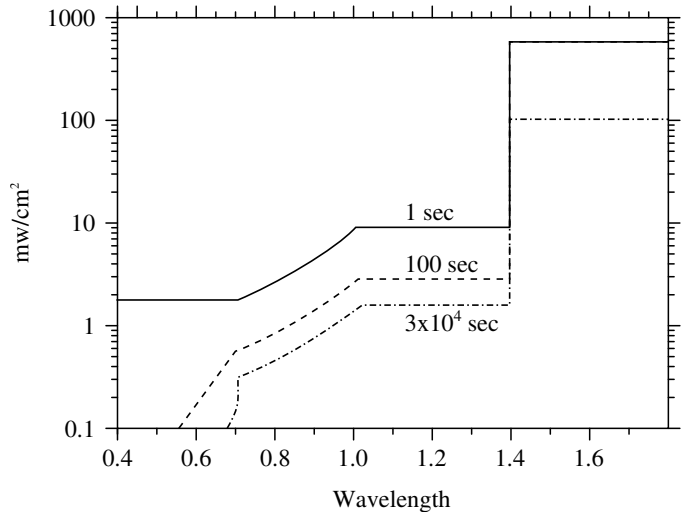

Figure 4.7: The maximum permissible exposure versus wavelength for several exposure duration [44].

4.6 Cascaded gratings for beam steering

In setting up the grating-based Pencil Radiating Antenna (PRA), it is important to know the positions and the coverage of the diffracted spots which are expected for the different gratings. These can be calculated easily by using the grating equation shown in Equation 2.21.

- In x-direction:

$$\theta_{x,m} = \arcsin(\sin\theta_{x,i} - \frac{m\lambda}{d_1}) \tag{4.10}$$

- In y-direction:

$$\theta_{y,m} = \arcsin(\sin\theta_{y,i} - \frac{m\lambda}{d_2}) \tag{4.11}$$

where d_1 and d_2 are the period of grating 1 and grating 2, respectively.

After the alignment process, the positions of the spots are measured and compared to the calculated tabulation to verify their positions. For further design calculations, please see Chapter 3.

4.7 Angular magnification

As shown in Section 3.2, the passive blazed gratings that are employed in this work are limiting the coverage to angles of approximately $6° \times 26°$ when used with a Free Spectral Range (FSR) of 100 nm. In order to further extend the angular coverage, an angle magnifier can be used. The simplest form of angle magnifier is an inverse Keplerian telescope, as shown in Figure 4.8. It is a simple construction which can be build using two lenses with focal lengths depending on the magnification factor desired. The angular magnification factor can be calculated using:

$$M = \frac{\tan\beta}{\tan\alpha} = \frac{f_1}{f_2} = \frac{d_1}{d_2} \tag{4.12}$$

where d_1 and d_2 are the diameter of the incoming and outgoing beams, f_1 and f_2 are the focal lengths of the input lens and output lens and α and β are the angle of the incoming and outgoing beams, respectively. Note that angular magnification ($\beta/\alpha > 1$) implies beam narrowing ($d_2/d_1 < 1$). Besides using a Keplerian telescope method, there are also variants with a positive and a negative lens, i.e. Galilean telescope setup.

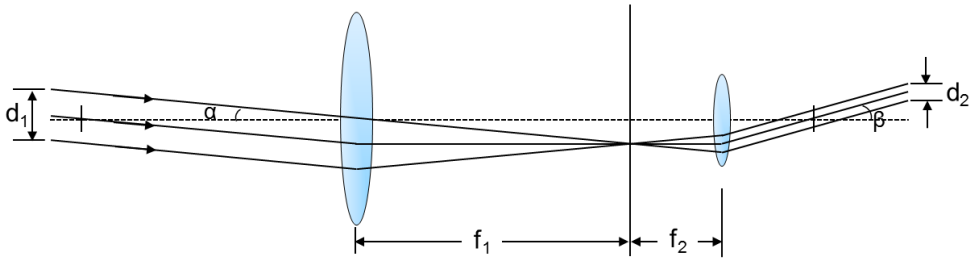

Figure 4.8: Basic setup for an angular magnifier.

4.8 Beam expansion

As we see in Section 4.7, angular magnification leads to beam narrowing. To compensate the narrow beam, we can first expand the beam size before transmitting it to the beam-steering module which is equipped with angular magnification to increase its angular steering coverage. As shown in Figure 4.8, the angle of the beam is expanded at the expense of a smaller output beam. Therefore, it is important to compensate the beam size by using a beam expander

to increase the beam size again. A basic setup of a lateral beam expander is shown in Figure 4.9. The lateral magnification factor can be calculated using:

$$M = \frac{f_2}{f_1} = \frac{d_2}{d_1} \tag{4.13}$$

The effective length of such configuration will be $f_1 + f_2$.

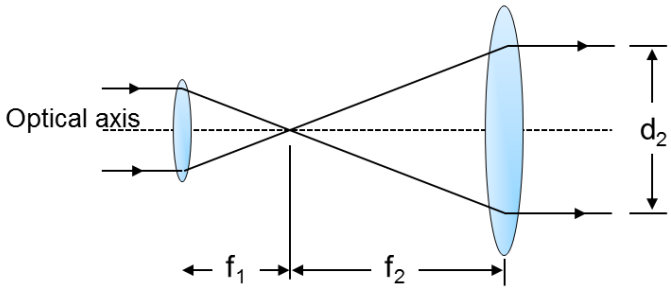

Figure 4.9: Basic setup of a lateral beam magnifier.

4.9 Beam steering control and localization

The beam steering control of the system is incorporated in the Central Communication Controller (CCC). The Keysight tunable laser 81960A, which is able to tune up to 200 nm/s and with a wavelength tuning range from 1505 nm to 1630 nm, is employed. The beam steering process, as described in Chapter 3.1, is initiated when a user transmits a 60 GHz signal to the phased-array antenna at the Radio Access Point (RAP). Instantaneous or low-latency identification of the position and tracking of the movements of mobile devices is important. As localization is not part of the work in this dissertation, only several examples of recently reported localization techniques which can be used for localization in indoor Optical Wireless Communication (OWC) are mentioned.

An interesting approach is to employ a localization technique based on the angle-of-arrival principle, reported by Kulakowski et al [173]. In this case, a mobile device transmits radio signal which is detected by a phased-array antenna at the access point and subsequently, the signals angle-of-arrival can be determined. The radio signal can be a separate beacon signal or a part of preamble of the upstream signal.

In 2011, Ke Wang et al. demonstrated an interesting method [146], in which the user first sends a "request" message to the transceivers mounted on the ceiling to activate the localization function. Upon receiving the "request" information, the transceiver starts a "search and scan" process by sending a specific code to each cell. After receiving the code, the user device copies and sends it back so that the transceiver is able to obtain the location information

of each user device through the specific code sent back. The "search and scan" process continues running to update the user device's localization information.

In the work of Liang et al. [152] in 2004, the receiver is placed at any position along the receiver plane, which is 2 m away from the grating beam steerer. The tunable laser tunes through a wavelength range and the received power recorded at each wavelength is used to find the maximum. Then, the tunable laser is set to the wavelength with the highest power recorded.

4.10 Automatic receiver alignment robot

In order to aid the alignment of the system setups, an automated alignment system was designed and built in order to aid the alignment of the receiver to the beam-emitting access point. However, it is important to note that this is not the final intended design. The assumption is that the final developed receiver have a wide Field of View (FoV) and therefore, as long as the beam is pointing towards the receiver, the alignment robot should be able to locate the beam very quickly and to optimize the alignment to the maximum power position. The four degrees-of-freedom alignment robot has been programmed with the capability to automatically search and optimized power collection by aligning the axis between the optical transmitter and receiver. In the future, better and faster optimization algorithms and learning algorithms can be programmed into the software. The alignment robot was developed within the master thesis project of Adrián Pérez Oliveros [174]. The task of the robot is to effectively align the receiver to the optimum power in the shortest time possible by only tuning the lens collimator at the receiver based on the received optical power. The alignment robot is able to work in two stages. The first stage is the establishment of optical link and the second stage is the alignment optimization using fine alignment. Exhaustive experimental results show that up to the 75% of the transmitted power can be collected at the receiver side at transmission distances of up to 2 m. The alignment time required, including the time the robot use to find the beam, is between 2 and 6 minutes on average using a lens with a FoV of 0.034°. This can be further improved by using optimization algorithms, for e.g. gradient descent optimization [175].

In order to build a simple alignment robot, only one parameter is measured to achieve the optimal alignment. This parameter is the received optical power. The receiver is built with four degrees-of-freedom in order to be able to move the receiver to obtain the peak power position (as shown in Figure 4.10). The robot has a horizontal transition in x-axis, vertical translation in y-axis, horizontal rotation θ and vertical rotation ϕ. The x- and y-translations are enabled by using 12-mm-travel-range actuators, one for each axis. A 360° motorized worm wheel drive rotation stage is used for θ rotation and a $\pm 8°$ goniometer is used for ϕ rotation. The operation of the robot is shown in Figure 4.11 [174]. A Thorlabs TC18FC-1550 triplet lens, as described in Chapter 4, is used to

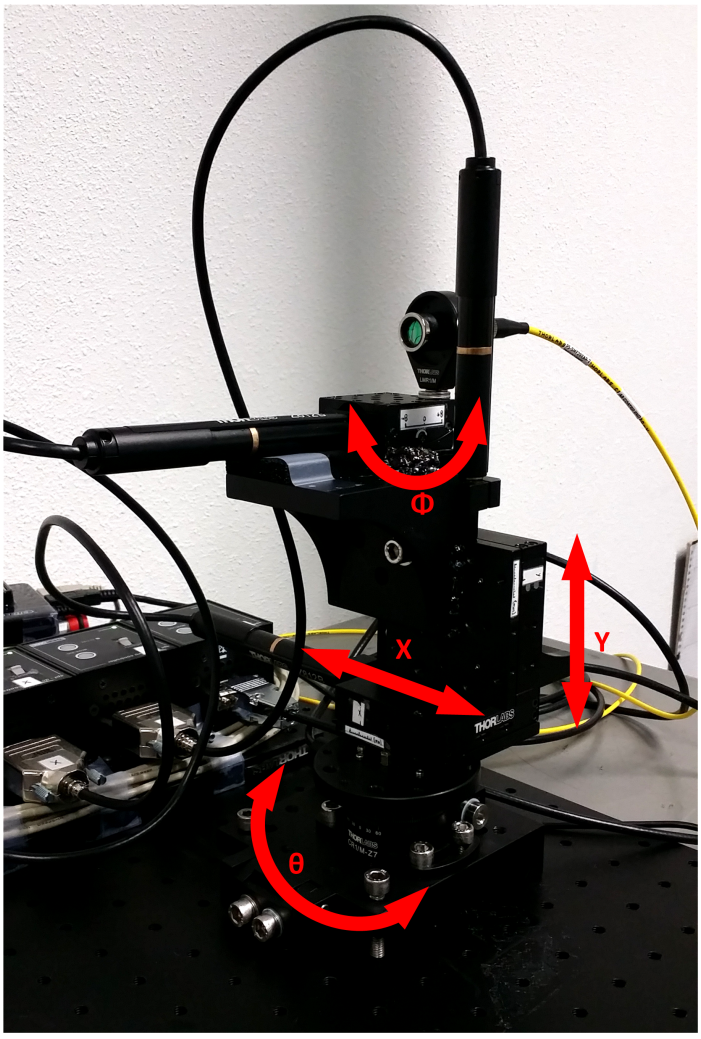

Figure 4.10: A 4 degrees-of-freedom alignment robot which has been programmed with the capability to automatically search and optimized power collection by aligning the axis between the optical transmitter and receiver [174].

couple the beam into a SMF. In order to detect an incoming beam, the positioning system is connected to a photodetector to measure the received optical power. After that, the positioning program executes the alignment command to move the receiver to the position where the received power is maximum. The alignment process is shown in the flowchart in Figure 4.12.

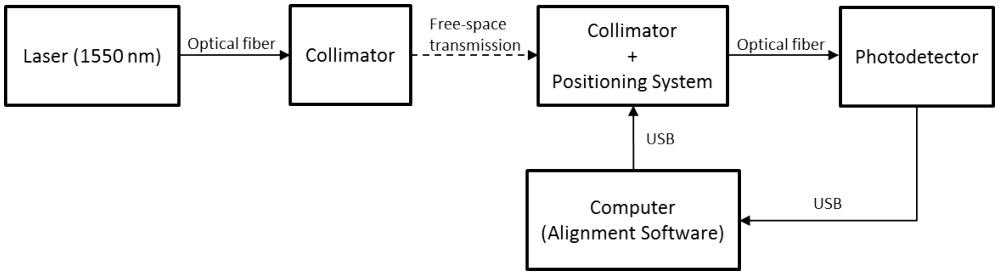

Figure 4.11: Automatic receiver alignment system design [174].

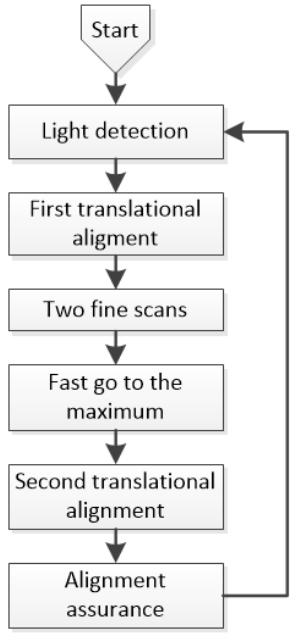

Figure 4.12: General flowchart of the alignment algorithm [174].

The complete software was implemented with LabVIEW® [176, 177], which is a comprehensive integrated development environment designed specifically for building measurements and control systems. In the design of the alignment program, modularity of the algorithms is essential. A modular programming allows a combination of complex algorithms by combining smaller independent sub-algorithms which can be developed individually and can be easily modified if needed, for e.g. the addition of new functionalities or for the implementation

of optimization algorithms into each module (sub-algorithm). A brief description of each sub-module is given as follows:

Light detection
This is the first sub-algorithm which starts of by moving the receiver in search of a connection. After the evaluation of several options, e.g. spiral search [178], spherical movement search was chosen for being the easiest to implement and the simplest in terms of computational complexity. It requires only the horizontal rotation θ and vertical rotation ϕ movements as shown in Figure 4.13. The flowchart for this sub-algorithm is shown in Figure 4.14. The receiver scans the area continuously until the measured power is above the power value set by the user in the software. The selection for the two rotation axis is not random but it is to align the beam such that it falls into the FoV of the receiver. For a receiver with a large FoV, the beam can be detected easily and therefore, this step can be skipped.

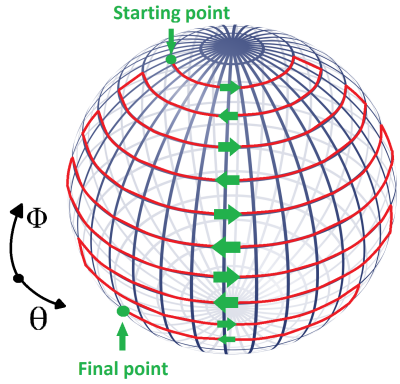

Figure 4.13: Light detection method based on horizontal rotation θ and vertical rotation ϕ movements [174].

First translational alignment
Once the beam is detected by the receiver, the horizontal transition in x-axis and vertical translation in y-axis are used to find the peak power of the beam. The peak power could be positioned anywhere on the receiver lens. By comparing the received power of the current location and the neighbors' (except for the previous location as the power is certainly smaller than the current location), this sub-algorithm moves the receiver by translating the X-Y axes to the location with the higher received power. The flowchart for this sub-algorithm is presented in Figure 4.15.

Two fine scans
Now that we have found the position with the maximum power, this could be just the apparent maximum power but not the true peak power of the beam, as

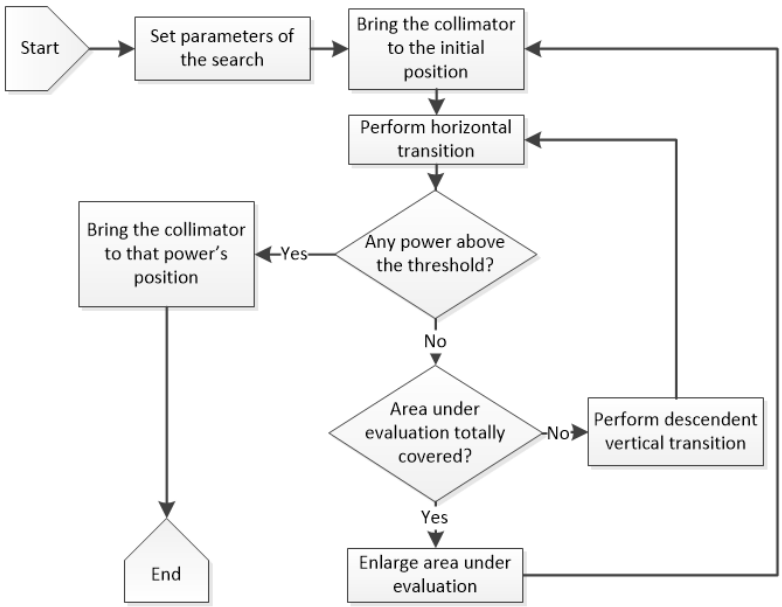

Figure 4.14: Flowchart for the light detection sub-algorithm [174].

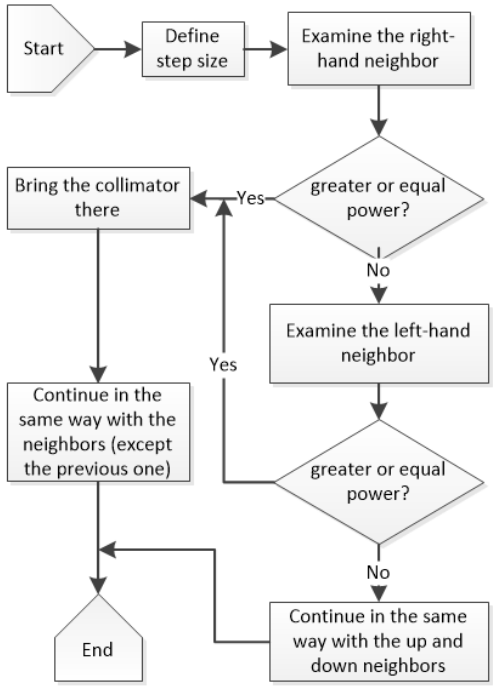

Figure 4.15: Flowchart for the 'First translational alignment' sub-algorithm [174].

shown in Figure 4.16. In this sub-algorithm, two scans with the first having a wider scan area than the second was implemented. The continuous horizontal rotation θ approaches a horizontal resolution of about 0.003°.

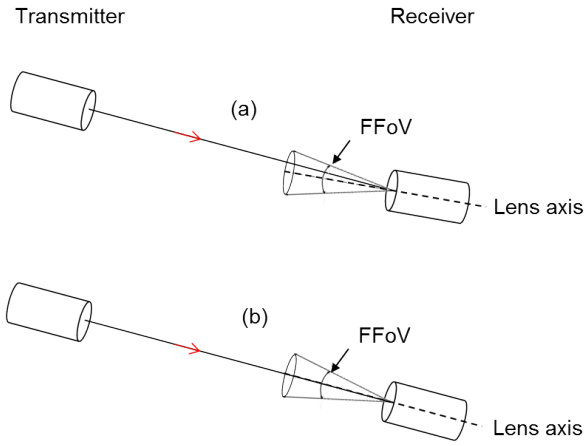

Figure 4.16: The apparent versus the true peak power [174]: (a) Receiver seems well-aligned but is not at the direction of the peak power. (b) Receiver is aligned to the direction of the peak power.

The difference between the angular transition in this sub-algorithm compared to the "Light detection" sub-algorithm is that instead of scanning to the left and right, this sub-algorithm moves the receiver back to the same position where the vertical rotation started to ensure that the step size is consistent in each movement. The sub-algorithm ends when the maximum received power in the horizontal position is above the threshold set. The flowchart for this sub-algorithm is presented in Figure 4.17.

Fast go to the maximum
The receiver is now very close to the ideal position. The receiver now scans the position vertically along the axis where the maximum point was found in the horizontal scan. The peak power should be along this vertical axis. The receiver is rotated vertically downwards along the vertical axis. The flowchart for this sub-algorithm is shown in Figure 4.18.

Second translational alignment
This sub-algorithm adjusts the X-Y translation axes to position the receiver precisely at the center of the aligned beam.

Alignment assurance
This sub-algorithm can be activated to track the alignment state. The module compares the current detected power with the previous received power in order to determine if the beam is misaligned. A power margin is used to set when

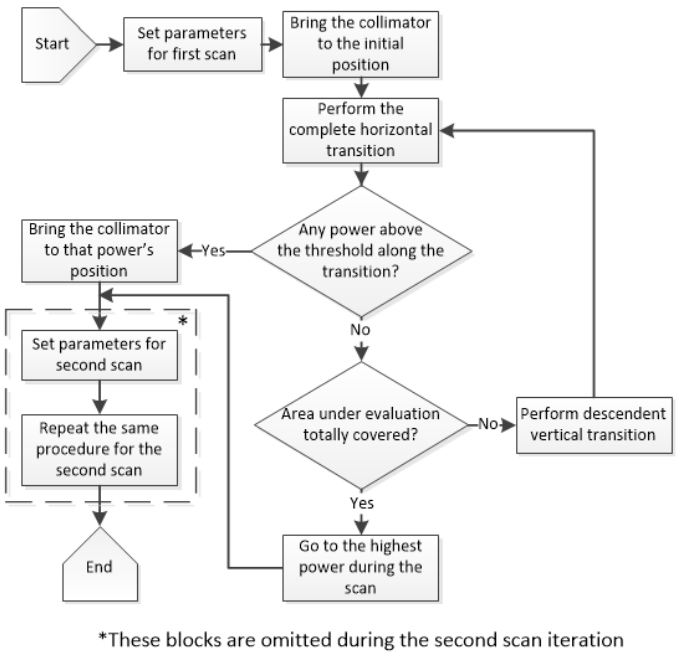

Figure 4.17: Flowchart for the 'Two fine scans' sub-algorithm [174].

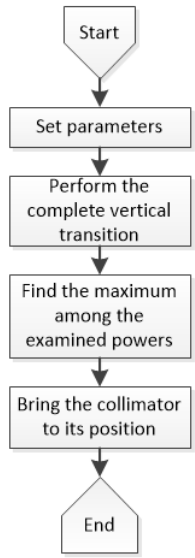

Figure 4.18: Flowchart for the 'Fast go to maximum' sub-algorithm [174].

the power drop is significant enough to activate re-alignment. The flowchart for this sub-algorithm is presented in Figure 4.19.

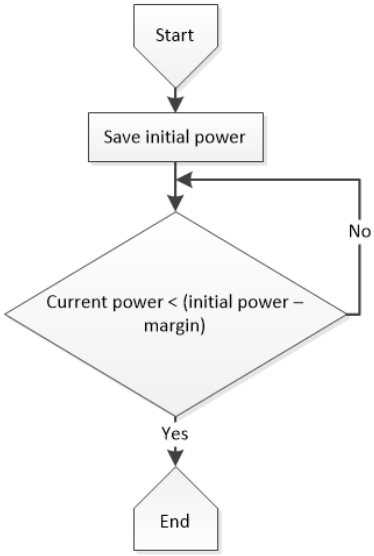

Figure 4.19: Flowchart of the alignment assurance sub-algorithm [174].

4.11 Chapter conclusion

In order to provide a smooth transition from the previous theoretical chapters, the practical issues regarding the implementation of optical free-space communication system are introduced in this chapter. The communication components which are used in the experimental demonstrations in the subsequent chapters are described. Important system design considerations such as the determination of the beam diameter, eye-safety, grating dispersion, and angular magnification are described. We have also seen the working mechanism of an automatic receiver alignment robot which was frequently employed in experimental evaluations.

In the next chapter, the system design and the evaluation of one-dimensional (1D) beam steering will be presented.

Chapter 5

1D beam steering - System design and experiments

Contents

After discussing the theoretical principles and devices available, this chapter will elaborate on the proof-of-concept experimental evaluations to characterize, and determine the feasibility of gratings for optical free-space transmission. In order to predict the area coverage, the theoretical calculation to determine the map of the diffracted beams' position versus wavelength is given. These beams are then aligned and measured on a screen at a certain distance to verify the calculated map. Finally, the chapter will be concluded with several experimental evaluations.

5.1 1D beam diffraction for 1D beam steering

The echelle grating that has been employed in this experiment is a Thorlabs GE2550-0875 model. The grating has 79 grooves/mm, a blaze angle, θ_B of 75° at a blaze wavelength of 25 μm and a linear dispersion of 3.25 nm/mrad. The

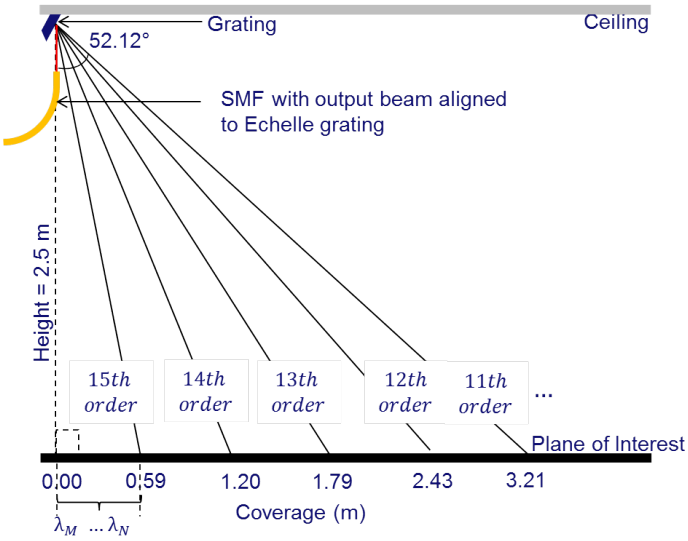

Figure 5.1: Map of diffracted beams at several grating orders for 1D beam steering. The wavelength employed is 1558.98 nm. The distance between the grating module to the plane of interest (where the devices are assumed to be) is taken to be 2.5 m [179].

size of the grating is 25 mm × 50 mm × 9.5 mm. The grooves are parallel to the shorter dimension. For more information, see Section 3.3.

The map of the diffracted beam of $\lambda = 1558.98$ nm, at different grating diffraction orders, is shown in Figure 5.1 for a free-space distance of 2.5 m (assuming the height of the Pencil Radiating Antenna (PRA) is 2.5 m from the plane of interest). These positions can be calculated using the grating equation 2.21:

$$m\lambda = d(n_1 \sin\theta_i + n_2 \sin\theta_m)$$

By rearranging the grating equation, we have:

$$\theta_m = \arcsin[\frac{1}{n_2}(\frac{m\lambda}{d} - n_1 sin\theta_i)]$$

Since a reflection blazed grating is used, the refractive indices n_1 and n_2 are equal to 1.

$$\theta_m = \arcsin[(\frac{m\lambda}{d} - sin\theta_i)]$$

In a Littrow configuration, the incidence angle, θ_i is equal to θ_B, so, θ_i is constant at 75°, d is the period of the grating, which is equal to 1 mm/79 grooves, therefore 12.6582 μm, and with $\lambda = 1558.98$ nm, the order can be calculated using the Littrow equation 2.24:

$$m = \frac{2d \sin\theta_m}{\lambda}$$

$$m = \frac{2(12.6582 \times 10^{-6}) \sin 75^\circ}{1558.98 \times 10^{-9}} = 15.69 \approx 15$$

We can finally calculate the position of each beam by using:

$$\theta_m = \arcsin[(\frac{m\lambda}{d} - sin\theta_i)]$$

The Littrow angle of 75° is set to be the normal to the plane of interest, in this case, the plane is at distance of 2.5 m away.

The first angular position of the diffracted beam of wavelength, $\lambda = 1558.98$ nm is:

$$\theta_{m1} = \arcsin[(\frac{15(1558.98 \times 10^{-9})}{12.6582 \times 10^{-6}} - sin75^\circ)] = 61.82^\circ$$

The delta angle between the normal at 75° and θ_{m1} is then $75^\circ - 61.82^\circ = 13.18^\circ$. The position of the beam at θ_{m1} at 2.5 m distance away from the normal is 2.5 m $\times \tan 13.18^\circ$ =0.59 m.

As discussed in Subsection 2.2.4, only spectral orders where $|m\lambda/d| < 2$ can exist. Therefore, with a constant λ and d, only the orders lower than $m = 15$ can exist. Therefore, we calculate the next position for order, m = 14. Correspondingly, the next angular position of the diffracted beam of wavelength, $\lambda = 1558.98$ nm is:

$$\theta_{m2} = \arcsin[(\frac{14(1558.98 \times 10^{-9})}{12.6582 \times 10^{-6}} - sin75^\circ)] = 49.32^\circ$$

The delta angle between the normal at 75° and θ_{m2} is then $75^\circ - 49.32^\circ = 25.68^\circ$. The position of the beam at θ_{m2} at 2.5 m distance away from the normal is 2.5 m $\times \tan 25.68^\circ$ =1.20 m.

The next angular position of the diffracted beam of wavelength, $\lambda = 1558.98$ nm, at m=13, is:

$$\theta_{m2} = \arcsin[(\frac{13(1558.98 \times 10^{-9})}{12.6582 \times 10^{-6}} - sin75^\circ)] = 39.43^\circ$$

The delta angle between the normal at 75° and θ_{m1} is then $75^\circ - 39.43^\circ = 35.57^\circ$. The position of the beam at θ_{m3} at 2.5 m distance away from the beam normal to the plane of interest is 2.5 m $\times \tan 35.57^\circ$ =1.79 m.

Similarly, for the 4th and 5th orders, the angular positions are at 30.80° and

22.88° away from the normal and at a distance of 2.5 m away, the beams are directed to positions, 2.43 m and 3.21 m, respectively.

To further illustrate 1D beam steering using different wavelengths, the beam position versus wavelength map is calculated, as shown in Figure 5.2. First, we look for the diffraction order of the corresponding wavelength by rearranging the Littrow equation 2.24 to:

$$m = \frac{2d \sin \theta_m}{\lambda}$$

Afterwards, the corresponding diffraction angles when the wavelength is changed can be obtained using:

$$\theta_m = \arcsin[(\frac{m\lambda}{d} - sin\theta_i)]$$

By steering the wavelength from 1529 nm to 1630 nm at diffraction order, $m = 15$, we achieve a steered distance of 772 mm.

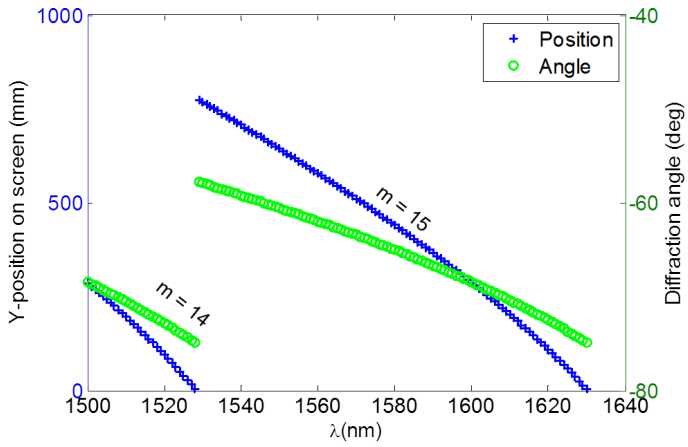

Figure 5.2: Diffraction angle and spatial distribution for a transmission distance of 2.5 m between the grating and the screen, with corresponding maximum steering angle of 17.16° by using diffraction order $m = 15$ for 1D beam-steering [154]. By steering the wavelength from 1529 nm to 1630 nm, we achieve a steered distance of 772 mm.

5.2 Channel bandwidth

The spectral response profile of a system has a major impact on the bandwidth of the overall system, next to the bandwidth of the receiver. As discussed in Subsection 2.2.4, the bandpass is determined at the Full Width Half Maximum (FWHM) of the normalized power or intensity curve 2.24(d). R.B. Passey et al.

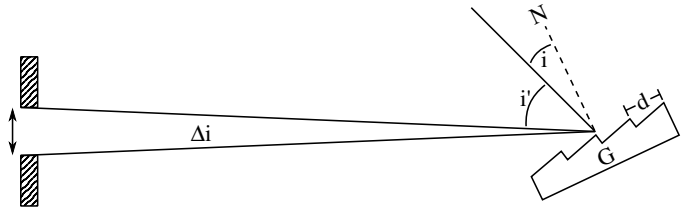

Figure 5.3: Diffraction grating and the exit slit from the monochromator [180]. i: angle of incidence, i': angle of diffracted light, N: normal line to grating, d: period of the grating, G: diffraction grating

[180] reported the method they used in calculating and measuring the spectral bandwidth of their monochromators in 1975. The method they used to measure the spectral bandwidth, as shown in Figure 5.3, is similar to the method used in this dissertation. The only difference is that, in this dissertation, a lens coupler, and hence, the lens aperture acts as the slit which determines the wavelength interval that passes through the aperture.

This dissertation presents two methods in measuring the spectral bandwidth of the steering module. The first is by tuning the laser in a range of wavelengths and measure the optical power, in which the spectral bandpass is then determined at the FWHM of the normalized power curve. The second method is by using the Optical Spectrum Analyzer (OSA) to capture the Amplified Spontaneous Emission (ASE) spectrum of an Erbium-Doped Fiber Amplifier (EDFA) whereby only a wavelength interval will be captured by the coupling lens.

The spectral bandwidth, $\Delta\lambda$, can be determined from the optical spectrum, and the bandwidth in frequency, $\Delta\nu$ can be obtained using:

$$\Delta\nu = \frac{c\Delta\lambda}{\lambda^2} \tag{5.1}$$

For example, a spectral bandwidth measurement was carried out by transmitting ASE wideband signal originating from an EDFA toward an echelle grating (Thorlabs GE2550-0875) which has 79 grooves/mm and a blaze angle of 75°. The receiver (triplet lens collimator from Thorlabs (TC18FC-1550) with a focal length of 18.36 mm, an opening aperture of 10 mm, and a full-angle divergence of 0.034°. The $1/e^2$ beam diameter is 3.33 mm at the focal plane. For further information on the lens collimator please refer to Section 4.1.) was placed at 1 m distance and the received beam is coupled into the optical input port of an OSA. The measured spectral bandwidth, as shown in Figure 5.4, is 0.17 nm at FWHM which by using Equation 5.1, we get the corresponding bandwidth of 21.27 Gigahertz (GHz) in frequency.

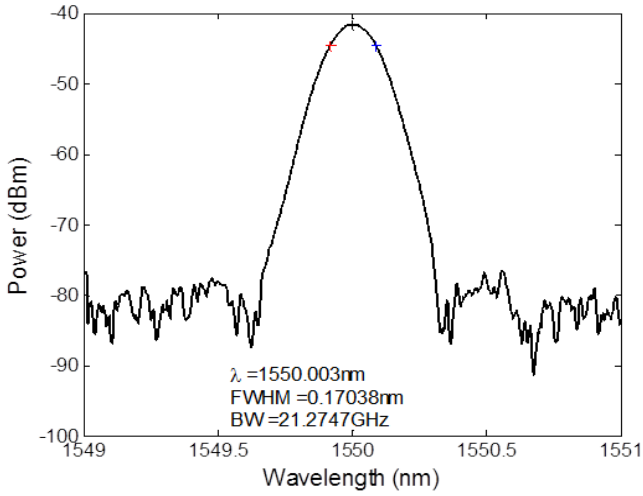

Figure 5.4: Spectral response curve of an echelle grating (Thorlabs GE2550-0875) which has 79 grooves/mm and a blaze angle of 75° used together with a triplet lens collimator from Thorlabs (TC18FC-1550) with a focal length of 18.36 mm, an opening aperture of 10 mm, and a full-angle divergence of 0.034°. The spectral response was measured using an optical spectrum analyzer with a resolution of 0.01 nm, at a transmission distance of 1 m.

5.3 Transmission using multiple grating orders

This subsection starts with a feasibility study on free-space transmission channels which are diffracted by a passive grating. The target of the demonstration is also to show the feasibility of a system which supports simultaneous multi-beams transmission [179, 181]. We first determine the performance of a 2 m long Single Mode Fiber (SMF) channel using a 2.5 Gbps On-Off-Keying (OOK) Non-Return-to-Zero (NRZ) signal directly modulated onto the 1558.98 nm Distributed Feedback Laser (DFB) laser diode. This transmission measurement will serve as a control or Back-to-Back (BtB) measurement for the subsequent free-space transmission channels. The setup for the BtB transmission is shown in Figure 5.5. The transmitted power is kept at 2.5 dBm. The data pattern is created with a $2^{31} - 1$ Pseudo Random Binary Sequence (PRBS) generator. The transmitted signal is measured using a 2.5 Gigabit per second (Gbps) receiver and the Bit Error Rate (BER) performance is evaluated.

The link performance measurement is repeated for direct free-space channel with the free space propagation distance extended using a mirror to 60 cm, as shown in Figure 5.6. This construction enables an extended distance to be constructed in a minimal testbed size by folding the path of the beam. A beam of 3.3 mm in diameter is launched through an SMF pigtailed triplet collimator (see Chapter 4) with a wavelength-adjusted focal length of 18.36 mm at wavelength of 1550 nm. The beam travels a distance of 25 cm, towards

a silver coated mirror, mounted at 45° with reference to the incident beam. The reflected beam is received by a similar SMF pigtailed collimator placed at 35 cm from the mirror, attenuated, and evaluated with a BER tester and eye-diagram measurement.

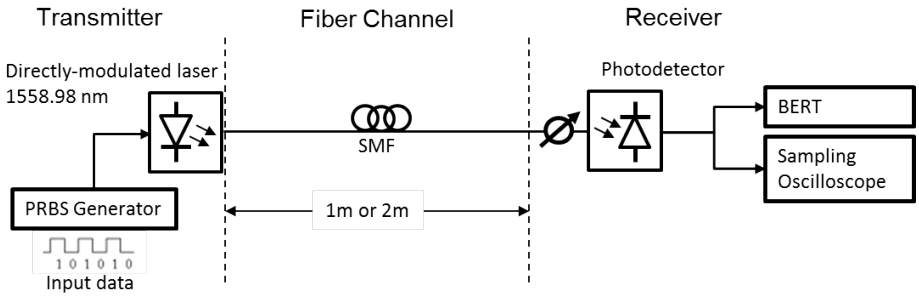

Figure 5.5: Simple fiber communication setup for BtB channel performance evaluation.

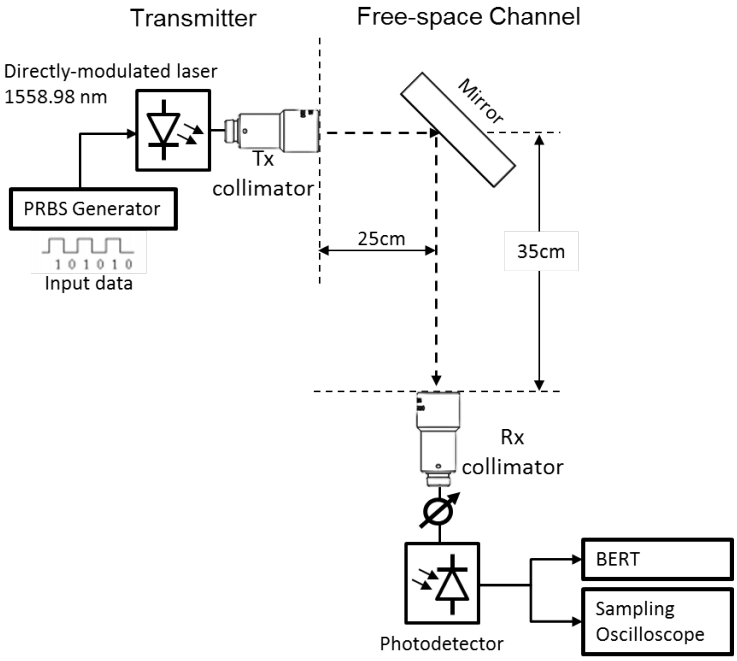

Figure 5.6: Point-to-point free-space channel setup.

The free-space channel of 60 cm distance was configured by aligning the receiving collimator to the beam which was reflected by the mirror towards the receiving collimator. The setup was aligned manually with best effort. The resulting optical power loss was $\leq$ 1dB, which was measured at the fiber output of the receiving fiber-pigtailed collimator. This loss is composed of

collective losses due to misalignment [182, 183] (see Figure 4.16), the insertion loss of the collimators by Thorlabs (see Figure 4.3), and the connector loss between the fiber and the pigtailed collimator at transmitting and receiving ends. As depicted in Figure 5.7, the BER performances of the different free-space distances resemble closely the performance of the BtB system. This shows that there is negligible signal attenuation and dispersion in the free-space optical link. The receiver sensitivity is measured to be approximately -26 dBm at a BER about 1×10^{-9} (generally considered error-free BER in this dissertation). With a less sensitive receiver, a higher transmission power will be needed in order to achieve near error-free transmission. Measurements have also been performed for 1 m free-space transmission with the ambient light (laboratory lighting) turned on and off, alternately. Ambient lighting is one of the concerns in visible light communication since the ambient lighting and the communication channels share the same optical spectrum. Besides, a receiver with a wide Field of View (FoV) will naturally detect more ambient light which leads to more noise from ambient lighting and therefore, results in a lower signal-to-noise ratio. In this system, as the FoV of the receiving collimator is very small, i.e. approximately 0.034 degree (see Section 6.6), we do not expect much ambient lighting to affect the communication channel and to be sure of this, the ambient lighting is also checked.

From the results shown in Figure 5.7, we see that the transmission distance and ambient lighting do not cause significant link attenuation and dispersion. On the other hand, the BER performance relies on the transmitted power, receiver sensitivity and power loss.

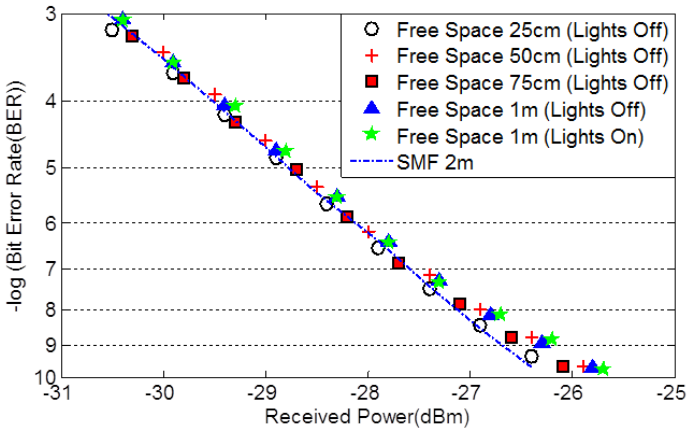

Figure 5.7: BER performance of links with varied free-space distances of 25 cm, 50 cm, 75 cm and 1 m for 2.5 Gbps system [179].

After the evaluation of single point-to-point link was done, an echelle grating (Thorlabs GE2550-0875) of 79 grooves/mm with a blaze angle of 75°, has been integrated into the system in order to provide instantaneously multiple

diffracted beams. The link quality of the diffracted transmission beams is evaluated by benchmarking against the BtB measurement and against a free-space beam reflected by a silver-coated mirror. Figure 5.8 illustrates the setup for the proof-of-concept experiment with 1.5 and 2.5 Gbps, OOK-NRZ directly modulated 1558.98 nm laser diode. The data pattern is generated with a PRBS of $2^{31} - 1$ bits. The transmission power of the laser diode is kept at 2.5 dBm. The mirror has been replaced by a near-Littrow-mounted echelle grating, while maintaining the rest of the setup.

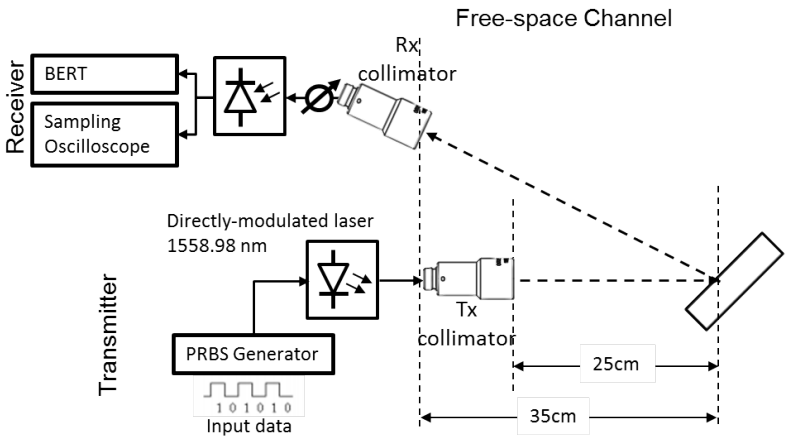

Figure 5.8: Free-space channel performance measurement setup for the feasibility of 1D diffracted beams for communication.

The resulting BER performance of the system, for 1.5 and 2.5 Gbps data rate, is presented in Figure 5.9. Up to 3 diffraction orders are measured at 2.5 Gbps and 1.5 Gbps. For both speeds, error-free links have been achieved at a receiver sensitivity of -28 dBm and -24 dBm for 1.5 and 2.5 Gbps, respectively. Both systems show a negligible power penalty of less than 1 dB with respect to BtB measurement. The eye-diagram shows negligible dispersion. The 1.5 Gbps diffracted links are additionally benchmarked to the free-space transmission system which uses a mirror. The BER performance of the free-space system corresponds perfectly with the BER performance of a 2 m long SMF. However, from the 1.5 Gbps BER performance result, it can be seen that the power penalties are slightly larger than in the 2.5 Gbps system. This could be due to the adjustment of the modulator which could perhaps be better, for e.g. the crossing and opening of the eye of the bit pattern. Nevertheless, the variation in power penalty is still within an acceptable 1 dB measurement error. The measurement error could be contributed by a slight change in temperature or a slight change in the setting of the polarization of the modulator, or a slight change in movement of the electrical cables or fibers. It is also noted that 2.5 Gbps system has a reduced slope. This shows that the system is affected by

more noise at higher data rate. This could be due to the signal distortion from direct modulation, causing slight change in system responses.

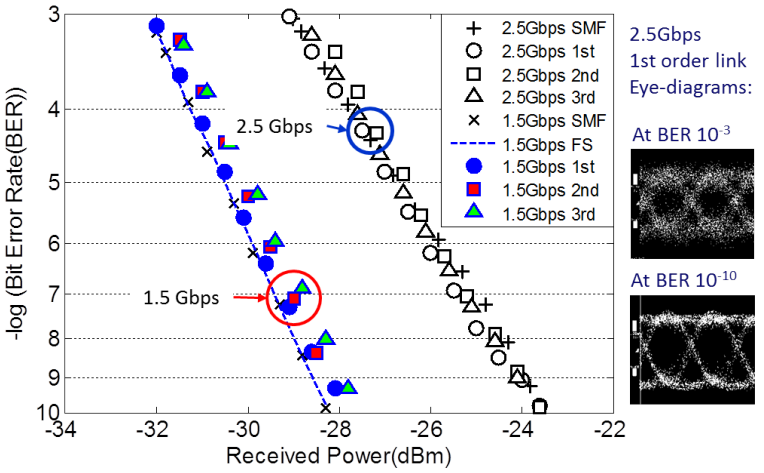

Figure 5.9: BER performances of SMF, free space (FS) and diffracted beams for 1.5 and 2.5 Gbps.

In conclusion, this section has evaluated and demonstrated a high-capacity optical indoor system using a passive diffraction grating. As a proof-of-concept, transmission of a 2.5 Gbps data stream over 60 cm free-space links has been shown. With a transmitted power of 2.5 dBm, a BER less than 10^{-9} over various links with negligible dispersion and power penalty has been observed.

5.4 1D wavelength beam steering

In this section, we extend the feasibility assessment with a longer free-space transmission distance of 2.5 m, and data rates of up to 10 Gbps using the OOK-NRZ modulation format [154]. Error-free links beam-steered over a total wavelength range of 130 nm, with steering angle of 17.16°, have been achieved. The echelle grating of 79 grooves/mm with a blaze angle of 75°, similar to the one in Section 5.3 is used. However, we observe the dependency on polarization as we work away from the blaze wavelength.

5.4.1 Polarization dependent loss measurement

In this subsection, the polarization-dependency of the selected echelle grating is characterized at far field over a wavelength range of 130 nm. The maximum insertion loss depicted by Transverse-Electric (TE) and Transverse-Magnetic (TM) propagation of the complete transmission system was characterized in a compact testbed setup with an effective transmission distance of more than 2.5 m, as shown in Figure 5.10.

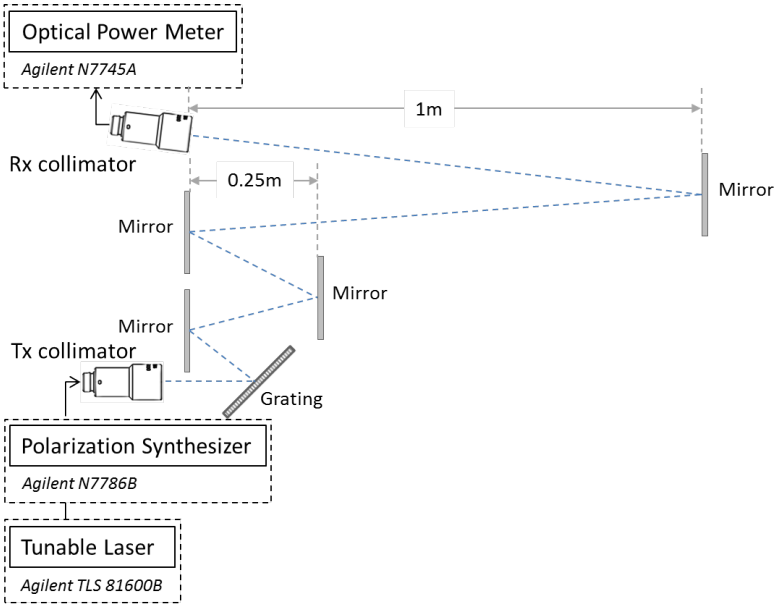

Figure 5.10: Experimental setup for insertion loss and polarization dependent loss measurement.

For the polarization-dependence characterization, a tunable laser source (TLS 81600B from Keysight, formerly Agilent Technologies) and a polarization synthesizer are connected directly to the transmitting (Tx) collimator and a power meter is connected directly to the receiving (Rx) collimator. Keysights polarization synthesizer, N7786B [184, 185], is based on the industry standard Mueller Matrix method for measuring Insertion Loss (IL) and Polarization Dependent Loss (PDL) spectra. It contains a fast polarization-state for single-sweep wavelength-dependent PDL measurements used in combination with the N7700A PDL software, Tunable Laser Source (TLS) 81600B tunable laser and N7745A optical power meter. The Rx and Tx collimators are selected from Thorlabs triplet fiber collimators range. These collimators are ideal for free-space transmission due to its small divergence angle of $0.034°$ and high coupling efficiency of $> 90\%$, hence, very flexible for further beam manipulation for experimental studies. However, these lenses have a limited Full-Field of View (FFoV), i.e. $0.034°$. Due to the narrow FFoV, the Rx coupler is relatively sensitive to position change. However, as long as there is sufficient power captured above the receiver sensitivity, the alignment of the Rx collimator in capturing the beam is sufficient. The tunable laser source is used with maximum power achievable at different wavelengths, as shown in Figure 5.11. The polarization synthesizer introduces 3 - 4 dB loss to the transmitter.

A free-space transmission distance of more than 2.5 m is realized by using silver-coated mirrors to extend the transmission distance on the testbed in between the transmitting and receiving collimator. The echelle grating is

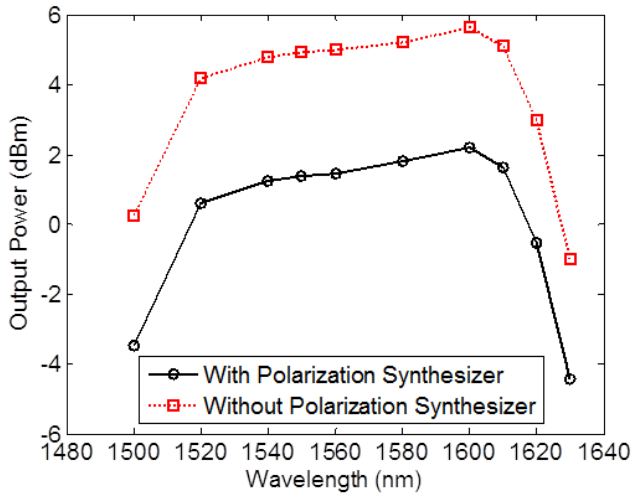

Figure 5.11: Measured output power just before the transmitting collimator.

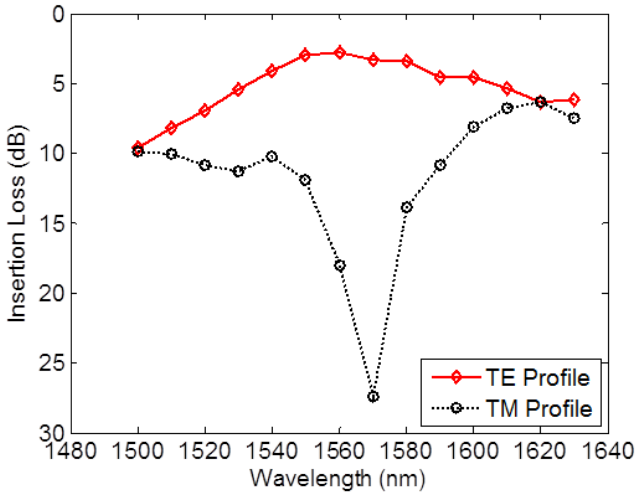

Figure 5.12: Loss measurement due to TE and TM polarization for 79 grooves/mm echelle grating blazed at 75°.

fixed near Littrow angle at the output of the Tx coupler. At each wavelength position, the laser is swept 4 nm, with a step size of 0.3 pm, in order to identify the insertion loss profile. For each wavelength change, which changes the spatial position of the beam, the Rx collimator and the mirrors need to be adjusted and re-aligned (with only four degrees of freedom) to recouple the beam. Beam divergence after diffraction and several reflections are observed but the full beam is captured within the collimators clear aperture diameter of 10 mm.

The insertion loss incurred by the free-space link was measured at the points between the input of the fiber connected to the transmitting fiber-pigtailed collimator and the output of the fiber connected to the receiving fiber-pigtailed collimator. The insertion loss when the beam was set to TE polarization was measured to be approximately 3 to 10 dB across all measurements for a wavelength range between 1500 nm to 1630 nm, see Figure 5.12. Correspondingly, when a TM beam was set, a loss between 6 to 27 dB was measured. The polarization-dependent loss peaks at 24 dB at 1570 nm.

In short, the measurements clearly show the dependence of the passive grating on polarization at different wavelengths. Therefore, a polarization controller is needed to adjust the polarization of light before the beam hits the echelle grating. Note that different gratings have different polarization characteristics.

5.4.2 OOK-NRZ transmission with coupling at different distances

For control and benchmarking, and to justify the independence of signal quality with (1) varied propagation distance ($\leq$ 2.5 m) and (2) varied bitrates, a measurement setup is arranged as shown in Figure 5.13. A tunable laser (TLS 81600B from Keysight) is data modulated with OOK-NRZ format at 1550 nm using a pattern generator with PRBS of length $2^{31} - 1$ and 10 Gbps amplitude modulator. First, a BtB measurement is carried out by connecting the output of the polarization controller directly to the input of the attenuator with a 2 m long SMF. After that, a pair of Tx and Rx couplers is employed for free-space transmission. The transmission distance is varied by repositioning the Rx coupler from position A to E. The transmitted free-space beam is then collimated by the Rx coupler into the SMF, and eventually into the PIN receiver. The signal is analyzed with the Bit Error Rate Tester (BERT) and the eye diagram is captured with a wide-bandwidth oscilloscope. The average transmission power measured at the output of the polarization controller is approximately -2 dBm and the average power captured by the Rx coupler at the input of the attenuator is approximately -3 dBm.

The link performance, represented by the BER values versus the receiver sensitivity, is plotted in Figure 5.14. The different links show a consistent overlap with the BtB measurements at different data rates. The power penalties

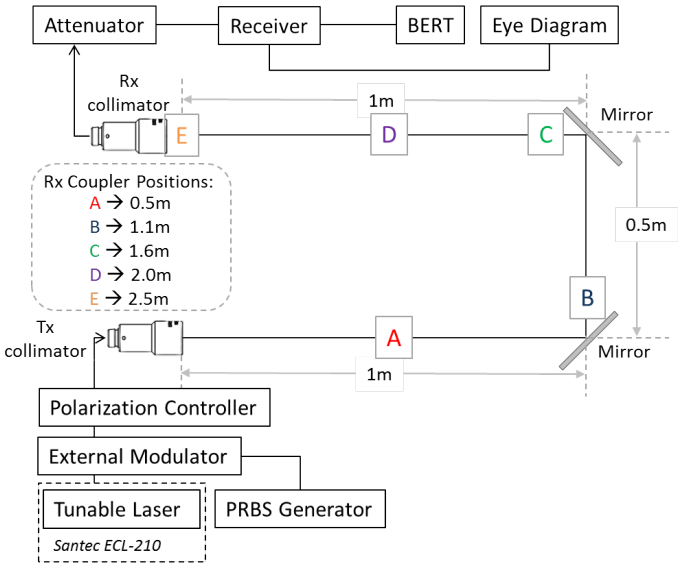

Figure 5.13: A setup for the measurement of free-space channel performance as transmission distance is varied from position A to E. Wavelength of transmission is fixed at 1550 nm.

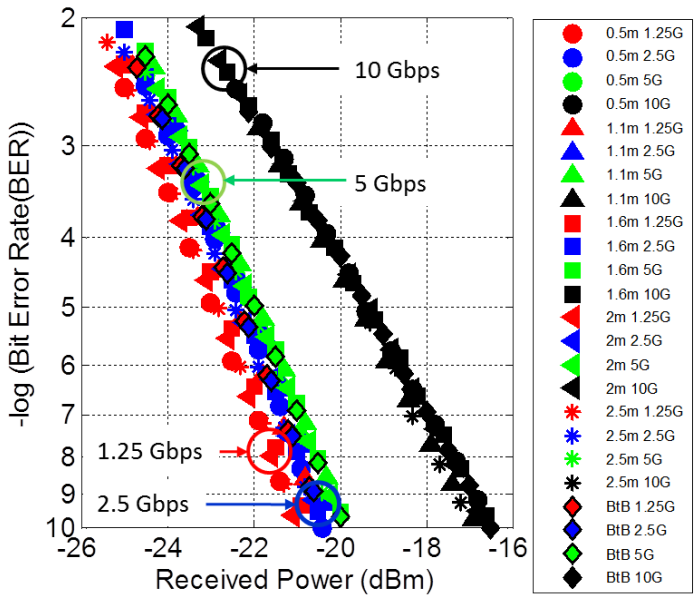

Figure 5.14: Link performance versus received power at 1.25 Gbps, 2.5 Gbps, 5 Gbps and 10 Gbps. The different colored notations refer to different data rates while the different symbol shape refer to different transmission length.

are within 1 dB with reference to the BtB measurement. The BtB receiver sensitivity at BER of 1×10^{-9} is found to be at -17 dBm, -20.2 dBm, -20.6 dBm and -20.7 dBm for 10 Gbps, 5 Gbps, 2.5 Gbps and 1.25 Gbps, respectively. It can be observed from the results that the quality of the link stays as good as in BtB transmission and has negligible dispersion. The position where the Rx collimator is placed, is independent of distance as long as there is sufficient transmission power. This is because with the Thorlabs TC18FC-1550 collimator, the beam's full-angle divergence (0.034°) is small, resulting in a diverged beam size which is still smaller than the aperture of the Rx collimator at a distance away. Accordingly, the coupling efficiency is specified to be more than 90% for a separation distance, between Tx collimator and Rx collimator, of 2.5 m [163].

5.4.3 OOK-NRZ transmission with 1D beam steering

In this subsection, the transmission quality of 1D diffracted links over 2.5 m distance with different wavelengths is measured. A tunable laser (TLS 81600B from Keysight), with wide wavelength tuning range between 1500 nm - 1630 nm, is used. The maximum power provided by the tunable laser changes according to wavelength change, as shown in Figure 5.11, and transmission power is limited to less than 0 dBm for the wavelengths 1500 nm, 1620 nm, and 1630nm. The laser power is attenuated with a built-in optical attenuator. For transmission, the tunable laser is data modulated with OOK-NRZ format at 1550 nm using a pattern generator with PRBS of length $2^{31} - 1$ and 10 Gbps amplitude modulator. Figure 5.15 illustrates the setup for 'Down' link measurement. For the 'Up' link measurement, the Tx coupler acts as the receiving collimator and the Rx collimator acts as the transmitting collimator. As such, the output from the polarization controller is connected to the Rx collimator and the input of the receiver is connected to the Tx collimator, accordingly. For the fiber BtB measurement, a variable optical attenuator is used to regulated the power entering the receiver.

In Figure 5.16, the 10 Gbps diffracted links, both the 'Down' and 'Up' directions, show a consistent match with the BtB measurement at corresponding data rates. Free-space links at 5 Gbps, 2.5 Gbps and 1.25 Gbps are also measured to show the adaptability of the system at different data rates. The corresponding eye diagrams for the 10 Gbps links are presented in Figure 5.17. The eye diagrams on the left column represent the quality for error-free (BER $\leq 1 \times 10^{-9}$) links while the eye diagrams on the right column represent the quality at BER $\approx 1 \times 10^{-3}$, with the first row eye diagrams for 10 Gbps BtB measurements, middle row for 10 Gbps 'Down' direction and the last row for 10 Gbps 'Up' direction. All eye diagrams are clear and open, thus, signifying good quality signals are received.

In summary, the presented Infrared (IR) Optical Wireless Communication (OWC) system can provide 1D beam steering using wavelength-tuning

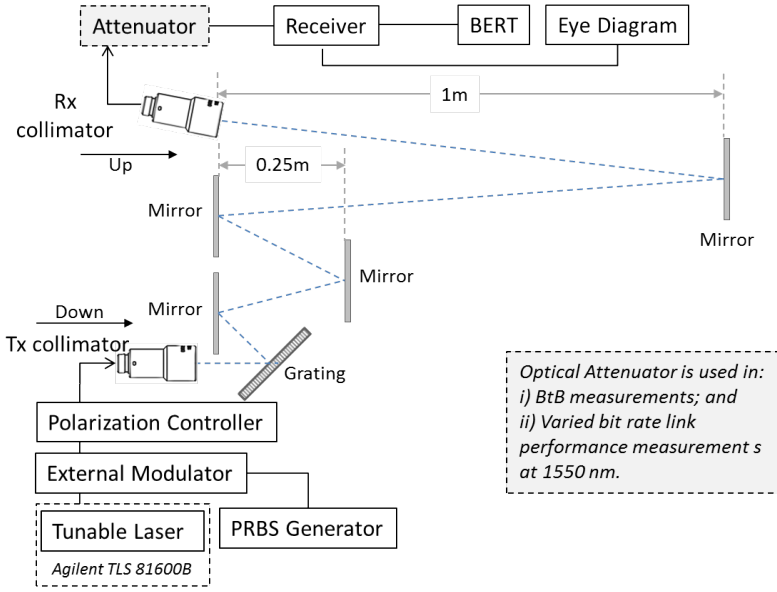

Figure 5.15: Compact testbed setup to measure link performance of 1D diffracted links using optical pencil beam. Mirrors are used to construct an effective propagation distance of more than 2.5 m.

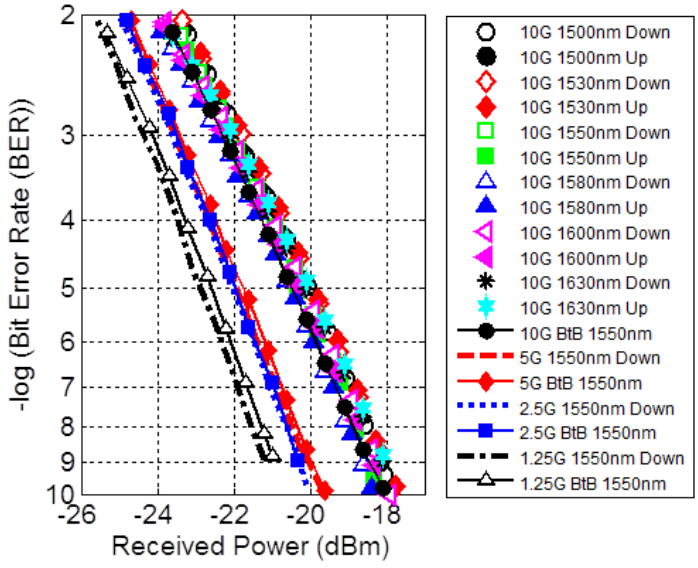

Figure 5.16: Diffracted link performance measured for both directions, termed as 'Up' and 'Down' links.

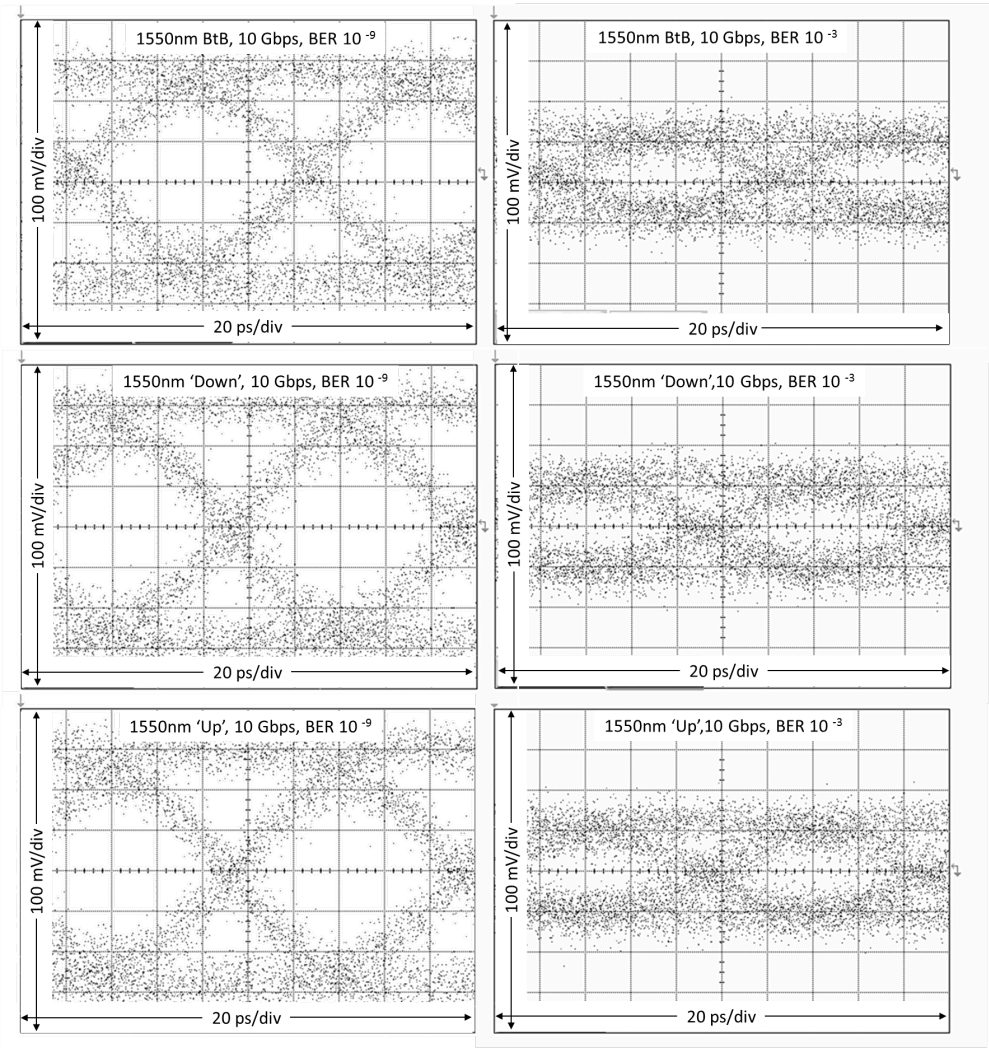

Figure 5.17: Eye diagrams for 10 Gbps links. Top: BtB; Middle: Diffracted Free-space 'Down' direction; Bottom: Diffracted Free-space 'Up' direction; Left column: BER$\leq 1 \times 10^{-9}$, Right column: BER$\leq 1 \times 10^{-3}$.

and a passive grating, with a transmission speed of up to 10 Gbps at a free-space distance of over 2.5 m. The corresponding polarization-dependent 79 grooves/mm echelle grating used in these one-dimensional steering experiments provides a maximum of 17.16° steering angle over a wavelength tuning range of 130 nm, which spatially covers a maximum distance coverage of 772 mm at 2.5 m as shown in Figure 5.2.

5.5 Capacity maximization using DMT modulation

After the positive performance evaluation of the OOK-NRZ data transmission using diffraction gratings, Discrete Multitone (DMT) modulation format is used to further maximize the capacity of the system which is bandwidth-limited to 10 GHz to limit the cost of components.

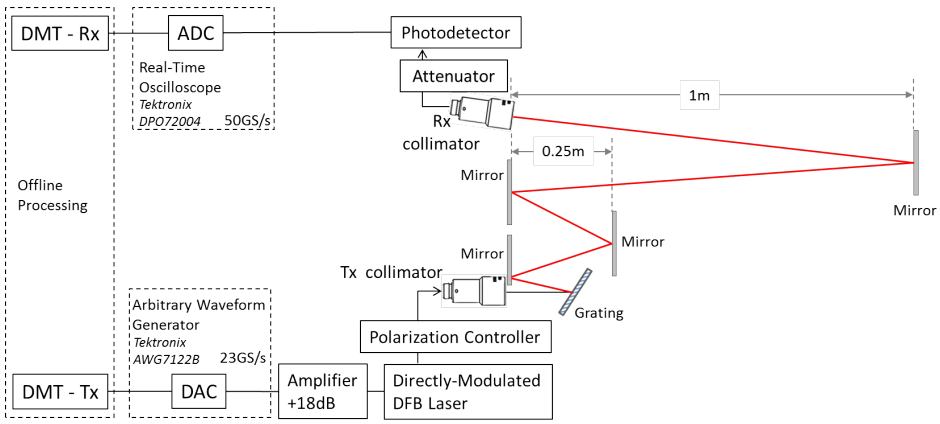

Figure 5.18: Compact experimental setup for diffracted link measurements with an effective distance of more than 2.5 m. Discrete Multitone (DMT), Digital-to-Analog Converter (DAC), Distributed Feedback (DFB), Transmitter (Tx), Receiver (Rx), Analog-to-Digital Converter (ADC).

Figure 5.18 shows a compact experimental setup for the performance measurement of multiple diffracted links for a distance of over 2.5 m using the DMT modulation format. The optical transmitter is a directly-modulated DFB laser with 10 GHz bandwidth. Temperature control is used to tune the wavelength of the DFB laser. The optical link is directly-modulated with a data signal generated by an Arbitrary Waveform Generator (AWG) at 23 Gigasymbol per second (GS/s). A rate-adaptive bit-loading and power-loading algorithm has been used to maximize the bit rate and bandwidth for a given BER. The signal is then fed into a polarization controller and launched to free space through a SMF fiber-pigtailed coupler. A beam of approximately 3.3 mm diameter is emitted through the coupling lens. The beam hits a 79 grooves/mm echelle grating (the same grating evaluated in the previous section) at incidence angle

of 75°. The diffracted beam then propagates via four silver-coated mirrors to construct a distance of more than 2.5 m in a compact setup. The beam is captured by a receiving lens coupler and attenuated subsequently to be detected by a photodetector. The resulting electrical signal is recorded by a Digital Phosphor Oscilloscope (DPO). Since a directly-modulated laser is used, the experiment is carried out for wavelengths between 1549.14 nm and 1550.14 nm. The wavelength change is achieved by tuning the temperature of the laser. The free-space transmission power is kept to less than 8.5 dBm in compliance with eye-safety regulations.

The experiment has successfully demonstrated a transmission of a free-space optical signal over more than 2.5 m, with an aggregate bit rate of 36.7 Gbps and 36.5 Gbps, at λ=1549.14 nm and λ=1550.14 nm, respectively. The averaged BER is $\leq 2 \times 10^{-3}$, which by using standard 7% Forward Error Correction (FEC), will be reduced to BER $< 10^{-12}$. After the deduction of DMT transmission overhead (cyclic prefix, preambles and 7% FEC) the net transmission bit rates are 32.8 Gbps and 32.6 Gbps, respectively. The results, together with the corresponding laser operating temperature, transmitted power and received power are tabulated in Table 5.1. The optimized DMT parameters are summarized in Table 5.2.

Table 5.1: Measurement results of 1D beam steering with DMT channels. P_{Tx} is measured at the output of the polarizer. Therefore, coupling loss between SMF patch cord and lens collimator is not taken into account.

Temp. (°C)	λ (nm)	P_{Tx} (dBm)	P_{Rx} (dBm)	Gbps	BER
15	1549.14	8.44	-1.08	36.7	9.4×10^{-4}
25	1550.14	8.53	0.8	36.5	1.16×10^{-3}

Table 5.2: DMT parameters for 1D beam-steered system.

Transmitter sampling rate	24 GSa/s
Receiver sampling rate	50 GSa/s
Digital clipping	12 dB
Number of subcarriers	512
Cyclic prefix length	8 points
Schmidl blocks	4 per 100 DMT frames
Number of DMT frames	2000

At a separation of $\Delta\lambda = 1$ nm between the wavelengths, the lateral distance difference (at the Rx plane) between both wavelengths is equal to 6.4 mm with angular difference of 0.1379°. Therefore, the first order diffraction link of $\lambda = 1549.14$ nm is positioned at 0.6495 m from the beam center at an angle of

14.564° and correspondingly, the first order diffraction link of $\lambda = 1550.14$nm is positioned at 0.6431 m from the beam center at an angle of 14.4261°.

Figure 5.19 presents the Signal-to-Noise Ratio (SNR), bit-loading and BER for the 512 subcarriers used in the DMT signal modulation, with a frequency range of up to 11.5 GHz; measured for both wavelengths. Up to 128-QAM has been utilized. It can be observed that not all subcarriers achieved a BER $\leq 2 \times 10^{-3}$ but the overall BER is still within the FEC limit for error-free transmission (note that in DMT transmission, the signal is not demodulated per subcarrier but as an entire frame). The constellation diagrams for up to 128-QAM are clearly distinguishable.

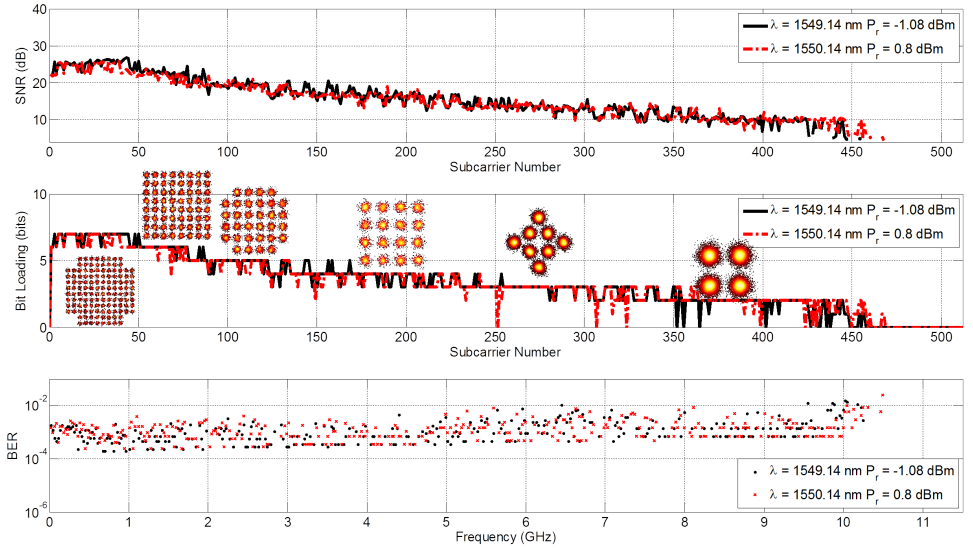

Figure 5.19: SNR, bit-loading and BER for each subcarrier for $\lambda = 1549.14$ nm and $\lambda = 1550.14$ nm.

In summary, an infrared-based indoor OWC system employing a passive diffraction grating for beam steering has been demonstrated at a record capacity. The system achieved an aggregate capacity of 36.7 Gbps, using spectrally-efficient and robust DMT modulation, with over more than 2.5 m transmission distance. DMT modulation with bit- and power-loading algorithm was applied in the experiment to compensate for power fluctuations and to increase the frequency utilization efficiency simultaneously.

5.6 Chapter conclusion

In this chapter, the analytical calculation and expected diffracted spots map were first presented. Then, the spectral bandwidth was defined. After that, the feasibility of transmission using a grating was evaluated at 35 cm. The

performance was compared to the performance of an SMF channel and also to the performance of direct free-space link. We saw that the grating had negligible dispersion effect on the diffracted free-space channels of up to 10 Gbps OOK-NRZ. The polarization dependent loss of the grating was also characterized to understand the TE and TM losses.

It was further shown that the propagation distance, as long as the beams are fully captured by the opening aperture of the coupling lens, did not affect the channel performance, indicating that the free-space channel did not add noticeable dispersion. The link performance was basically limited by the available transmitted power, grating loss and receiver sensitivity. Transmission measurement of up to 2.5 m were also evaluated using OOK-NRZ and DMT signal formats, in which up to 10 Gbps and 36.7 Gbps were demonstrated, respectively.

Chapter 6

2D beam steering - System design and experiments

Contents

After the proof-of-principle evaluation for one-dimensional (1D) beam steering in Chapter 5, in this chapter, we shall investigate the cascading of gratings to implement a two-dimensional (2D) passive beam-steering module in a bandwidth-limited optical wireless system [186]. No local control at the steering module is needed. In order to have a 2D area coverage and a scanning functionality as proposed in this work, two gratings have to be orthogonally cascaded to each other [156]. The idea is that the first grating should have a multiple times smaller Free Spectral Range (FSR) than the second grating.

The detailed analysis is given in Section 3.2. We perform an analysis of the 2D beam-steering modules which includes characterization of the spectral response, the beam profile and the receiver's Full-Field of View (FFoV). We further demonstrate transmission experiments using On-Off-Keying (OOK)-Non-Return-to-Zero (NRZ), Pulse Amplitude Modulation (PAM) and Discrete Multitone (DMT) modulation formats, and analyze the high-speed performance for channels of different wavelengths.

In this chapter, the characterization of the two pairs of cascaded gratings that are deployed will be investigated:

Module 1: A cascade of two reflection gratings
The cascade of a reflection grating with a blaze angle of 63° and 31.6 grooves/mm (Thorlabs GE2550-0363), and a reflection grating with a blaze angle of 75° and 79 grooves/mm (Thorlabs GE2550-0875).

Module 2: A cascade of a reflection grating and a transmission grating
The cascade of a reflection grating with a blaze angle of 80.7° and 13.33 grooves/mm (Newport 53004BK06-182E), and a fused silica transmission grating with 1000 grooves/mm.

For more information on the selection of gratings, see Section 3.3.

A large portion of the dissertation work reported in this chapter has been reported in [186].

6.1 Distribution of beam steering positions

The diffracted beam's positions due to the cascaded gratings of Module 1, i.e. the cascade of two reflection gratings, and Module 2, i.e. the cascade of a reflection grating and a transmission grating, can be estimated using the grating equations as shown in Section 4.6. The limits of the angular tuning range are determined as explained in Section 3.2.

Figure 6.1 shows the 2D distribution of diffracted beams resulting from Module 1 and Figure 6.2 shows the 2D distribution of diffracted beams resulting from Module 2.

From Figures 6.1 and 6.2, we observe that Module 2 has a better resolution with 7 scan lines within an angular coverage of $12.15° \times 5.62°$ by wavelength tuning between 1511 nm and 1627 nm compared to the Module 1 which only provided 2 scan lines in a comparable angular coverage of $12.67° \times 5.61°$ between 1529 nm and 1611 nm.

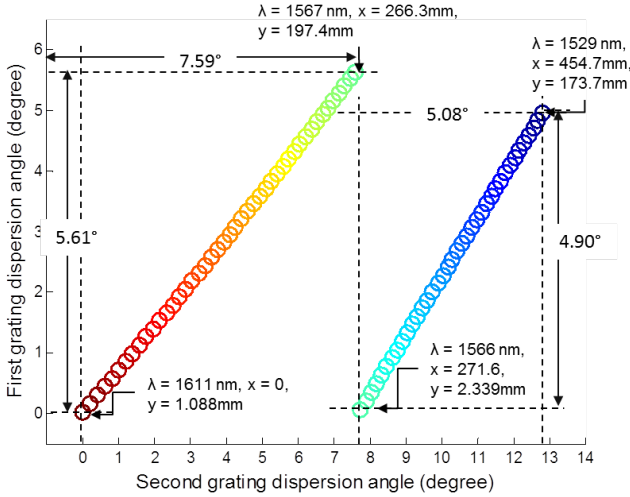

Figure 6.1: Calculated distribution of diffracted beams from a cross-mounted pair of reflection gratings (blaze angle 63° with 31.6 grooves/mm and blaze angle 75° with 79 grooves/mm; product numbers Thorlabs GE2550-0363 and Thorlabs GE2550-0875, respectively) over a wavelength range between 1529 nm and 1611 nm. Lateral size of coverage is calculated for a distance of 2 m. Both gratings are mounted near-Littrow angle.

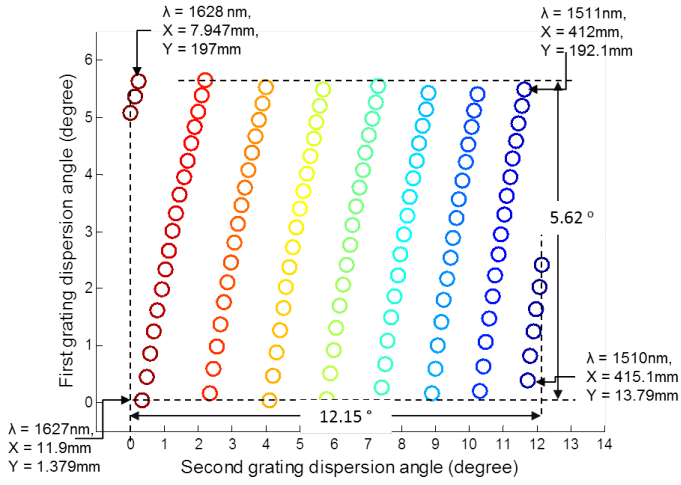

Figure 6.2: Resulting two-dimensional area scan using a combination of cascaded reflection grating (blaze angle 80.7° and 13.33 grooves/mm, mounted near-Littrow angle; product number Newport 53004BK06-182E) with a fused silica transmission grating of 1000 grooves/mm over a wavelength range between 1505 nm and 1630 nm mounted with incidence angle near 49.9° (product number Ibsen PING-sample-083). Lateral size of coverage is calculated for a distance of 2 m.

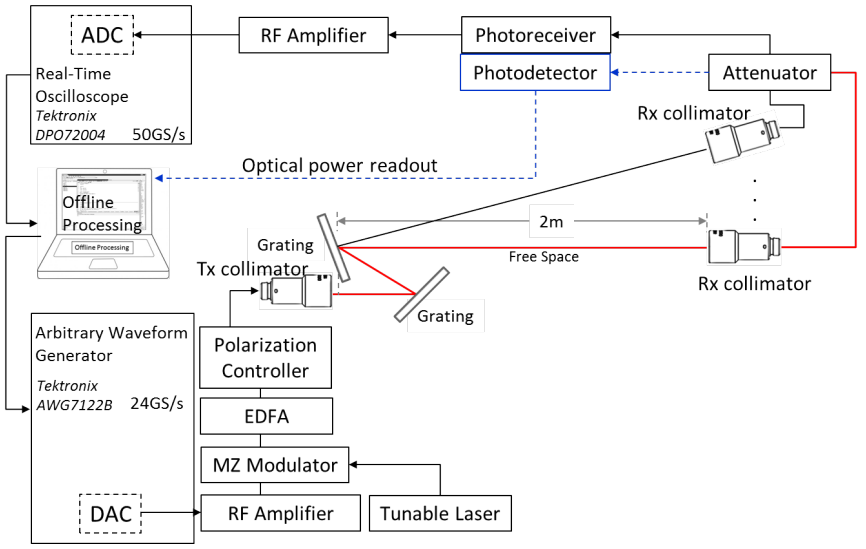

Figure 6.3: Testbed setup for 2 m transmission with cascaded reflection gratings. Digital-to-Analog Converter (DAC), Analog-to-Digital Converter (ADC), Transmitting (Tx), Receiving (Rx), Mach-Zehnder (MZ), Erbium-doped Fiber Amplifier (EDFA), Radio Frequency (RF).

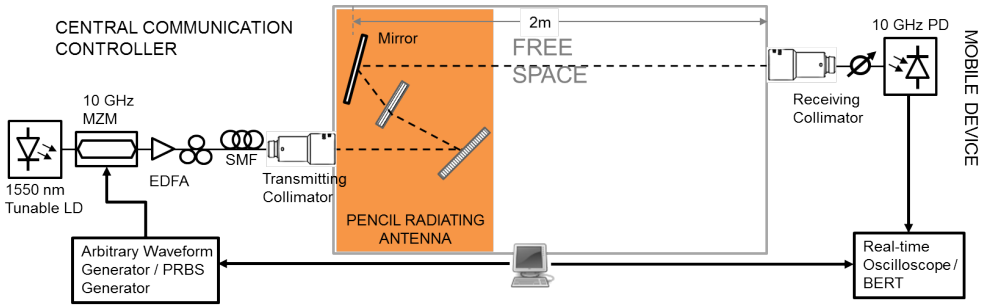

Figure 6.4: Experimental setup for a 2D beam-steered free-space transmission system with cascaded reflection and transmission gratings. Laser diode (LD), Mach-Zehnder modulator (MZM), Erbium-doped fiber amplifier (EDFA), Photodetector (PD), Bit error rate tester (BERT).

6.2 Testbed setup for 2D beam steering

In the systems which are constructed using Module 1 (i.e. the cascade of two reflection gratings) or Module 2 (i.e. the cascade of a reflection grating and a transmission grating), the transmitting (Tx) power just before free space is set to $\leq$ 9.2 dBm to warrant eye-safety. The polarization controlled beam is transmitted to free space through the triplet lens collimator from Thorlabs (TC18FC-1550) with a focal length of 18.36 mm, an opening aperture of 10 mm, and a full-angle divergence of 0.034°. The $1/e^2$ beam diameter is 3.33 mm at the focal plane. For further information on the lens collimator please refer to Section 4.1.

For the system based on Module 1, the transmitted beam hits the first echelle grating (Thorlabs GE2550-0363) at 63° incidence angle at a near-Littrow angle. The grating grooves are aligned perpendicularly to the optical table. The second grating (Thorlabs GE2550-0875) has a 75° incidence angle at a near-Littrow angle and is cascaded orthogonally to the first, so the grooves are aligned parallel to the optical table, creating a cross dispersion effect.

For the system based on Module 2, the transmitted beam first hits the echelle grating (Newport 53004BK06-182E) at 80.7° incidence angle and then the transmission grating (Ibsen PING-sample-083) at 49.9°.

After the steering module, the free-space beam is re-coupled back into the Single Mode Fiber (SMF) by means of another identical receiving (Rx) collimator. This Rx collimator is mounted on the alignment robot introduced in Section 4.10. The optical signal is sent to the photoreceiver via a fiber.

Please note that these two variant of systems, one based on Module 1, i.e. the cascade of two reflection gratings, and the other based on Module 2, i.e. the cascade of a reflection grating and a transmission grating, will be used in the characterization of both Module 1 and Module 2 in terms of power efficiency, channel bandwidth, beam size and receiver's Field of View (FoV), which are key properties which have an impact on the systems' performance.

6.3 System characterization: Optical power loss

Table 6.1 and Table 6.2 report the optical power loss across wavelengths in the free-space systems for Module 1, i.e. the cascade of two reflection gratings, and Module 2, i.e. the cascade of a reflection grating and a transmission grating, respectively. The optical power loss is the power difference measured at the fiber level just before the Tx lens collimator and right after the Rx lens collimator.

Module 1 has a loss between 13.5 dB and 16.8 dB (4.5% and 2.1% power efficiency) between wavelengths 1530 nm and 1600 nm. Module 2 has a loss of only between 4.79 dB and 6.15 dB (33.2% and 24.3% power efficiency) between wavelengths 1518 nm and 1600 nm. The main power loss contributions are from the collective losses of the gratings, misalignment, the specified insertion loss

Table 6.1: Measured free-space loss at each wavelength for cascaded reflection gratings (Module 1).

Wavelength (nm)	1530	1540	1550	1560	1570	1580	1590	1600
Free-space loss (dB)	14.8	13.5	13.7	15.7	16.8	16	15.8	16

Table 6.2: Measured free-space loss at each wavelength for cascaded reflection and transmission gratings (Module 2).

Wavelength (nm)	1518	1534	1550	1566	1583	1600
Free-space loss (dB)	5.95	4.87	5.47	5.05	4.79	6.15

of the collimators (see Figure 4.3), and the connector losses between the fiber and the pigtailed collimator at transmitting and receiving ends.

In Module 1, the first echelle grating, designated for blaze wavelength of 57 μm, operates at orders 35 and 36 while the second echelle grating, designated for blaze wavelength 25 μm, operates at order 15 (see Subsection 2.2.4, Equation 2.29). As blazed gratings are designed for maximum efficiency at the designated wavelengths, while these gratings are used at much higher orders for wavelengths, between 1530 nm and 1600 nm, these gratings are not optimal in terms of efficiency but they provide the FSRs needed for the proof-of-concept demonstration of steering with cascaded gratings. The power efficiency of echelle gratings could typically achieve up to $50\% - 75\%$ (less than 3 dB loss) [187] and with transmission gratings, efficiencies of over 90% (less than 0.5 dB loss) are achievable.

Module 2, on the other hand has been carefully selected to minimize on power loss. The first grating is an echelle grating with an efficiency between $30 - 50\%$ (see Figure 3.6) and the second grating is a transmission grating with efficiency approaching 90% (see Figure 3.7).

6.4 System characterization: Channel bandwidth

The objective of this section is to provide information of the system's bandwidth. The spectral response profile of a system has a major impact on the bandwidth of the overall system, next to the bandwidth of the receiver. Therefore, the spectral responses of both the systems (which are based Module 1, i.e. the cascade of two reflection gratings, and Module 2, i.e. the cascade of a reflection grating and a transmission grating) are measured in order to determine the bandwidth limitation that the steering modules impose on the free-space transmission channels.

For Module 1, the spectral bandwidth is measured in a testbed constructed for 2D diffracted transmission over 2 m, as shown in Figure 6.3. The spectral response of Module 2 is measured using the testbed shown in Figure 6.4.

Two methods of measurement were used. The first method is by using a tunable laser to sweep the wavelength across the receiving (Rx) collimator whereby the power is then measured with a power meter. The optical power detected at each position is recorded as the wavelength is varied. The second method is carried out by transmitting an Amplified Spontaneous Emission (ASE) wideband signal originating from an Erbium-Doped Fiber Amplifier (EDFA) and measuring the received beam's power with an Optical Spectrum Analyzer (OSA) at a resolution of 0.01 nm.

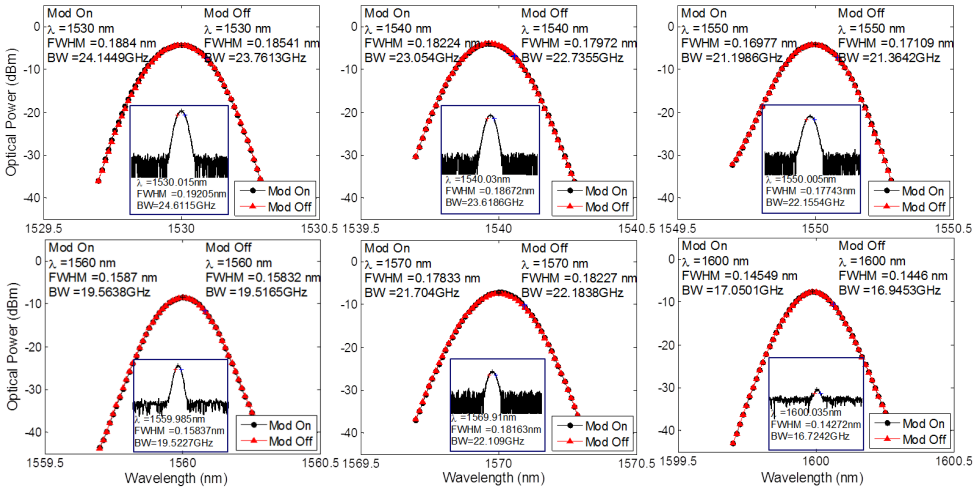

Figure 6.5: Spectral responses of 2D beam-steered channels for wavelengths between 1530 nm and 1600 nm at 2 m distance for cascaded refection gratings (Module 1). Modulation (Mod), wavelength (λ), Full Width at Half Maximum (FWHM), spectral bandwidth (BW).

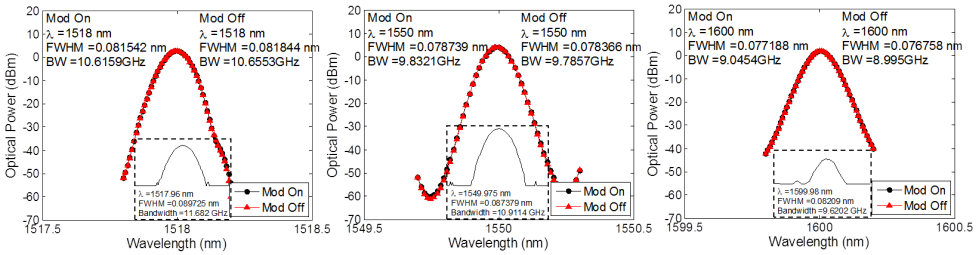

Figure 6.6: Spectral bandwidths at λ = 1518 nm, 1550 nm and 1600 nm at 2 m distance for cascaded reflection and transmission gratings (Module 2).

For Module 1, Figure 6.5 shows the spectral responses of the static channels

(denoted by the red triangles) with wavelengths originating from the tunable laser. The spectral response recorded using the OSA (see inset) corresponds agreeably. In general, the measurements stay in good agreement for both measurement methods giving a range of spectral bandwidths between 16.7 Gigahertz (GHz) and 24.6 GHz for wavelengths between 1530 nm and 1600 nm. As the cascaded gratings behave as a filter of approximately 20 GHz wide, the channels will be limited in bandwidth to 20 GHz. In order to fully utilize the bandwidth for data transmission, the spectrum-efficient DMT modulation format can be used. We observe in Fig. 6.5 that when data modulation is turned on, the DMT signal shows negligible effect on the curves (denoted by the black circles). Note that this is dependent on the optical spectrum broadening by the modulation; if it would be bigger than the static optical bandwidth, then, we may expect a bigger impact.

For Module 2, as observed in Figure 6.6, an average recorded spectral bandwidth of 9.53 GHz is recorded for wavelengths between 1518 nm and 1600 nm. When DMT modulation is turned on, an average bandwidth of 9.55 GHz is measured. Thus, we see that modulation of the signal has a negligible effect on the spectral bandwidth. This means that spectral broadening is negligible with DMT modulation of approximately 10 GHz. Again, note that this is dependent on the optical spectrum broadening by the modulation; if it would be bigger than the static optical bandwidth, then, we may expect a bigger impact. The insets, bordered by dashed-lines, show the spectral bandwidth for non-modulated signals measured using the OSA which results in an average of 10.74 GHz. The difference of about 1.2 GHz may be attributed to the re-alignment of the system in the separate transmission measurement and spectral bandwidth measurement.

6.5 System characterization: Beam profile

The beam profiles of the 2D-steered beams have been measured by using the alignment robot, introduced in Section 4.10, to displace the position of the receiving lens in order to map the optical power across the beam. At 2 m distance, the profiles naturally give a larger beam diameter than at the originating beam waist which is 3.33 mm in diameter at 12.91 mm in front of the collimator housing. The Full Width Half Maximum (FWHM) and $1/e^2$ (= reference point at the beam waist) can be obtained from the Gaussian profiles which are measured when the DMT modulation is turned on and turned off. This way, we can observe the effects of modulation on the dispersion and the size of the beam after transmission. In Figure 6.7, we observe that the FWHM and $1/e^2$ diameter due to Module 1, i.e. the cascade of two reflection gratings, remain consistent for all measurements. Between 1530 nm and 1600 nm, we measured FWHM values between 2.23 mm and 2.42 mm, and a minimum $1/e^2$ diameter between 3.76 mm and 4.11 mm.

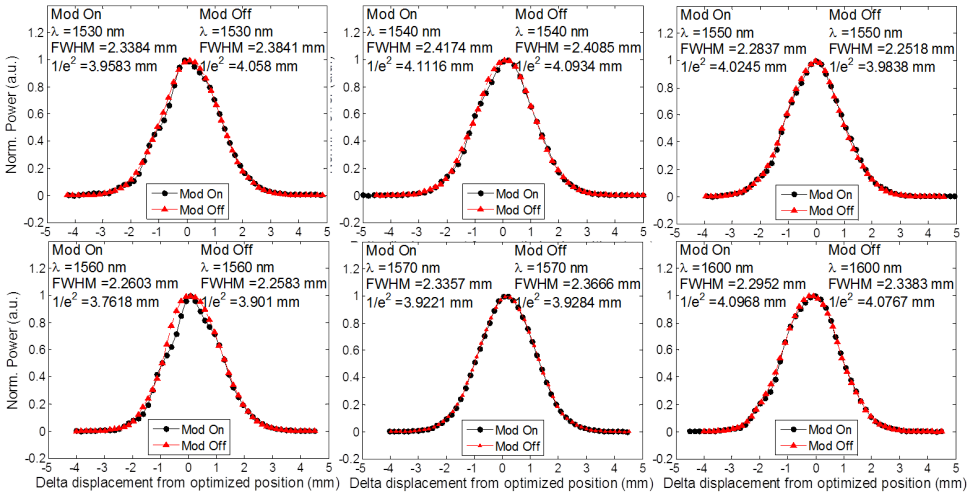

Figure 6.7: Beam profiles of 2D beam-steered channels for wavelengths between 1530 nm and 1600 nm at 2 m distance for cascaded reflection gratings (Module 1). Modulation (Mod), wavelength (λ), Full Width at Half Maximum (FWHM).

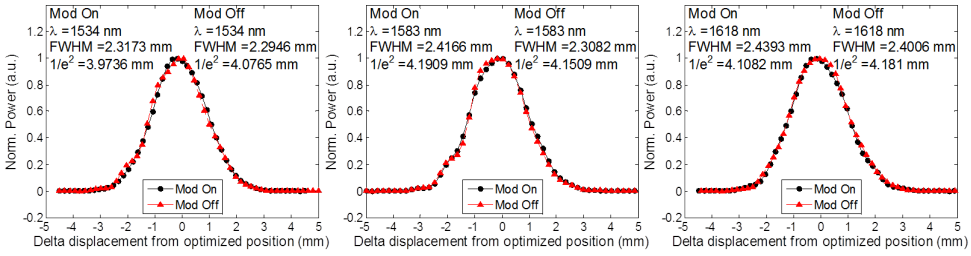

Figure 6.8: Beam profiles of channels measured at 2 m distance with $\lambda = 1534$ nm, 1583 nm and 1618 nm, for cascaded reflection and transmission gratings.

For module (2), i.e. the cascade of a reflection grating and a transmission grating, the beam profiles of wavelengths 1518 nm, 1534 nm, 1550 nm, 1566 nm, 1583 nm, 1600 nm and 1618 nm, as shown in Figure 6.8, are measured. On average, the beam width measured at FWHM is 2.41 mm and at $1/e^2$ is 4.13 mm. When DMT modulation is turned on, the beam width measured at FWHM is 2.44 mm and at $1/e^2$ is 4.13 mm. By comparing the results for static and modulated channels, we observe negligible difference in the beam profiles.

6.6 System characterization: Receiver full-field of view

In this section, we measure the extent of tilt for the collimators introduced in Chapter 4. In general, the small FFoV (see Section 4.3) limits the receivers acceptance angle and demands a tedious alignment.

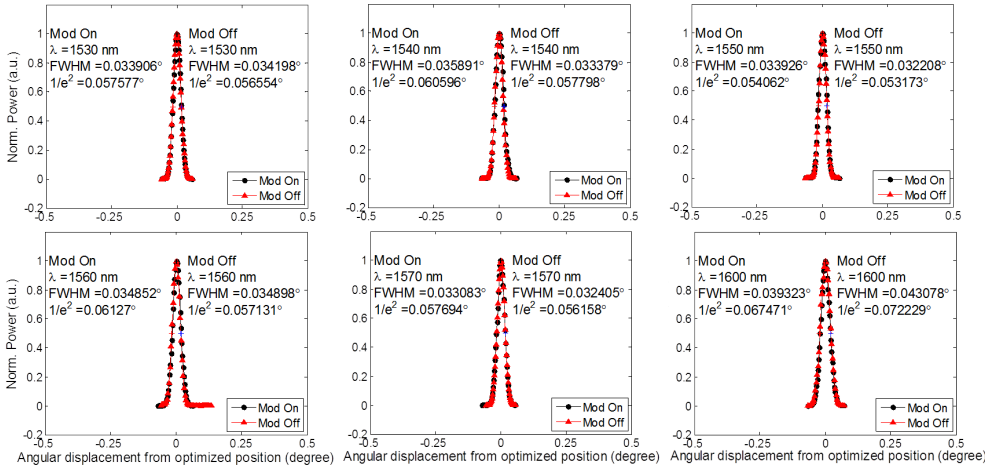

Figure 6.9: Lens tilt tolerance measured with wavelengths between 1530 nm and 1600 nm at 2 m distance with casceded reflection gratings (Module 1). Modulation (Mod), wavelength (λ), Full Width at Half Maximum (FWHM).

The measurement results, measured using Module 1, i.e. the cascade of two reflection gratings, are shown in Figure 6.9. Measurements have been made for wavelengths between 1530 nm and 1600 nm, with and without DMT modulation. All the measured profiles match consistently. Without modulation, FWHM angles are between 0.032° and 0.043° and $1/e^2$ angles between 0.053° and 0.072°. When DMT modulation is turned on, the angles measured at FWHM are between 0.033° and 0.039°, and at $1/e^2$ the angles are between 0.054° and 0.067°.

The measurements are also repeated for Module 2, i.e. the cascade of a reflection grating and a transmission grating. The results are shown in Figure

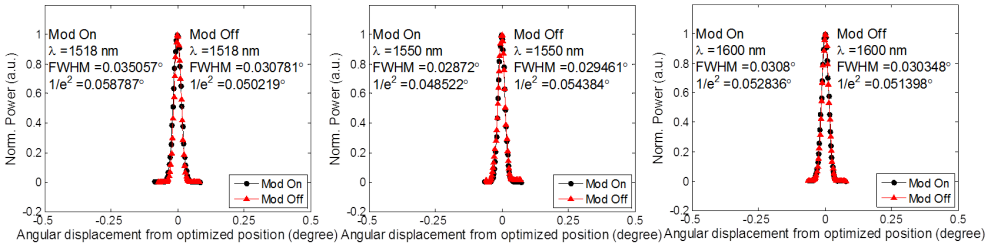

Figure 6.10: Measurement of the lens tilt tolerance at $\lambda = 1518$ nm, 1550 nm and 1600 nm at 2 m distance for cascaded reflection and transmission gratings (Module 2.

6.10. Of the seven measurements taken, the angles measured at FWHM are between 0.029° and and 0.031°, and at $1/e^2$ the angles are between 0.050° and 0.054°. When DMT modulation is turned on, the angles measured at FWHM are between 0.029° and 0.035°, and at $1/e^2$ the angles are between 0.049° and 0.059°.

Both systems show very similar results in their beam widths measured at FWHM and $1/e^2$. The measurements show that the steering system is very precise. Although these collimators have excellent light collimation efficiency, with a loss of < 1 dB over 2 m, their reception angle is very small, thus, requiring tedious alignment at the receiving end. Therefore, it is vital to implement a small form factor receiver with larger FFoV in order to ease channel establishment and reception in a practical scenario. This is one subject that needs to be developed further to ease the system's alignment and consequently, the ease of connection establishment.

6.7 Transmission: Cascaded reflection gratings (Module 1)

The transmission experiments for both Module 1, i.e. the cascade of two reflection gratings, and Module 2, i.e. the cascade of a reflection grating and a transmission grating, are reported separately in two different sections. This section, i.e. Section 6.7, evaluates the transmission performance for Module 1, and the next section, i.e. Section 6.8, evaluates the transmission performance for Module 2.

In this section, a complete 2D beam-steered system using OOK-NRZ (in Subsection 6.7.1) and DMT (in Subsection 6.7.2) signals in a testbed constructed as illustrated in Figure 6.3 is evaluated. The channel performances at different positions (by changing the wavelengths) are measured with the receiving collimator placed at various positions. These positions are compared to the theoretically calculated spots as shown in Figure 6.1 and the wavelengths

are confirmed using the OSA.

6.7.1 2.5 m free-space transmission with OOK-NRZ signaling

This experiment is conducted on the testbed for Module 1, as shown in Figure 6.3. The 2D steered system using Module 1 has been evaluated using an OOK-NRZ signal with a Pseudo Random Binary Sequence (PRBS) of length $2^{31}-1$ bits. The data is modulated onto a 1550 nm laser beam using an Mach-Zehnder Modulator (MZM). The transmitted power of the laser used is measured to be $\leq$ 9.3 dBm (thus, below the eye-safety limit). The signal quality is evaluated with the Bit Error Rate Tester (BERT) and the eye diagram is viewed on an oscilloscope. The measurement is repeated for an optical carrier wavelength of 1549 nm. Back-to-Back (BtB) measurements are carried out by connecting a 2 m long SMF from the output of the polarizer controller to the input of the attenuator.

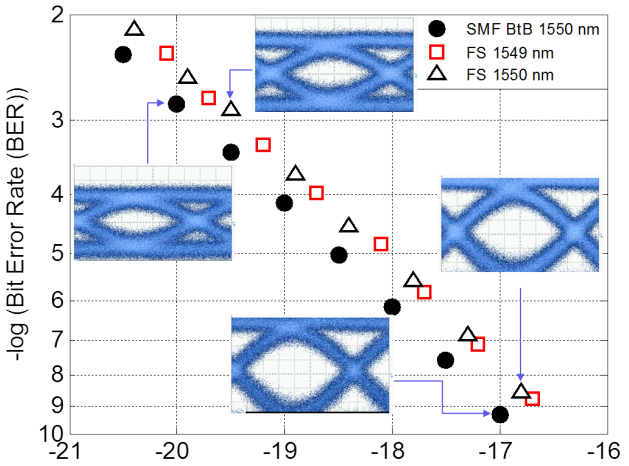

Figure 6.11: BER performance of OOK-NRZ transmission for diffracted beams at 1549 nm, 1550 nm and SMF BtB; Eye-diagrams for BtB and 2.5 m free-space (FS) 1550 nm link.

The performance of the free space diffracted OOK signals is plotted in Figure 6.11. Consistent overlapping of the 2.5 m link curves with the BtB curves show that the free-space beam can achieve error-free transmission (BER $\leq 1 \times 10^{-9}$), similar to transmission through a SMF.

The dissertation work in this section was published in C.W. Oh et al. [188].

6.7.2 2 m free-space transmission with DMT signaling

This experiment is conducted on the testbed for Module 1, as shown in Figure 6.3. We first evaluate the direct point-to-point 2 m link using a SMF (BtB

measurement) and compare that to a 2 m direct point-to-point free-space link, without any steering module. We employed the highly robust and spectrally efficient DMT modulation format to obtain the optimized capacity that can be achieved in a direct point-to-point free-space link.

The input DMT data signal is generated with Matlab as a digitized DMT signal and an Arbitrary Waveform Generator (AWG) is used to convert the DMT signal from digital to analog, which is then intensity-modulated onto the laser beam via a 10 Gigabit per second (Gbps) MZM. The captured signal is received by a 10 GHz photoreceiver and then converted from analog to digital via the Real-Time Oscilloscope (RTO) to be further processed offline with Matlab for obtaining the achievable data rates, Bit Error Rates (BERs) and constellations.

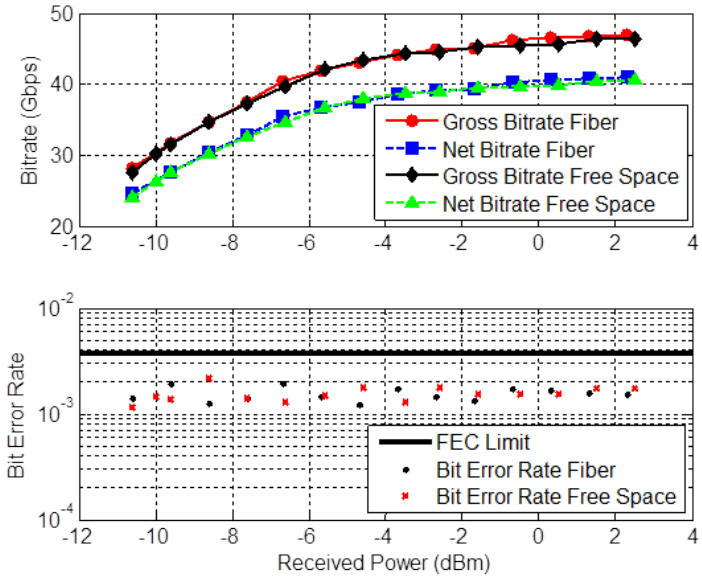

Figure 6.12: Channel performance of a fiber BtB versus a free-space link at wavelength of 1550 nm. The bitrate and BER performance as the input power into the photoreceiver is varied.

Figure 6.12 shows an increasing curve as more optical power is received, approaching up to gross and net bitrates of 46.9 Gbps and 40.9 Gbps, respectively, at 2.3 dBm received optical power for BtB, and gross and net bitrates of 46.4 Gbps and 40.5 Gbps, respectively, at 2.5 dBm for the free-space link. The increase in bitrate approaches saturation at about 0 dBm received optical power. These results are based on an average BER of less than 2×10^{-3}, thereby, correctable with Forward Error Correction (FEC) coding to obtain near error-free channels at BER $\leq 1 \times 10^{-9}$. The net transmission bitrate is achieved after the deduction of the DMT's cyclic prefix (guard against inter-

frame interference due to channel dispersion), preambles (training and channel estimation) and 7% overhead for FEC coding from the gross bitrate. FEC coding is not implemented but is considered and included in the calculation of bitrate. In DMT transmission, the signal is not demodulated per subcarrier but as an entire frame, therefore, the average BER is considered. The optimized DMT parameters are summarized in Table 6.3.

Table 6.3: DMT parameters for transmission system with Module 1.

Transmitter sampling rate	23 GSa/s
Receiver sampling rate	50 GSa/s
Digital clipping	10 dB
Number of subcarriers	512
Cyclic prefix length	10 points
Schmidl blocks	6 per 100 DMT frames
Number of DMT frames	2000

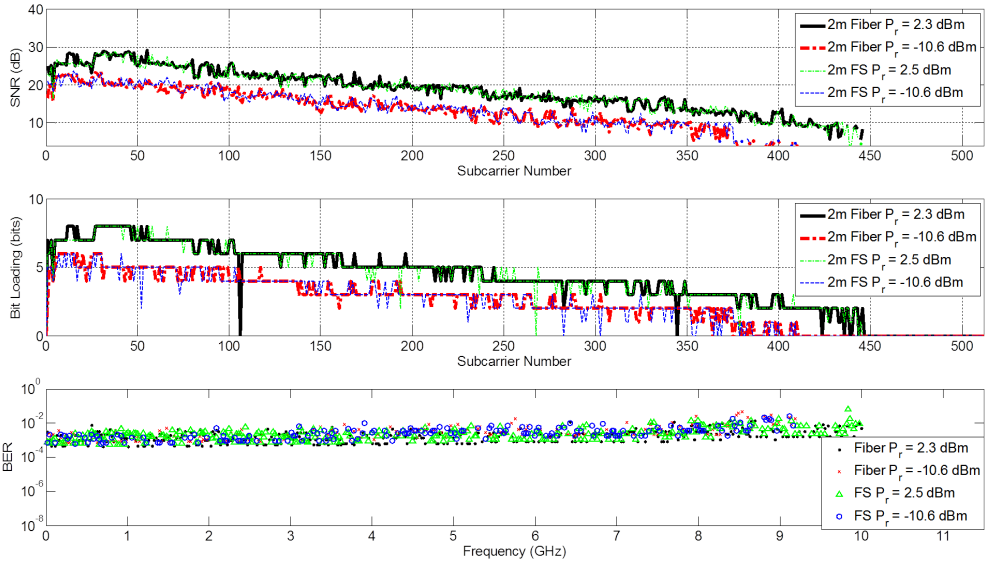

Figure 6.13: Transmission over fiber BtB versus free-space (FS) point-to-point at wavelength of 1550 nm: The SNR and bit loading at different subcarriers and the corresponding BER of the different carrier frequencies at comparable received powers.

In Figure 6.13, the corresponding Signal-to-Noise Ratio (SNR) and bit-loading curves are overlaid to compare the BtB performance to free-space at received optical power of 2.3/2.5 dBm and -10.6 dBm. All curves are well fitted to their counterparts at corresponding power levels. This shows that

the channel performance of DMT links are similar in both BtB and free-space transmission.

Bit-loading for BtB transmission at 2.3 dBm is allocated up to 10.43 GHz compared to the direct free-space beam at 2.5 dBm up to 10.41 GHz. Bit-loading for BtB transmission at -10.6 dBm is allocated up to 9.586 GHz compared to the direct free-space beam at -10.6 dBm up to 9.563 GHz. The difference in the effective bandwidths for free-space channel compared to BtB transmission is negligible. The corresponding constellations can be observed in Figure 6.14. The constellations are clear, undistorted and no amplitude nor phase noise is observed. We observe that at a higher received optical power, up to 256-Quadrature Amplitude Modulation (QAM) can be achieved while up to only 64-QAM is achieved at -10.6 dBm.

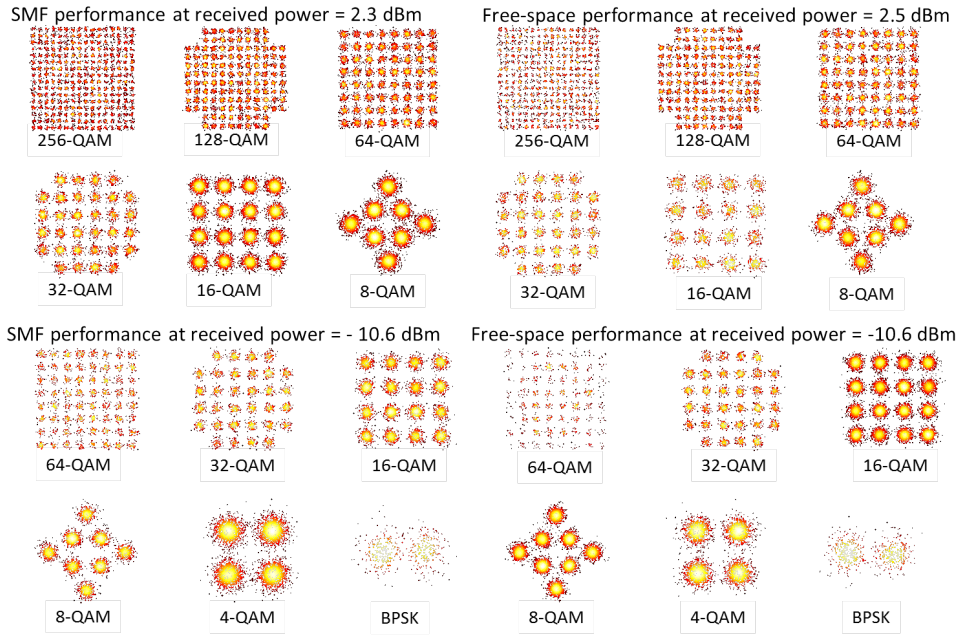

Figure 6.14: Constellation diagrams measured for direct transmission over BtB (SMF) and free-space point-to-point of 2 m distance at 2.3/2.5 dBm and -10.6 dBm.

In summary, the results showed that the performance of the DMT channel in BtB transmission and in free-space direct point-to-point transmission, of 2 m distance, are comparable.

Now, we include the 2D steering module (Module 1) into the complete system as seen in Figure 6.3 to evaluate the channel performance of the 2D diffracted beams using DMT modulation format. We benchmark the measured results of the 2D-steered channels to a direct point-to-point free-space link.

Figure 6.15 shows the comparison between the direct point-to-point free-space transmissions versus 2D-steered transmissions. We see that the measurements from the 2D-steered beams fall along the curve of the direct free-space transmission curve consistently at comparable received power levels. Thus, we can safely conclude that the steering module has negligible effect on the performance of the channels and that the steered channel performance is comparable to that of the BtB transmission.

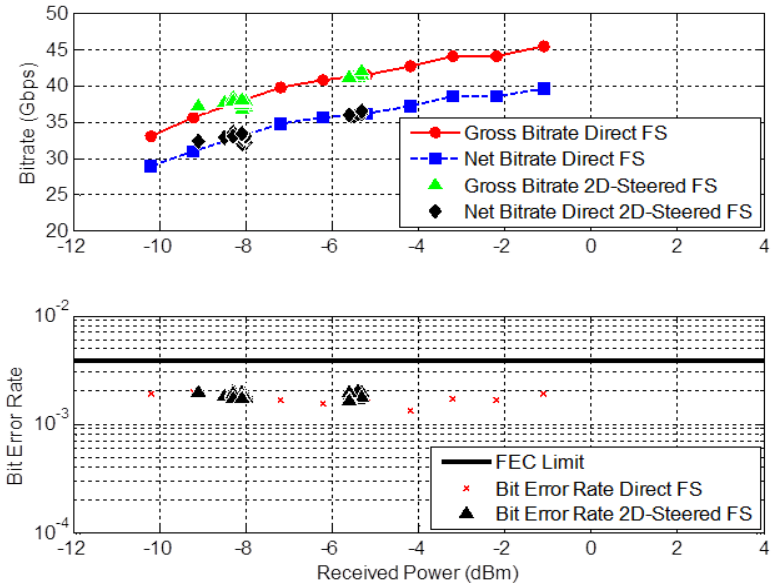

Figure 6.15: Comparison between 2D beam-steered channels and direct point-to-point free-space (FS) channels for 8 wavelengths.

In Figure 6.16, the achieved gross and net bitrates at different wavelengths are reported. The net transmission bitrate is achieved after deduction of the cyclic prefix (guard against inter-frame interference due to channel dispersion), preambles (training and channel estimation) and 7% overhead for FEC coding from the gross bitrate. FEC coding is not implemented but is considered and included in the calculation of bitrate. The highest bitrate achieved is at 1540 nm with a gross bitrate of 41.9 Gbps and net bitrate of 36.5 Gbps at -5.3 dBm. Each wavelength is represented with four measurements. All of the measured bitrates have a BER of less than 2×10^{-3} (within the FEC limit for near error-free transmission with BER $< 1 \times 10^{-9}$). The power is measured with an inline power meter set at 1550 nm. It can be observed that the data rates behave consistently with the power measurements.

Figure 6.17 shows the SNR, the bit loading for each subcarrier and the corresponding BER performance at the various subcarrier frequencies of the channel for 2D steered transmission measured at 1540 nm (with gross bitrate of 41.9 Gbps) and the worst channel measured, which is at 1600 nm (with

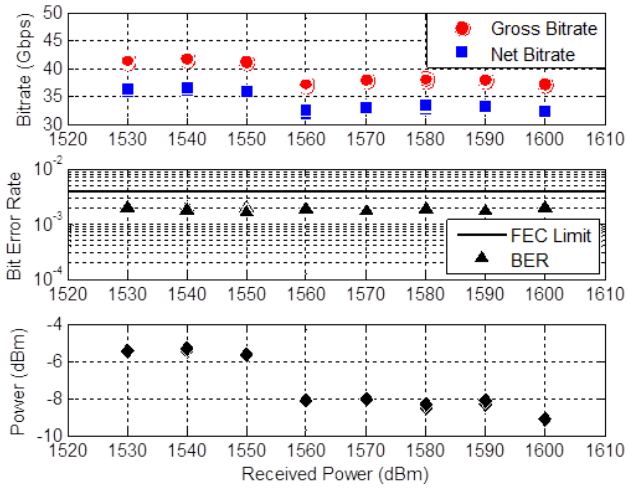

Figure 6.16: Gross and net bitrates achievable with 2D beam steering with cross-mounted reflection gratings for wavelengths between 1530 nm to 1600 nm. The corresponding bit error rates and received optical powers are given.

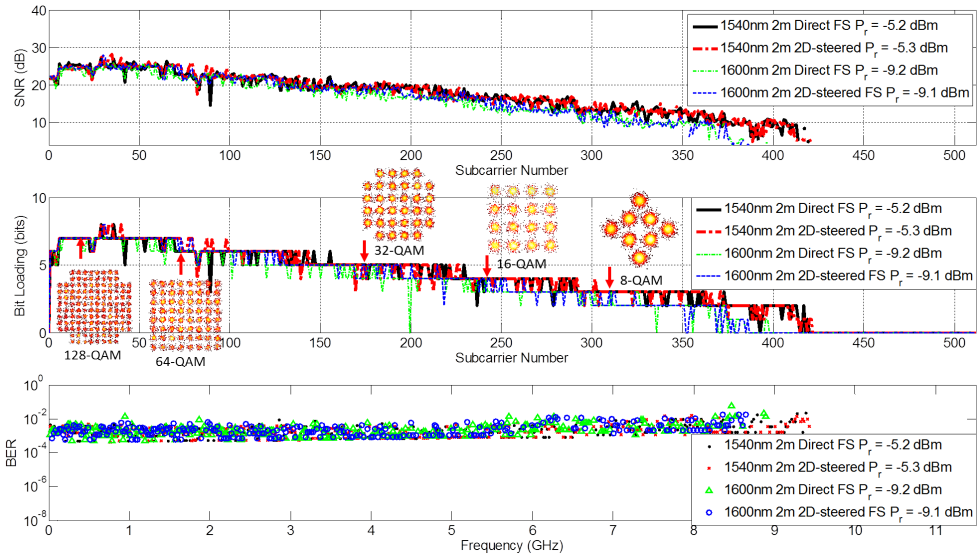

Figure 6.17: Transmission of direct free-space (FS) point-to-point versus 2D steered channels. The Signal-to-Noise Ratio (SNR), bit loading at different subcarriers with constellation diagrams for received power, P_r = -5.3 dBm, and the BER of the different carrier frequencies at comparable received powers have been plotted.

gross bitrate of 37.2 Gbps). These measurements are benchmarked to the corresponding free-space direct point-to point link measured at similar received power, i.e. -5.2 dBm and -9.2 dBm. Again, consistently matched curves are obtained.

Bit loading for 1540 nm direct point-to-point beam at -5.2 dBm is allocated up to 9.39 GHz compared to the 2D-steered beam at -5.3 dBm with up to 9.43 GHz. Bit loading for 1600 nm direct point-to-point beam at -9.2 dBm is allocated up to 8.9 GHz compared to the 2D-steered beam at -9.1 dBm with up to 8.65 GHz. In general, up to a maximum of 128-QAM levels were used with sporadic allocation of 256-QAM levels. As for BER performance, not all subcarriers achieved a BER $\leq 2 \times 10^{-3}$ but the average BER is still within the FEC limit for error-free transmission. Constellations corresponding to the loaded bits are shown for 1540 nm channel at a received power of -5.3 dBm. The constellations are clear and undistorted, and no amplitude nor phase noise is observed.

This section contains the comprehensive evaluation of the system and is an extension to the work published in C.W. Oh et al. [186, 188]. The paper reported a preliminary measurement with another AWG and Digital Phosphor Oscilloscope (DPO) pair used. A record high aggregate bitrate of 42.8 Gbps (net bitrate of 37.3 Gbps) at BER $= 1.27 \times 10^{-3}$ was reported [188].

In summary, we have seen the feasibility of implementing the 2D beam steering using cross-mounted passive reflection gratings (Module 1) with bitrates up to 41.9 Gbps (net 36.5 Gbps) at -5.3 dBm received power within 9.43 GHz bandwidth. With the consistently matched performance shown between fiber BtB and free space, and between 2D beam-steered free space and point-to-point direct free-space transmissions, we can safely conclude that a fiber BtB equivalent performance can be obtained with the 2D-steered free-space communication for indoors, implying that the 2D passive steering module only introduces negligible impact on the channel performance while it supports ultra-high data capacity.

6.8 Transmission: Cascaded reflection and transmission gratings (Module 2)

The performance of the 2D-steered system employing the cross-mounted reflection and transmission gratings (Module 2) is evaluated using OOK-NRZ (Subsection 6.8.1) signaling and the communication channels are further optimized using the spectrum-efficient DMT modulation format (subsection 6.8.2) which is widely employed in copper-based Digital Subscriber Line (DSL) user access networks for high speed transmission. Finally in Subsection 6.8.3 and Subsection 6.8.4, we evaluate a 2D-steered free-space transmission of 3 m distance using OOK-NRZ and 4-PAM modulation formats.

6.8.1 2 m free-space transmission with OOK-NRZ signaling

This experiment is conducted on the testbed for Module 2, as shown in Figure 6.4. A laser beam with a wavelength of 1550 nm is employed as the optical carrier signal. An OOK-NRZ signal is generated using a pattern generator with a PRBS length of $2^{31} - 1$ bits. The modulated signal from the pattern generator is amplified with an EDFA up to at most 9 dBm. The signal is then transmitted to free space through a triplet lens collimator from Thorlabs (TC18FC-1550) with a focal length of 18.36 mm and a full-angle divergence of 0.034°. The $1/e^2$ beam diameter is 3.33 mm at the focal plane. For further information on the lens collimator please refer to Section 4.1.

The beam is illuminated onto the highly dispersive reflective echelle grating and then onto the fused silica transmission grating. Then, the beam is reflected on a mirror to be collected by an identical collimator after a free-space distance of 2 m. The collimated beam is directed into the receiver and thereby, the BER performance is computed. The eye-diagram is sampled on an Agilent sampling scope. BtB measurements are made by replacing the free-space link with a SMF of 1 m in length. The complete experiment is repeated by varying the data rate generated by the pattern generator. The optical power loss in free space is measured up to 6.15 dB as shown in Table 6.2.

Using the energy-efficient and simple-to-implement OOK-NRZ modulation format, error-free transmission, i.e. an error-free channel at bit error rate, BER $\leq 1 \times 10^{-9}$, of up to 15 Gbps is obtained. Figure 6.18 shows the BER performance measured between 6 Gbps up to 13 Gbps. For transmission up to 10 Gbps, the free-space channels have at maximum a negligible 1 dB penalty from the BtB performance. The penalty increases to more than 1 dB at 11 Gbps and above. This shows that the free-space steering module has a bandwidth limitation of approximately 10-11 Gbps. The observed eye diagrams for 10 Gbps at BER $= 1.61 \times 10^{-3}$ and BER $= 1.46 \times 10^{-9}$ are shown in Figure 6.18 in comparison to the BtB SMF performance at BER $= 1.05 \times 10^{-3}$ and BER $= 1.47 \times 10^{-9}$. Further extending the measurements to the FEC limit (BER at 1×10^{-3}), up to 16 Gbps transmission is achieved, as shown in Figure 6.19. The corresponding eye-diagrams at 15 Gbps transmission with BER $= 1.50 \times 10^{-3}$ and at BER $= 1.67 \times 10^{-9}$ have distorted eyes although they are still open and clean.

In addition, the spectrum of the transmitted signal through a SMF and through our free-space system is measured. Figures 6.20 and 6.21 show the spectrums for 10 Gbps and 15 Gbps signals, respectively, through SMF (measured after the EDFA) and free space (after the receiving collimator). The grating module in combination with the aperture of the transmitting and receiving lens coupler, behaves as a bandpass filter that allows the baseband spectrum. ASE noise from the EDFA is also significantly filtered.

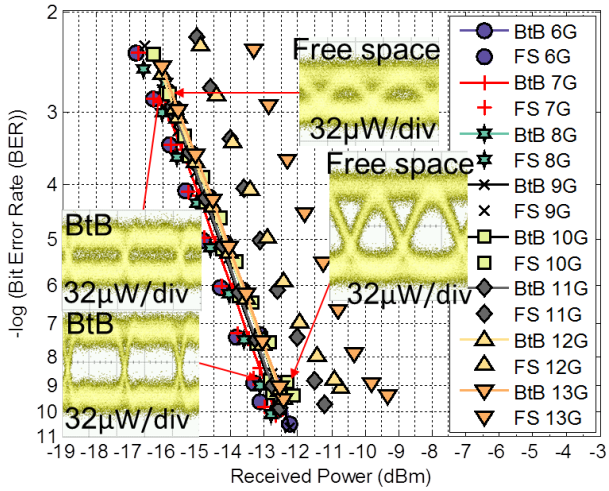

Figure 6.18: Link performance at OOK-NRZ between 6 Gbps and 13 Gbps transmissions with eye diagrams for 10 Gbps free space and BtB.

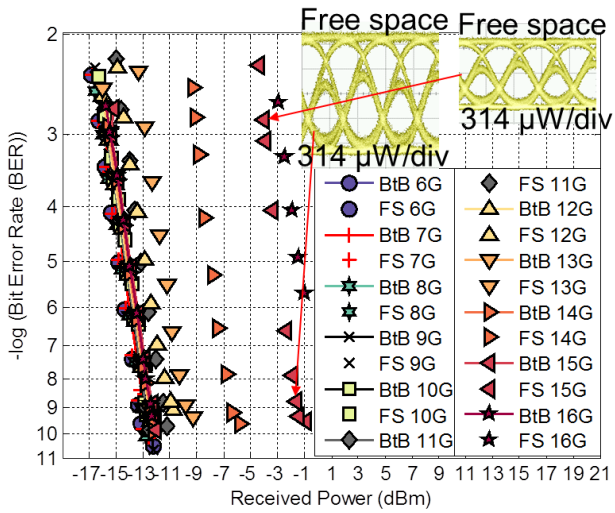

Figure 6.19: Link performance at OOK-NRZ between 6 Gbps and 16 Gbps transmissions with eye diagrams for 15 Gbps free space.

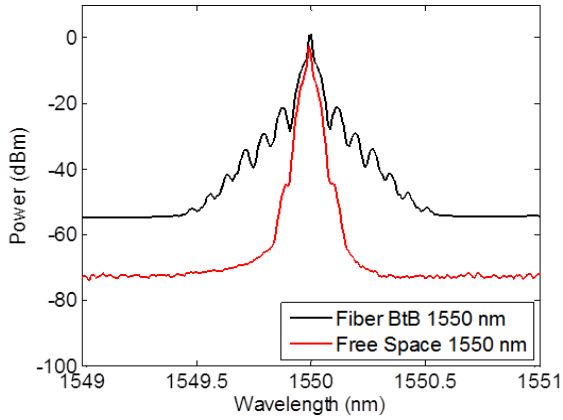

Figure 6.20: Transmission spectrum in SMF versus steered free-space channel at 10 Gbps. The peaks seen in the Fiber BtB repeats at approximately 10 GHz interval. Shaping of the spectrum by the free-space beam steering module can be clearly observed.

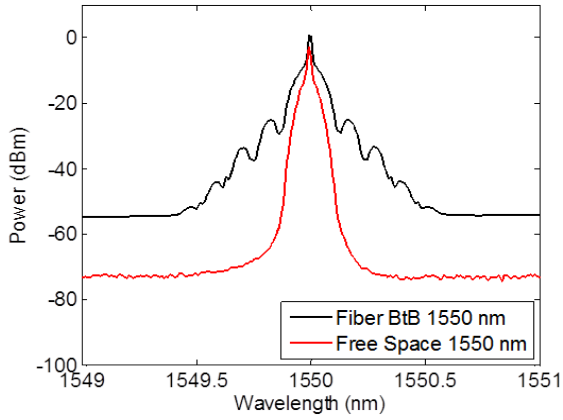

Figure 6.21: Transmission spectrum in SMF versus steered free-space channel at 15 Gbps. Shaping of the spectrum by the free-space beam steering module can be clearly observed.

6.8.2 2 m free-space transmission with DMT signaling

This experiment is conducted on the testbed for Module 2, as shown in Figure 6.4. The data signal is generated using an AWG and modulated onto the optical carrier via a 10 GHz bandwidth MZM. The free-space beam is received with a 10 Gbps bandwidth photoreceiver and the signal is captured with a real-time scope and processed with Matlab to calculate the BER and signal constellations. The experiment is repeated for several wavelengths from different diffraction orders (scanning lines) of the steering module. These measurements are compared to the 2 m distance performance of a direct free-space link (without steering modules) as a BtB benchmark.

Figure 6.22 shows the performance of the DMT signals at 1518 nm, 1534 nm, 1550 nm, 1566 nm, 1583 nm, and 1600 nm. These measurements are compared to a direct free-space link, which acts as the BtB measurement. The bitrates reported are measured at FEC-limit BER of 1×10^{-3} and with a received optical power of 0 dBm except at $\lambda = 1600$ m, at 0.5 dBm. In general, we see a consistent data rate penalty of about 5 Gbps between the free-space BtB and the steered channels. This is due to bandwidth limited performance of the beam-steered optical channel (see Section 6.4).

Figure 6.23 shows the channel performance with a DMT signal at different wavelengths. We observe that for the direct free-space BtB channel, 9.95 GHz channel is bit-loaded corresponding to the SNR. For the 2D-steered free-space beams, transmission bits are only allocated in bandwidths of 8.625 GHz, 8.962 GHz, 8.67 GHz, 8.603 GHz, 8.647 GHz and 8.603 GHz for the above mentioned wavelengths respectively. The highest bitrate is achieved at $\lambda = 1583$ nm with a gross bitrate of 41.4 Gbps and a net bitrate (after the deduction of the cyclic prefix, preambles and 7% overhead for FEC coding) of 36.2 Gbps. For frequency carriers with sufficient SNR, a signal constellation up to 8 bits, equivalent to 256-QAM, is allocated. The optimized DMT parameters are summarized in Table 6.4. The corresponding constellation diagrams shown in Figure 6.23 are undistorted and distinguishable.

Table 6.4: DMT parameters for transmission system with Module 2.

Transmitter sampling rate	23 GSa/s
Receiver sampling rate	50 GSa/s
Digital clipping	10 dB
Number of subcarriers	512
Cyclic prefix length	10 points
Schmidl blocks	6 per 100 DMT frames
Number of DMT frames	2000

The measurements are repeated at different distances between the Pencil Radiating Antenna (PRA) and the receiver, and also with three different wave-

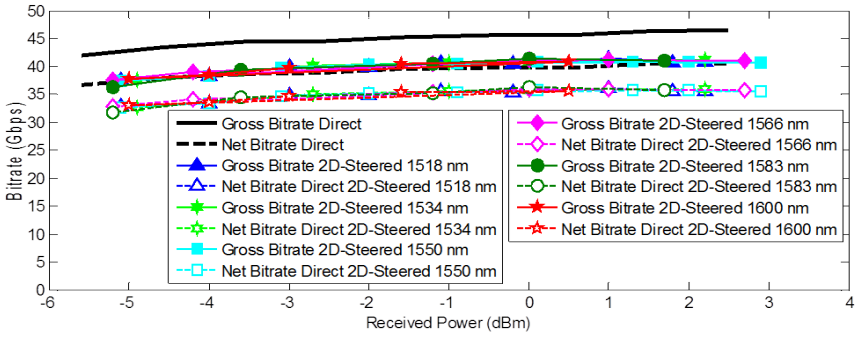

Figure 6.22: Performance of 2D beam-steered channels compared to free-space BtB channel, with DMT signaling.

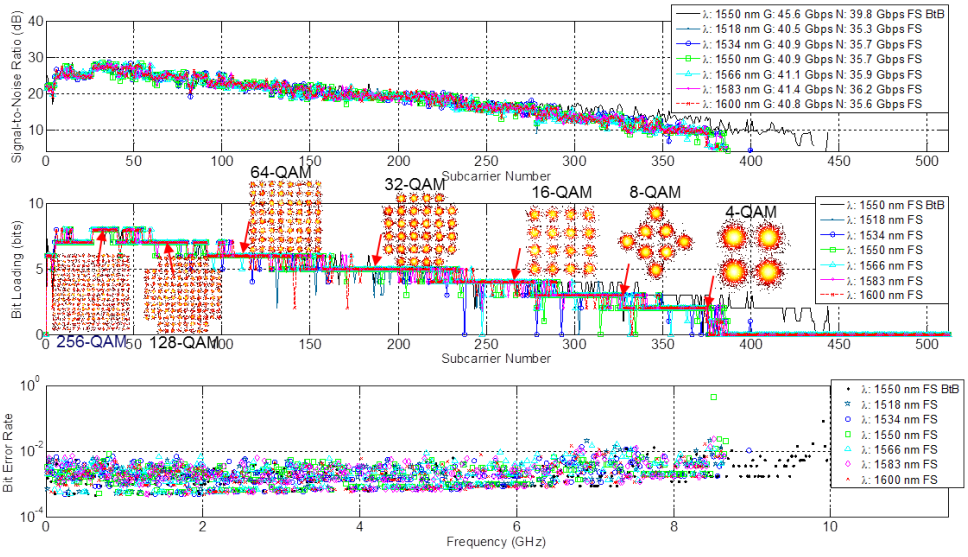

Figure 6.23: SNR, bit loading and BER of DMT signals at multiple wavelengths in a cascaded reflection and transmission gratings setup.

lengths. The optical channel performance has been consistent for measurements at different receiver-to-PRA distances, as shown in Figure 6.24. We see that there is no correlation between the distance and the performance since the beam width up to about 4 mm is still within the opening aperture size of the collimator with negligible dispersion. Gross and net bitrates of up to 41.6 Gbps and 36.3 Gbps are achieved with BERs of less than 2×10^{-3} i.e. below the hard-decision FEC limit for near error-free performance.

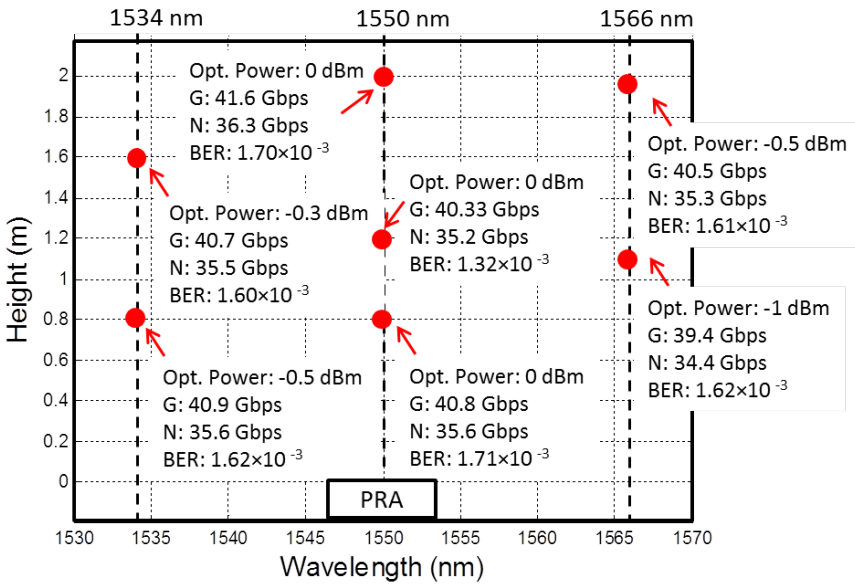

Figure 6.24: Measurements at different distances/height between devices and the PRA.

6.8.3 3 m free-space transmission with OOK-NRZ

A testbed, as depicted in Figure 6.26, is constructed to evaluate beam-steering with wavelength tuning over 3 m distance. An OOK-NRZ signal is generated with a PRBS of length $2^{31}-1$ bits. An MZM is used for data modulation onto a 12.5 dBm optical carrier signal. The MZM has a loss of approximately 7-8 dB. A 3.3 mm wide optical beam is then transmitted to free space through a triplet lens collimator from Thorlabs (TC18FC-1550) with a focal length of 18.36 mm and a full-angle divergence of 0.034°. The $1/e^2$ beam diameter is 3.33 mm at the focal plane. For further information on the lens collimator please refer to Section 4.1. The free-space beam impinges onto the pair of crossed reflection and transmission gratings. Silver-coated mirrors are used to extend the free-space distance to over 3 m. At the receiving device, an identical lens collimator is used to collimate the propagated beam into an optical receiver. Finally, the electrical signal is analyzed by observing the eye-pattern on a sampling scope

and the BER performance is evaluated by a BERT.

Figure 6.25 shows the BER performance for 10 Gbps OOK-NRZ signals. In general, steered free-space channels have < 1 dB penalty from fiber BtB performance, which is an acceptable system penalty [189]. However, penalty of $1 - 2$ dB is seen for wavelengths 1583, 1618 nm and 1518 nm. The additional penalty is contributed by the optimization of the modulator each time the wavelength of transmission is changed, and the dispersion caused by slight wavelength dependence of the modulator as can be seen from the BtB measurements. Additionally, for wavelength 1518 nm and 1618 nm, the tunable laser provides a lower output power, as shown in Figure 5.11. This results in a lower SNR compared to the other channels.

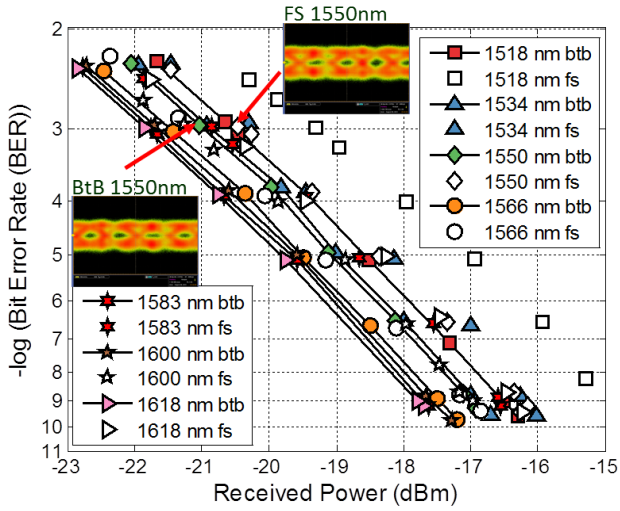

Figure 6.25: BER performance for OOK-NRZ transmission at 10 Gbps. Insets: eye-diagrams at BER= 1×10^{-3} for fiber BtB and steered free-space (fs) transmission at 1550 nm.

6.8.4 3 m free-space transmission with PAM transmission

For the evaluation of 4-PAM transmission, the testbed as shown in Figure 6.26 is used. The data signal is generated from an AWG and evaluated using a real-time oscilloscope.

Extensive measurements have been carried out for two wavelengths, i.e. 1520 nm and 1550 nm. The target for error-free performance with hard decision FEC is BER $\leq 2 \times 10^{-3}$. Optical fiber BtB measurements were carried out to benchmark the performance of free-space links. Figure 6.27 shows the BER performance measured at 12, 14, 15 and 16 Gigabaud (GBaud) for 1550 nm, and at 15 and 16 GBaud for 1520 nm. In Figure 6.27(a) for 1550 nm, we observe power penalties of 0.63 dB (12 GBaud), 1 dB (14 GBaud), 1.93 dB

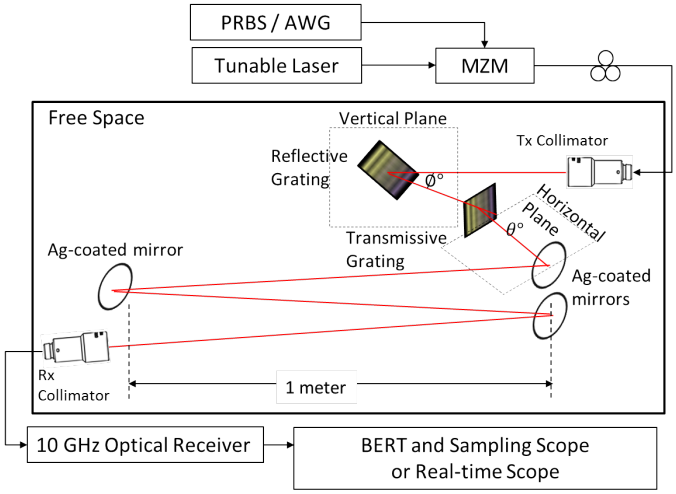

Figure 6.26: Testbed setup for free-space transmission with 2D optical beam-steering over 3 m distance.

(15 GBaud), and 2.07 dB (16 GBaud) while from Figure 6.27(b) for 1520 nm, we observe power penalties of 2.46 dB (15 GBaud) and 1.21 dB (16 GBaud). The inconsistency seen in Figure 6.27(b) is highly likely due to the imperfect adjustment and alignment of the link when changing over from BtB to free space reconfiguration. The measurements for Figure 6.27(a) were completed for free space and BtB without reconfiguring the system in between. All the measured performances were below hard decision FEC threshold of BER $\leq 2 \times 10^{-3}$. Figure 6.28 shows the observed eye-diagrams for BtB and free-space performances at 15 GBaud for both 1550 nm and 1520 nm. At BER $\leq 1 \times 10^{-3}$, the eye levels are still distinguishable with negligible eye-skew.

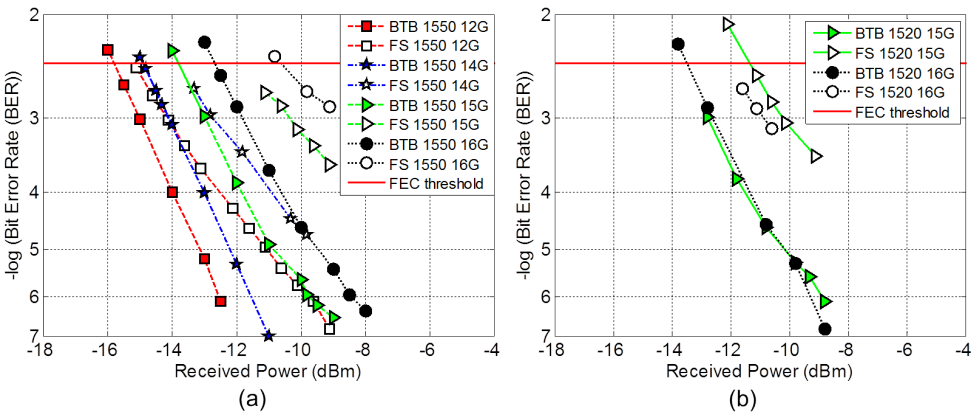

Figure 6.27: BER Performance: (a) 1550nm (12,14,15 & 16 GBaud); (b) 1520nm (15 & 16 GBaud); FS: Free space, BtB: Back-to-back.

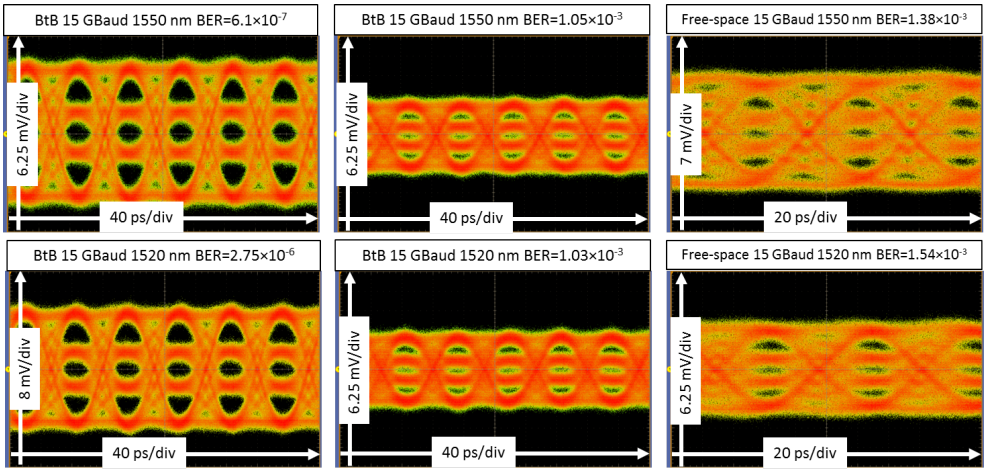

Figure 6.28: Eye-diagrams for top row: 1550 nm, and bottom row: 1520 nm; columns 1 and 2: Back-to-back ; column 3: Free space

6.9 Chapter conclusion

In summary, a novel indoor optical wireless communication system employing 2D beam steering established by orthogonally cascading two passive reflection gratings were built and evaluated. Free-space channel capacity per user of at least 37.2 Gbps up to 41.9 Gbps (between 1530 nm and 1600 nm) has been measured over a free-space transmission distance of 2 m in a 10 GHz system. As demonstrated in the measurement results, the proposed optical wireless system has a comparable performance to that of a SMF transmission system. However, the first beam-steering module could only provide 2 scan lines in an angular coverage of $12.67° \times 5.61°$ between 1529 nm and 1611 nm, as shown in Figure 6.1. Losses coming mainly from the module were measured to be between -13.5 to -16.8 dB between 1530 nm and 1600 nm, as shown in Table 6.1.

The design was further improved after exploring the limits of the tuning range of the gratings. Subsequently, an improved steering module employing an orthogonal cascade of a reflection and a transmission grating has been presented. The module is able to scan an area with a density of 7 lines using remote wavelength tuning over an angular scan of $5.62° \times 12.15°$ with wavelengths between 1511 nm and 1627 nm, as shown in Figure 6.2. The second module has only up to 6.15 dB loss in the full steering range between 1518 nm to 1600 nm, as shown in Table 6.2. The end-to-end link bandwidth is approximately 10 GHz. Therefore, a spectrum efficient modulation format such as DMT and PAM could be employed to further maximize the capacity of the channels. In the experimental demonstrations, a promising bitrate of 15 Gbps error-free channel is achieved using OOK-NRZ modulation format. In this ex-

periment, we observed the ASE reduction in the free-space channel obtained by the optical filtering of the 2D steering modules which may help to improve SNR performance of the system as a bonus. Further, by employing the DMT modulation format in order to increase spectrum efficiency, up to a gross bitrate of 41.4 Gbps with a corresponding net bitrate of 36.2 Gbps at the hard decision FEC limit is achieved.

The free-space transmission distance was further improved to 3 m distance and evaluated using OOK-NRZ signaling in which 10 Gbps was achieved with BER $\leq 1 \times 10^{-9}$, with wavelength tuning of up to seven wavelengths. With 4-PAM signaling, up to 32 Gbps at 16 GBaud was achieved with FEC-correctable transmission (BER $\leq 2 \times 10^{-3}$). For systems further than 3 m distance, we will have to take into account the beam size due to the divergence of the Gaussian beam. As long as the diverged beam has a diameter smaller than the size of the receiving collimator, lens receiver, photodetector surface, etc., we can expect to achieve a performance close to the reported results. However, when the diverged beam size becomes larger than the effective area of the receiver, the ratio between the effective receiving area and the diverged beam size at the receiving plane has to be taken into account, as shown in [143].

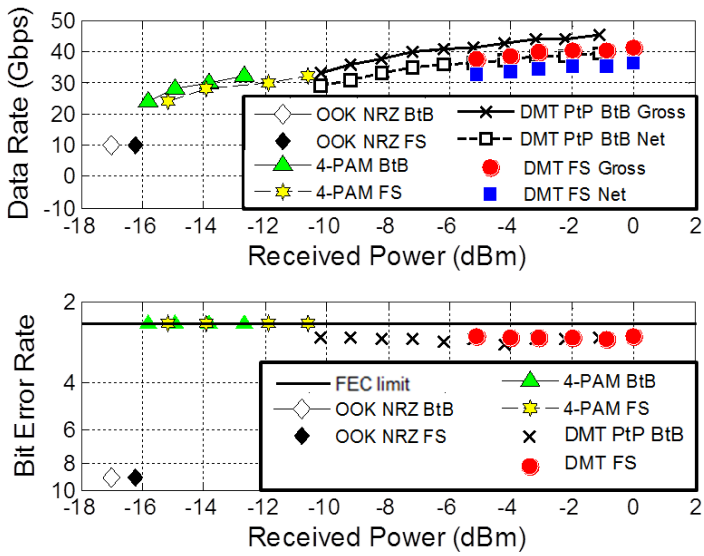

Figure 6.29: Summary of measured performances for OOK-NRZ, 4-PAM and DMT signals.

In summary, by employing a 10 GHz bandwidth-limited system, 32 Gbps at -10.62 dBm was achieved using 4-PAM and 41.4 Gbps (net 36.2 Gbps) at 0 dBm was achieved with DMT, as shown in Figure 6.29, both below the FEC limit. The results show that 4-PAM signaling can have at least the same channel performance as the more complex DMT signaling while being easier

to realize in real-time circuitry and having less latency. The 4-PAM system shows interesting results for the realization of future high-capacity narrow-beam optical wireless systems without the need for further complex signal processing at the user side such as needed for DMT.

Chapter 7

All-optical duplex communication

Contents

At present, much attention is seen in improving the downlink communication in terms of robustness, ease of implementation, capacity and coverage. However, only few progressive works are seen for the uplink optical communication. Often, the uplink communication in an optical wireless duplex communication system requires a separate channel, i.e. by using a radio wireless technique, Light Emitting Diode (LED) or laser [82, 149]. However, by using the radio technique, the uplink typically offers a lower channel capacity than the optical downlink channel giving rise to a system with asymmetric speeds. The broad beam profile of LEDs necessitates a compromise on the link budget and so also asymmetric. As for laser communication, the need for uplink beam steering, for e.g. as reported in [82, 149], leads to latency and complicated receiver hardware due to the time, software and hardware needed to align the narrow beam to the access point each time the user terminal moves.

In this thesis, a novel full-duplex solution based on the principle of reversibility of an optical light path and carrier recovery method to provide a high capacity uplink with simultaneous alignment, is proposed. It builds on the 2D pencil beam-steered system concepts we introduced earlier. The novel concept eases channel management since the same wavelength is used for both

uplink and downlink, and the actual wavelength provides crucial information about the location of the mobile terminal.

The work in this chapter is reported in C.W. Oh et al. [190, 191].

7.1 All-optical bi-directional OWC

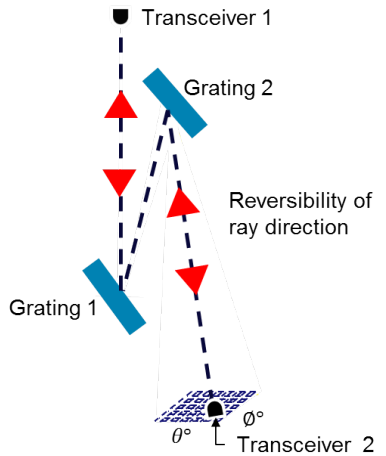

Figure 7.1: Bi-directional propagation path in a two-dimensional steering system. The reversibility holds for individual rays.

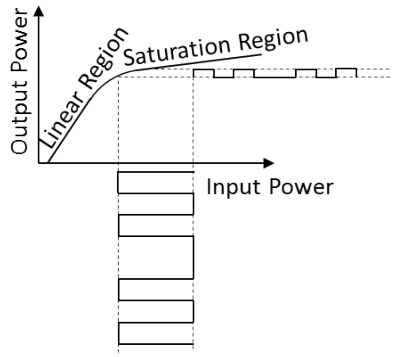

Figure 7.2: SOA output power versus input power curve. SOA is operated in the saturation region for data erasure.

The idea is based on two principles. Firstly, we use the reversibility principle of optics whereby light follows the same path that it traversed when the beam is reversed, as illustrated in Figure 7.1. The major advantage here is that the receiver module does not need an additional beam-steering device while maintaining a narrow beam. Secondly, we employ the data erasure and

re-write technique using Semiconductor Optical Amplifiers (SOAs). The concept of data erasure in a low Extinction Ratio (ER) signal by means of an SOA has been proposed before for Passive Optical Networks (PONs) [192]. ER is commonly used to describe the performance of a transmitter and is simply the ratio of the power used to transmit a logic level '1' to the energy used to transmit a logic level '0' [193, 194]:

$$\text{Extinction ratio} = \frac{\text{'1' power level}}{\text{'0' power level}} \tag{7.1}$$

In order to achieve a good Bit Error Rate (BER) performance, an extinction ratio where significant separation between the power used to transmit a logical '1' and the power used to transmit a logical '0' is required [193, 194].

Wavelength re-write is implemented by first erasing the downlink data by operating the SOA in its saturation region (as shown in Figure 7.2), and then, re-writing the carrier with the uplink data. This method enables mass production of identical wavelength-agnostic [195] and therefore, potentially low-cost receivers. In a preliminary work in C.W. Oh et al. [190], the feasibility of a symmetric 10 Gbps system has been presented.

In this thesis, evaluation of the system in terms of crosstalk, the effect of the Pseudo Random Binary Sequence (PRBS) pattern length and the impact of the downstream ER are given. In addition, the transmission performance of a system with symmetric speeds of 10 Gbps and an asymmetric system (10 Gbps downlink / 2.5 Gbps uplink) will be given.

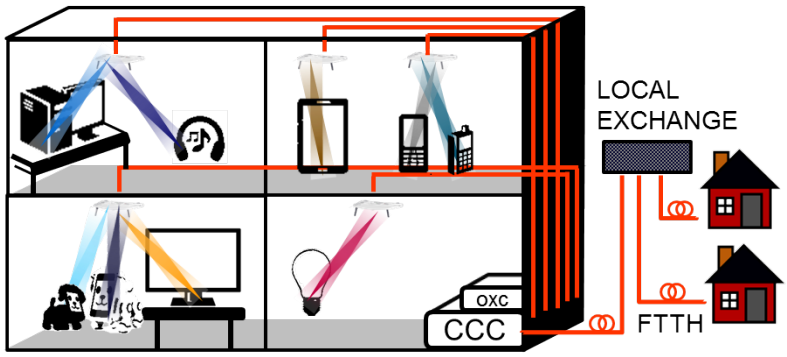

Figure 7.3: Bi-directional indoor all-optical wireless network with pencil beams. Central Communication Controller (CCC), Optical Cross Connect (OXC).

Figure 7.3 shows an all-optical bi-directional wireless system concept for indoors. The difference, compared to the architecture proposed in Beam-steered Reconfigurable Optical-Wireless System for Energy-efficient communication (BROWSE) in Section 1.3, is that the BROWSE system uses a radio uplink while in this work, as shown in Figure 7.3, only optical pencil beams are used for both up- and down-link. Subsequently in this scenario, at the user

side, fixed and mobile devices are equipped with an optical Transceiver (TRx) that supports data erasure and carrier recovery (for e.g. SOAs) and a modulator for data rewrite on the same wavelength. This eliminates the need for a laser source at the user's device which has its own wavelength offset and phase noise.

Section 7.2 will present the testbed and method for crosstalk evaluation on symmetric 10 Gbps and asymmetric (10 Gbps downlink / 2.5 Gbps uplink) duplex communication channels using a wavelength of 1550 nm in our 2D beam-steered system. Section 7.3 presents the testbed and method to demonstrate the performance of the 2D-steered duplex communication channels using symmetric and asymmetric bitrates, using downstream data erasure and modulation at the user's device side with different PRBS pattern lengths and downstream extinction ratios. Results and discussions of the two systems are given in Section 7.4.

7.2 Experimental setup for crosstalk evaluation in 2D-steered duplex link

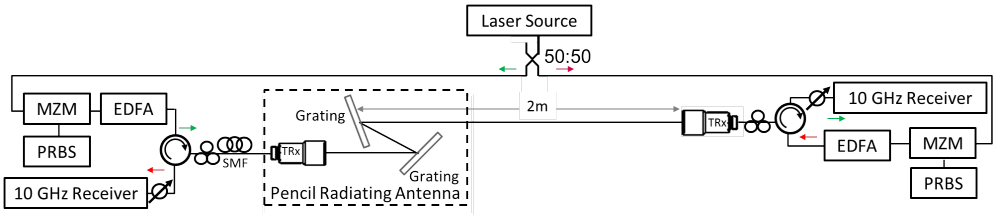

Figure 7.4: Testbed setup for crosstalk evaluation of a full-duplex 2D-steered free-space communication using wavelength re-use. Erbium-doped fiber amplifier (EDFA), Mach-Zehnder modulator (MZM), Pseudorandom binary sequence (PRBS).

Figure 7.4 illustrates the testbed for the crosstalk evaluation of an all-optical wireless system with 2D beam steering over 2 m free space. A laser source of 1550 nm is distributed 50:50 to provide identical optical input power and wavelength for the downlink and uplink transmission [196]. Note that the user's device is fed via fiber by the same laser as used for downstream (50% power) with no carrier recovery. This setup is for measurement evaluation only, not for a practical system setup. The downlink Mach-Zehnder Modulator (MZM) modulates the beam with an Non-Return-to-Zero (NRZ)-On-Off-Keying (OOK) signal with PRBS $2^7 - 1$ bits. An Erbium-Doped Fiber Amplifier (EDFA) is used to amplify the optical signal up to 8.9 dBm just before transmission to free space through the triplet lens collimator from Thorlabs (TC18FC-1550), which has a focal length of 18.36 mm, an opening aperture of 10 mm, and a full-angle divergence of 0.034°. The $1/e^2$ beam diameter is 3.33

mm at the focal plane. For further information on the lens collimator please refer to Section 4.1.

The launched beam then hits the 2D steering module, which is constructed by cascading a reflection grating with a blaze angle of 63° and 31.6 grooves/mm (Thorlabs GE2550-0363), and a reflection grating with a blaze angle of 75° and 79 grooves/mm (Thorlabs GE2550-0875) (see Section 3.3 for more details). The diffracted beam is captured by another triplet collimator and received with a 10 Gigahertz (GHz) Single Mode Fiber (SMF) photoreceiver from Discovery Semiconductors, Inc, Part number DSC-R402AC-39-FC/UPC-K-2. For the uplink, the same laser source is modulated with an NRZ-OOK signal with PRBS $2^7 - 1$ bits using an MZM at the user's side and the optical signal is amplified to 8.9 dBm by an EDFA before transmission. The beam then traverses the same path as the downlink, but in reverse, towards the diffractive modules, is collected by the collimator and finally, is detected at the receiver at the head-end side. The uplink measurement is repeated using PRBS $2^{31} - 1$ bits. The power loss in the free space path is measured to be as low as 13.7 dB at $\lambda = 1550$ nm.

7.3 Experimental setup for 2D-steered full-duplex transmission

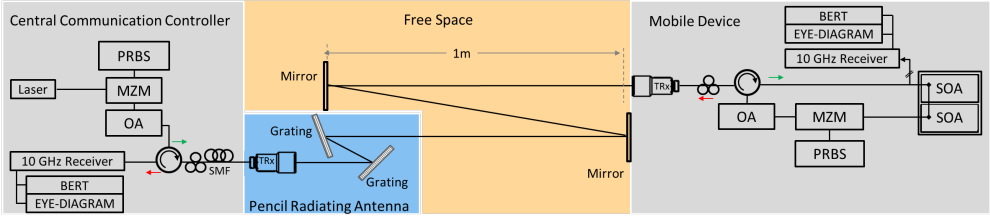

Figure 7.5: Testbed setup for full-duplex free-space transmission with two-dimensional beam steering and wavelength re-use. Optical amplifier (OA), Mach-Zehnder modulator (MZM), Pseudorandom binary sequence (PRBS), Semiconductor optical amplifier (SOA).

Figure 7.5 illustrates the testbed setup for a symmetrical or asymmetrical full-duplex 2D-steered communication system with optical carrier recovery at the mobile device. As in the proposed architecture, the testbed consists of the Central Communication Controller (CCC), the free space region and the mobile device. The CCC unit hosts a laser tuned to transmit at $\lambda = 1550$ nm. The transmitted beam acts as the carrier signal. A data signal of PRBS $2^7 - 1$ bits is modulated onto the carrier signal using an MZM at 10 Gbps. The ER of the signal is set by observing the signal on a sampling scope. An Optical Amplifier (OA) is used to amplify the optical signal to ≤ 9 dBm. In this

experiment, an EDFA is employed. Alternatively, an SOA may be preferred as SOAs can be accommodated in Photonic Integrated Circuits (PICs) and thus, enable miniaturization of the receiver units in the future. PIC technology is capable of integrating various photonic components such as lasers, modulators, optical amplifiers, photodetectors, and waveguide gratings on a single substrate [197]. The output signal of the MZM is then carried through SMF. The signal is emitted into free space through the TRx collimator and travels towards the 2D beam-steering module. The transmission distance is extended to 3 m, by means of two silver-coated mirrors.

At the receiving device, an identical TRx collimator is used to capture the signal. The received signal is carried towards the SOAs for data erasure. The re-modulated upstream data signal is created using PRBS $2^{31}-1$ bits. In order to compensate for the loss caused by the MZM, an OA (in this experiment, an EDFA is employed) is placed to amplify the signal to $\leq$ 8 dBm. This uplink signal then travels through the TRx collimator, and by the principle of reversibility, the signal travels through the same path as the downlink signal in the optical system. The signal is then collimated by the TRx collimator and sent to the 10 GHz PIN photoreceiver, and thereafter, evaluated using a Bit Error Rate Tester (BERT) and sampling scope for the eye diagram.

7.4 Results and discussion

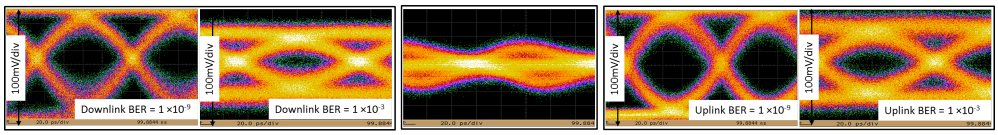

Figure 7.6: Eye-diagram for symmetrical 10 Gbps full-duplex transmission with wavelength re-use system with a downlink ER = 3.6 dB: (a) downlink signal at BER 1×10^{-9} and 1×10^{-3} (b) Erased signal after SOA (c) Re-modulated uplink signal at BER 1×10^{-9} and BER 1×10^{-3}.

Figure 7.6 shows the eye-diagrams for downlink signal with ER = 3.6 dB for (a) downlink signal (b) erased signal (c) re-modulated signal. We observe that data erasure and re-modulation is achieved with open eyes.

With regard to the crosstalk evaluation, the BER performance and eye diagrams are measured and observed. Again, note that the user's device is fed via fiber by the same laser as used for downstream (50% power) with no carrier recovery. Crosstalk measurements are carried out for (i) both the uplink and downlink when both links are operational, (ii) the downlink when the uplink is disconnected, and (iii) the uplink when the downlink is disconnected. Transmission measurements are carried out for symmetric (10 Gbps) and asymmetric

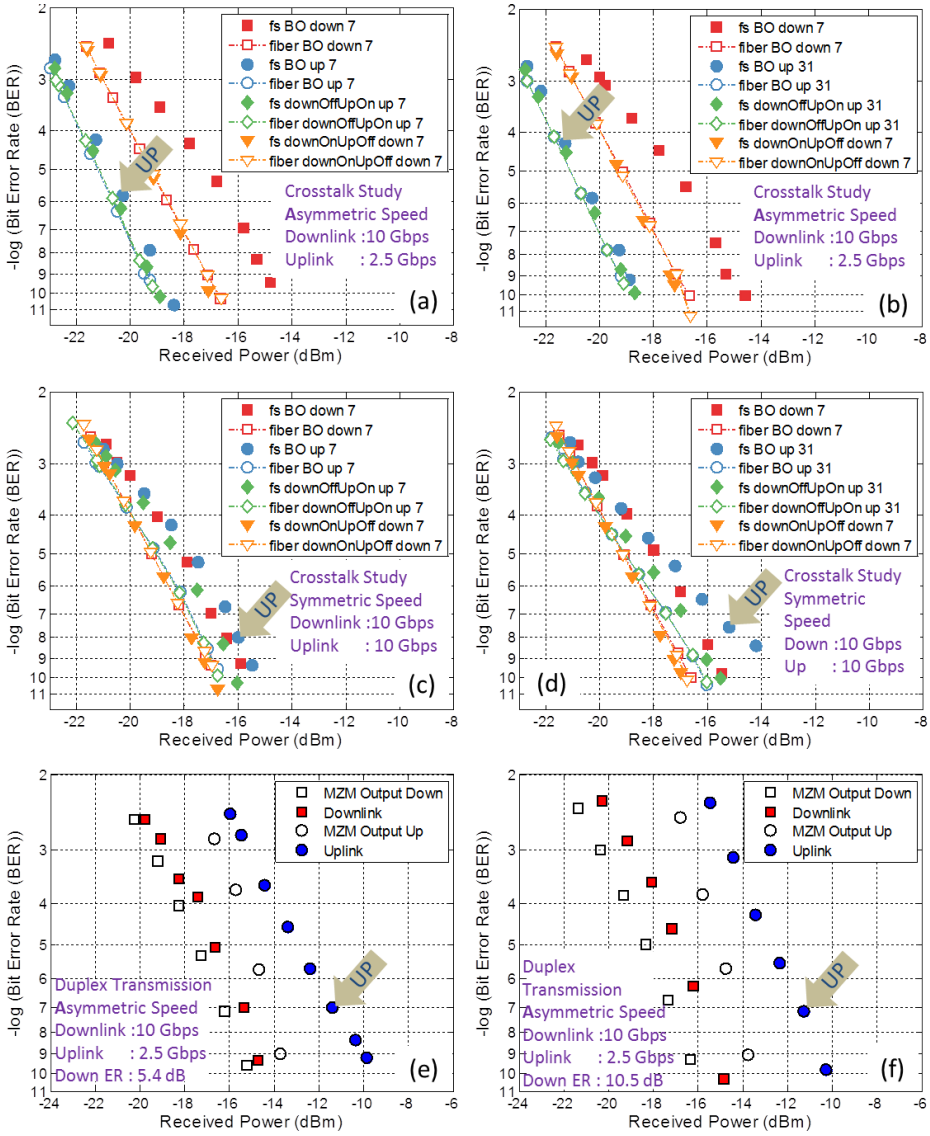

Figure 7.7: BER performances: (a) Asymmetric channels crosstalk PRBS 2^7-1 downlink and uplink, (b) Asymmetric channels crosstalk PRBS 2^7-1 downlink PRBS $2^{31}-1$ uplink, (c) Symmetric channels crosstalk PRBS 2^7-1 downlink and uplink, (d) Symmetric channels crosstalk PRBS 2^7-1 downlink PRBS $2^{31}-1$ uplink, (e) Asymmetric channels with wavelength re-use PRBS 2^7-1 downlink PRBS $2^{31}-1$ uplink with downlink ER = 5.4 dB, and (f) Asymmetric channels with wavelength re-use PRBS 2^7-1 downlink PRBS $2^{31}-1$ uplink with downlink ER = 10.5 dB. Both channels are transmitting (BO), free space (fs).

(2.5 Gbps uplink and 10 Gbps downlink) duplex transmissions. SMF transmission, in place of free space for the same configurations, is also performed for Back-to-Back (BtB) transmission measurements.

From the results in Figure 7.7, we observe that the crosstalk performance of asymmetric full-duplex channels (Figure 7.7(a) and Figure 7.7(b)) stays consistent whether PRBS 2^7-1 bits or $2^{31}-1$ bits is set for the uplink. However, the downlink suffers from a 2 dB penalty (in comparison to their corresponding BtB measurements) when both uplink and downlink are transmitted. On the other hand, we observe that for symmetric full-duplex channels (Figure 7.7(c) and Figure 7.7(d)), the power penalty is less than 2 dB for PRBS $2^7 - 1$ bits but when PRBS $2^{31} - 1$ bits is used, the uplink BER performance for symmetric duplex transmission tends towards the noise floor, giving a penalty of about 3 dB at BER of 1×10^{-9}. We observe that longer pattern length gives rise to a larger penalty for the symmetric transmission due to a more severe crosstalk effect. This trend could also be due to high pass response (note that no low pass filter is used in the experiment) and bias drift. Additional investigation in future work will be needed to determine the dominant cause(s). Crosstalk problems are commonly due to reflections at interfaces such as at the circulators, the fiber-pigtailed collimators, and the gratings. It has also been widely accepted that Rayleigh backscattering noise, which is due to the intrinsic property of the optical fiber, is a challenge in a full-duplex bi-directional single fiber system using the same wavelength [198, 199]. The reflected signals then add up and incur crosstalk and beat noise at the receiver. With reference to a similar experimental results reported by H. Y. Hsu et al. [196], the bi-directional point-to-point free-space transmission of 10 m distance results in a power penalty of less than 0.8 dB compared to BtB link with SMF and a penalty of only 0.2 dB compared to unidirectional transmission. The crosstalk penalty of 10 km full-duplex transmission in a single fiber using the same wavelength has also been analyzed in [200].

Figure 7.7(e) and Figure 7.7(f) show the transmission performance in the testbed of Figure 7.5 for asymmetric channels with 10 Gbps downlink and 2.5 Gbps uplink. The performances are consistent in both trials using downlink ER = 5.4 dB and ER = 10.5 dB. The downlink has a negligible penalty of < 1 dB but both uplink channels suffer from about 4 dB power penalty. This is mainly due to the non-ideal erasure of the signal in addition to the Amplified Spontaneous Emission (ASE) noise from the EDFAs and from the two-stage SOAs.

Figure 7.8 illustrates the results for symmetric channels of 10 Gbps. As the downlink channel has a smaller ER, the sensitivity of the downlink is worse than the uplink. However, it can be seen that the downlink sensitivity improves from -9 dBm to -12 dBm and -14 dBm as its ER is increased from 2.0 to 3.6 and 4.3 dB, respectively. Conversely, the performance of the uplink channel is compromised as expected due to less effective compression as the SOA is fed with a larger input signal. Moreover, a similar performance curve

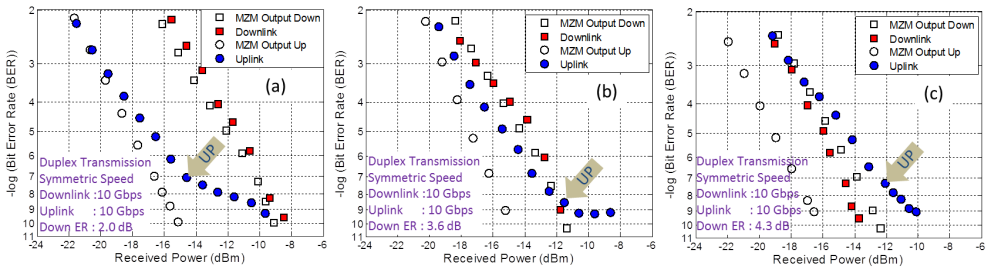

Figure 7.8: BER performance of symmetrical 10 Gbps full-duplex with wavelength re-use, PRBS $2^7 - 1$ for downlink and PRBS $2^{31} - 1$ uplink with initial downlink signal ER of (a) 2.0 dB, (b) 3.6 dB and (c) 4.3 dB.

as the crosstalk performance in Figure 7.7(d) is observed, nonetheless with additional effect contributed by the not-perfectly erased downlink signal [192]. We see here that there is a compromise between downstream and upstream performance in the bi-directional system, i.e. we need a large ER for good downlink performance, but a small ER for clean carrier recovery and good uplink performance.

7.5 Chapter conclusion

In summary, a novel full-duplex all-optical wireless system supporting symmetric 10 Gbps downlink and uplink channels with OOK-NRZ signaling has been demonstrated. The experiment is conducted over a free space distance of 3 m deploying an all-optical solution at $\lambda = 1550$ nm. The uplink is implemented using a carrier recovery and re-modulation technique enabled by erasing the downlink OOK signal by means of two cascaded SOAs operating in the saturation region. Error-free links with BER $< 1 \times 10^{-9}$ have been achieved for both downlink and uplink for a downlink signal ER of up to 4.3 dB.

The asymmetric full-duplex system has been demonstrated for 10 Gbps downlink and 2.5 Gbps uplink for a downlink signal ER of up to 10.5 dB. All channels attained a BER $< 1 \times 10^{-9}$. The concept is scalable to higher data rates by designing proper SOAs for data erasure or with the use of spectrum efficient amplitude modulation such as Discrete Multitone (DMT) as reported by K.A. Mekonnen et al. [201].

An alternative method to implement an all-optical duplex system is by using phase or frequency modulation for downlink and amplitude modulation for uplink. For e.g. in phase modulation such as binary phase shift keying (BPSK), only the phase changes while the amplitude stays the same. Subsequently, amplitude modulation can be used for the uplink in which no carrier erasure will be needed since amplitude modulation only affects the amplitude of the signal. Higher level phase shift keying (PSK) formats, such as Quadrature Phase-Shift Keying (QPSK)/4-PSK and 8-PSK, can be employed to increase

the data rate.

Chapter 8

Optics-assisted system and time-slotted transmission

Contents

8.1 Wide angle lens receiver

In Chapter 5, Chapter 6, and Chapter 7, we have presented measurements made with a fiber pigtailed collimator, Thorlabs TC18FC-1550 model, with a focal length of 18.36 mm and a full-angle divergence of 0.034°. The $1/e^2$ beam diameter is 3.33 mm at the focal plane. For further information on the lens collimator please refer to Section 4.1. The collimator has a very limited Field of View (FoV), i.e. 0.034° theoretically. The transmitter's narrow FoV results in very precise measurement with reduced path loss as narrow beams could better concentrate the optical power within a small area compared to a wide beam. The narrow FoV at the receiver would mean less background light is captured since the FoV is very small and accepts only near parallel beam. This also avoids multipath distortion from beams coming from angles

larger than can be received in the small FoV of the receiver. These results in less noise being captured, and thus, improve the Signal-to-Noise Ratio (SNR) of the signal. However, the alignment of such narrow FoV collimators is a tedious process and is definitely not feasible for practical implementation in a nomadic or mobile system due to the inherent long latency for alignment and user detection. Therefore, besides having a high coupling efficiency optical system, a wide angle optical receiver is desired.

An important factor in light coupling, which we should take into consideration, is the étendue, $\acute{\varepsilon}$, of the optical system [202]. Étendue denotes the geometrical extent or spread of light. It is a product of the effective emitting or receiving area (A_{eff}), and the solid angle (Ω). The fundamental principal of étendue is the conservation of energy, or the conservation of the number of rays, in an optical system [203], as shown in Figure 8.1. Étendue is conserved as light travels through optical systems where it undergoes perfect reflections or refractions. The étendue of light can only increase due to scattering, but can never decrease.

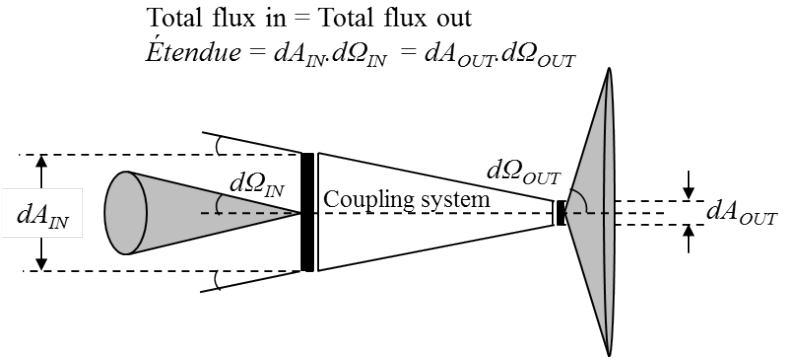

Figure 8.1: Conservation of étendue.

The étendue factor sets the fundamental limit for effective light coupling of the system. In order to get perfect coupling, the étendue of the emitter and receiver has to match. In an optical system, the component which has the lowest étendue sets the limit of the entire system. For example, light coming from a larger étendue source will only be partially accepted by the limiting component of the lowest étendue in the receiving optical system [204]. In the opposite case where the receiving optical system has a larger étendue than the source, almost all the light can be coupled into the optical system. The collected power or the radiant flux, F, is related to the étendue, $\acute{\varepsilon}$, and radiance, L^e, as the following:

$$\begin{aligned} L^e &= \frac{dF}{dA_{eff}.d\Omega} \\ dF &= L^e.dA_{eff}.d\Omega = L^e.d^2\acute{\varepsilon} \end{aligned} \tag{8.1}$$

where $dA_{eff}.d\Omega$ determines the étendue, $dA_{eff} = dA\cos\theta$ and $d\Omega = \sin\theta d\theta d\phi$. Radiance is the radiant flux of a given infinitesimal surface in an infinitesimal solid angle around a given direction, divided by the product of effective area and solid angle [205]. We see that, at a constant radiance, by having a larger étendue at the receiving optical system, more power can be collected.

In a free-space optical transmission system which employs a fiber coupling sub-system at the receiver, the sub-system is limited by the étendue of the fiber. The small diameter and numerical aperture of the optical fiber determines the étendue factor. The étendue factor for a fiber can be determined as follows [204, 206]:

$$d^2\acute{\varepsilon} = dA_{eff}.d\Omega \tag{8.2}$$

$$\acute{\varepsilon} = A\iint \cos\theta \sin\theta d\theta d\phi \tag{8.3}$$

$$= \pi A \sin^2\theta$$

where $\sin\theta$ is the angle corresponding to the numerical aperture of the fiber.

Whereas in a system which employs a photodetector together with an optical coupling sub-system with lenses and / or concentrators, the étendue is determined by the effective aperture (taking into consideration the aperture stop and field stop [205]) and the solid angle from which the light is accepted. The θ is then the angle corresponding to the angle of the half-field of view of the system.

Table 8.1: Comparison of étendue limits for SMF [207], MMF [208, 209, 210], and photodetector based receiver [210]. θ_{half}: Half-field of view angle, Ω: Solid angle, d: diameter, A_{eff}: Effective detection area, $\acute{\varepsilon}$: étendue, SI: Step-index, GI: Graded-index, SMF: Single mode fiber, MMF: Multimode fiber, PD: photodetector.

Component	θ_{half} [°]	Ω [sr]	d [μm]	A_{eff} [mm^2]	$\acute{\varepsilon}$ [mm^2.sr]
SMF 1060XP	8.05	6.19×10^{-2}	9.5 ± 0.5	7.09×10^{-5}	4.4×10^{-6}
SMF 980HP	11.54	0.13	6.8 ± 0.5	3.63×10^{-5}	4.6×10^{-6}
GI-MMF GIF625	15.96	0.24	62.5 ± 2.5	3.07×10^{-3}	7.3×10^{-4}
SI-MMF FP1000ERT	30	0.84	1000 ± 15	7.85×10^{-1}	6.2×10^{-1}
New Focus 12 GHz	80	5.19	25	4.91×10^{-4}	1.5×10^{-3}

Table 8.1 compares the étendue limit of two Single Mode Fibers (SMFs), two Multimode Fibers (MMFs) and a 12 GHz photodetector from Newport/New Focus. The fibers are selected such that they have a large numerical aperture and / or large effective detection area. We observe that a reasonably large étendue can be achieved by using a step-index MMF. The half-field of view is modest and can be improved using an optical sub-system to increase the field of view of the free-space receiver. However, the effective detection area

will have to be compromised due to the conservation of étendue. Another interesting component is the Newport/New Focus 12 GHz photodetector. The detection area is much smaller than that of the step-index MMF but it has the advantage of an inherently large field of view.

Consider also that for a photodetector of a higher bandwidth, BW, the junction capacitance, C_j [211] has to be decreased as in the following relation:

$$BW = \frac{1}{2\pi R_{Load} C_j} \tag{8.4}$$

where R_{Load} is the load resistance. In a transmission system, the load resistance is typically 50 Ω. Correspondingly, the area of the photodetector has to decrease to provide a lower capacitance as in the following relation:

$$C_j = \frac{\varepsilon_s A}{w} \tag{8.5}$$

where ε_s is the permittivity of the semiconductor material, A is the diffusion layer area / detection area and w is the depletion layer width which depends on the carrier transit time and the carrier drift velocity [211].

As seen in the relations explained above, a challenge in employing high speed receivers is the small photodetector area. We can increase the effective area and field of view, and consequently the effective étendue, for example by employing an array of photodetectors.

The following are some techniques used to improve the receiving angles of the optical receivers. The techniques using **(1) Compound parabolic concentrator** [145] and **(2) Angular magnifier in combination with an SLM** [149], as shown in Figure 8.2 and Figure 8.3, respectively, are not inherently wide angle as they are limited by the étendue of the fiber which limits the product of aperture and field of view. Both systems require tracking and alignment to achieve wide angle operation. In (1), the coupling system has to be adjusted to align the beam to the fiber and in (2), the Spatial Light Modulator (SLM) is used as the alignment adjustment.

Techniques **(3) Angle diversity receiver** [212] and **(4) Hemispherical lens** [213], as shown in Figure 8.4 and Figure 8.5, respectively, show photodetector based receivers which have a much larger field of view as their detection areas tend to be larger and their field of view is at least 90° theoretically.

Technique **(5) Fiber bundle arrays** is another way of increasing the effective étendue of the system by using a lens array and fiber bundle, together with an alignment process. Each bundle is placed at the focal distance behind each microlens in the array and each bundle is composed of multimode fibers. The microlens array is controlled using piezoelectric transducer to translate the lens array as a whole. The reported FFoV is approximately 20° [215]. The design of such a receiver is shown in Figure 8.6.

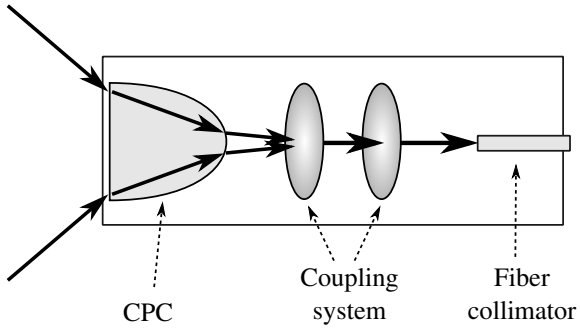

Figure 8.2: Free-space receiver using compound parabolic concentrator (CPC) with an FFoV of 90°, used together with coupling lenses [145].

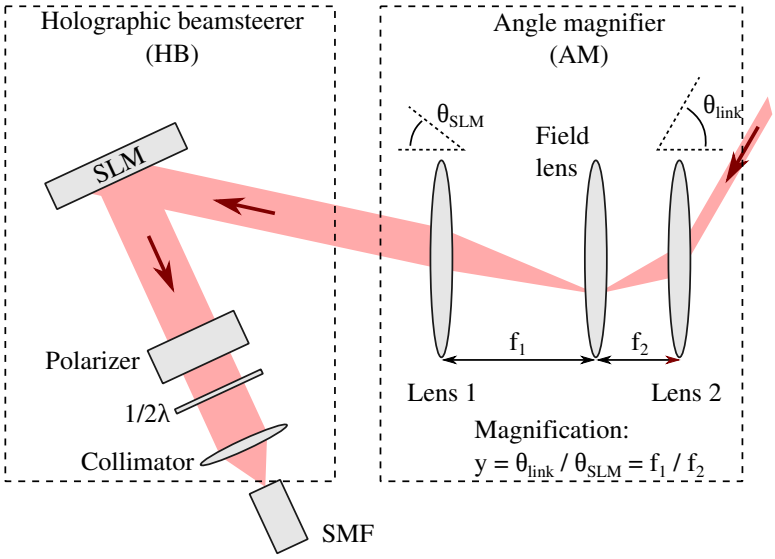

Figure 8.3: Receiver module which employed an angular magnifier in combination with a spatial light modulator to achieve up to 60° FFoV. The 'red arrow' shows the incoming beam from the access point. The beam then travels in the direction pointed by the red arrow towards the receiver through a lens collimating system and single mode fiber (SMF) [149].

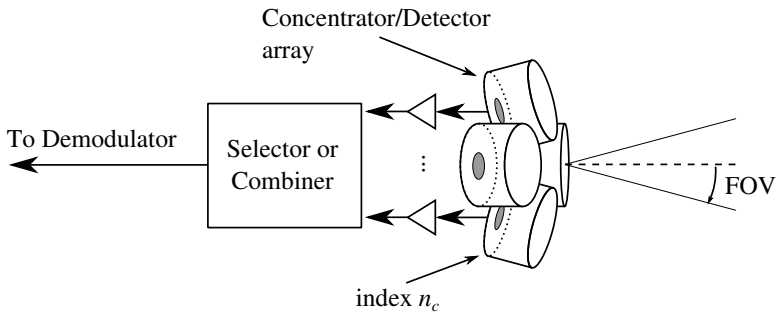

Figure 8.4: Angle diversity receiver with an array of four receiver elements ($8 \times 20°$ and $8 \times 31°$ configurations), in which each receiver optics consists of an optical filter, a concentrator and a photodetector [212].

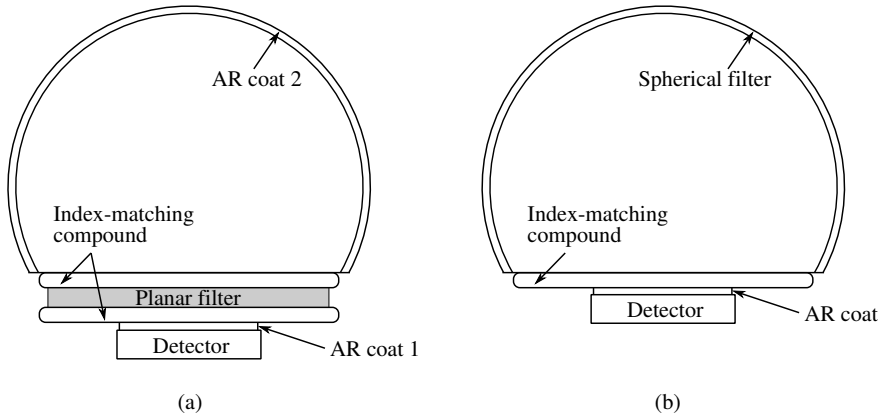

Figure 8.5: Receiver with hemispherical lens with: (a) a planar fillter and (b) a spherical filter, to reject ambient light [214]. This method has demonstrated an FFoV of up to 156° besides providing optical gain on a 1 cm^2 detection area [213].

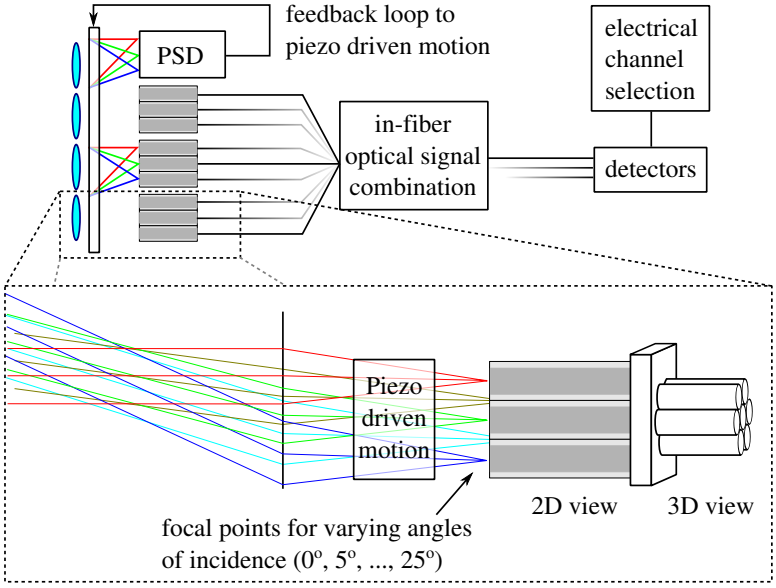

Figure 8.6: Conceptual design of lens array/fiber bundle wide field of view free-space receiver. A position sensing detector (PSD) provides a feedback to control the position of a microlens array such that an incident beam is always coupled into one fiber of a bundle behind the microlens array [215].

In this thesis a commercial ultra-wide angle lens, also known as the fish eye lens, of 180° meant for mobile phones is proposed. This is an existing clip-on lens which is commercially available in the market for mobile phones. Users can deploy it for communication in addition to the primary function of taking wide angle pictures.

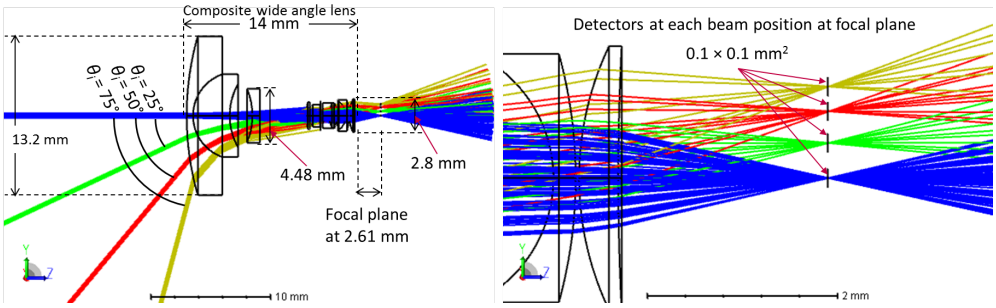

Figure 8.7: Principle of a wide angle lens. Simulation using a 200° ultra-wide angle lens / fisheye lens model from Zemax.

The advantage of using such a wide angle lens is its ability to provide a wide field of view by bending light into a small area, as shown in Figure 8.7. The figure shows the ability to achieve an FFoV of 200°. This lens model is an

existing wide angle lens model provided by Zemax, which can be found in the 'samples' folder provided by Zemax OpticStudio 16 software (Default directory *../MyDocuments/Zemax/Sample/Sequential/Objectives*). It is not in scale with the lens used in the experimental demonstration. The purpose the model is used is to show how the rays travel through a wide angle lens.

From Figure 8.7, we observe that a sufficiently large photodetector area, which can include an array of photodetectors, at the focal plane of the wide angle lens will be required. The figure shows that the lens, with dimensions shown in the picture, is able to couple light up to a half angle of 75° with a full photodetector diameter of about 2 mm. Assuming a 12 GHz photodetector [210] which has a diameter of 25 μm will be used, we will need 2 mm/25 μm $<$ 80 arrayed phtotodetectors (spacing between photodetectors are not included). This method could potentially allow a simple and low form-factor construction of receivers for mobile devices. Additionally, the arrayed photodetectors may allow simultaneous localization and tracking of a device by getting the information of the direction of the beam through the light intensity falling on the photodetector array. Another method of using the wide angle lens is by using an alignment system to align a fiber to the focused beam at the focal plane. This technique would be similar to the techniques shown in Figure 8.6.

8.1.1 Experimental setup to evaluate the fish-eye lens receiver

The lens used in the experimental demonstration is a fish eye lens of FFoV of 180° with a front lens diameter (where the beam strikes) of 2 cm and an aperture at the back of approximately 1.1 cm. In the testbed implemented here, due to the absence of an array or large surface detector for 10 Gigahertz (GHz), a collimator is aligned using the alignment robot introduced in Section 4.10 to capture each incoming beam. In a practical scenario, it would be ideal to have the final receiver device implemented with a large effective detector area.

The setup of the measurement testbed is shown in Figure 8.8. A tunable Laser Diode (LD) provides a beam with a wavelength of 1550 nm with an optical power of $<$ 9.5 dBm. The beam is transmitted to free space through a fiber-pigtailed collimator from Thorlabs (TC18FC-1550), which has a focal length of 18.36 mm, an opening aperture of 10 mm, and a full-angle divergence of 0.034°. The $1/e^2$ beam diameter is 3.33 mm at the focal plane. For further information on the lens collimator please refer to Chapter 4. The free-space beam travels over a distance of approximately 25 cm. The 3.33 mm free-space beam is collected using another fiber-pigtailed zoom collimator (from Thorlabs, product number ZC618FC-C, with a focal length between 6-18mm, and a numerical aperture of 0.25) to optimize the light collection. The measurement is repeated for each re-placement of the transmitter at different incidence angle. The 4-axis alignment robot is used to detect the beams falling on the detection plane. A photo of the setup is shown in Figure 8.9.

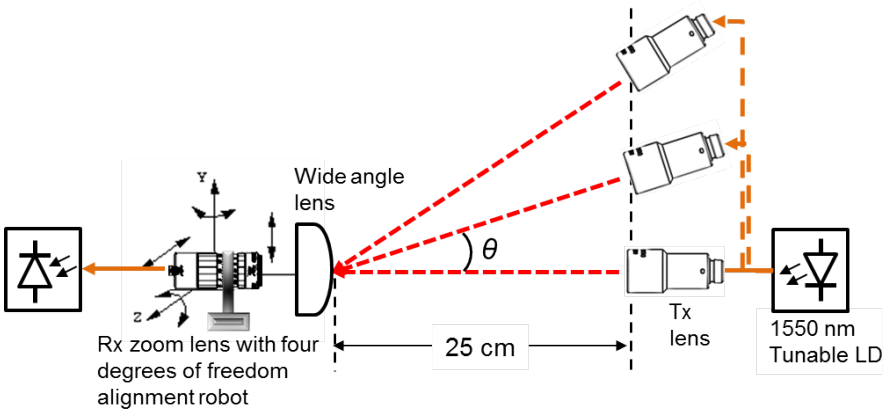

Figure 8.8: Measurement setup for wide angle receiver using commercial 180° fish eye lens.

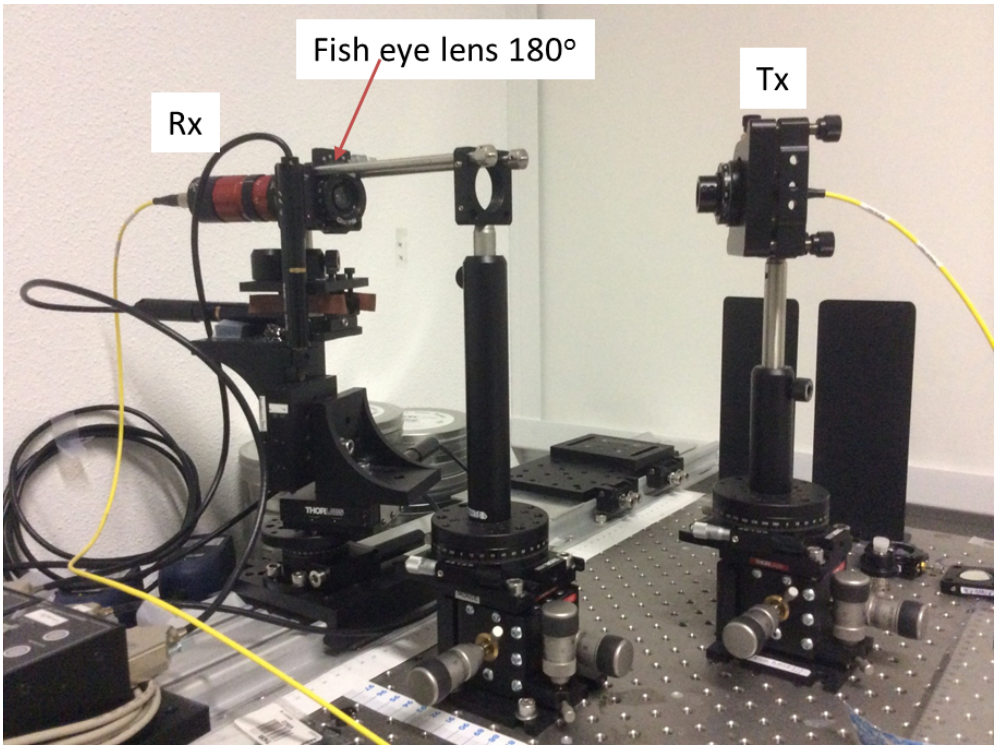

Figure 8.9: Photo of setup for wide angle receiver measurement.

8.1.2 Results and discussion

Figure 8.10 shows the measurement results as the angle of incidence of the beam is increasing. Observe that the Full Width Half Maximum (FWHM) of the curve is at approximately 40°, which corresponds to a FFoV of 80°. This FFoV is limited by the effective area of the collimator aperture.

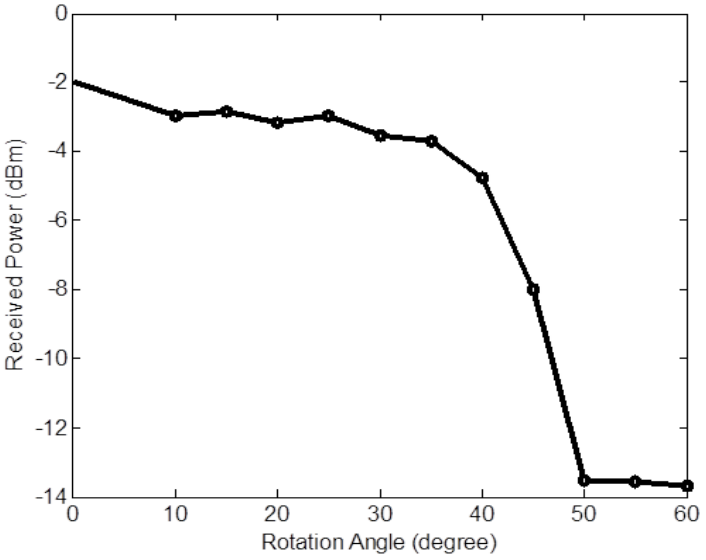

Figure 8.10: Measured coupled light at different incidence angle.

In summary, this is a very simple idea and technique using an existing commercially available lens. Other lenses which are available commercially for mobile phones can also be potential solutions for wide angle light coupling. The required effective photoreceiver aperture area and the appropriate beam size are interdependent. A large beam size will require a larger effective photoreceiver aperture area in order to guarantee adequate received optical power for data transmission. In a more advanced approach, receivers can be made from an array of photodetectors. Another alternative could be to use an array of micro mirrors to focus the beams into an array of fibers but this may result in a bulky construction [215].

A guide for the relation between the effective detector size needed versus the beam size has been reported in A.M.J. Koonen at al. [143]. The assumption was that the Pencil Radiating Antenna (PRA) covers an area of $L \times L$ with a 2D tabulation of spots with a beam diameter of D_{beam}, as shown in Figure 8.11. The number of scanning steps needed is, $N = (L/D_{beam})^2$. With a tuning range of $\Delta\lambda$, the tuning step size will be $\delta\lambda = \Delta\lambda/N = \Delta\lambda \times (D_{beam}/L)^2$. The lower bound for the beam diameter is given by $D_{beam} > L\sqrt{\delta\lambda_{min}/\Delta\lambda}$. The receiver aperture has a diameter of D_{rx} and the PRA is fixed in the middle of the ceiling of height, H. We assume that the intensity of the beam falling

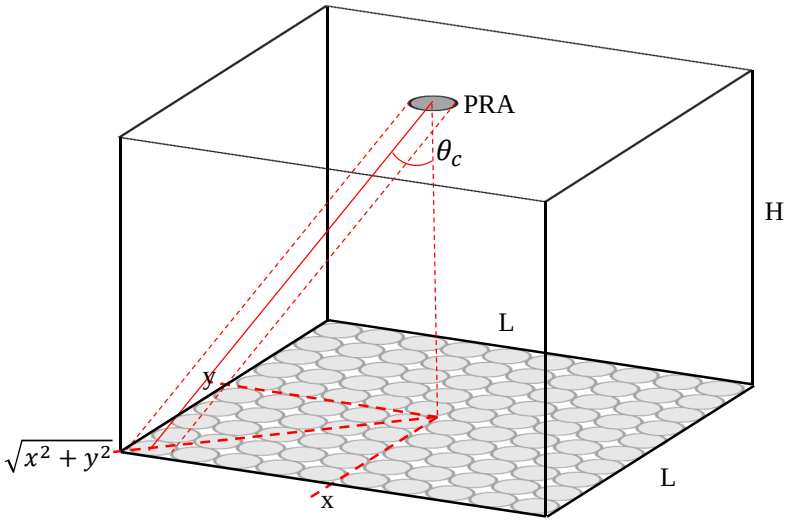

Figure 8.11: Scanning of a room with optical beams.

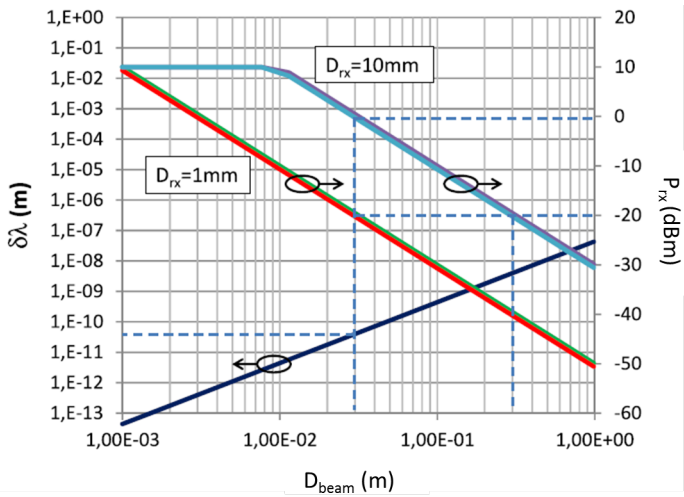

Figure 8.12: Corresponding beam diameter, D_{beam}, due to tuning step, $\delta\lambda$ and effective photoreceiver aperture diameter, D_{rx}, to yield the corresponding received optical power, P_{rx} [143].

across the receiver diameter is uniform, and the minimum power received in the elliptical spot in the corner of the room is given by:

$$P_{rx_min} = P_{beam} \cos\theta_c \frac{A_{rx}}{A_{spot}} = \frac{P_{beam}(\frac{D_{rx}}{D_{beam}})^2}{1 + \frac{L^2}{2H^2}} \tag{8.6}$$

which implicitly sets the upper bound to the beam diameter in order to guarantee an adequate minimum received power level. It is assumed here that the received power is not restricted by the field of view of the receiver. This approximation holds when the received light is incident directly on the active area of the photodetector. Intermediate optics such as a Compound Parabolic Concentrator (CPC) or condensor lens may yield a larger effective detection area, D_{rx} but due to the conservation of étendue, also restrict the field of view.

Figure 8.12 shows how D_{beam} can be determined with the corresponding tuning step size and minimum receiver sensitivity. The calculation was made for a coverage area of 1.5×1.5 m^2, a height 2.5 m between the access point and the user terminal, a free-space beam power P_{beam} of 10 mW (10 dBm) and an effective receiver aperture diameter, D_{rx} of 1 mm or D_{rx} of 10 mm [143]. As we can see from Figure 8.12, a photoreceiver aperture area of 10 mm can couple adequate received optical power of -20 dBm for data transmission of near error-free 10 Gbps On-Off-Keying (OOK)-Non-Return-to-Zero (NRZ) signal from a beam with a diameter of 30 cm.

In our line-by-line 2D scanning techniques, $M = L/D_{beam}$ lines need to be scanned to completely cover an area of $L \times L$. Each line corresponds to passing through one Free Spectral Range (FSR) of the highly dispersive grating.

8.2 Angular magnification

In Section 3.2, it is shown that a cascaded gratings solution has a 2D steering angle limitation of approximately $6° \times 26°$. Here, an angular magnification method by employing the reverse telescope construction is proposed to further increase the angular coverage. The theoretical construction of the reverse telescope configuration has been discussed in Section 4.7.

A photo of the 2D steering module integrated with an angular magnifier is shown in Figure 8.13. The angular magnifier is constructed using two lenses configured as shown in Figure 8.14. The first lens in the simulation is Thorlabs ACL7560 aspheric condenser lens with a 60 mm Effective Focal Length (EFL) and a 40.3 mm Back Focal Length (BFL), a diameter of 75 mm, and a numerical aperture of 0.61. The second lens is an Edmund Optics 67252 lens with 15 mm EFL and 8.42 mm BFL, and a diameter of 25 mm.

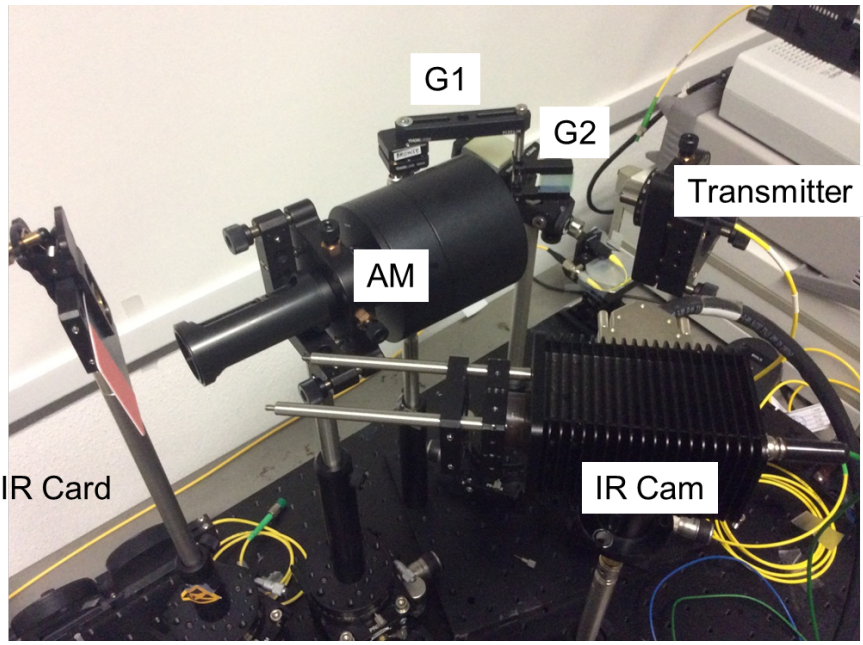

Figure 8.13: Photo of setup configuration with angular magnification. IR: Infrared, IR Cam: Infrared Camera, AM: Angle Magnifier, G1: Grating 1, G2: Grating 2.

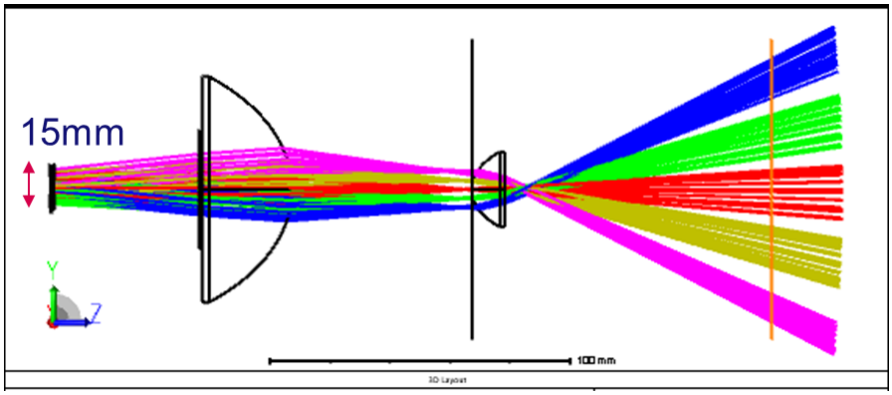

Figure 8.14: Angular magnification using two aspheres.

Aspheric lenses were chosen due to their small f-number. f-number typically is defined as the ratio of the focal length, f, of a lens to the diameter, D, of the lens, as below:

$$\text{f-number} = \frac{f}{D} \tag{8.7}$$

The larger the diameter of a lens, the more light can be collected in the system. The main reason aspheric lenses are chosen is due to the need for a small (as small as possible preferably < 1) f-number lens especially for the second lens. Firstly, we want the second lens to have a focal length as short as possible in order to have a high magnification factor and also a small receiver size. As we see in Equation 4.12, the angular magnification factor, M is equal to f_1/f_2. Therefore, a shorter focal length for the second lens, f_2 would give a higher angular magnification factor. Although we want the focal length to be as small as possible, we also want a large lens diameter. This is so that we can capture a beam at as large an angle as possible. This scenario is illustrated in Figure 8.15. In this figure, the angular magnification factor is 2.5, with Lens 1 having a focal length 2.5 times that of the focal length of Lens 2. Observe also the limitation of the second lens to capture the Ray 2 of angle θ_2.

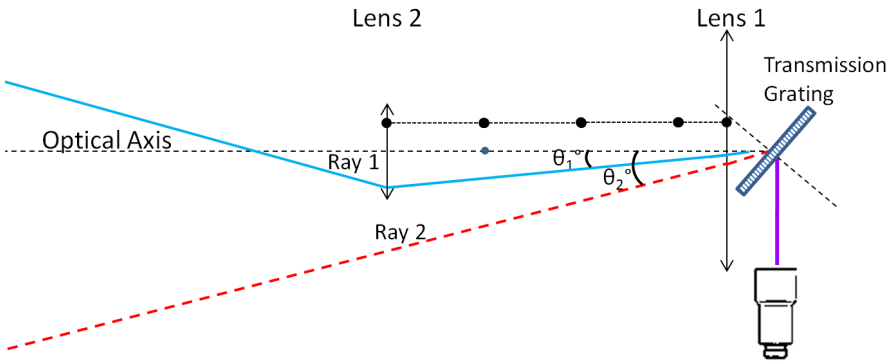

Figure 8.15: Angular magnification ray diagram. Input beam from lens collimator is diffracted into two components, Ray 1 and Ray 2 (emulating different wavelengths). Lens 1 has a focal length, f_1, 2.5 times larger than the focal length of Lens 2, f_2, therefore, M = $f_1/f2 = 2.5$. Ray 2 fails to pass through Lens 2.

In the proof-of-concept experimental demonstration, we employed two lenses from Thorlabs. The first being Thorlabs ACL7560 aspheric condenser lens and the second is Thorlabs LA1805C plano-convex lens with 29.9 mm EFL and 24.2 mm BFL. These lenses are selected due to their availability in the laboratory. By using Equation 4.12, the achieved angular magnification factor, M is equal to $f_1/f_2 = 60/29.9 \approx 2\times$.

8.2.1 Experimental setup to evaluate angular magnification in the system

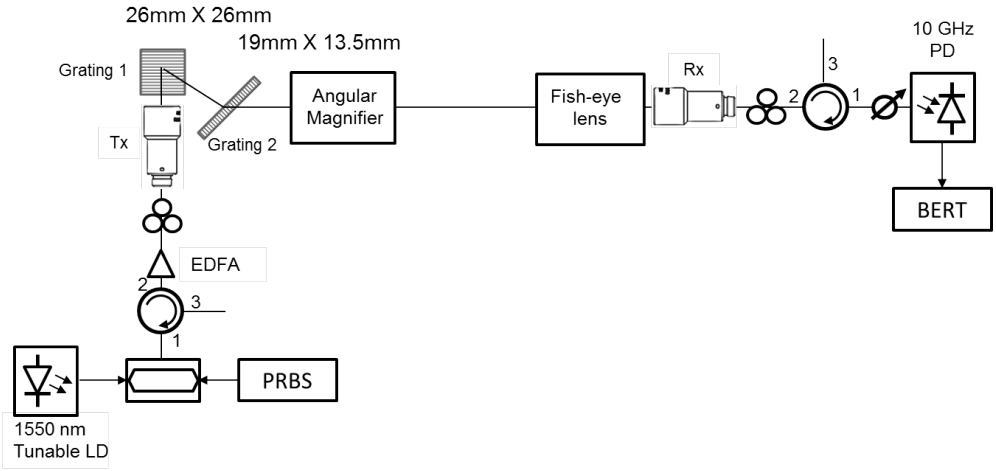

Figure 8.16: Testbed setup with angle magnifier and fish-eye lens. Grating 1 is a reflection grating with a blaze angle of 80.7° and 13.33 grooves/mm (Newport 53004BK06-182E). Grating 2 is a transmission grating with an incidence angle of 49.9° and 1000 grooves/mm (Ibsen PING-sample-083). LD: laser diode, EDFA: Erbium-doped Fiber Amplifier, PD: Photodetector, BERT: Bit Error Rate Tester.

A testbed for the experimental demonstration of the 2D beam steering system employing the angular magnifier and wide angle receiver is shown in Figure 8.16. A compact tunable laser source model 81960A from Keysight Technologies, which is an external cavity laser which has a wavelength tuning range from 1505 nm to 1630 nm and a capability to tune up to 200 nm/s, is used to provide the optical carrier which is then modulated with OOK-NRZ data with Pseudo Random Binary Sequence (PRBS) of $2^{31} - 1$ bits. An Erbium-Doped Fiber Amplifier (EDFA) is used to adjust the optical power to < 9.5 dBm. The beam is transmitted to free space through fiber-pigtailed triplet collimator (Thorlabs TC18FC-1550 model, with a focal length of 18.36 mm, an opening aperture of 10 mm, and a full-angle divergence of 0.034°. The $1/e^2$ beam diameter is 3.33 mm at the focal plane. For further information on the lens collimator please refer to Chapter 4.). The 2D beam-steering module is constructed by cascading a reflection grating with a blaze angle of 80.7° and 13.33 grooves/mm (Newport 53004BK06-182E), and a transmission grating with an incidence angle of 49.9° and 1000 grooves/mm (Ibsen PING-sample-083) (see Section 3.3 for more details). The angular magnifier has a magnification factor of 2, as calculated previously in Section 8.2. The beam is then sent to towards the 180° fish eye lens with a front lens diameter (where the beam strikes) of 2 cm and an aperture at the back of approximately 1.1 cm (see Section 8.1) and the

beam focused behind the fish-eye lens is captured by the fiber-pigtailed zoom lens. A zoom lens is used so that the focal length of the lens can be changed, shorter focal length for a more divergent beam and wider acceptance angle, without changing discrete collimator itself. This helps to maintain the alignment of the system besides having to purchase multiple collimators of different focal length. For example, a similar triplet collimator (TC06FC-1550) with a focal length of 6.18 mm at alignment wavelength of 1550 nm has a full-angle divergence of 0.101° compared to the introduced triplet collimator TC18FC-1550 model with a focal length of 18.36 mm at alignment wavelength of 1550 nm with only a full-angle divergence of 0.034° [163]. The optical beam is then captured by the 10 GHz SMF photoreceiver from Discovery Semiconductors, Inc [216], Part number DSC-R402AC-39-FC/UPC-K-2, and sent to the Bit Error Rate Tester (BERT). The measurement was repeated for three different wavelengths, i.e. 1518 nm, 1550 nm and 1583 nm.

8.2.2 Results and discussion

The measured performance of the free-space channels with wavelengths of 1518 nm, 1550 nm and 1583 nm is plotted against their corresponding fiber Back-to-Back (BtB) performance, as shown in Figure 8.17. We see that nearly error-free 10 Gbps channels with Bit Error Rate (BER) $\leq 1 \times 10^{-9}$ are successfully obtained with less than 1 dB penalty between the free space and BtB channels.

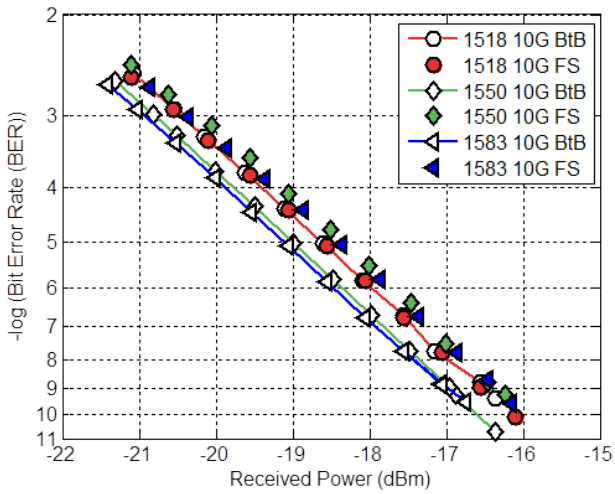

Figure 8.17: Channel performance at 10 Gbps with OOK-NRZ signaling at wavelengths λ = 1518 nm, 1550 nm and 1583 nm. BtB: Back-to-back, FS: Free Space.

The spectral bandwidth of the system as shown in Figure 8.18(b) is compared to Figure 8.18(a) which is the spectral bandwidth of the previous system

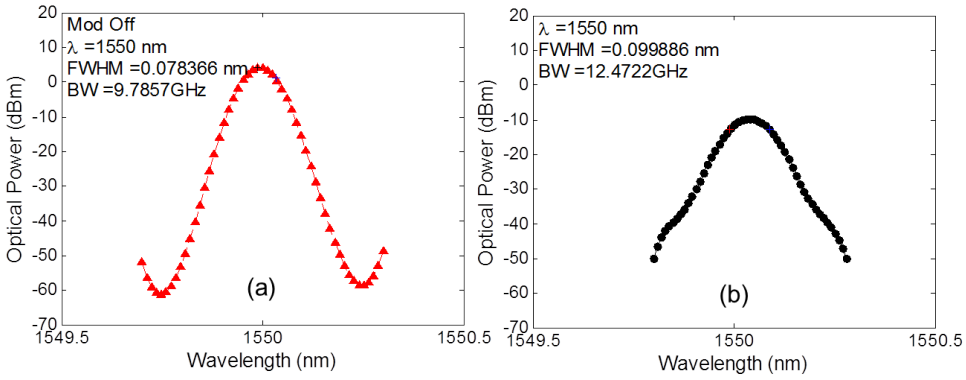

Figure 8.18: Measured spectral bandwidth for (a) Setup without angular magnification and fish-eye lens (see testbed setup for Module 2 in Section 6.2); (b) Setup with angular magnification and fish-eye lens (Figure 8.16). FWHM: Full Width at Half Maximum, BW: Bandwidth.

which was not equipped with angular magnifier and wide angle lens. We see that the -3 dB bandwidth is 12.47 GHz, which is larger compared to the previous setup with only 9.79 GHz. This is contributed largely by the larger aperture of the wide angle lens which is approximately 2 cm.

By tuning the wavelength of the tunable laser, Figure 8.19 shows the measured continuous tabulation of the system which is without angular magnifier (see testbed setup for Module 2 in Section 6.2), and Figure 8.20 shows the measured tabulation of the current system which consists of the angular magnifier. These measurements are made at 5 - 10 cm in order to capture all the beams. The field-of-view of the camera is not large enough to captured all the beams at 2 m distance. At the actual two meter distance, these spots of 3.33 mm from the fiber-pigtailed triplet collimator (Thorlabs TC18FC-1550), will be spaced far apart. Without the angular magnifier, the spots are spaced according to the tangent of the diffraction angle. When an angular magnifier is employed, the diffraction angles are doubled with a magnification factor of two. Therefore, as the distance increases from 5 cm to 2 m, the diffracted spots spread apart from each other increasingly. The coverage of the area at 2 m can be improved by using larger parallel beam spot size or divergent beams as will be discussed in Subsection 10.2.5.

When measured at this distance of 5 - 10 cm, we can see that the scanning lines are twice further apart by using the M = 2× angle magnifier in Figure 8.20 compared to without angle magnifier as seen in Figure 8.19. The spot size in Figure 8.20 are in general smaller compared to Figure 8.19, in which we expect twice smaller. We also observe a few missing spots. This is due to human error as this measurement was done manually by first tuning the laser and then capturing the image on a computer on the other end. In this case,

the laser wavelength was not changed before capturing the next image on the computer.

Figure 8.21 shows a photo of the 2D steered lines from an input beam originated from the Amplified Spontaneous Emission (ASE) noise contributed by cascaded Semiconductor Optical Amplifiers (SOAs). As the spectrum of an SOA is continuous, we can see the continuous lines on the screen placed at approximately 5 - 10 cm after the angular magnification module.

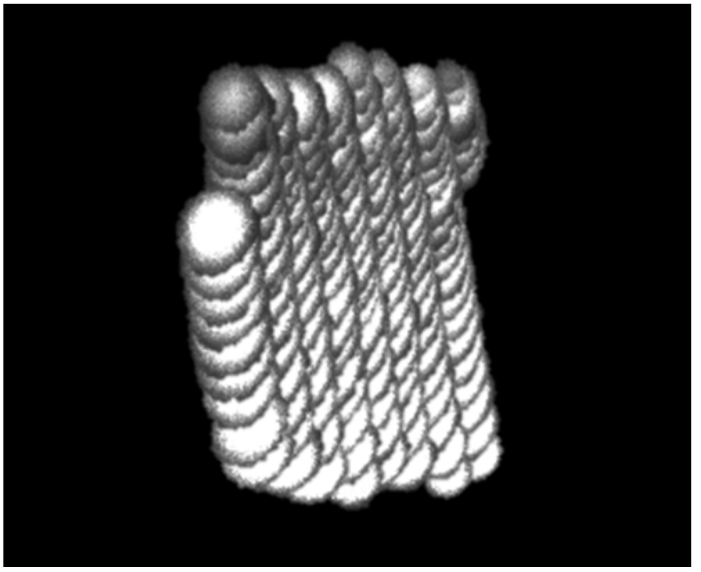

Figure 8.19: Photo of a 2D tabulation of diffracted spots at approximately 5-10 cm after the steering module. The steering module is constructed by cascading a reflection grating with a blaze angle of 80.7° and 13.33 grooves/mm (Newport 53004BK06-182E), and a transmission grating with an incidence angle of 49.9° and 1000 grooves/mm (Ibsen PING-sample-083).

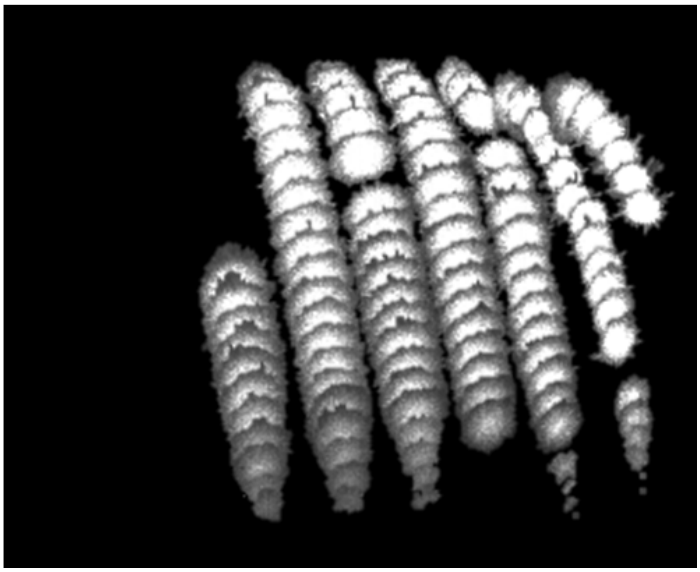

Figure 8.20: Photo of a 2D tabulation of diffracted spots after 2× angular magnification with screen position at approximately 5-10 cm after the magnification module. The magnification module is placed after the steering module, which is constructed by cascading a reflection grating with a blaze angle of 80.7° and 13.33 grooves/mm (Newport 53004BK06-182E), and a transmission grating with an incidence angle of 49.9° and 1000 grooves/mm (Ibsen PING-sample-083). Some spots are missing due to human error during the process of capturing the images of the spots. In this case, the laser wavelength was not changed before capturing the next image on the computer or the same image was saved for a neighboring wavelength.

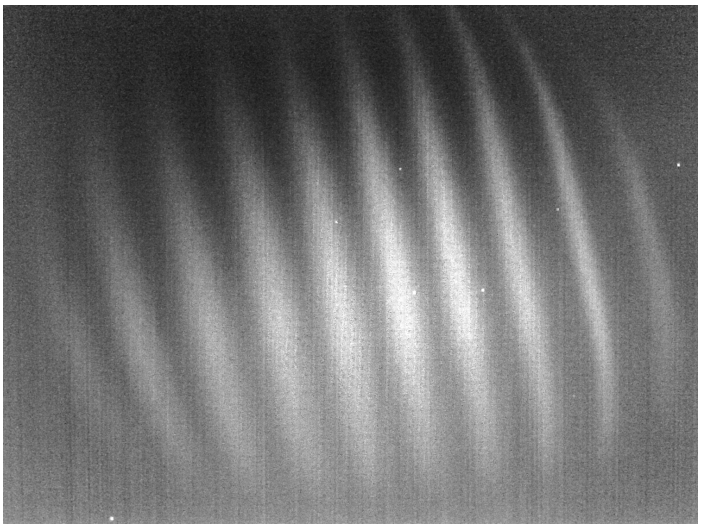

Figure 8.21: Photo of steering lines from 2D steering module with ASE spectrum from cascaded SOAs. Screen position is at approximately 5-10 cm after the magnification module.

8.3 Time-slotted transmission

For cost-efficient in-building networks, it is important that the resources needed are minimized and their usage is maximized in order to optimize the cost, link performance and energy usage of the system. Time-slotted indoor transmission is feasible with Optical Wireless Communication (OWC) since most services require less bandwidth than can be delivered. Thus, this thesis proposes a low-cost yet high performance reconfigurable 2D beam-steered OWC system with resource sharing. This work has been reported in C.W. Oh et al. in 2015 [75].

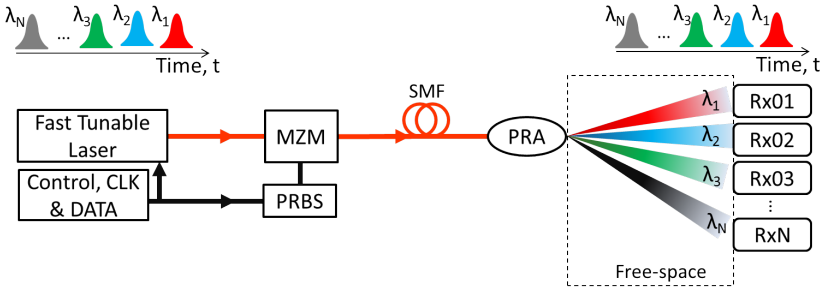

Figure 8.22: The concept of time-sharing a fast tunable laser.

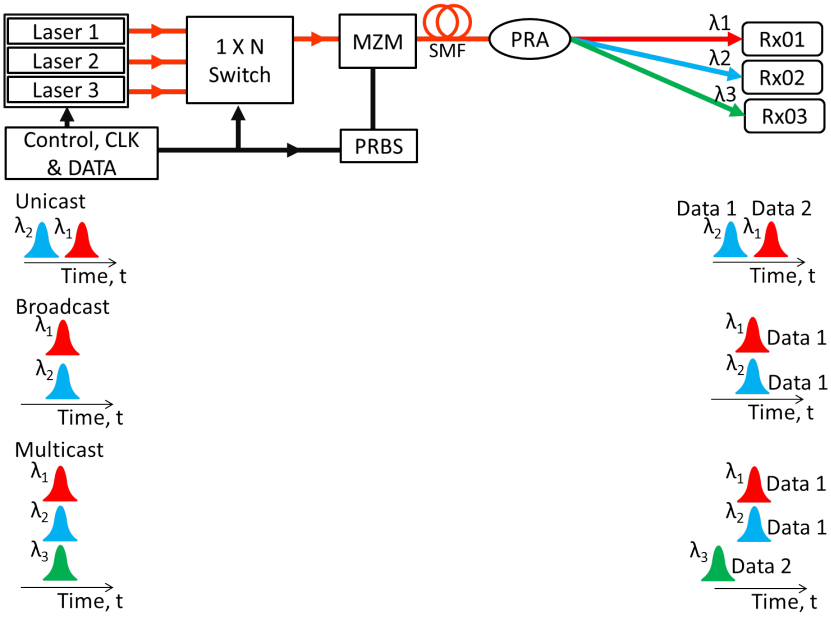

Figure 8.23: Optical wireless system architecture with unicasting, broadcasting and multicasting schemes.

In the proposed concept of using narrow optical pencil beams, which are 2D beam-steered by passive diffractive devices and simple wavelength tuning, we can share the tunable laser diodes by applying fast switchable wavelength tuning and thus sharing a laser diode among a number of beams. Depending on the number of lasers used, three different supported modes of operation, i.e. unicasting, multicasting and broadcasting, can be implemented.

In order to provide wavelength re-configurability, a fast switchable tunable laser is employed. As the capacity of each Line-of-Sight (LoS) optical link can be enormous, time-sharing of the tunable laser, as illustrated in Figure 8.22, is proposed. In addition, time-slotted transmission allows dynamic resource allocation according to the capacity required by the wireless devices. Finally, the laser sources, together with a crossbar switch [217] and the passive gratings (at the PRA), easily enable unicasting, broadcasting and multicasting schemes, as shown in Figure 8.23.

8.3.1 Experimental setup for time-slotted transmission

The schemes for unicasting and broadcasting have been constructed in an experimental testbed, as shown in Figure 8.24. In this experiment, a tunable laser is emulated by utilizing two Distributed Feedback Laser (DFB) lasers and a 2-by-2 Mach-Zehnder Interferometer (MZI) switch, where a switching speed of 1 ns is attainable. This way, the switching of wavelengths as well as the concept and feasibility for broadcasting can be demonstrated. Laser 1 is set to 1549 nm at input port 1 of the switch and laser 2 is set to 1550 nm at input port 2. The optical power of each lasers is set to 10 dBm. An Mach-Zehnder Modulator (MZM) modulator of 10 Gigabit per second (Gbps) is used to modulate an OOK-NRZ PRBS pattern of length $2^{31}-1$. An EDFA is placed after the MZM to amplify the optical power to approximately 8 dBm, which is within the eye-safety limit, for free-space transmission. The data signal is then sent to the (a) BtB link made up of a 2 m long SMF fiber (b) free space with 2D optical beam-steering.

For the free-space setup, the data signal is transmitted to free space using a collimator from Thorlabs (TC18FC-1550). The data signal is then directed accordingly to the receiving collimator's positions depending on the wavelengths emitted by the PRA, which consists of a pair of cascaded reflection gratings. The first reflection grating has a blaze angle of 63° and 31.6 grooves/mm (Thorlabs GE2550-0363), and the second reflection grating has a blaze angle of 75° and 79 grooves/mm (Thorlabs GE2550-0875) (see Section 3.2 for more details). The coupled data beam is then sent to the receiver and analyzed by observing the eye-diagrams via the oscilloscope and the BER via the BERT.

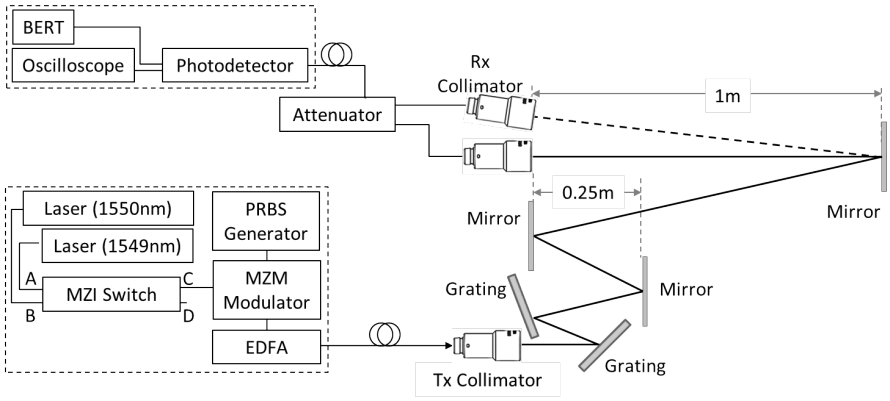

Figure 8.24: Experimental setup for a time-slotted optical wireless transmission with 2D beam-steering.

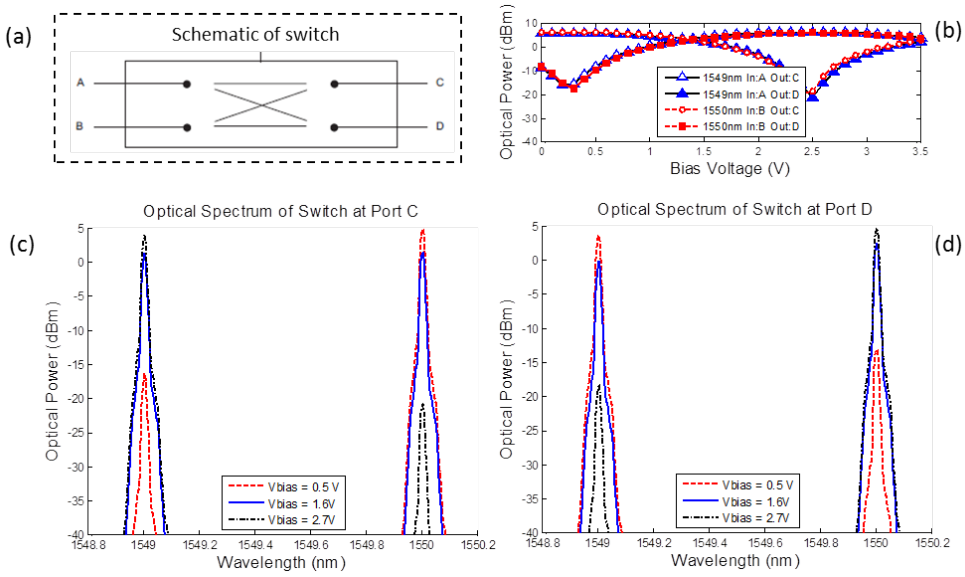

Figure 8.25: Switch characterization with input ports A and B, and output ports C and D.

8.3.2 Results and Discussion

The schematic of the MZI switch and the optical output behavior at port C and port D of the 2-by-2 MZI switch, as the bias voltage is varied, is shown in Figures 8.25(a-b). The three points of operation have been identified from the switch characterization, as shown in Figures 8.25(b-d). The first is when the switch is biased near 0.5 V and at approximately 2.5 V. At these two biases, the input at port B (1550 nm) and the input at port A (1549 nm) is routed to output port C, respectively. Unicasting can be realized at these biases. For multicasting or broadcasting, the bias of the switch can be set at approximately 1.5 V such that both input wavelengths are selected and transmitted at 50% to the PRA.

As the switch and modulator contribute optical power losses of up to 5 dB and 8 dB respectively, an EDFA is added to the output of the modulator to keep the free-space transmission power to approximately at 18 dBm. The crossed gratings contribute at max 15 dB of optical power loss collectively. The BER performance for BtB measurement and for the free-space transmission is shown in Figure 8.26. Both systems show a consistently good performance. The power penalty of the free-space transmission compared to BtB is negligible, i.e. less than 1 dB. The corresponding eye-diagrams are shown in Figure 8.27. The eyes are open with negligible distortions observed.

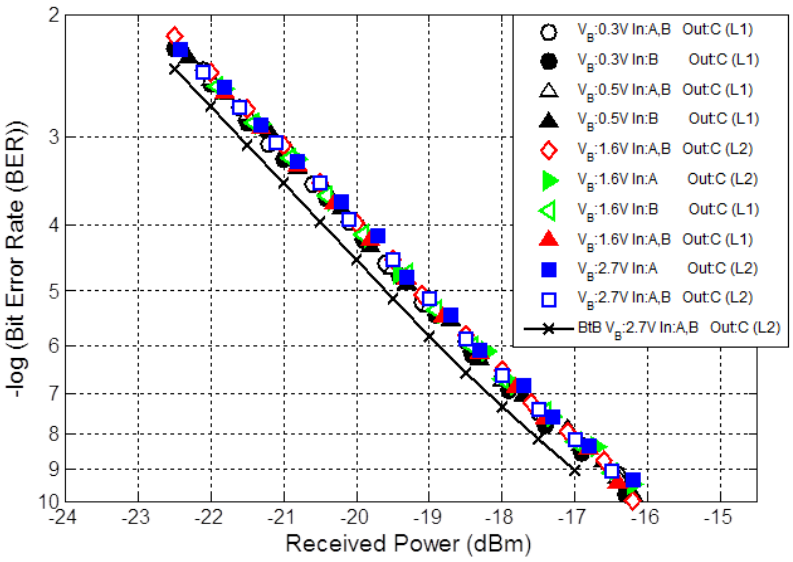

Figure 8.26: Free-space OOK-NRZ performance with 2D beam-steering and time-slotted transmission with input ports A and B, and output ports C and D. L1: Laser 1 (1549 nm), L2: Laser 2 (1550 nm).

On estimating the steering speed of a continuously tunable laser, the tun-

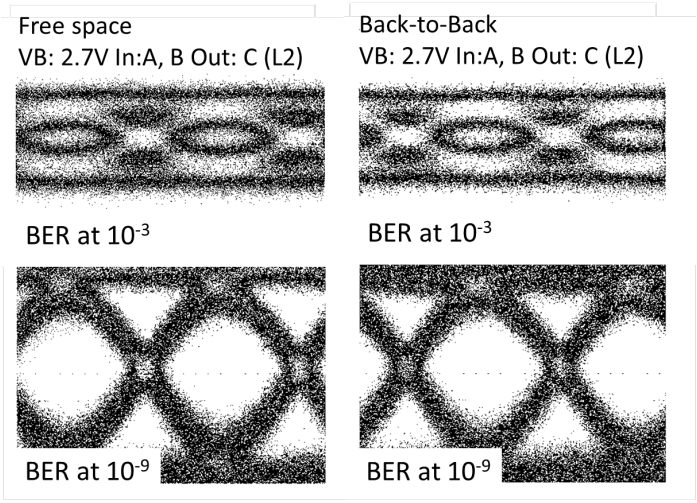

Figure 8.27: Eye-diagrams of 10 Gbps links with input ports A and B, and output ports C and D. L1: Laser 1 (1549 nm), L2: Laser 2 (1550 nm).

able laser employed in this thesis, which is a Keysight model 81960A with a tuning range from 1505 nm to 1630 nm, has been evaluated. This laser has a continuous tuning speed, ν, of up to 200 nm/s. The effective transmission bitrate depends on the total transmission bits, b, the buffer time (guard time needed during laser tuning), $\frac{\Delta\lambda}{\nu}$ where $\Delta\lambda$ is the change in wavelength and ν is the speed of continuous laser tuning within the $\Delta\lambda$ range, and data transmission time, $\frac{n_s}{D}$ where n_s is the number of symbols and D is the baud rate of transmission in symbols/s.

The total transmission bits is:

$$b = n_{b/s} \times n_s \tag{8.8}$$

where $n_{b/s}$ is the number of bits per symbol and n_s is the number of symbols.

Therefore, the capacity of the channel due to laser tuning time and the data transmission time, can be calculated by:

$$C = \frac{b}{\frac{\Delta\lambda}{\nu} + \frac{n_s}{D}} = \frac{n_{b/s}.n_s}{\frac{\Delta\lambda}{\nu} + \frac{n_s}{D}} \tag{8.9}$$

where C is the maximum achievable data rate, b is the number of transmission bits, $\Delta\lambda$ is the change in wavelength, ν is the laser tuning speed, n_s is the number of symbols and D is the baud rate of transmission in symbols/s.

Figure 8.28 shows the achievable capacity at different tuning speeds, with different transmission and buffer time, and a baud rate of 10 Gigabaud (GBaud).

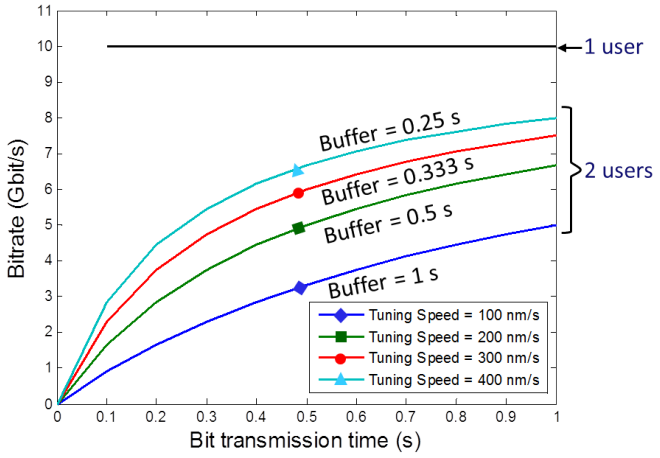

Figure 8.28: Laser tuning delay calculated for two users at different laser tuning speeds at a clock frequency of 10 GHz and $\Delta\lambda = 100$ nm and ν, of up to 200 nm/s.

The wavelength difference, is set to $\Delta\lambda = 100$ nm. Total transmission bits can be obtained by multiplying the number of symbols, n_s, with the number of bits per symbol, $n_{b/s}$.

In summary, time-slotted transmission with fast switchable tunable laser(s) enables time-sharing of resources among users and is a viable method to lower the system cost for high-performance indoor OWC networks. On top of that, this system can be configured to support dynamic resource allocation according to the capacity required. Also, unicasting, broadcasting and multicasting schemes can be implemented. Such a scheme has been emulated in an experimental testbed for 10 Gbps with OOK-NRZ signal over 2.5 m. The results showed good performance, and therefore, the feasibility of implementing the proposed time-sharing system for in-building optical wireless networks. Fast laser tuning is required in order to reduce idle time and thus to maximize data throughput.

8.4 Chapter conclusion

This chapter started with the discussion of methods to improve the field-of-view of the free-space receiver. As discussed, a large area photodetector composed of a large array of photodetectors with low capacitance would be the ideal solution. Typically at high data rates, the area of the photodetector needs to be smaller for adequate bandwidth and low capacitance. Therefore, this thesis proposes the use of a commercially available wide angle lens with the assumption that a wide effective area of photodetectors will be available. A large array of photodetectors or potentially a large array of MMF could also

be employed but these will require alignment process. In this thesis work, a fiber-pigtailed coupling lens is used to focus the collected beam from the fish-eye lens at the back of the lens, into an SMF. With this method, up to 80° FFoV was achieved.

The next section presented the angular magnification technique using a reverse-telescope configuration in which an angular magnification of 2× was demonstrated in a testbed. By employing the angle magnifier together with the fish-eye lens at the receiver side, up to 10 Gbps using OOK-NRZ signaling was achieve at a near error-free BER of 1×10^{-9}. Photos of 2D steering modules in a system without angular magnification and another with angular magnification was also shown.

This chapter concludes with Section 8.3, in which the time-sharing approach which can support unicasting, multicasting and broadcasting implementations, were introduced and demonstrated. By sharing tunable laser resources in a time-slotted way, system costs can be lowered, at the expense of somewhat reduced data throughput (in which the number of fast tunable lasers can be minimized).

Chapter 9

2D beam steering with arrayed waveguide grating

Contents

This chapter is meant as a supplementary chapter to report the progress of IR-OWC related work in our group. The 2D beam-steering setup which will be described in this short chapter employs an Arrayed Waveguide Grating (AWGr), which was designed by Prof. A.M.J. Koonen and evaluated by Dr. A. M. Khalid [218]. This work has been introduced and reported in [218, 219].

9.1 High port count arrayed waveguide grating steering concept

This is a straightforward approach to implement 2D passive beam steering, i.e. by employing a simple 2D arrangement of the fiber outputs of an arrayed waveguide grating module. The advantages of this method include its construction simplicity, its potentially larger coverage area and that it is passive. The 2D fiber array design determines the coverage of the area while the AWGr provides the output ports which carry different wavelength channels to each of the ports of the 2D fiber array.

The theoretical principle is illustrated in Figure 9.1(a). An optical lens with a focal length, f, is placed in front of the 2D array of fibers. The fibers are displaced by an amount $\Delta x = x_n - x_{n-1}$. The spot size, D_o, at the image plane

of length, L, is determined by using $D_o = 2f \tan\alpha$, with α being the half-angle divergence of the Gaussian beam out of the fiber. The distance between adjacent spots is determined using $\Delta b = \Delta x \frac{d}{f}$, where Δx is the pitch between the fibers in the array. The optimum configuration is when the spots are adjacent, so when $\Delta b = D_o$ with the corresponding pitch of $\Delta x = (2f^2 \tan\alpha)/d$. For an image plane of $L \times L$, m^2 spots with diameter D_o, with $m = L/D_o$ are required. Finally the fiber pitch can be determined using:

$$\Delta x = \frac{L^2}{2dm^2 \tan\alpha} \tag{9.1}$$

and the focal length:

$$f = \frac{L}{2m \tan\alpha} \tag{9.2}$$

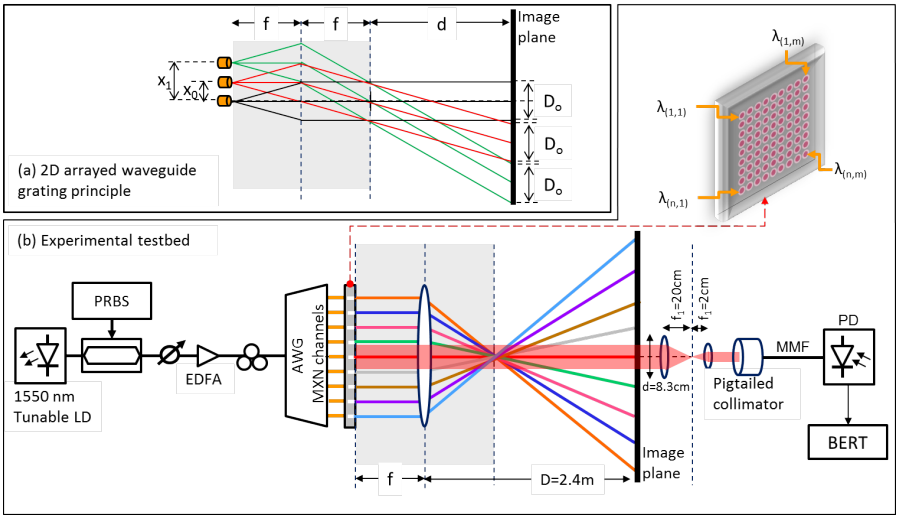

Figure 9.1: 2D arrayed waveguide grating technique; (a) Principle of operation; (b) Testbed setup for demonstration.

9.2 Experimental setup for 2D beam steering with arrayed waveguide grating

An experimental proof-of-concept setup is configured as shown in Figure 9.1(b). The wavelength of the tunable laser is set to $\lambda = 1544.26$ nm and its optical power is -5 dBm. The optical carrier is modulated externally using an Mach-Zehnder Modulator (MZM). The Non-Return-to-Zero (NRZ)-On-Off-Keying (OOK) data signal is generated using Pseudo Random Binary Sequence (PRBS) $2^{23} - 1$ bits. The modulated optical signal is then amplified by using an Erbium-Doped Fiber Amplifier (EDFA) and fed into the input port

of the arrayed waveguide grating. The transmitted optical power is 9.5 dBm, which is below the eye safety limit at $\lambda > 1.4\mu$m. The Gemfire arrayed waveguide grating (product identification: 80ch AWG DMX LC/UPC) has 1×80 channels AWGr. Each channel is spaced at 50 Gigahertz (GHz) within wavelengths ranging from 1529.10 nm to 1569.80 nm. Using this 80-port arrayed waveguide grating, a $(9 \times 9) - 1$ 2D fiber array has been constructed. From the calculations for a room height of 2.5 m, the 9×9 2D fiber array pitch = 13 mm, spot size = 8.3 cm and the focal length of lens = 39.8 cm. This results in a coverage area of 0.75×0.75 m^2 and an angular coverage of $17° \times 17°$.

The optical beams from the central output ports of the fiber array, i.e. ports 40 and 41 are launched into free space and are incident on the large lens with $f = 40$ cm and diameter, $D = 20$ cm). The 2D fiber array is positioned in the focal plane of the lens. The receiver is placed 2.4 m away from the lens. The size of the spot is de-magnified $10\times$ by a reverse telescope setup to a smaller beam before being coupled into the Multimode Fiber (MMF) which has a core diameter of 50 μm and a Numerical Aperture (NA) of 0.22. The optical signal is then transported to a 12 GHz PIN photodiode with Transimpedance Amplifier (TIA). The output is evaluated using a Bit Error Rate Tester (BERT).

9.3 Results and discussion

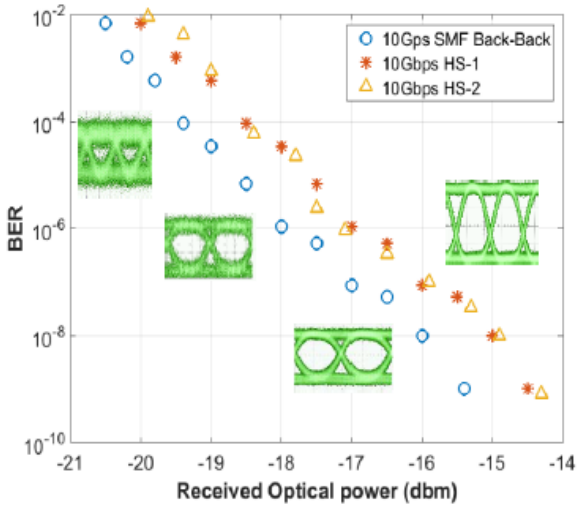

Figure 9.2: BER performance of HS-1 and HS-2 from ports 40 and 41 versus BtB SMF performance. Image taken from [218]

The results are shown in 9.2. The Bit Error Rate (BER) performances for HS-1 ($\lambda_{41} = 1544.26$ nm) and HS-2 ($\lambda_{42} = 1544.66$ nm) are measured at 2.4 m distance. A data rate of 10 Gbps is achieved near error-free BER of 1×10^{-9}. Approximately 1 dB penalty is observed with respect to a Single Mode

Fiber (SMF) Back-to-Back (BtB) connection. The eye-diagrams at different received powers are also given.

9.4 Chapter conclusion

This chapter presented another form of 2D beam steering by using a simple configuration of 2D arrayed fibers fed by a high port count arrayed waveguide grating. Up to 10 Gbps was achieved using OOK-NRZ signaling, at BER $\leq 1\times10^{-9}$, with a sufficient beam size of 8.3 cm in a coverage area of 0.75×0.75 m^2.

This straightforward approach is definitely advantageous in terms of simplicity. However, the demonstration was constructed using bulky arrays and lenses. Currently, a re-design of the method is being carried out to scale down on the size of the components.

Chapter 10

Conclusions and future outlook

Contents

10.1 Findings and contributions

The rapid growth of wireless bandwidth demand has introduced immense pressure on the limited radio frequency spectrum. Indoor wireless networks have to support more and more devices ('Internet of things') and already today, more traffic is generated from devices indoor than outdoor [1, 3] . Alternative solutions, such as utilizing the 60 Gigahertz (GHz) band, multilevel modulation formats, complex digital signal processing and Multiple-Input-Multiple-Output (MIMO) techniques, moving towards smaller radio cells (pico- and femtocells), and acquiring more radio spectrum, are on the rise, but we are still struggling with the limited radio spectrum resources. Ultimately, Optical Wireless Communication (OWC) is viewed as a promising alternative or complementary solution to high speed radio wireless communication systems. The benefits of optical wireless technique are in its fundamentally wide bandwidth,

inherent immunity against electromagnetic interference, physically secure and unregulated bandwidth.

To combat the imminent radio frequency spectrum crunch, Beam-steered Reconfigurable Optical-Wireless System for Energy-efficient communication (BROWSE) is taking a radical approach by performing wireless communication using optical pencil beam techniques in hybrid configuration with Radio Frequency (RF) 60 GHz radio technology. The key to practical implementation of ultra-high bandwidth optical beam links is in the technique to be used to direct these high capacity links in providing wireless channels to many users individually, simultaneously and dynamically. Beam steering modules, termed Pencil Radiating Antenna (PRA)s in BROWSE, are required to direct the beams to multiple users for the last meters, bridging the gap between end-users and the fiber infrastructure. In short, BROWSE will provide high-performance and large bandwidth uncongested wireless connectivity to indoor users by creating a synergy between wired (optical fiber), optical wireless (free space) downlink and radio wireless uplink communication technologies.

Consequently, this thesis investigated the challenges in using narrow pencil beams free-space optical communication to attain ultra-high capacities for indoor wireless communication. Several optical-related techniques were proposed and proof-of-concept experimental setups were demonstrated and reported in this thesis.

First, literature reviews on the history and types of optical wireless communication was elaborated in **Chapter 1**.

Next, a collection of the various active and passive beam steering techniques were presented at the beginning of **Chapter 2** to give an impression to the reader about possible techniques for beam steering and to familiarize the reader with the principles, characteristics and functions of the different techniques. After that, the state-of-the-art optical wireless beam steering techniques in optical wireless communication systems demonstrated in recent literature was given. Brief discussions were given on the capability of, and the beneficial characteristics in each system, in terms of simplicity, Field of View (FoV), adaptive beam control and transmission speed, next to discussing the drawbacks of each system. In summary, the drawbacks of the systems reported include mechanical dependency, where its speed is limited due to inertia, single channel steering, which means more elements such as mirrors or Spatial Light Modulator (SLM) segments are needed to steer more channels, and the need for local powering, to activate control functions at the beam-steering module. We also discussed a one-dimensional (1D) passive beam steering approach using a reflective grating by Kafei Liang et al. This work has some connection to the BROWSE project's approach towards the realization of passive beam-steering techniques for two-dimensional (2D) optical beam steering. A transmission of 1.25 Gigabit per second (Gbps) using On-Off-Keying (OOK) signaling over 2 m with a receiver FoV of 12° was achieved.

After that, the beam steering concept in this dissertation was introduced

in **Chapter 3**. The theory and derivations required in designing the passive beam steering modules using diffraction gratings were presented. From the analytical calculations, this thesis showed that the angular coverage is limited to approximately $6^\circ \times 26^\circ$ for a wavelength range between 1500 nm to 1599 nm (100 nm tuning). In this chapter also the analytical calculation of the positions of the diffracted spots from a diffraction grating is experimentally verified.

Then, in **Chapter 4**, several design aspects of the systems implemented in the experimental demonstrations reported in this thesis were introduced. These include the beam diameter, eye-safety limits, theoretical formula for the arrangement of cascaded gratings, angular magnification, beam expansion, beam-steering control and localization. This chapter also serves as a transition for readers from the theoretical work into system-level experiments. That is, the key system components were laid out, followed by several technical details on the optics used.

Chapter 5 reports the proof-of-principle evaluation of 1D steering using one reflective echelle grating with 79 grooves/mm blazed at 75°. The map of the diffracted spots is analytically calculated and experimentally verified. This thesis also proposed the use of an automatic receiver alignment robot which, ultimately, can be used to maximize the captured power. In the process to find and capture the beam, additional functions were implemented in the robot, to ease the alignment process of the receiver module due to the lack of a large FoV receiver. In the first 1D steering system demonstration, this thesis proposed the use of a single grating for a multicasting system due to the availability of several diffraction orders. Up to 5 diffraction orders were measured, with bit rates of 1.5 Gbps error-free OOK-Non-Return-to-Zero (NRZ) channels, and with a transmission power of 2.5 dBm, over 60 cm free-space distance. The second experiment incorporated a tunable laser to demonstrate 1D steering using wavelength tuning. With OOK-NRZ modulation, up to 10 Gbps error-free channels were obtained with wavelengths from 1500 nm up to 1630 nm. With Discrete Multitone (DMT) capacity maximization, an aggregate bit rate was achieved of up to 36.7 Gbps (net bit rate of 32.8 Gbps) at a Bit Error Rate (BER) of 9.4×10^{-4}, which is below the Forward Error Correction (FEC)-correctable limit. These results were promising for the deployment of gratings as the beam steering module for indoor optical wireless system.

This thesis further proposed two solutions for 2D beam-steering in **Chapter 6**. The first was an initial 2D steering evaluation based on the use of cascaded reflection gratings. The system evaluation has shown the capability of achieving error-free channels of 10 Gbps and a record high 42.8 Gbps at BER $= 1.27 \times 10^{-3}$ with OOK-NRZ and DMT modulation, and a net bitrate (after the deduction of the cyclic prefix, preambles and 7% overhead for FEC coding) of 37.3 Gbps. In the complete evaluation presented in this thesis, it was shown that free-space channel capacity per user of at least 37.2 Gbps up to 41.9 Gbps (between 1530 nm and 1600 nm) can be realized over a free-space transmission distance of 2 m in a 10 GHz bandwidth-limited system. As demonstrated in

the measurement results, the proposed optical wireless system has a performance comparable to that of Back-to-Back (BtB) (Single Mode Fiber (SMF)) transmission. With the minimum measured capacity of 37.2 Gbps per beam (out of 8 wavelengths measured), the system has a potential capability of supporting an aggregate capacity of at least 37.2 Gbps $\times$ 8 channels = 297.6 Gbps, depending on the number of channels.

Moreover, in chapter 6 the proposal of an improved pair of cascaded gratings is presented, by orthogonally cascading a reflection and a transmission grating. These modules demonstrated a 7-line scan in an angular coverage of $12.15^\circ \times 5.62^\circ$ between wavelengths 1511 nm and 1627 nm, compared to the cascaded reflection gratings module which could only provide a 2-line scan within an angular coverage of $12.67^\circ \times 5.61^\circ$ with wavelength tuning between 1529 nm and 1611 nm. In terms of link loss within the tuning range, the cascaded reflection and transmission grating setup was measured to have, at worst, 6.15 dB (loss) compared to the cascaded reflection gratings which contributed at worst 16.8 dB (loss). This loss was mostly contributed by the gratings and partly by the alignment errors and the reflections. However, the trade-off is in the spectral bandwidth, whereby cascaded reflection gratings achieved approximately 20 GHz compared to the cascaded reflection and transmission gratings approach, which measured only at approximately 10 GHz. In terms of data rate, the orthogonally cascaded reflection and transmission gratings performed competitively, offering up to 10 Gbps with OOK-NRZ at BER $\leq 1 \times 10^{-9}$ in a 10 GHz bandwidth-limited system setup, 16 Gbps with OOK-NRZ at BER $< 1 \times 10^{-3}$, 32 Gbps with Pulse Amplitude Modulation (PAM)-4 at BER $< \times 10^{-3}$, and 41.4 Gbps with DMT and a net bit rate of 36.2 Gbps at BER $= 1.97 \times 10^{-3}$.

Next, in an effort to achieve an all-optical OWC system, **Chapter 7** demonstrated a novel all-optical bi-directional wireless communication setup using a carrier recovery method. High-speed symmetrical duplex channels were reported at a date rates of 10 Gbps, using the OOK-NRZ modulation format.

Then, **Chapter 8** discusses three improvements, namely by increasing the field of view of the receiver, by increasing angular coverage of the steering module, and by maximizing resource usage (decreasing costs) through time-slotted transmission. The first section of this chapter covered a wide angle lens receiver. Narrow FoV collimators are difficult to deploy due to their tedious alignment process and are, therefore, unsuitable for moving users. In addition, the small (in the order of micrometers) photodetector area for increasing transmission bandwidth further limits the amount of light that can be received. To counter this issue, a large effective photodetector area, which can be made up by for example an array of photodetectors, is needed. However, due to the lack of such arrays at this point of time, this thesis proposed the use of a wide-angle fish-eye lens, together with a fiber-pigtailed coupler, to capture the beams at the focal plane behind the lens. By using this method, a Full-Field of View (FFoV) of 80° was achieved.

The following section in Chapter 8 discussed angular magnification to increase the angular coverage of the steering module which was limited to $6° \times 26°$. Angular magnification relieves the initial angular coverage of the steering module. In fact, an initial angle of a few degrees $< 5°$ actually improves the beams since they pass through the second lens easily. In addition, beams transmitted through a lens closer to the optical axis will not be subjected to large distortion as much as beams which pass through the lens at a distance away from the optical axis closer to the edge.

The third section of Chapter 8 proposed time-slotted indoor transmission. This concept is feasible in OWC since most services require less bandwidth than can maximally be delivered. In addition, this methods also supports the use of resource sharing. Depending on the number of lasers used, three different supported modes of operation, i.e. unicasting, multicasting and broadcasting, can be implemented.

Chapter 9 reported another 2D beam steering mechanism which was based on Arrayed Waveguide Grating (AWGr). The steering module was constructed based on a brute-force approach to realize 2D beam steering by using a 2D array of fibers connected to a high port count arrayed waveguide grating. For this setup, performance up to 10 Gbps, using an OOK-NRZ modulation format, was reported.

A summary of power budget for the demonstrated systems are given in Table 10.1.

10.2 Discussion and future work

10.2.1 Receiver with wide full-field of view

A crucial area of research in OWC is in the realization of a wide angle receiver despite the limitation of detector active area which is limited to a few tens of micrometer for a bandwidth of 10 GHz and more. In Section 8.1, we saw a few distinct solutions from the literature. These include the use of angle diversity receivers, hemispherical lenses and Compound Parabolic Concentrators (CPCs). In order to improve on coupling efficiency, ideally, an effective large area of detection could be implemented using an array of photodetectors. In improving the FFoV of a receiver, simple constructions without requiring an additional beam-steering module at the receiver could be achieved using wide angle lenses or CPCs. However, this would be at the expense of a reduced effective collection aperture which reduces the link margin due to the conservation of étendue.

10.2.2 Angular coverage

It is undeniably very interesting to employ passive optics for 2D beam steering to eliminate local powering at the access point. It is also important that the

Table 10.1: Summary of power budget for demonstrated transmission systems. Free-space loss is the collective losses due to the steering module, misalignment, insertion loss of the collimator and connector loss.

Section 5.5: With one reflection grating		
Power launch into free space, P_{TX}	10	dBm
Maximum free-space loss (Refer Figure 5.12)	10	dB
Minimum power at receiver, P_{RX}	0	dBm
Receiver sensitivity at 10 Gbps	16	dBm
Total system power margin	16	dBm

Section 6.7: With cascaded reflection gratings		
Power launch into free space, P_{TX}	10	dBm
Maximum free-space loss (Refer Table 6.1)	16.8	dB
Minimum power at receiver, P_{RX}	-6.8	dBm
Receiver sensitivity at 10 Gbps	16	dBm
Total system power margin	9.2	dBm

Section 6.8: With cascaded reflection & transmission gratings		
Power launch into free space, P_{TX}	10	dBm
Maximum free-space loss (Refer Table 6.2)	6.15	dB
Minimum power at receiver, P_{RX}	3.85	dBm
Receiver sensitivity at 10 Gbps	16	dBm
Total system power margin	19.85	dBm

Section 8.1: With wide angle lens at Rx		
Power launch into free space, P_{TX}	10	dBm
Maximum free-space loss (Refer Figure 8.10)	12	dB
Minimum power at receiver, P_{RX}	-2	dBm
Receiver sensitivity at 10 Gbps	16	dBm
Total system power margin	14	dBm

Section 8.2: With AM at PRA & a wide angle lens at Rx		
Power launch into free space, P_{TX}	10	dBm
Maximum free-space loss	22	dB
Minimum power at receiver, P_{RX}	-12	dBm
Receiver sensitivity at 10 Gbps	16	dBm
Total system power margin	4	dBm

beam-steering module has a large angular coverage. As derived in Section 3.2, by employing blazed gratings, only an angular coverage of $6° \times 26°$ is achievable in a wavelength range between 1500 nm - 1599 nm. As reported in the high port count arrayed waveguide grating approach, an angular coverage of $17° \times 17°$ was achieved. These angles should be further improved to approximately 45° or more in order to cover a large area in a room instead of just a small corner.

The steering module can be combined with optical techniques for angular and lateral magnification to increase the angular and beams size. In fact, by using optical expansion techniques, the initial angular coverage becomes less crucial. It is actually better if the initial angles are small when using a reverse telescope beam expansion, since the limitation is on the size of the second lens. If smaller angles of only a few degrees are used, the beam travels more towards the center of the second lens. When larger angles are used, the larger angle beams will travel closer to the edge of the lens which results in larger lens aberration errors and thus distortion of the final beam shape. This can be seen in Figure 8.14. In this diagram, the beams are directed from the source at 0°, 3° and 6°. The resulting spots, tabulated on a screen 100 mm away from the second lens, are shown in Figure 10.1. Due to the distortion when beams are used close to the edge of the lens, it is clear that a small initial angular coverage is sufficient. In addition to this, future work can concentrate on steering methods that increase the resolution of the beam spots, for example with hundreds of scan lines resulting from operating a Virtually Imaged Phased Array (VIPA) at high orders, while leaving the angular coverage to further optical techniques for beam manipulation and shaping.

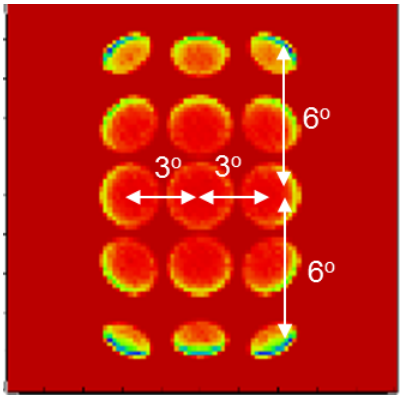

Figure 10.1: Resulting spots from initial launch angles of 0°, 3° and 6° on a screen at 100 mm in front of the second lens in the reverse telescope configuration.

10.2.3 All-optical duplex communication

In view of a future Heterogeneous Network (HetNet) integration with OWC and Wireless Fidelity (WiFi) for wireless communication [3], radio and wide beam light communication can be used in parallel for backing up narrow beam communications to maintain connectivity. In order to be able to provide ultra-high speed for up- and downlink, it is required to provide ultra-high speed beams for uplink transmission as well. In Chapter 7 of this thesis, we proposed to use the carrier re-modulation technique enabled by carrier recovery and erasure of the downlink OOK signal by means of two cascaded Semiconductor Optical Amplifiers (SOAs) operating in the saturation region. This technique can be implemented with, for example, DMT modulation format for higher data rates [201], and secondly, by designing proper SOAs for data erasure. An alternative method is by using phase/frequency modulation for the downlink and amplitude modulation for the uplink.

10.2.4 Localization

Localization of the (mobile) user devices is another important subject in optical wireless systems. A relatively simple way of solving this challenge is by employing established radio techniques. It is a common method that localization is initiated by a mobile device starting the communication to signal its presence. One way forward, while keeping the system in an all-optical framework, is to establish the uplink using a broad beam approach towards the access point. Localization communication requires only a small bandwidth, e.g. a speed in the kbps range, should be sufficient. Therefore, a wide beam for uplink can be used while spreading the power of the beam over a large area. A detector with a large area and a large FoV can definitely come in handy to ease light detection and therefore, reduces localization latency. Beam-scanning is then activated to search for the user terminal, as illustrated in Figure 10.2a. In another approach, a reasonably broad beam from the user terminal is directed towards a wavelength-dependent steering module such as the grating-based modules proposed in this dissertation. The control center proceeds to determine the location of the user terminal by determining the wavelength received, as illustrated in Figure 10.2b [220]. Once localized, adaptive optics yielding a narrow beam can be used to resume ultra-high speed communication. When the user moves to a different location, this process could be repeated and, while on the move, the user may have to resort to other techniques, such as WiFi.

10.2.5 Beam dimensioning

In order to improve the system design, it is also important to consider which beam type should be used, i.e. parallel, diverging or mix, and how large the steering angle should be to implement coverage of the plane-of-interest, as defined in Figure 10.3.

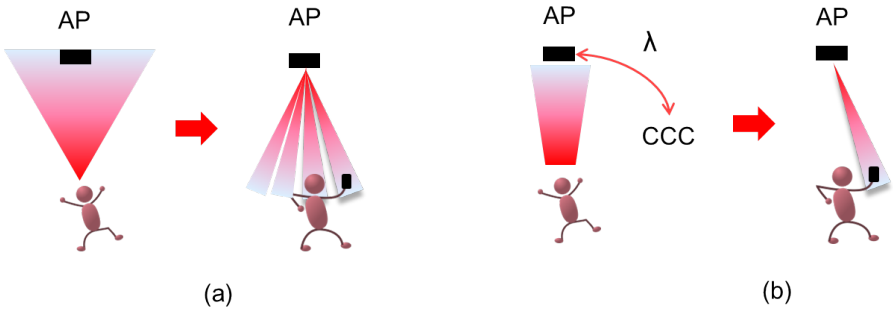

Figure 10.2: All-optical localization methods: (a) The user terminal directs a wide beam towards the access point (AP) to indicate its presence, followed by beam-scanning process to locate user. (b) A reasonably wide beam is directed towards the AP, followed by the determination of wavelength (λ) for communication at the central communication controller (CCC).

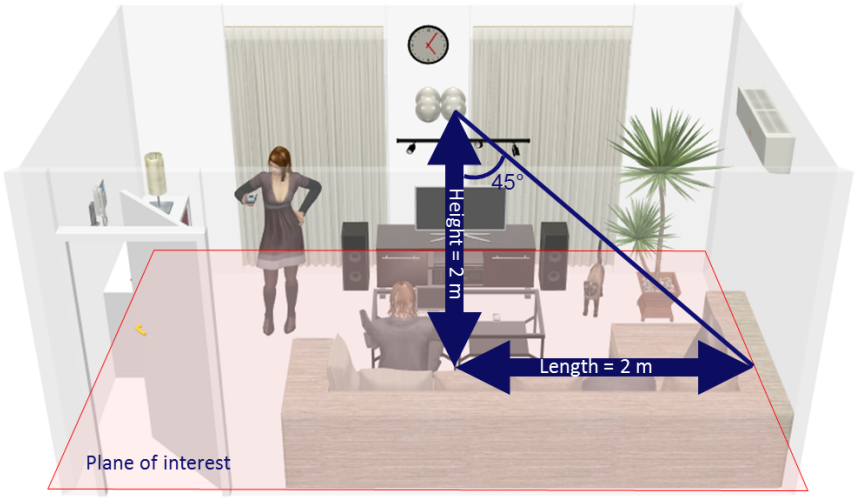

Figure 10.3: Plane-of-interest for the planning of spots tabulation desired.

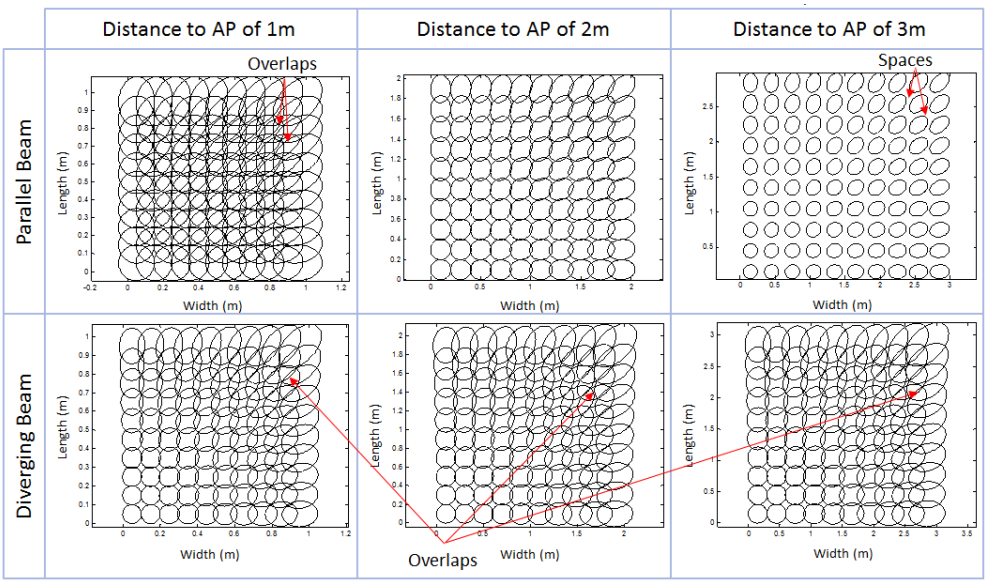

Figure 10.4: The effect of varying the receiving plane away from plane-of-interest on the spots tabulation. AP: Access Point.

In using passive gratings for steering, we saw that the spots can be continuously tuned in one-dimension while remaining constant in the orthogonal dimension. Here we assumed both dimensions are discrete, such as the steering spots given using the AWGr-based 2D fiber array method. Now, let's consider using a module with 10×10 spots. For a 2 m coverage, this would mean spots with diameter of 20 cm. Figure 10.4 shows the spot tabulation for a 45° angle steering module for parallel and diverging beams, at three different distances of the plane of interest from the Access Point (AP) i.e. 1 m, 2 m (plane-of-interest), and 3 m. For parallel beams, we observe that as the distance decreases towards the AP the beams overlap, while when the distance extends beyond the plane-of-interest, empty spaces appear.

On the other hand, for diverging beams, the pattern formation is consistent whether we move closer towards the AP or further away. The divergence of the beams should be in relation to the step size (scanning resolution) of the laser. One advantage of using diverging beams is the consistent pattern which may decrease the software complexity. Software control using beam variation and time-sharing techniques are viable options. A possible drawback might be a lower signal strength as distance increases. However, this may be mitigated by the available power budget. Thus, diverging beams may provide a better coverage for varying distance to a PRA.

10.2.6 Towards photonic integrated circuits technology

At this point in time, the proposed systems can offer a very high uncontested capacity per user. However, they need to be further improved in order to be ready for commercial roll-out. One important aspect is the cost of the proposed systems which, so far, is quite high. Also, the bulky devices that were deployed are mainly for testbed proof-of-principle evaluations. As for eventual commercial implementation, we will need to move from discrete bulky devices to Photonic Integrated Circuit (PIC) technology for potentially low cost, small footprint, light weight and low power consumption products. Placing a pair of passive diffraction module at the access point may not be a concern but the receiver module is preferred to be small, light weight, low cost and low in energy consumption.

At present, PIC technology is already able to integrate various photonic components such as lasers (including tunable lasers), modulators, optical amplifiers, photodetectors, and waveguide gratings on a single substrate [103, 197, 221, 222]. In terms of beam deflection, PIC optical phased arrays have the potential to provide compact, fast and stable beam deflection. Steering applications, for e.g. in optical wireless communication and autonomous vehicle application [223], typically require an angular coverage exceeding 45°. PICs can generate narrow beams, wide steering angles and have Gigahertz range tuning speed [222].

Driven by the high-bandwidth requirements in telecom and datacom applications, the PIC technology seems to converge to a few platforms including a hybrid of these technologies [222]. The silicon photonics platform is highly developed and is a mature platform for large-scale photonic integration [224]. The Silicon-On-Insulator (SOI)-based high index contrast waveguide system allows high optical confinement. Silicon-based Optical Phased Arrays (OPAs) can benefit from the Complementary Metal-Oxide-Semiconductor (CMOS)-compatible silicon processes. CMOS processing techniques are highly advance and allows densely integrated microelectronics.

Silicon nitride (Si_3N_4) is an alternative moderate-index-contrast system to the SOI platform. The low non-linearity of Si_3N_4 allows the handling of higher optical power density and Si_3N_4 is also more robust to fabrication induced phase variation than silicon [223].

Indium Phosphide (InP) like silicon, is also a mature platform for large-scale photonic integration [225]. It supports not only passive but also active devices, such as tunable lasers, photodetectors and SOAs in which a single SOA could generate a maximum optical power of up to 20 mW [225]. The phase shifters with current injections can achieve Gigahertz bandwidth, for e.g., a sampled-grating distributed Bragg reflector (SG-DBR) laser [226], which can be tuned in less than 5 nanoseconds [225, 227]. Thus, a very fast optical beam-steering can be achieved.

Early in year 2005, Xiao et al. [228] proposed a 1D wavelength-controlled

OPA beam steering. The desired phase slopes formed at the ends of non-uniformly spaced array of optical waveguides can be changed by varying the optical wavelength. By combining 1D OPA and surface grating, in 2010, Van Acoleyen et al. [229] proposed a 2D OPA using thermo-optic and wavelength tuning. The benefit of this design is that it allows individual control for each axis. However, there is no way to actively compensate accumulated phase errors between individual channels and thermal crosstalk [103]. A complete 2D wavelength-controlled OPA was also reported by Van Acoleyen et al. [105] a year later. The chip was totally passive without any phase tuning elements, but with the drawback of a relatively wide beam of 4°.

In 2011, Doylend et al. proposed a 16-channel OPA in which the phase of each channel is individually controlled on SOI platform. Doylend et al. also presented on a hybrid III-V/Silicon platform, the first [230] fully-integrated phased array chip with an on-chip laser, waveguide splitter, amplifiers, phase modulators and surface gratings. In 2014, Sun et al. [231] has proposed an array of 64×64 emitters which is highly tolerant to phase errors. The demonstrated OPA consists of as many as 12,288 optical elements, making it the largest and densest silicon photonic integration back then. Hulme et al. [104] proceeded with a hybrid III-V/Silicon integration with a total of 164 components with 9 different component types.

Recently, a 1D OPA which is based on the silicon nitride platform has been demonstrated by Poulton et al. [232]. The decent tuning range of $\pm 23°$ with a narrow near diffraction limited beam size of $0.021°$ demonstrates another promising approach. As proposed in this dissertation and also in [225], lenses can be employed to magnify the angular range in order to improve the beam steering coverage. Table 10.2 summarizes the remarkable advances of the PIC optical phased arrays from literature.

10.3 Conclusions

This thesis presented, proposed, designed, demonstrated and discussed several technicalities in the realization of an optical wireless communication system. A brief history and the evolution of optical wireless communication so far were discussed. Related optical techniques for beam deflection for active and passive beam-steering were provided in order to give an overview of and insight in the available optical techniques. The state-of-the-art optical techniques employing narrow beams with beam-steering were also provided.

In the context of the BROWSE project, this thesis has addressed the challenges of designing and deploying free-space optical communication for indoor using a passive 2D beam-steering module based simply on a passive structure of two reflection gratings for optical wireless communication supported by the flexible fibre backbone network, by radio-over-fiber uplink and by network control intelligence. We have shown the basic feasibility with a 1D steering

Table 10.2: Comparison of PIC optical phased array technologies at telecom C-band.

Source	Technology	Footprint (mm^2)	Array/ Antenna Design	Tunable Angle per order	Beam Size	Tuning Method	Power Usage (mW)	Loss (dB)
Van Acoleyen et al. 2010 [229]	SOI, CMOS	-	2 × 2 4 × 4	±1.5°	4.8° × 9.6°	Wavelength Tuning	-	3
Van Acoleyen et al. 2011 [105]	SOI, CMOS	-	1D OPA + grating	15° × 50° per 100 nm	4.0° × 4.0°	Wavelength Tuning	Passive	< 9
Doylend et al. 2011 [103]	SOI	-	1D OPA + grating	±20° × ±14°	0.6° × 1.6°	Thermo-Optic/ Wavelength Tuning	215 ±15 per π phase shift	25.4
Doylend et al. 2012 [233]	SOI, III-V	-	Fully Integrated 1D OPA+ grating	12°	1.8° × 0.6°	Thermo-Optic	97 per π phase shift	20.7
Guo et al. 2013 [225]	InP	-	Fully Integrated 1D OPA + grating	±12° × ±6°	0.2° × 1.7°	Thermo-Optic/ Wavelength Tuning	-	-
Yaacobi et al. 2014 [223]	SOI, CMOS	-	1D OPA	51°	3.3°	Thermo-Optic	18 per antenna	-
Sun et al. 2013 [230, 231]	SOI, CMOS	0.009 × 0.009 Unit Cell	64 × 64 32 × 32	±6°		-	Passive	-
Sun et al. 2013 [230, 231]	SOI, CMOS	0.009 × 0.009 Unit Cell	8 × 8	±6°		Thermo-Optic	8.5 per π phase shift per unit cell	-
Hulme et al. 2015 [104]	SOI, III-V	6 × 11.5	Fully Integrated 1D OPA + surface grating	23° × ±3.6°	1° × 0.6°	Thermo-Optic/ Wavelength Tuning	160 per π phase shift per unit cell	-
Poulton et al. 2016 [232]	Si_3N_4	-	1D OPA	±23°	0.021° × 0.021°	-	-	13.6

module. A 2D passive steering module, constructed using orthogonally cascaded reflection gratings, was demonstrated with a record aggregate speed of 42.8 Gbps at BER = 1.27×10^{-3} and a net bitrate (after the deduction of the cyclic prefix, preambles and 7% overhead for FEC coding) of 37.3 Gbps at 2 m free-space transmission. The steering module provided a 2-lines scan with an angular coverage of $12.67° \times 5.61°$ between 1529 nm and 1611 nm.

The 2D steering module was further improved by a pair of orthogonally cascaded reflection and transmission gratings. This module demonstrated 7-line scan in an angular coverage of $12.15° \times 5.62°$ between wavelengths 1511 nm and 1627 nm. The improved steering module also gained advantage in terms of the measured power loss of only 6.15 dB at worst compared to the cascaded reflection gratings which contributed at worst 16.8 dB. However, a major drawback is in the spectral bandwidth, whereby cascaded reflection gratings achieved approximately 20 GHz compared to the cascaded reflection and transmission gratings approach which achieved only approximately 10 GHz. In terms of data rate, the improved pair of orthogonally cascaded reflection and transmission gratings performed competitively, achieving up to 16 Gbps with OOK-NRZ at BER $< 1 \times 10^{-3}$, 10 Gbps with OOK-NRZ at BER $\leq 1 \times 10^{-9}$ in 10 GHz bandwidth-limited system setup, 32 Gbps with PAM-4 at BER $< 1 \times 10^{-3}$ and 41.4 Gbps with DMT with a net bitrate of 36.2 Gbps at BER = 1.97×10^{-3}.

The small angular range of the passive gratings no longer needs to be a major issue as angular and lateral beam expansion techniques were introduced in this thesis to complement dense or very highly dispersive grating with small dispersion angles, which finally translates to a large angular coverage with dense scanning lines. The challenge of micro-sized effective detection area of photodetectors, compounded with the need to accommodate larger beam sizes, requires a larger effective detector size with enlarged angular coverage and efficiency by using wide angle lenses. Using a wide-angle fish-eye lens with automated fiber-coupled collimator, up to 80° receiving angle was measured. A simple and direct method of using a 2D fiber array together with an Arrayed Waveguide Grating is another alternative to realize a passive 2D beam-steering device. Preliminary results measured using an 80-port AWGr achieved 10 Gbps with an angular coverage of $17° \times 17°$.

In addressing the challenge of having symmetric bi-directional optical wireless full-duplex channels, 10 Gbps full-duplex all-optical channels were demonstrated with OOK-NRZ signaling, deploying carrier recovery and remodulation for upstream transmission at the user's device side. Finally, time-slotted indoor transmission was demonstrated with the idea to promote resource sharing and to establish unicasting, multicasting and broadcasting schemes.

An optical wireless system can have a comparable performance to an SMF transmission system, and maybe even better as dispersion in an optical wireless beam channel can be less than in a fiber. Consequently, using the fiber for the "last-mile" communication, in conjunction with optical wireless link for the last meters to the mobile user, is seen as the most powerful solution

to provide the ultimate capacity for wireless communication. By engaging this benefit, this thesis has proposed and demonstrated several novel ideas for indoor optical wireless communication systems employing 2D beam steering, within the framework of the BROWSE project. The passive optical beam-steering methods do not require local powering while providing instantaneous remotely controlled steering by just wavelength-tuning of the signal. By steering the pencil beams to the required positions only, this method offers energy savings, secure communication and the ultimate uncongested capacity to individual users. The system is also easily scalable by just adding wavelengths to yield additional beams, and thus, able to accommodate more users independently without affecting the channel capacity of other users. This thesis has also addressed several other challenges in optical wireless communication.

Finally, narrow beam free-space transmission is still at its infancy and there are definitely many more aspects, such as those highlighted in Section 10.2, that need to be addressed. Much effort is still needed as the technology matures towards realizing functional, small form factor, low-cost, and efficient mobile modules for a practical implementation. With regard to the viability of this technology, the proof-of-principle demonstrations in this thesis have shown promising results which support the adoption of optical wireless communication as the next major breakthrough for providing ultra-high capacity optical wireless communication services.

Appendix A

Power Consumption

A.1 Power Consumption of Transmission Systems

Table A.1: The power consumption of different discrete components in the demonstrated transmission systems.

Component	Watt
81960A Tunable laser	< 60
DFB laser	0.2
PRO800 Temperature Controller	< 220
10 Gbps Mach-Zehnder modulator with integrated RF amplifier	7.15
10 GHz Photoreceiver	< 1
Semiconductor optical amplifier	< 1

A.2 Power Consumption of Transceivers

The power consumption of transceivers in general depends on factors such as the (maximum) bitrate of the transmission, the modulation format used, and the wavelength range. For the transmitter part specifically, the consumption also depends on the optical output power. Similarly, the receiver power usage also depends on its sensitivity. These factors are also dependent on which type of lasers (e.g DFB or ECL) and receivers (e.g. PIN or APD) are employed.

As shown in Table A.2 [234], at present, the transceivers that transmit less than 5 dBm in the 0.1–2 Gbps range consume around 1 Watt, while those operating in the 10 Gbps range consume around 2 Watt. With technological advances these numbers may reduce as, for example, modulation formats could be implemented more efficiently. There is, of course, a the minimum electrical power required to generate a certain optical output power, depending on the

component's conversion efficiency, η, given by the formula:

$$\eta = \frac{\text{optical output power}}{\text{electrical input power}} \times 100\%$$

The optical output power in mW, P_{mW}, and W, P_W, could be expressed in dBm, and vice versa, using the following equations:

$$P_{dBm} = 10 \times log_{10} \frac{P_{mW}}{1 \text{ mW}}$$

$$P_{mW} = 1\text{mW} \times 10^{(P_{dBm}/10)}$$

$$P_{dBm} = 30 + 10 \times log_{10} \frac{P_W}{1 \text{ W}}$$

$$P_W = 1\text{W} \times 10^{((P_{dBm}-30)/10)}$$

While the beam steering method proposed in this thesis is passive and is not affected by such factors, it does attenuate the optical signal and, thus, has an effect on the power budget that is required of the transceivers. Nevertheless, this requirement is mainly at the Central Communication Controller (CCC), and does not need to be accounted for at each Access Point (AP) placed across the home. An active system might need amplifiers at every AP, multiplying the energy consumption by the number of APs used.

Table A.2: The power consumption of different transceivers depends on their maximum achievable bitrate, optical in/output power capabilities, and wavelength range [234].

Part	Max speed (Gbps)	Optical Power output (dBm)	Rx sensitivity (dBm)	Wavelength (nm)	Power usage (Watt)
FTLF1523P1xTL	0.15	0	-34	1480-1580	1.1
FTLF1518P1BTL	1.25	5	-22	1270-1600	1.1
FTLF1619P1xCL	2.125	5	-28	1540-1570	1.1
FTLF1519P1xNL	2.125	5	-21	1540-1570	1.1
FTLF1519P1xCL	2.125	5	-21	1540-1570	1.1
FTLF1621S1xCL	2.67	3	-28	1500-1580	1.2
FTLX1812M3BTL	11.3	4	-22.5	1530-1565	3.5
FTLX6871MCC	11.3	3	-27	1260-1600	2.2
FTLX6872MCC	11.3	3	-27	1260-1600	2.2
FTLX1871M3BCL	11.3	4	-24	1530-1565	1.7
FTLX1672D3BCL	11.3	2	-15	1260-1600	1.5
FTLQ1381N7NL	44.6	3	-7	1530-1565	8

Appendix B

Optical versus Radio Wireless Technologies

Table B.1: Comparison of technical features of various wireless LAN technologies by Singh et al. [235].

Technology	Optical Wireless			Radio/Microwave	
	DFIR	DBIR	QDIR	RF	DSSS/ FHSS
Data rate	< 10 Mbps	< 150 Mbps	< 20 Mbps	5 - 10 Mbps	2-20 Mbps/ 1 - 3 Mbps
Mobility	Portable	Stationary with LoS	Portable	Stationary	Portable
Coverage (m)	5 - 10	20 - 30	10 - 20	10 - 40	30 - 200/ 30 - 100
Radiated Power	< 0.5 mW	< 10 mW	< 5 mW	< 25 mW	< 1 W
Safety Problems	Significant	Significant	Significant	Near transmitter	Near transmitter
Multipath Fading	No	No	No	Yes	Yes
Technology Cost	Medium	Low	Medium[a]	Medium	High

[a] should be low in near future.

References

[1] Cisco, "The internet of things," 2011. Available: http://share.cisco.com/internet-of-things.html

[2] S. Cherry, "Edholms law of bandwidth: telecommunications data rates are as predictable as moores law," *IEEE Spectrum*, vol. 58, 2004.

[3] M. Ayyash, H. Elgala, A. Khreishah, V. Jungnickel, T. Little, S. Shao, M. Rahaim, D. Schulz, J. Hilt, and R. Freund, "Coexistence of WiFi and LiFi toward 5G: concepts, opportunities, and challenges," *IEEE Communications Magazine*, vol. 54, no. 2, pp. 64–71, 2016.

[4] U. D. of Commerce, "United states frequency allocations." Available: https://upload.wikimedia.org/wikipedia/commons/5/5d/United_States_Frequency_Allocations_Chart_2003_-_The_Radio_Spectrum.pdf

[5] L. Yang, "60GHz: opportunity for gigabit WPAN and WLAN convergence," *ACM SIGCOMM Computer Communication Review*, vol. 39, no. 1, pp. 56–61, 2008.

[6] D. Su, "ISSCC 2013: Wireless trends." Available: http://www.maltiel-consulting.com/ISSCC-2013-Wirelessl-Trends.html

[7] Cisco, "Forecast and methodology, 2014-2019 white paper," Cisco Visual Networking Index, Tech. Rep., 2015. Available: http://zenithoptimedia.ru/Documents/Visual%20Networking%20Index.pdf

[8] M. Reardon, "Wireless spectrum: What it is, and why you should care," 2012. Available: http://www.cnet.com/news/wireless-spectrum-what-it-is-and-why-you-should-care%20/

[9] T. McCall and M. Mahoney, "Spectrum of issues." Available: http://visual.ly/spectrum-issues

[10] V. Chandrasekhar, J. G. Andrews, and A. Gatherer, "Femtocell networks: a survey," *IEEE Communications Magazine*, vol. 46, no. 9, pp. 59–67, 2008.

[11] D. Chambers, "What's the difference between picocells and femtocells?" Available: https://www.thinksmallcell.com/FAQs/whats-the-difference-between-picocells-and-femtocells.html

[12] S. Dimatteo, P. Hui, B. Han, and V. O. Li, "Cellular traffic offloading through WiFi networks," in *2011 IEEE Eighth International Conference on Mobile Ad-Hoc and Sensor Systems*. IEEE, 2011, pp. 192–201.

[13] Cisco, "Cisco visual networking index: Global mobile data traffic forecast update, 20152020 white paper," 2016. Available: http://www.cisco.com/c/en/us/solutions/collateral/service-provider/visual-networking-index-vni/mobile-white-paper-c11-520862.html

[14] Aptilo Networks, "Mobile data offloading," 2016. Available: https://www.aptilo.com/mobile-data-offloading/wifi-offload-3g-4g

[15] J. M. Kahn and J. R. Barry, "Wireless infrared communications," in *Proceedings of the IEEE*, vol. 85, no. 2. IEEE, 1997, pp. 265–298.

[16] J. R. Barry, *Wireless infrared communications*. Springer Science & Business Media, 2012, vol. 280.

[17] ANSI, "American national standard for safe use of lasers ANSI z136.1," *American National Standards Institute, Inc.*, 2007.

[18] IEC, "International standard IEC 60825-1.2 2001-8," *International Electrotechnical Commission, Geneva*, 2001.

[19] K. Cui, G. Chen, Q. He, and Z. Xu, "Indoor optical wireless communication by ultraviolet and visible light," in *SPIE Optical Engineering+ Applications*. International Society for Optics and Photonics, 2009, pp. 74 640D–74 640D.

[20] A. G. Bell, "On the production and reproduction of sound by light," *American Journal of Science*, no. 118, pp. 305–324, 1880.

[21] M. Groth, "Photophones revisted," in *Amateur Radio magazine*. Wireless Institute of Australia, Melbourne, 1987, vol. 55, p. 14. Available: http://www.bluehaze.com.au/modlight/GrothArticle1.htm

[22] T. H. Maiman, "Stimulated optical radiation in ruby," *Nature*, no. 187, pp. 493–494, August 1960.

[23] N. Zheludev, "The life and times of the LED – a 100-year history," *Nature Photonics*, vol. 1, no. 4, pp. 189–192, 2007.

[24] N. Holonyak Jr and S. Bevacqua, "Coherent (visible) light emission from $Ga(As_{1-x}P_x)$ junctions," *Applied Physics Letters*, vol. 1, no. 4, pp. 82–83, 1962.

[25] D. M. Forin, A. Teixeira, B. Geiger, E. Leitgeb, F. Nadeem, G. Incerti, G. T. Beleffi, L. Costa, and P. D. B. Andre, *Free space optical technologies*. INTECH Open Access Publisher, 2010.

[26] A. K. Majumdar and J. C. Ricklin, *Free-space laser communications: principles and advances*. Springer Science & Business Media, 2010, vol. 2.

[27] S. Das, H. Henniger, B. Epple, C. I. Moore, W. Rabinovich, R. Sova, and D. Young, "Requirements and challenges for tactical free-space lasercomm," in *Military Communications Conference, 2008. MILCOM 2008. IEEE*. IEEE, 2008, pp. 1–10.

[28] Y. J. Gawdi *et al.*, "Underwater free space optics," 2006.

[29] M. Toyoshima, "Trends in satellite communications and the role of optical free-space communications [invited]," *Journal of Optical Networking*, vol. 4, no. 6, pp. 300–311, 2005.

[30] J. C. Juarez, A. Dwivedi, A. R. Hammons, S. D. Jones, V. Weerackody, and R. A. Nichols, "Free-space optical communications for next-generation military networks," *IEEE Communications Magazine*, vol. 44, no. 11, pp. 46–51, November 2006.

[31] T. Yoshizawa, *Handbook of optical metrology: Principles and Applications*. CRC Press, 2015.

[32] D. C. OBrien, M. Katz, P. Wang, K. Kalliojarvi, S. Arnon, M. Matsumoto, R. Green, and S. Jivkova, "Short-range optical wireless communications," in *Wireless world research forum*, 2005, pp. 1–22.

[33] D. O'Brien and M. Katz, "Optical wireless communications within fourth-generation wireless systems [invited]," *Journal of optical networking*, vol. 4, no. 6, pp. 312–322, 2005.

[34] H. Elgala, R. Mesleh, and H. Haas, "Indoor optical wireless communication: potential and state-of-the-art," *IEEE Communications Magazine*, vol. 49, no. 9, pp. 56–62, 2011.

[35] D. Wisely and I. Neild, "A 100 Mbit/s tracked optical wireless telepoint," in *Personal, Indoor and Mobile Radio Communications, 1997. Waves of the Year 2000. PIMRC'97., The 8th IEEE International Symposium on*, vol. 3. IEEE, 1997, pp. 964–968.

[36] D. R. Wisely, "A 1 Gbit/s optical wireless tracked architecture for ATM delivery," in *Optical Free Space Communication Links, IEEE Colloquium on.* IET, 1996, pp. 14–1.

[37] D. C. O'Brien, G. E. Faulkner, K. Jim, E. B. Zyambo, D. J. Edwards, M. Whitehead, P. N. Stavrinou, G. Parry, J. Bellon, M. J. Sibley *et al.*, "High-speed integrated optical wireless transceivers for in-building optical LANs," in *Information Technologies 2000.* International Society for Optics and Photonics, 2001, pp. 104–114.

[38] V. Jungnickel, A. Forck, T. Haustein, U. Kruger, V. Pohl, and C. Von Helmolt, "Electronic tracking for wireless infrared communications," *IEEE Transactions on Wireless Communications*, vol. 2, no. 5, pp. 989–999, 2003.

[39] F. R. Gfeller, H. R. Muller, and P. Vettiger, "Infrared communication for in-house applications," in *IEEE COMPCON*, vol. 78, 1978, pp. 132–138.

[40] M. D. Kotzin and A. P. van den Heuvel, "A duplex infra-red system for in-building communications," in *Vehicular Technology Conference, 1986. 36th IEEE*, vol. 36. IEEE, 1986, pp. 179–185.

[41] T. Minami, K. Yano, T. Touge, H. Morikawa, and O. Takahashi, "Optical wireless modem for office communication," in *Proceedings of the May 16-19, 1983, national computer conference.* ACM, 1983, pp. 721–728.

[42] C. J. Georgopoulos and A. K. Kormakopoulos, "A 1-Mb/s IR LED array driver for office wireless communication," *IEEE Journal of Solid-State Circuits*, vol. 21, no. 4, pp. 582–584, 1986.

[43] K. Pahlavan, "Wireless communications for office information networks," *IEEE Communications Magazine*, vol. 23, no. 6, pp. 19–27, 1985.

[44] T.-S. Chu and M. Gans, "High speed infrared local wireless communication," *IEEE Communications Magazine*, vol. 25, no. 8, pp. 4–10, 1987.

[45] R. T. Miyahira and K. Fasen, "Wireless optical communication system," November 1989, US Patent 4,882,770.

[46] R. Ramirez-Iniguez and R. J. Green, "Indoor optical wireless communications," in *Optical Wireless Communications (Ref. No. 1999/128), IEE Colloquium on.* IET, 1999, pp. 14–1.

[47] P. P. Smyth, P. L. Eardley, K. T. Dalton, D. R. Wisely, P. McKee, and D. Wood, "Optical wireless: a prognosis," in *Photonics East'95*. International Society for Optics and Photonics, 1995, pp. 212–225.

[48] A. M. Street, P. N. Stavrinou, D. C. O'Brien, and D. J. Edwards, "Indoor optical wireless systems–a review," *Optical and Quantum Electronics*, vol. 29, no. 3, pp. 349–378, 1997.

[49] H. Le Minh, D. O'Brien, G. Faulkner, O. Bouchet, M. Wolf, L. Grobe, and J. Li, "A 1.25-Gb/s indoor cellular optical wireless communications demonstrator," *IEEE Photonics Technology Letters*, vol. 22, no. 21, pp. 1598–1600, 2010.

[50] K. Werner, "Higher visibility for LEDs," *IEEE spectrum*, vol. 31, no. 7, pp. 30–34, 1994.

[51] S. Nakamura, T. Mukai, and M. Senoh, "Candela-class high-brightness ingan / algan double-heterostructure blue-light-emitting diodes," *Applied Physics Letters*, vol. 64, no. 13, pp. 1687–1689, 1994.

[52] G. Pang, T. Kwan, H. Liu, and C.-H. Chan, "Optical wireless based on high brightness visible LEDs," in *Industry Applications Conference, 1999. Thirty-Fourth IAS Annual Meeting. Conference Record of the 1999 IEEE*, vol. 3. IEEE, 1999, pp. 1693–1699.

[53] Y. Tanaka, T. Komine, S. Haruyama, and M. Nakagawa, "Indoor visible communication utilizing plural white LEDs as lighting," in *Personal, Indoor and Mobile Radio Communications, 2001 12th IEEE International Symposium on*, vol. 2. IEEE, 2001, pp. F–81.

[54] T. Komine and M. Nakagawa, "Fundamental analysis for visible-light communication system using LED lights," *IEEE Transactions on Consumer Electronics*, vol. 50, no. 1, pp. 100–107, 2004.

[55] F.-M. Wu, C.-T. Lin, C.-C. Wei, C.-W. Chen, Z.-Y. Chen, and K. Huang, "3.22-Gb/s WDM visible light communication of a single RGB LED employing carrier-less amplitude and phase modulation," in *Optical Fiber Communication Conference*. Optical Society of America, 2013, pp. OTh1G–4.

[56] "ITU-T recommendation, G.975.1," Feb. 2004.

[57] D. Tsonev, H. Chun, S. Rajbhandari, J. J. McKendry, S. Videv, E. Gu, M. Haji, S. Watson, A. E. Kelly, G. Faulkner *et al.*, "A 3-Gb/s single-LED OFDM-based wireless VLC link using a gallium nitride," *IEEE Photonics Technology Letters*, vol. 26, no. 7, pp. 637–640, 2014.

[58] G. Cossu, W. Ali, R. Corsini, and E. Ciaramella, "Gigabit-class optical wireless communication system at indoor distances (1.5–4 m)," *Optics Express*, vol. 23, no. 12, pp. 15 700–15 705, 2015.

[59] H. Chun, S. Rajbhandari, G. Faulkner, D. Tsonev, E. Xie, J. J. D. McKendry, E. Gu, M. D. Dawson, D. C. O'Brien, and H. Haas, "LED based wavelength division multiplexed 10 Gb/s visible light communications," *Journal of Lightwave Technology*, vol. 34, no. 13, pp. 3047–3052, July 2016.

[60] R. X. Ferreira, E. Xie, J. J. McKendry, S. Rajbhandari, H. Chun, G. Faulkner, S. Watson, A. E. Kelly, E. Gu, R. V. Penty *et al.*, "High bandwidth gan-based micro-leds for multi-gb/s visible light communications," *IEEE Photonics Technology Letters*, vol. 28, no. 19, pp. 2023–2026, 2016.

[61] Navigant Consulting Inc., "Energy savings potential of solid-state lighting in general illumination applications." Available: http://apps1.eere.energy.gov/buildings/publications/pdfs/ssl/ssl_energy-savings-report_jan-2012.pdf

[62] E. T. Won, D. Shin, D. Jung, Y. Oh, T. Bae, H.-C. Kwon, C. Cho, J. Son, D. O'Brien, T.-G. Kang, and T. Matsumura, "Visible light communication tutorial." Available: http://www.ieee802.org/802_tutorials/2008-03/15-08-0114-02-0000-VLC_Tutorial_MCO_Samsung-VLCC-Oxford_2008-03-17.pdf

[63] H. Le Minh, Z. Ghassemlooy, D. O'Brien, and G. Faulkner, "Indoor gigabit optical wireless communications: challenges and possibilities," in *2010 12th International Conference on Transparent Optical Networks*. National Institute of Telecommunications, June 2010, pp. 1–6.

[64] Y. Wang, N. Chi, Y. Wang, L. Tao, and J. Shi, "Network architecture of a high-speed visible light communication local area network," *IEEE Photonics Technology Letters*, vol. 27, no. 2, pp. 197–200, Jan 2015.

[65] PureLiFi^{TM}, "Purelifi," 2016. Available: http://purelifi.com/

[66] H. Haas, L. Yin, Y. Wang, and C. Chen, "What is LiFi?" *Journal of Lightwave Technology*, vol. 34, no. 6, pp. 1533–1544, 2016.

[67] S. Rajagopal, R. D. Roberts, and S.-K. Lim, "IEEE 802.15. 7 visible light communication: modulation schemes and dimming support," *IEEE Communications Magazine*, vol. 50, no. 3, pp. 72–82, 2012.

[68] A. Sewaiwar, S. V. Tiwari, Y. H. Chung, and C. J. Ahn, "Color cell based bidirectional VLC with user mobility," in *2016 IEEE International Conference on Communications Workshops (ICC)*, May 2016, pp. 21–25.

[69] J. Voke, "Radiation effects on the eye," *Part 3b-Ocular effects of ultraviolet radiation. Optometry Today*, pp. 37–40, 1999.

[70] D. J. Heatley, D. R. Wisely, I. Neild, and P. Cochrane, "Optical wireless: the story so far," *IEEE Communications Magazine*, vol. 36, no. 12, pp. 72–74, 1998.

[71] P. P. Smyth, D. Wood, S. Ritchie, and S. Cassidy, "Optical wireless: New enabling transmitter technologies," in *Communications, 1993. ICC '93 Geneva. Technical Program, Conference Record, IEEE International Conference on*, vol. 1, May 1993, pp. 562–566 vol.1.

[72] Cisco, "Fiber types in gigabit optical communications," Cisco Systems, Inc., Tech. Rep. C11-463661-00, 2008.

[73] Fiber to the home council Europe, "Breaking news from the FTTH conference 2016." Available: http://ftthcouncil.eu/documents/PressReleases/2016/PR20160217_FTTHranking_panorama_award.pdf

[74] A. Burger, "Total FTTH subscribers surpass 100 million, one billion subs on the horizon." Available: https://www.benton.org/headlines/report-total-ftth-subscribers-surpass-100-million-one-billion-broadband-\subs-horizon

[75] C. W. Oh, E. Tangdiongga, and A. M. J. Koonen, "Time-sharing resources for low cost and high performance indoor optical wireless networks," in *Optical Communication (ECOC), 2015 European Conference on*. Valencia: IEEE, 2015, pp. 1–3.

[76] W. Guo, P. R. A. Binetti, C. Althouse, L. A. Johansson, and L. A. Coldren, "InP photonic integrated circuit with on-chip tunable laser source for 2D optical beam steering," *Optical Society of America, OFC/NFOEC Technical Digest*, 2013.

[77] H. Ishii, K. Kasaya, H. Oohashi, Y. Shibata, H. Yasaka, and K. Okamoto, "Widely wavelength-tunable DFB laser array integrated with funnel combiner," *IEEE Journal of Selected Topics in Quantum Electronics*, vol. 13, no. 5, pp. 1089–1094, 2007.

[78] Wikipedia, "Laser safety," 2016. Available: https://en.wikipedia.org/wiki/Laser_safety

[79] K. A. Mekonnen, C. W. Oh, A. M. Khalid, N. Calabretta, E. Tangdiongga, and A. M. J. Koonen, "PIC-Assisted high-capacity dynamic indoor network utilizing optical wireless and 60-GHz radio-over-fiber techniques," in *Photonics Society Summer Topical Meeting Series (SUM), 2016 IEEE*. IEEE, 2016, p. TuC4.3.

[80] F. Winkler, E. Fischer, E. Graß, and G. Fischer, "A 60 GHz OFDM indoor localization system based on DTDOA," in *Proc. of the 14th IST Mobile and Wireless Communications Summit*. Citeseer, 2005, pp. 1–5.

[81] G. Cossu, M. Presi, R. Corsini, P. Choudhury, A. M. Khalid, and E. Ciaramella, "A visible light localization aided optical wireless system." in *GLOBECOM Workshops*, 2011, pp. 802–807.

[82] K. Wang, A. T. Nirmalathas, C. Lim, and E. Skafidas, "Experimental demonstration of optical wireless indoor localization system with background light power estimation," in *Optical Fiber Communication Conference*. Optical Society of America, 2015, pp. W2A–63.

[83] A. Gomez, K. Shi, C. Quintana, G. Faulkner, B. C. Thomsen, and D. O'Brien, "A 50 Gb/s transparent indoor optical wireless communications link with an integrated localization and tracking system," *Journal of Lightwave Technology*, vol. 34, no. 10, pp. 2510–2517, 2016.

[84] P. F. McManamon, T. A. Dorschner, D. L. Corkum, L. J. Friedman, D. S. Hobbs, M. Holz, S. Liberman, H. Q. Nguyen, D. P. Resler, R. C. Sharp *et al.*, "Optical phased array technology," *Proceedings of the IEEE*, vol. 84, no. 2, pp. 268–298, 1996.

[85] P. B. Chu, S.-S. Lee, and S. Park, "MEMS: the path to large optical crossconnects," *IEEE Communications Magazine*, vol. 40, no. 3, pp. 80–87, 2002.

[86] E. Pengwang, K. Rabenorosoa, M. Rakotondrabe, and N. Andreff, "Scanning micromirror platform based on MEMS technology for medical application," *Micromachines*, vol. 7, no. 2, p. 24, 2016.

[87] J. D. Zook, "Light beam deflector performance: a comparative analysis," *Applied Optics*, vol. 13, no. 4, pp. 875–887, 1974.

[88] D. J. Pines, D. B. Hakala, and R. Malueg, "Lightweight high-performance dual-axis gimbal for space applications," in *SPIE's 1995 Symposium on OE/Aerospace Sensing and Dual Use Photonics*. International Society for Optics and Photonics, 1995, pp. 261–273.

[89] T. G. Sandwich and D. Backup, "Lightweight mirror structures for mechanical beam steering," *Lincoln Laboratory Journal*, vol. 1, no. 2, 1988.

[90] J. Bowers, R. Helkey, C. Corbalis, R. Sink, S. Lee, N. MacDonald *et al.*, "Micro-electro-mechanical-system (MEMS) mirror device," Feb. 1 2000, US Patent App. 09/497,270.

[91] L. Zhou, J. M. Kahn, and K. S. Pister, "Scanning micromirrors fabricated by an SOI/SOI wafer-bonding process," *Journal of Microelectromechanical Systems*, vol. 15, no. 1, pp. 24–32, 2006.

[92] J. Sun, S. Guo, L. Wu, L. Liu, S.-W. Choe, B. S. Sorg, and H. Xie, "3D in vivo optical coherence tomography based on a low-voltage, large-scan-range 2D MEMS mirror," *Optics Express*, vol. 18, no. 12, pp. 12 065–12 075, 2010.

[93] J.-c. Tsai and M. C. Wu, "Gimbal-less MEMS two-axis optical scanner array with high fill-factor," *Journal of Microelectromechanical Systems*, vol. 14, no. 6, pp. 1323–1328, 2005.

[94] D. M. Burns, V. M. Bright, S. C. Gustafson, and E. A. Watson, "Optical beam steering using surface micromachined gratings and optical phased arrays," in *Optical Science, Engineering and Instrumentation'97*. International Society for Optics and Photonics, 1997, pp. 99–110.

[95] B.-W. Yoo, M. Megens, T. Chan, T. Sun, W. Yang, C. J. Chang-Hasnain, D. A. Horsley, and M. C. Wu, "Optical phased array using high contrast gratings for two dimensional beamforming and beamsteering," *Optics Express*, vol. 21, no. 10, pp. 12 238–12 248, 2013.

[96] A. Tuantranont, V. Bright, J. Zhang, W. Zhang, J. Neff, and Y. Lee, "Optical beam steering using MEMS-controllable microlens array," *Sensors and Actuators A: Physical*, vol. 91, no. 3, pp. 363–372, 2001.

[97] J. Morrison, M. Imboden, T. D. Little, and D. Bishop, "Electrothermally actuated tip-tilt-piston micromirror with integrated varifocal capability," *Optics Express*, vol. 23, no. 7, pp. 9555–9566, 2015.

[98] R. M. Matic, "Blazed phase liquid crystal beam steering," in *OE/LASE'94*. International Society for Optics and Photonics, 1994, pp. 194–205.

[99] S. Khan and N. Riza, "Demonstration of 3-dimensional wide angle laser beam scanner using liquid crystals," *Optics Express*, vol. 12, no. 5, pp. 868–882, 2004.

[100] J. Sun, R. A. Ramsey, Y. Chen, and S.-T. Wu, "Submillisecond-response sheared polymer network liquid crystals for display applications," *Journal of Display Technology*, vol. 8, no. 2, pp. 87–90, 2012.

[101] X. Wang, Z. Huang, Q. Tan, L. Kong, and Q. Qiu, "Stochastic scanning method to shorten acquisition time using liquid crystal optical phased array," *Optical Engineering*, vol. 55, no. 2, pp. 026 109–026 109, 2016.

[102] F. Vasey, F. K. Reinhart, R. Houdre, and J. M. Stauffer, "Spatial optical beam steering with an AlGaAs integrated phased array," *Applied Optics*, vol. 32, no. 18, pp. 3220–3232, 1993.

[103] J. K. Doylend, M. J. R. Heck, J. T. Bovington, J. D. Peters, L. A. Coldren, and J. E. Bowers, "Two-dimensional free-space beam steering with an optical phased array on silicon-on-insulator," *Optics Express*, vol. 19, no. 22, pp. 21 595–21 604, 2011.

[104] J. Hulme, J. Doylend, M. Heck, J. Peters, M. Davenport, J. Bovington, L. Coldren, and J. Bowers, "Fully integrated hybrid silicon two dimensional beam scanner," *Optics Express*, vol. 23, no. 5, pp. 5861–5874, 2015.

[105] K. Van Acoleyen, W. Bogaerts, and R. Baets, "Two-dimensional dispersive off-chip beam scanner fabricated on silicon-on-insulator," *IEEE Photonics Technology Letters*, vol. 23, no. 17, pp. 1270–1272, 2011.

[106] K. Nakamura, J. Miyazu, Y. Sasaki, T. Imai, M. Sasaura, and K. Fujiura, "Space-charge-controlled electro-optic effect: Optical beam deflection by electro-optic effect and space-charge-controlled electrical conduction," *Journal of Applied Physics*, vol. 104, no. 1, p. 013105, 2008.

[107] R. Meyer, "Optical beam steering using a multichannel lithium tantalate crystal," *Applied Optics*, vol. 11, no. 3, pp. 613–616, 1972.

[108] Y. Ninomiya, "Ultrahigh resolving electrooptic prism array light deflectors," *IEEE Journal of Quantum Electronics*, vol. 9, no. 8, pp. 791–795, 1973.

[109] M. Ziemkiewicz, S. R. Davis, S. D. Rommel, D. Gann, B. Luey, J. D. Gamble, and M. Anderson, "Laser-based satellite communication systems stabilized by non-mechanical electro-optic scanners," in *SPIE Defense+ Security*. International Society for Optics and Photonics, 2016, pp. 982 808–982 808.

[110] T. Smith and A. Korpel, "Measurement of light-sound interaction efficiencies in solids," *IEEE Journal of Quantum Electronics*, vol. 1, no. 6, pp. 283–284, 1965.

[111] E. Spencer, P. Lenzo, and K. Nassau, "Optical interactions with elastic waves in lithium niobate," *IEEE Journal of Quantum Electronics*, vol. 2, no. 3, pp. 69–70, 1966.

[112] E. Gordon, "A review of acoustooptical deflection and modulation devices," *Applied Optics*, vol. 5, no. 10, pp. 1629–1639, 1966.

[113] I. Chang, "Acoustooptic devices and applications," *IEEE Transactions on Sonics and Ultrasonics*, vol. 23, no. 1, p. 2, 1976.

[114] A. Korpel, "Acousto-optics – a review of fundamentals," *Proceedings of the IEEE*, vol. 69, no. 1, pp. 48–53, 1981.

[115] F. Mugele and J.-C. Baret, "Electrowetting: from basics to applications," *Journal of Physics: Condensed Matter*, vol. 17, no. 28, p. R705, 2005.

[116] N. R. Smith, D. C. Abeysinghe, J. W. Haus, and J. Heikenfeld, "Agile wide-angle beam steering with electrowetting microprisms," *Optics Express*, vol. 14, no. 14, pp. 6557–6563, 2006.

[117] I. Filinski and T. Skettrup, "Fast dispersive beam deflectors and modulators," *IEEE Journal of Quantum Electronics*, vol. 18, no. 7, pp. 1059–1062, 1982.

[118] Z. Yaqoob, A. A. Rizvi, and N. A. Riza, "Free-space wavelength-multiplexed optical scanner," *Applied Optics*, vol. 40, no. 35, pp. 6425–6438, 2001.

[119] T. K. Chan, J. Karp, R. Jiang, N. Alic, S. Radic, C. F. Marki, and J. E. Ford, "1092 channel 2-D array demultiplexer for ultralarge data bandwidth," *Journal of Lightwave Technology*, vol. 25, no. 3, pp. 719–725, 2007.

[120] S. A. van den Berg, S. van Eldik, and N. Bhattacharya, "Mode-resolved frequency comb interferometry for high-accuracy long distance measurement," *Scientific reports*, vol. 5, 2015.

[121] L. Enloe, J. Murphy, and C. Rubinstein, "Hologram transmission via television," *Bell System Technical Journal*, vol. 45, no. 2, pp. 335–339, 1966.

[122] D. Gabor, "Holography, 1948-1971," *Proceedings of the IEEE*, vol. 60, no. 6, pp. 655–668, June 1972.

[123] S. Piazzolla and B. K. Jenkins, "Holographic grating formation in photopolymers," *Optics Letters*, vol. 21, no. 14, pp. 1075–1077, 1996.

[124] J. P. Huignard, A.-M. Roy, and C. Slezak, "Electro-optical deflection apparatus using holographic grating," Sep. 1976.

[125] R. L. Forward, "Passive beam-deflecting apparatus," U.S. Patent 3 612 659 A, 1971.

[126] Z. Yaqoob, M. A. Arain, and N. A. Riza, "High-speed two-dimensional laser scanner based on Bragg gratings stored in photothermorefractive glass," *Applied Optics*, vol. 42, no. 26, pp. 5251–5262, 2003.

[127] Z. Yaqoob and N. A. Riza, "Low-loss wavelength-multiplexed optical scanners using volume Bragg gratings for transmit-receive lasercom systems," *Optical Engineering*, vol. 43, no. 5, pp. 1128–1135, 2004.

[128] M. K. Smit and C. Van Dam, "Phasar-based wdm-devices: Principles, design and applications," *IEEE Journal of selected topics in quantum electronics*, vol. 2, no. 2, pp. 236–250, 1996.

[129] X. J. Leijtens, B. Kuhlow, and M. K. Smit, "Arrayed waveguide gratings," in *Wavelength Filters in Fibre Optics*. Springer, 2006, pp. 125–187.

[130] M. Smit, "New focusing and dispersive planar component based on an optical phased array," *Electronics Letters*, vol. 24, no. 7, p. 385, 1988.

[131] H. Takahashi, S. Suzuki, K. Kato, and I. Nishi, "Arrayed-waveguide grating for wavelength division multi/demultiplexer with nanometre resolution," *Electronics letters*, vol. 26, no. 2, pp. 87–88, 1990.

[132] C. Dragone, "An n* n optical multiplexer using a planar arrangement of two star couplers," *IEEE Photonics Technology Letters*, vol. 3, no. 9, pp. 812–815, 1991.

[133] T. Chan, E. Myslivets, and J. E. Ford, "2-Dimensional beamsteering using dispersive deflectors and wavelength tuning," *Optics Express*, vol. 16, no. 19, pp. 14 617–14 628, 2008.

[134] K. Takada, M. Abe, T. Shibata, and K. Okamoto, "5 GHz-spaced 4200-channel two-stage tandem demultiplexer for ultra-multi-wavelength light source using supercontinuum generation," *Electronics Letters*, vol. 38, no. 12, p. 1, 2002.

[135] S. O. Kasap, *Optoelectronics & Photonics: Principles & Practices: International Edition*. Pearson Higher Ed, 2001.

[136] M. K. Giles, R. Hughes, and J. Thompson, "Angular dispersion of diffraction gratings used for tuning organic dye lasers," *Applied Optics*, vol. 12, no. 2, pp. 421–422, 1973.

[137] A. Balakrishnan, S. Bidnyk, and M. Pearson, "Double diffraction grating with flat passband output," US Patent 7,149,387, Dec., 2006.

[138] C. A. Palmer and E. G. Loewen, *Diffraction grating handbook*. Newport Corporation Springfield, Ohio, USA, 2005.

[139] J. Workman Jr and A. Springsteen, *Applied spectroscopy: a compact reference for practitioners*. Academic Press, 1998.

[140] M. Born and E. Wolf, *Principles of optics: electromagnetic theory of propagation, interference and diffraction of light*. CUP Archive, 2000.

[141] M. Shirasaki, "Large angular dispersion by a virtually imaged phased array and its application to a wavelength demultiplexer," *Optics Letters*, vol. 21, no. 5, pp. 366–368, 1996.

[142] M. Shirasaki, "Virtually imaged phased array," *Fujitsu Scientific & Technical Journal*, vol. 35, no. 1, pp. 113–125, 1999.

[143] T. Koonen, J. Oh, K. Mekonnen, Z. Cao, and E. Tangdiongga, "Ultra-high capacity indoor optical wireless communication using 2D-steered pencil beams," *Journal of Lightwave Technology*, vol. 34, no. 20, pp. 4802–4809, Oct 2016.

[144] H. Kosaka, T. Kawashima, A. Tomita, M. Notomi, T. Tamamura, T. Sato, and S. Kawakami, "Photonic crystals for micro lightwave circuits using wavelength-dependent angular beam steering," *Applied Physics Letters*, vol. 74, no. 10, pp. 1370–1372, 1999.

[145] K. Wang, A. Nirmalathas, C. Lim, and E. Skafidas, "High-speed duplex optical wireless communication system for indoor personal area networks," *Optics Express*, vol. 18, no. 24, pp. 25 199–25 216, 2010.

[146] K. Wang, A. Nirmalathas, C. Lim, and E. Skafidas, "4 x 12.5 Gb/s WDM optical wireless communication system for indoor applications," *J. Lightwave Technol.*, vol. 29, no. 13, pp. 1988–1996, Jul 2011. Available: http://jlt.osa.org/abstract.cfm?URI=jlt-29-13-1988

[147] K. Wang, A. Nirmalathas, C. Lim, and E. Skafidas, "Experimental demonstration of a full-duplex indoor optical wireless communication system," *IEEE Photonics Technology Letters*, vol. 24, no. 3, pp. 188–190, 2012.

[148] P. Brandl, S. Schidl, A. Polzer, W. Gaberl, and H. Zimmermann, "Optical wireless communication with adaptive focus and MEMS-based beam steering," *IEEE Photonics Technology Letters*, vol. 25, no. 15, pp. 1428–1431, 2013.

[149] A. Gomez, K. Shi, C. Quintana, M. Sato, G. Faulkner, B. C. Thomsen, and D. O'Brien, "Beyond 100-Gb/s indoor wide field-of-view optical wireless communications," *IEEE Photonics Technology Letters*, vol. 27, no. 4, pp. 367–370, 2015.

[150] N. A. Riza, "Reconfigurable optical wireless," in *LEOS'99. IEEE Lasers and Electro-Optics Society 1999 12th Annual Meeting*, vol. 1. IEEE, 1999, pp. 70–71.

[151] N. A. Riza and Y. Huang, "High speed optical scanner for multi-dimensional beam pointing and acquisition," in *LEOS'99. IEEE Lasers and Electro-Optics Society 1999 12th Annual Meeting*, vol. 1. IEEE, 1999, pp. 184–185.

[152] K. Liang, H. Shi, S. J. Sheard *et al.*, "Transparent optical wireless hubs using wavelength space division multiplexing," in *Optical Science and Technology, the SPIE 49th Annual Meeting*. International Society for Optics and Photonics, 2004, pp. 80–87.

[153] H. Shi, K. Liang, S. J. Sheard, D. C. O'Brien, and G. E. Faulkner, "Two-dimensional wavelength routing for transparent optical wireless networking," in *Optics & Photonics 2005*. International Society for Optics and Photonics, 2005, pp. 58 920Z–58 920Z.

[154] C. W. Oh, E. Tangdiongga, and A. M. J. Koonen, "Steerable pencil beams for multi-Gbps indoor optical wireless communication," *Optics Letters*, vol. 39, no. 18, pp. 5427–5430, 2014.

[155] C. W. Oh, R. van der Linden, G. Sutorius, E. Tangdiongga, and A. M. J. Koonen, "2D passive optical beam-steering module with 7 scan lines within $12.2^\circ \times 5.6^\circ$ for free-space indoor communication," in *European Conference on Optical Communication (ECOC), 18-22 September*, Düsseldorf, Germany, 2016, paper Tu2.C.

[156] A. M. J. Koonen, C. W. Oh, and E. Tangdiongga, "Reconfigurable free-space optical indoor network using multiple pencil beam steering," in *19th Optoelectronics and Communications Conference (OECC) and the 39th Australian Conference on Optical Fibre Technology (ACOFT)*. Engineers Australia, 2014, p. 204.

[157] A. M. J. Koonen, P. G. Baltus, and A. Liotta, "Two-dimensional optical beam steering module," US Patent 9,246,589, Jan., 2016, US Patent 9,246,589.

[158] A. M. J. Koonen, J. Oh, K. Mekonnen, and E. Tangdiongga, "Ultra-high capacity indoor optical wireless communication using steered pencil beams," in *Microwave Photonics (MWP), 2015 International Topical Meeting on.* IEEE, 2015, pp. 1–4.

[159] T. Koonen, J. Oh, A. Khalid, K. Mekonnen, M. T. Vega, Z. Cao, and E. Tangdiongga, "2D beam-steered high-capacity optical wireless communication," in *Photonics Society Summer Topical Meeting Series (SUM), 2016 IEEE.* IEEE, 2016, pp. 132–133.

[160] T. Koonen, J. Oh, K. Mekonnen, Z. Cao, and E. Tangdiongga, "Ultra-high capacity indoor optical wireless communication using 2D-steered pencil beams," *Journal of Lightwave Technology*, vol. 34, no. 20, pp. 4802–4809, Oct 2016.

[161] Newport Corporation, "Echelle gratings," 2016. Available: #http://www.gratinglab.com/Products/Product_Tables/T3.aspx#

[162] Newport, "DIFFRACTION GRATING SPECIFICATION SHEET." Available: http://www.gratinglab.com/Products/Product_Tables/Efficiency/Efficiency.aspx?catalog=53-*-182E

[163] Thorlabs, "Triplet fiber optic collimators/couplers." Available: https://www.thorlabs.de/newgrouppage9.cfm?objectgroup_id=5124&pn=TC18FC-1550#7057

[164] Ibsen, "Ping-sample-083." Available: http://ibsen.com/products/transmission-gratings/ping-telecom-gratings/telecom-c-band-gratings/ping-sample-083

[165] R. P. Encyclopedia, "M^2 factor." Available: https://www.rp-photonics.com/m2_factor.html

[166] K. Schneider and H. Zimmermann, *Highly sensitive optical receivers.* Springer, 2006.

[167] J. Lee, "Discrete multitone modulation for short-range optical communications," Ph.D. dissertation, Eindhoven University of Technology, 2009.

[168] K. D. Langer, *Visible Light Communication.* Cambridge: Cambridge University Press. Cambridge Books Online, February 2015, ch. DMT modulation for VLC.

[169] Corning, "Corning®SMF-28e+®photonic optical fiber," 2010. Available: https://www.corning.com/media/worldwide/csm/documents/Corning%20SMF28e%2B%C2%AE%20Photonic%20Specialty%20Fiber.pdf

[170] H. Kogelnik and T. Li, "Laser beams and resonators," *Applied Optics*, vol. 5, no. 10, pp. 1550–1567, 1966.

[171] J. Alda, "Laser and gaussian beam propagation and transformation," *Encyclopedia of Optical Engineering*, vol. 2013, pp. 999–1013, 2003.

[172] K. Schulmeister, R. Gilber, F. Edthofer, B. Seiser, and G. Vees, "Comparison of different beam diameter definitions to characterize thermal damage of the eye," in *Lasers and Applications in Science and Engineering*. International Society for Optics and Photonics, 2006, pp. 61 011A–61 011A.

[173] P. Kułakowski, J. Vales-Alonso, E. Egea-López, W. Ludwin, and J. García-Haro, "Angle-of-arrival localization based on antenna arrays for wireless sensor networks," *Computers & Electrical Engineering*, vol. 36, no. 6, pp. 1181–1186, 2010.

[174] A. Pérez Oliveros, "Automated alignment system for indoor optical wireless system," Master's thesis, Eindhoven University of Technology, 2015.

[175] S. Ruder, "An overview of gradient descent optimization algorithms," *arXiv preprint arXiv:1609.04747*, 2016.

[176] National Instruments, "What can you do with labview?" Available: http://www.ni.com/labview/why/

[177] R. Bitter, T. Mohiuddin, and M. Nawrocki, *LabVIEW: Advanced programming techniques*. CRC Press, 2006.

[178] P. Brugarolas and W. Breckenridge, "Efficient algorithm for rectangular spiral search," 2008.

[179] C. W. Oh, F. M. Huijskens, Z. Cao, E. Tangdiongga, and A. M. J. Koonen, "Toward multi-Gbps indoor optical wireless multicasting system employing passive diffractive optics," *Optics Letters*, vol. 39, no. 9, pp. 2622–2625, 2014.

[180] R. B. Passey, R. L. Gillum, and J. B. Fuller, "Measurement of spectral bandwidth, as exemplified with the beckman" enzyme analyzer system TR spectrophotometer"," *Clinical chemistry*, vol. 21, no. 11, pp. 1582–1584, 1975.

[181] C. W. Oh, E. Tangdiongga, and A. M. J. Koonen, "Simultaneous 1.5 Gbps multilink indoor optical wireless system using diffractive optics," in *Proceedings of the 18th Annual Symposium of the IEEE Photonics Benelux*, 2013, pp. 121–124.

[182] M. M. Tilleman, A. Kozhekin, R. Cohen, D. Haronian, and I. Nusinsky, "Coupling losses in multimode waveguides due to misalignment," *IEE Proceedings - Optoelectronics*, vol. 152, no. 3, pp. 145–150, June 2005.

[183] S. Yuan and N. A. Riza, "General formula for coupling-loss characterization of single-mode fiber collimators by use of gradient-index rod lenses," *Applied optics*, vol. 38, no. 15, pp. 3214–3222, 1999.

[184] Keysight Technologies, "Keysight n7786b polatization synthesizer." Available: http://literature.cdn.keysight.com/litweb/pdf/5989-8115EN.pdf

[185] Keysight Technologies, "IL and PDL spectra with the n7786b polarization synthesizer and the n7700a photonic application suite." Available: http://literature.cdn.keysight.com/litweb/pdf/5990-3779EN.pdf

[186] C. W. Oh, Z. Cao, E. Tangdiongga, and A. M. J. Koonen, "Free-space transmission with passive 2D beam steering for multi-gigabit-per-second per-beam indoor optical wireless networks," *Optics Express*, vol. 24, no. 17, pp. 19 211–19 227, 2016.

[187] Richardson Gratings, "Technical note 6: Echelle gratings," Tech. Rep., 1971. Available: http://www.gratinglab.com/Information/Technical_Notes/TechNote6.aspx

[188] C. W. Oh, E. Tangdiongga, and A. M. J. Koonen, "42.8 Gbit/s indoor optical wireless communication with 2-dimensional optical beam-steering," in *Optical Fiber Communication Conference*. Optical Society of America, 2015, pp. M2F–3.

[189] Y.-L. Yu, S.-K. Liaw, E. Skaljo, H. L. Minh, and Z. Ghassemlooy, "Bidirectional wavelength reconfigurable module based on tunable fiber bragg grating and remote pump amplifier," *Fiber and Integrated Optics*, vol. 33, no. 5-6, pp. 383–394, 2014.

[190] C. W. Oh, Z. Cao, E. Tangdiongga, and T. Koonen, "10 Gbps all-optical full-duplex indoor optical wireless communication with wavelength reuse," in *Optical Fiber Communication Conference*. Optical Society of America, 2016, pp. Th4A–6.

[191] C. W. Oh, Z. Cao, K. A. Mekonnen, E. Tangdiongga, and A. M. J. Koonen, "Low-crosstalk full-duplex all-optical indoor wireless transmission with carrier recovery," *IEEE Photonics Technology Letters*, 2017, (accepted).

[192] H. Takesue and T. Sugie, "Wavelength channel data rewrite using saturated SOA modulator for WDM networks with centralized light sources," *Journal of Lightwave Technology*, vol. 21, no. 11, pp. 2546–2556, 2003.

[193] Agilent Technologies, "Measuring extinction ratio of optical transmitters," 2016. Available: http://cp.literature.agilent.com/litweb/pdf/5966-4316E.pdf

[194] C. DeCusatis, *Handbook of fiber optic data communication: a practical guide to optical networking.* Academic Press, 2013.

[195] C. Wagner, M. Eiselt, S. Zou, M. Lawin, B. Teipen, K. Grobe, J. V. Olmos, and I. T. Monroy, "Wavelength-agnostic wdm-pon system," in *Transparent Optical Networks (ICTON), 2016 18th International Conference on.* IEEE, 2016, pp. 1–4.

[196] H. Hsu, W. Lu, Z. Ghassemlooy, H. Le Minh, Y. Yu, and S. Liaw, "Dwdm bidirectional wavelength reuse optical wireless transmission in 2× 80 gbit/s capacity," in *Optical Wireless Communications (IWOW), 2013 2nd International Workshop on.* IEEE, 2013, pp. 128–131.

[197] S. T. Stopinski, "InP-based photonic integrated circuits for high-speed data readout systems," Ph.D. dissertation, Eindhoven University of technology, 2014.

[198] Q. Feng, W. Li, Q. Zheng, J. Han, J. Xiao, Z. He, M. Luo, Q. Yang, and S. Yu, "Impacts of backscattering noises on upstream signals in full-duplex bidirectional pons," *Optics express*, vol. 23, no. 12, pp. 15 575–15 586, 2015.

[199] Q. Guo and A. V. Tran, "Mitigation of rayleigh noise and dispersion in ream-based wdm-pon using spectrum-shaping codes," *Optics express*, vol. 20, no. 26, pp. B452–B461, 2012.

[200] V. Bhatt, "Cross-talk in bi-directional, single wavelength, single fiber gigabit ethernet links," *URL: http://www. ieee802. org/3/efm/public/jul01/bhatt_1_0701. pdf*, 2001.

[201] K. A. Mekonnen, C. Oh, Z. Cao, N. M. Tessema, E. Tangdiongga, and A. M. J. Koonen, "Reconfigurable optical backbone network for ultra-high capacity indoor wireless communication," in *International Topical Meeting on Microwave Photonics (MWP), 2-6 October*, Hawaii, USA, 2016, paper TuM1.3.

[202] A. Ryer and V. Light, "Light measurement handbook," 1997.

[203] K. T. McDonald, "Intensity, brightness andetendue of an aperture lamp," 2013.

[204] H. Zhu and P. Blackborow, "Etendue and optical throughput calculations," 2011. Available: http://www.energetiq.com/TechLibrary/Technical_Notes/Etendue%20and%20Optical%20Throughput%20Calculations%20-%20Feb%202011.pdf

[205] R. Baets and G. Roelkens, "Fotonica Photonics," *Universiteit Gent,(syllabus 2010-2011)*, 2015.

[206] A. Nicia, "Lens coupling in fiber-optic devices: efficiency limits," *Applied optics*, vol. 20, no. 18, pp. 3136–3145, 1981.

[207] Thorlabs, "Single mode fiber 980 to 1600 nm," 2017. Available: https://www.thorlabs.com/newgrouppage9.cfm?objectgroup_id=949

[208] Thorlabs, "Graded-index multimode fibers," 2017. Available: https://www.thorlabs.com/newgrouppage9.cfm?objectgroup_id=358

[209] Thorlabs, "Step-index multimode fiber, 0.50 na," 2017. Available: https://www.thorlabs.com/newgrouppage9.cfm?objectgroup_id=362

[210] New Focus, "12-GHz amplified free-space photoreceivers." Available: http://assets.newport.com/webDocuments-EN/images/15173.PDF

[211] G. Keiser, *Optical fiber communications*. Wiley Online Library, 2000.

[212] J. Carruther and J. M. Kahn, "Angle diversity for nondirected wireless infrared communication," *IEEE Transactions on Communications*, vol. 48, no. 6, pp. 960–969, 2000.

[213] G. W. Marsh and J. M. Kahn, "50-Mb/s diffuse infrared free-space link using on-off keying with decision-feedback equalization," *IEEE Photonics Technology Letters*, vol. 6, no. 10, pp. 1268–1270, 1994.

[214] J. R. Barry and J. M. Kahn, "Link design for nondirected wireless infrared communications," *Applied Optics*, vol. 34, no. 19, pp. 3764–3776, 1995.

[215] D. V. Hahn, D. M. Brown, N. W. Rolander, J. E. Sluz, and R. Venkat, "Fiber optic bundle array wide field-of-view optical receiver for free space optical communications," *Optics Letters*, vol. 35, no. 21, pp. 3559–3561, 2010.

[216] Discovery Semiconductors, "10 GHz linear InGaAs PIN+TIA optical receiver with optional CDR," 2016. Available: http://www.discoverysemi.com/Product_Pages/DSCR402PIN.php

[217] A. R. Dias, R. F. Kalman, J. W. Goodman, and A. A. Sawchuk, "Fiber-optic crossbar switch with broadcast capability," *Optical Engineering*, vol. 27, no. 11, 1988.

[218] A. M. Khalid, A. M. J. Koonen, C. W. Oh, Z. Cao, K. A. Mekonnen, and E. Tangdiongga, "10 Gbps indoor optical wireless communication employing 2D passive beam steering based on arrayed waveguide gratings," in *Photonics Society Summer Topical Meeting Series (SUM), 2016 IEEE*. IEEE, 2016, pp. 134–135.

[219] T. Koonen, J. Oh, A. Khalid, K. A. Mekonnen, M. T. Vega, Z. Cao, and E. Tangdiongga, "2D beam-steered high-capacity optical wireless communication," in *IEEE Photonics Society Summer Topical Meeting Series (SUM),26-30 September*, NewPort Beach, California, USA, 2016, paper TuC2.2.

[220] K. A. Mekonnen, C. W. Oh, J. H. C. van Zantvoort, N. Calabretta, E. Tangdiongga, and A. M. J. Koonen, "Over 40 Gb/s dynamic bidirectional all-optical indoor wireless communication using photonic integrated circuits," in *Optical Fiber Communication Conference (OFC), 19-23 March*, Los Angeles, California, USA, 2017, (paper Tu2F.1, accepted).

[221] M. J. Heck, J. F. Bauters, M. L. Davenport, J. K. Doylend, S. Jain, G. Kurczveil, S. Srinivasan, Y. Tang, and J. E. Bowers, "Hybrid silicon photonic integrated circuit technology," *IEEE Journal of Selected Topics in Quantum Electronics*, vol. 19, no. 4, pp. 6 100 117–6 100 117, 2013.

[222] M. J. Heck, "Highly integrated optical phased arrays: photonic integrated circuits for optical beam shaping and beam steering," *Nanophotonics*, vol. 6, no. 1, pp. 93–107, 2017.

[223] A. Yaacobi, J. Sun, M. Moresco, G. Leake, D. Coolbaugh, and M. R. Watts, "Integrated phased array for wide-angle beam steering," *Optics letters*, vol. 39, no. 15, pp. 4575–4578, 2014.

[224] R. Baets, A. Z. Subramanian, S. Clemmen, B. Kuyken, P. Bienstman, N. Le Thomas, G. Roelkens, D. Van Thourhout, P. Helin, and S. Severi, "Silicon photonics: silicon nitride versus silicon-on-insulator," in *Optical Fiber Communications Conference and Exhibition (OFC), 2016*. IEEE, 2016, pp. 1–3.

[225] W. Guo, P. R. A. Binetti, C. Althouse, M. L. Mašanović, H. P. Ambrosius, L. A. Johansson, and L. A. Coldren, "Two-dimensional optical beam steering with InP-based photonic integrated circuits," *IEEE*

Journal of Selected Topics in Quantum Electronics, vol. 19, no. 4, pp. 6 100 212–6 100 212, 2013.

[226] L. A. Coldren, "Monolithic tunable diode lasers," *IEEE Journal of Selected Topics in Quantum Electronics*, vol. 6, no. 6, pp. 988–999, 2000.

[227] J. E. Simsarian, M. C. Larson, H. E. Garrett, H. Xu, and T. A. Strand, "Less than 5-ns wavelength switching with an sg-dbr laser," *IEEE photonics technology letters*, vol. 18, no. 4, pp. 565–567, 2006.

[228] F. Xiao, W. Hu, and A. Xu, "Optical phased-array beam steering controlled by wavelength," *Applied optics*, vol. 44, no. 26, pp. 5429–5433, 2005.

[229] K. Van Acoleyen, H. Rogier, and R. Baets, "Two-dimensional optical phased array antenna on silicon-on-insulator," *Optics express*, vol. 18, no. 13, pp. 13 655–13 660, 2010.

[230] J. Sun, E. Timurdogan, A. Yaacobi, Z. Su, E. S. Hosseini, D. B. Cole, and M. R. Watts, "Large-scale silicon photonic circuits for optical phased arrays," *IEEE Journal of Selected Topics in Quantum Electronics*, vol. 20, no. 4, pp. 1–15, 2014.

[231] J. Sun, E. Timurdogan, A. Yaacobi, E. S. Hosseini, and M. R. Watts, "Large-scale nanophotonic phased array," *Nature*, vol. 493, no. 7431, pp. 195–199, 2013.

[232] C. V. Poulton, M. J. Byrd, M. Raval, Z. Su, N. Li, E. Timurdogan, D. Coolbaugh, D. Vermeulen, and M. R. Watts, "Large-scale silicon nitride nanophotonic phased arrays at infrared and visible wavelengths," *Optics Letters*, vol. 42, no. 1, pp. 21–24, 2017.

[233] J. Doylend, M. Heck, J. Bovington, J. Peters, M. Davenport, L. Coldren, and J. Bowers, "Hybrid iii/v silicon photonic source with integrated 1d free-space beam steering," *Optics letters*, vol. 37, no. 20, pp. 4257–4259, 2012.

[234] Finisar, "Optical transceivers," 2017. Available: https://www.finisar.com/optical-transceivers?f[0]=field_protocol_general%3AEthernet

[235] C. Singh, J. John, Y. N. Singh, and K. Tripathi, "A review of indoor optical wireless systems," *IETE Technical review*, vol. 19, no. 1-2, pp. 3–17, 2002.

Curriculum Vitae

Chin Wan (Joanne) Oh started working towards the Ph.D. degree at the Technical University of Eindhoven in 2013. She received her B. Eng. (hons.) degree in Electronics majoring in Optical Engineering from Multimedia University in Malaysia (2006). She received her Erasmus Mundus MSc. in Photonics from Ghent University and Vrije Universiteit Brussel in Belgium (2010), and KTH Royal Institute of Technology in Sweden (2011).

Prior to her postgraduate studies, she was attached to Avago Technologies as an optics design engineer (2006) and was shortly after, awarded a fellow of the Yayasan Tuanku Fauziah foundation with its mission Women in Search of Excellence. Following this, she was offered and completed a comprehensive on-job training by Siemens Malaysia as a Siemens scholar in the Integrated Business Solutions (2007) and Siemens IT Solutions & Services (Germany) (2007). Subsequently, she was assigned to their Osram R&D Asia facility as a process development lighting engineer (2008) and later, as a project leader in product development for solid state lighting (2009).

Her current research interest is on optical wireless communication, optics, Light Emitting Diode (LED) lighting and system development.